Distribution Agreement

In presenting this thesis or dissertation as a partial fulfillment of the requirements for an advanced degree from Emory University, I hereby grant to Emory University and its agents the non-exclusive license to archive, make accessible, and display my thesis or dissertation in whole or in part in all forms of media, now or hereafter known, including display on the world wide web. I understand that I may select some access restrictions as part of the online submission of this thesis or dissertation. I retain all ownership rights to the copyright of the thesis or dissertation. I also retain the right to use in future works (such as articles or books) all or part of this thesis or dissertation.

Signature:

_____ _____

Amber M. Scharnow Date

Leveraging Chemical Tools to Target Bacterial Membranes
and Combat Antimicrobial Resistance

By

Amber M. Scharnow

Doctor of Philosophy

Chemistry

_____

William, M. Wuest, Ph.D.
Advisor

_____

Jennifer M. Heemstra, Ph.D.
Committee Member

_____

Katherine M. Davis, Ph.D.
Committee Member

Accepted:

_____

Kimberly J. Arriola, Ph.D.
Dean of the James T. Laney School of Graduate Studies

_____

Date

Leveraging Chemical Tools to Target Bacterial Membranes and Combat Antimicrobial Resistance

By

Amber M. Scharnow
B.A., Barnard College of Columbia University, 2017

Advisor: William M. Wuest, Ph.D.

An abstract of
A dissertation submitted to the Faculty of the
James T. Laney School of Graduate Studies of Emory University
in partial fulfillment of the requirements for the degree of
Doctor of Philosophy in Chemistry
2022

Abstract

Leveraging Chemical Tools to Target Bacterial Membranes
and Combat Antimicrobial Resistance

By Amber M. Scharnow

The need for antibacterials with novel mechanisms of action is dire, particularly in the face of the COVID-19 pandemic. The drastic increases in mis-prescriptions, hospital visits, and use of antibacterials have created a perfect storm for antimicrobial resistance. To combat this looming public health crisis, a diverse range of strategies must be employed, as tapping into new biological and druggable spaces enhances the likelihood of evading resistance mechanisms. The work described herein uses a multi-faceted approach that includes natural product total synthesis, diverted total synthesis, and simplification, as well as small molecule derivatization. The first project I detail focuses on the diverted total synthesis of carolacton, a natural product that exhibits a unique, acid-mediated anti-biofilm effect against *Streptococcus mutans*. Through the development of a second generation of simplified carolacton analogs, we discovered a more potent compound that enabled the identification of a novel *Streptococcus* protein target, glucan-binding protein B (GbpB). This molecule is the first compound to target an essential bacterial cell wall division hydrolase and provides a fruitful starting point for further tool and antibiotic development to treat Streptococcal infections. Additionally, we demonstrated enzymatic activity of the full length, recombinant protein for the first time, which will enable drug discovery campaigns. The second project outlines progress toward the total synthesis of α-santal-11-en-10-one, an inhibitor of *S. mutans* and *Porphyromonas gingivalis,* that likely works via a cell membrane mechanism. This molecule displays more potent activity against the Gram-negative strain, which challenges the typical paradigm and suggests a unique target. The final project aimed to develop improved quaternary phosphonium compounds (QPCs) inspired by the cannon of work on their nitrogen counterparts, the quaternary ammonium compounds (QACs). We identified a scaffold that outcompetes the best-in-class quaternary ammonium compounds (QACs) from our lab and the best-in-class antibacterials currently used. Most importantly, this compound displays a unique resistance profile signifying a new mechanism of action. Collectively this thesis highlights the utility of chemical synthesis and chemical biology in the pursuit of antibiotic development and the fight against antimicrobial resistance.

Leveraging Chemical Tools to Target Bacterial Membranes and Combat Antimicrobial Resistance

By

Amber M. Scharnow
B.A., Barnard College of Columbia University, 2017

Advisor: William M. Wuest, Ph.D.

A dissertation submitted to the Faculty of the
James T. Laney School of Graduate Studies of Emory University
in partial fulfillment of the requirements for the degree of
Doctor of Philosophy in Chemistry
2022

Acknowledgements

Firstly, I would like to thank my advisor, Bill, for guiding me through my career path and giving me opportunities to succeed. Working in his lab has allowed me to grow as a scientist, mentor, writer, and more. I would also like to thank him for recognizing my love for biology even before I did.

Throughout my time in the Wuest lab, I have had the wonderful opportunity of working with and befriending so many wonderful people. I would like to thank Dr. Amy Solinski for being the best mentor I could have asked for. Her enthusiasm for science is contagious and she made work fun every single day. She taught me to push for projects that I believe in and to believe in myself. I would also like to thank the fifth years for going on this crazy adventure with me. I can't imagine going through it with anyone else. I would also like to thank Savannah Post and Cassie Schrank for their unconditional love, support, and friendship in and out of the lab. I want to thank Marina Michaud and Christian Sanchez for joining me on the QPC and carolacton projects, respectively. It has been such a joy mentoring and working with you both. I cannot wait to see where the projects go. I also want to thank Marina Michaud and Martina Golden for editing my thesis.

Throughout graduate school, I have had the fortunate opportunity to facilitate a bicoastal and international collaboration. I would like to thank the Dr. Hui Wu and Dr. Hua Zhang at Oregon Health and Science University, Dr. Ines Hübner and Dr. Stephan Sieber at the Technical University of Munich, Dr. Daria Van Tyne at the University of Pittsburgh, and Dr. Meghan Blackledge at High Point University. I would like to separately acknowledge Dr. Dan Kahne at Harvard University for giving me the opportunity to push my research in new and exciting directions. I would also like to thank the members of the Kahne lab and Walker lab, Dr. Vadim Baidin, Sebastian Rowe, and Julia Page, for their mentorship, patience, guidance, and continuous efforts on the carolacton project.

Outside of lab, there are so many others who have enriched my life over the last five years.

I would like to thank Brea Manuel for being such an incredible friend and cheerleader. They always believe in me even when I do not. I would like to thank Andrew Mahoney for his nightly hilarious snapchats and endless humor. I want to thank Erika Csatary and Donovan Workman for their friendship and for always being ready for a double date. My friends from college and from home have remained pillars in my life throughout this time and I cannot express my gratitude enough.

My family has also been instrumental in my journey. I would like to thank my mom, stepdad, sister, and niece for their endless love and support. I would like to thank Rachel for being my rock during my lowest times of graduate school and life, and my biggest cheerleader in moments of triumph. Living life with her has been one of the greatest experiences I could have asked for and I can't wait to continue this journey. Lastly, I want to thank Drew. Without him, I wouldn't be here today. His love and support have carried me through the years, and I have cherished every moment.

Table of Contents

List of figures:

List of Schemes:

List of Tables:

Abbreviations

$(COCl)_2$ – oxalyl chloride
9-BBN – 9-borabicyclo(3.3.1)nonane
A.a – Aggregatibacter actinomycetemcomitans
Ack – acetate kinase
AcOH – acetic acid
ADP – adenosine diphosphate
AgDS – agmatine deiminase; two-component system
AgI/II – antigen I/II surface proteins
ATP – adenosine triphosphate
ATR – acid tolerance response
BOS- Biology oriented synthesis
BCA – bicinchoninic acid protein assay
BrpA – biofilm regulatory protein A
BzCl – benzoyl chloride
CcpA – carbon catabolite protein A
CFU/mL – colony forming unit per milliliter
CLMS – Confocal laser microscopy
CodY – global regulator
ComDE – two-component system; recognizes CSP
CSA – camphorsulfonic acid
CSP – competence stimulating peptide
ddH_2O – double-distilled water
DDQ – 2,3-Dichloro-5,6-Dicyanobenzoquinone
DexA – dextranase A
DIBAL-H – diisobutylaluminum hydride
DivIVa – cell division proteins
DMA – dimethylacetamide
DMAP – 4-dimethylaminopyridine
DMP – Dess-Martin periodane
DMSO – dimethyl sulfoxide
DNA – deoxyribonucleic acid
DSO- double strand replication origin
DTS – diverted total synthesis
DTT – dithiothreitol
EDC – coupling reagent; 1-ethyl-3-(3-dimethylaminopropyl)carbodiimide
EPS – extracellular polymeric substances
EzrA – cell shape regulator
FolD – folate dehydrogenase
FruA – fructosidase
Ftf – fructosyltransferase
FtsA – cell division protein
FtsX – cell division protein

G – glycine
GbpB – glucan binding protein B
GbpC – glucan binding protein C
GFP – green fluorescent protein
GlnA – glutamine synthase
GlnR – controls nitrogen assimilation into cell
Gtfs – Glucosyltransferases
HEPES – (4-(2-hydroxyethyl)-1piperazineethanesulfonic acid
HF•pyr – hydrogen fluoride pyridine
HGT-horizontal gene transfer
iPrOH – isopropyl alcohol
KD – binding affinity; dissociation constant
L – leucine
LFQ – Label free quantification
$LiAlH_4$ – lithium aluminum hydride
LiHMDS – lithium hexamethyldisilazide,
LiOH – lithium hydroxide
MBC – minimum bactericidal concentration
MBIC – minimum biofilm inhibition concentration
mbrABCD – genes associated with bacitracin resistance
MeCN – acetonitrile
MeOH – methanol
MIC – minimum inhibition concentration
MNBA – 2-methyl-6-nitrobenzoic anhydride
MS – mass spectrometry
$NaClO_2$ – sodium chlorite
$NaIO_4$ – sodium periodate
NaOCl – sodium hypochlorite
NEt3 – triethylamine
P – proline
PBS – phosphate buffer saline solution
PcsB – peptidoglycan hydrolase
Pd/C – palladium on carbon, loading 10 wt. %
PknB – serine/threonine-protein kinase B
PMB – p-methoxybenzyl
PPI – protein-protein interaction
PPTS – pyridimium p-toluenesulfonic acid.
Pta – phosphotransacetylase
pTSA – p-Toluenesulfonic acid
PyrR – regulates transcription of pyrimidine nucleotide
QPC- Quaternary phosphonium compounds
QS – quorum sensing
RCM – ring closing metathesis
RhN_3 – rhodium azide

RT – room temperature
SAR – structure-activity relationship
SDS – sodium dodecyl sulfate
SrtA – sortase A
SSO- single strand replication origin
T – threonine
TBAF – tetra-n-butylammonium fluoride
TBAI – tetrabutylammonium iodide
TBS – tert-Butyldimethylsilyl
TBSCl – tert-Butyldimethylsilyl chloride
TBTA – tris[(1-benzyl-1H-1,2,3-triazol-4-yl)methyl]amine
tBuOH – tert-Butyl alcohol
TCBC – 2,4,6-trichlorobenzoyl chloride
TCEP – (tris(2-carboxyethyl)phosphine
TCS – two-component system
TEAB – triethylammonium bicarbonate
TEM- Transmission electron microscopy
TEMPO – 2,2,6,6-tetramethylpiperidin-1-yl)oxyl or (2,2,6,6-tetramethylpiperidin-1-yl)oxidanyl
TESOTf – triethylsilyl trifluoromethanesulfonate
TFA – trifluoroacetic acid
THB – Todd Hewitt Broth
THB-S – Todd Hewitt Broth with 0.1% sucrose
THBY- Todd Hewitt Broth with 1% yeast extract
THF – tetrahydrofuran
TolC – outer membrane efflux protein
VicRK – two component system
WapA – cell-wall associated protein
WapE – cell-wall associated protein
X – any amino acid

1 Introduction

1.1 The discovery of anti-infectives

In the age of COVID-19, it is widely understood that microorganisms cause disease, but throughout history this wasn't always the case. It wasn't until the late 1800s when Louis Pasteur and Robert Koch reported on germ theory, the idea that invisible microbes caused and spread disease between humans.[1,2] This discovery drastically changed how society approached health care. Establishing a clearer picture of pathogenesis was a prerequisite to discovering and developing effective therapeutics. Not long after germ theory took over, Paul Ehrlich embarked on a search for "a magic bullet," or a chemical compound that would treat infection without harming the host, leading to the discovery of a syphilis treatment, arsphenamine (**1.1**) (Figure 1.1).[1] Unfortunately, except for one arsphenamine derivative, the search for a magic bullet halted there. Twenty years later, a substantial paradigm shift occurred with the serendipitous discovery of penicillin (**1.1**)[3] that launched a worldwide effort toward antibiotic discovery and development. This movement unveiled an arsenal of antibiotics that spanned a vast amount of chemical space and biological space. Unfortunately, this period of momentous innovation was short-lived.

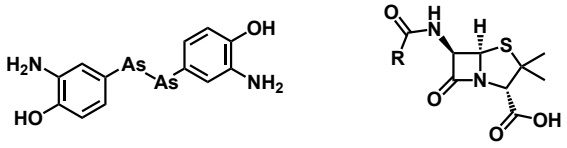

Arsphenamine (1.1) **penicillin (1.2)**

Figure 1.1 First anti-infectives discovered

The rapid rise of resistance has rendered most antibiotics from this discovery period ineffective and the pipeline towards new treatments has stalled substantially. In fact, despite over a million people dying in 2019 due to antibiotic-resistant bacterial infections, less than 50 new compounds were in clinical trials as of early 2021.[4,5] Moreover, most compounds in the pipeline utilize common mechanisms of action that are prone to known resistance mechanisms. The lack of antibiotics and antibacterials in the pipeline is already concerning, but the drastic spike in disinfectant use in response to COVID-19 will have detrimental consequences on antimicrobial resistance.[6] Specifically, sub-MIC concentrations of many active antibacterial ingredients have been shown to promote horizontal gene transfer (HGT) of their own resistance genes, and resistance genes associated with other commonly used antibiotics.[6–9] As such, we must continue to build on our knowledge of the current antibacterials and discover novel compounds with new mechanisms of action to evade current resistance mechanisms.

1.2 Antibiotics – Mechanisms of action and resistance

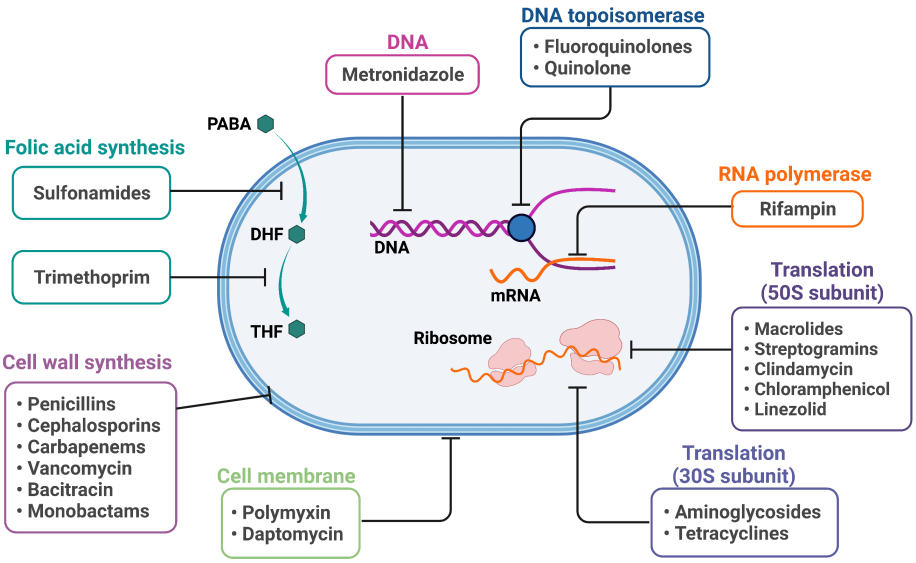

Figure 1.2 Summary of antibiotic mechanisms of action

Our current arsenal of antibiotics generally targets fundamental life processes including cell wall synthesis, DNA synthesis, RNA synthesis, and protein synthesis (Figure 1.2). Two other

pathways commonly targeted by antibiotics are folic acid synthesis and disruption of the cell membrane. The overreliance on this small handful of mechanisms that primarily target essential life processes has led to a rapid rise in resistance. Bacteria have evolved numerous strategies to combat antibiotic treatment (Figure 1.3). Alteration in the cellular membrane can prevent entry of the antibiotic into the cell, so that it cannot reach its cytosolic target. In the case that the drug can get in, bacteria have evolved efflux pumps to remove them, which can decrease the effective concentration. Alternatively, the cell can make changes directly to the protein target, either through amplification of its expression, or through a chemical modification of the binding site. Finally, bacteria can also completely disarm the drug through drug inactivation, or modification. The former typically breaks down the compound to remove electrophilic or nucleophilic activity, whereas the latter entails the addition of a chemical moiety to the compound that would prevent binding to the target. A brief discussion of the antibiotic classes, their mechanism of action, and their resistance mechanisms follows.

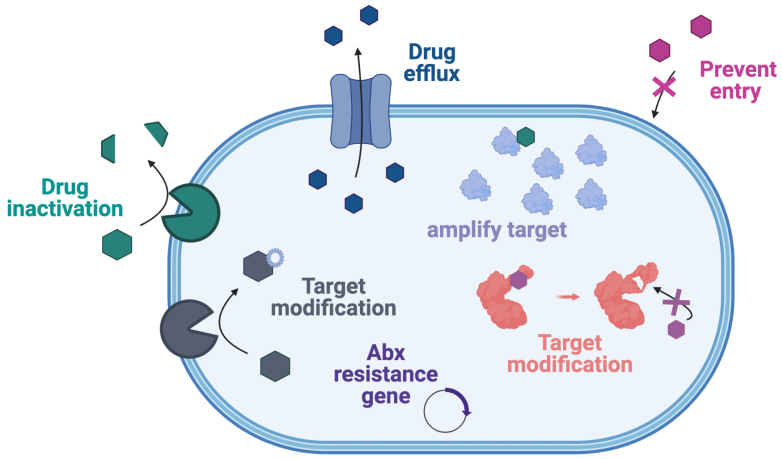

Figure 1.3 Antibiotic resistance mechanisms

1.2.1 Nucleic acid synthesis inhibitors

The quinolone antibiotics, such as levofloxacin (**1.3**) kill through disruption of DNA replication (Figure 1.4). They enact this mechanism by binding DNA topoisomerases and inducing double-stranded DNA breaks and subsequent cell death. Rifamycin (**1.4**) and other semi-synthetic

ansamycins derived from **1.4** are characterized as lipophilic macrocycles bearing two rings and a long chain (Figure 1.4). These compounds inhibit RNA synthesis by sterically blocking the growing RNA chain through RNA polymerase (RNAP).[10–12] Resistance to antibiotics is mediated by target modification that alters the ability of these drugs to bind their target.[12–14]

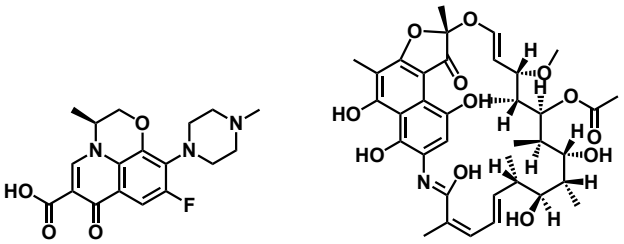

Figure 1.4 Nucleic acid inhibitors

1.2.2 Protein synthesis inhibitors

The 70S ribosome responsible for protein synthesis is another common target manipulated by many classes of antibiotics to induce cell death.[15] These classes target the two different subunits, namely the 50S subunit and 30S subunit, at different stages of protein synthesis. The classes that inhibit the larger 50S subunit include macrolides (azithromycin, **1.5**), lincosamides (clindamycin, **1.6**), chloramphenicol (**1.7**), and oxazolidinones (posizolid, **1.8**) (Figure 1.5). Macrolides contain a macrocyclic lactone ring decorated with deoxy sugar(s), lincosamides bear a glycosylated pyrrolidine ring, and oxazolidinones are characterized by a 5-membered cyclic containing a carbonyl flanked by an oxygen and a nitrogen.[15–18] Resistance to these compounds is facilitated by efflux, target modification and structural modification.[19–24] Aminoglycosides (streptomycin, **1.9**) consist of an amino sugar core, and tetracyclines (tetracycline, **1.10**) contain a tetracyclic carboxamide scaffold. Both classes stall protein translation via the 30S subunit (Figure 1.5). Aminoglycosides and tetracyclines are both subject to structural modification that reduces their efficacy.[25–28]

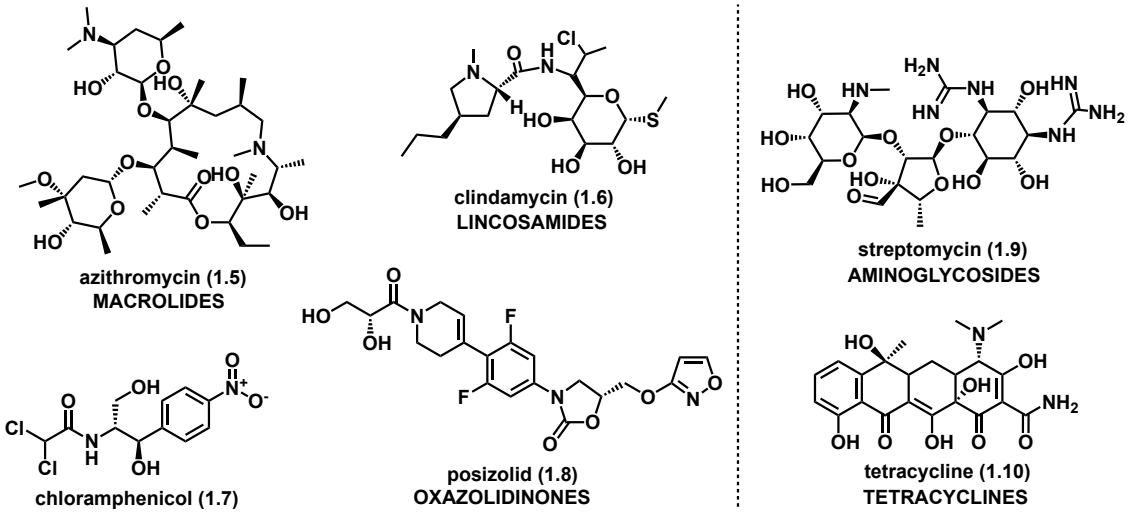

Figure 1.5 Protein synthesis inhibitors

1.2.3 Cell membrane disruptors

The phospholipid bilayer membrane that protects the cell is decorated with long polysaccharides crosslinked with short peptide chains. As these biostructures provide protection from external stresses, they also are viable targets to disrupt bacterial fitness and proliferation. Many antibiotics have exploited this strategy, including the polymyxins (colistin, **1.11**) and the lipopeptide, daptomycin (**1.12**), which disrupt the integrity of the membrane resulting cell death (Figure 1.6).[29] Interestingly, a secondary mode of action has emerged for the polymyxins. They were found to inhibit essential respiratory enzymes.[30,31] Unlike the polymyxins, which causes leakage of cytoplasmic content, daptomycin (**1.12**) is purported to cause leakage of cations through the cytoplasmic membrane causing a loss of membrane potential and cell viability. An additional mechanism that has been proposed is lipid extraction from the membrane. However, the exact mechanism is still debated today, underscoring the difficulty of fully elucidating the mechanism of antibiotics.[32–35] Since daptomycin works binding the cation Ca^{2+}, cells can protect themselves by reversing the charge of the membrane which repels daptomycin binding.[36]

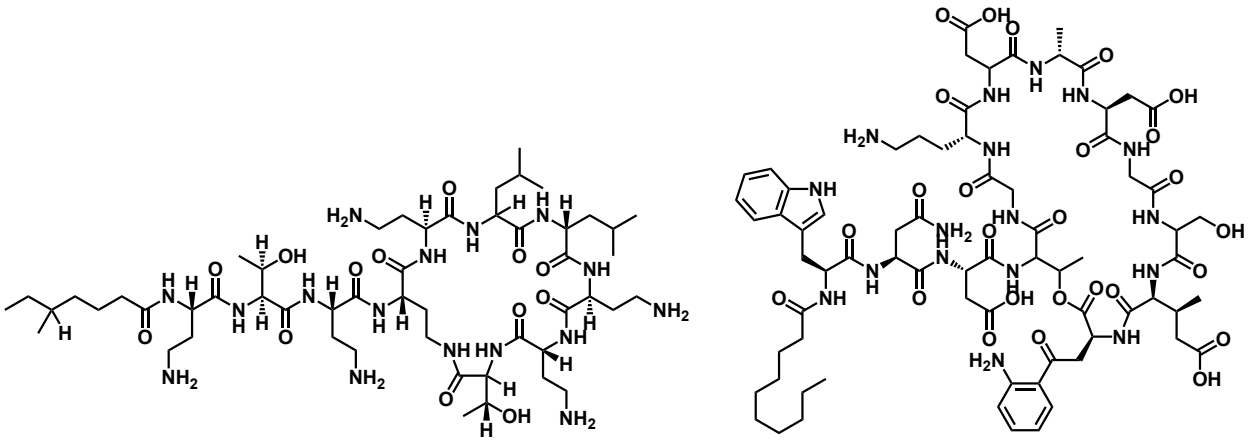

colistin (1.11)
POLYMYXINS

daptomycin (1.12)
LIPOPEPTIDES

Figure 1.6 Cell membrane disruptors

1.2.4 Cell wall inhibitors

The other integral components of the cell membrane are the peptidoglycan chains on the outside of the membrane. Targeting the biosynthesis of the cell wall was the first strategy employed in the early development of antibiotics, with the implementation of penicillin (**1.2**) into the clinic, and has remained an important target (Figure 1.7).[37,38] Two compounds, fosfomycin (**1.13)** and D-cycloserine (**1.14**), have been discovered that can access the cytoplasm and inhibit the early steps of lipid II synthesis.[38,39] The latter compound **1.14** also inhibits protein synthesis on account of the oxazoldinone core. Resistance to these compounds has been incurred via decreased uptake of these drugs, which prevents them from reaching the target and inhibits their bioactivity. Beta-lactams, such as amoxicillin (**1.15**), are characterized by their beta-lactam ring that is structurally mimics the D-Ala D-Ala dipeptide moiety at the terminus of the stem peptide.[40] As such, they are recognized by the peptidases responsible for either transpeptidation that forms the crosslink, or removal of the terminal Ala residue. This class of antibiotics is susceptible to hydrolysis by β-lactamases, which destroys the electrophilic warhead and renders the antibiotic ineffective.[41–43] Glycopeptides are glycosylated (poly)cyclic nonribosomal peptides as shown in vancomycin (**1.16**). This class of molecules bind to the terminal dipeptide, D-Ala D-Ala, and

prevent their incorporation into the existing peptidoglycan structure, preventing further cell wall synthesis.[38,39] Resistance to vancomycin is caused by thickening of the cell wall that impedes entry of the glycopeptide, as well as reducing binding affinity through alterations in the stem peptide.[44–46] The large polycyclic peptide lantibiotics bind lipid II at the carbohydrate head which blocks incorporation and, in some cases, results in pores and subsequent lysis.[47,48] The lantibiotics are disarmed through alterations in the stem peptide, changes in membrane composition, upregulation of resistance genes, and more.[49]

Other lipid II binding antibiotics include members of the cyclic depsipetides, the mannose-containing mannopeptomycins, and ramoplanin.[38,50–52] Bacitracin (**1.17**) a cyclic dodecylpeptide, and some lipopeptides disrupt cell wall homeostasis through complexation to the unadecaprenyl-pyrophosphate (C_{55}-PP) (Figure 1.7).[53–55] This biomolecule facilitates the translocation of cell wall fragments, and functions as a transporter of sugar moieties needed for synthesis of additional species-specific polymers (wall techoic acids, rhamnose-glucose polymers, etc.) often found on the cell surface and integral to the integrity of the cell membrane.

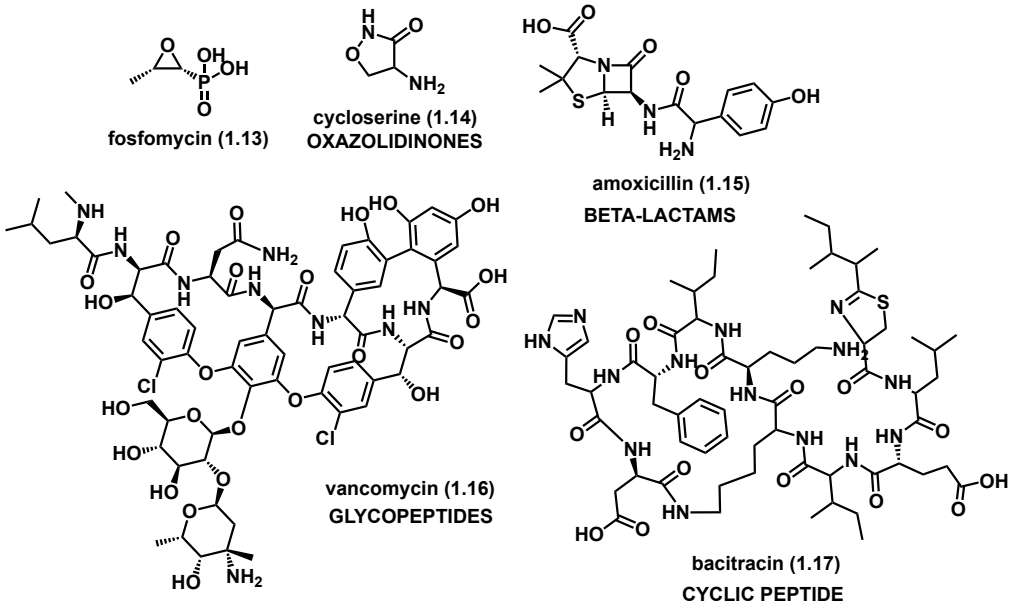

Figure 1.7 Cell wall inhibitors

1.2.5 Folate synthesis inhibitors

The final common antibiotic mechanism of action is inhibition of folate synthesis, a required pathway for cell proliferation. The sulfonamide, sulfamethoxazole (**1.18**), and trimethoprim (**1.19**) inhibit different steps in the pathway (Figure 1.8). The former acts as a competitive inhibitor of dihydropteroate synthase, the enzyme responsible for the first step in folate biosynthesis. The latter directly binds dihydrofolate reductase, the enzyme responsible for the formation of tetrahydrofolic acid from dihydrofolic acid. They are often used in combination under the name Bactrim due to their synergistic relationship.[56,57] These compounds are susceptible to almost all the potential resistance mechanisms, namely alteration of the permeability barrier and/or efflux, regulation changes, naturally fewer sensitive enzymes, acquisition of a drug resistant enzyme, and mutational changes in the enzyme.[58]

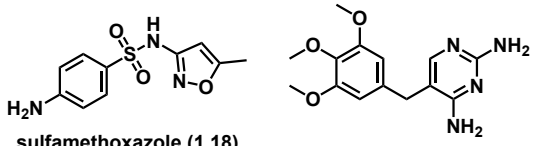

Figure 1.8 Inhibitors of folate biosynthesis.

1.3 Biofilms in disease

In addition to the previously discussed ways that bacteria resist antibiotic treatment (Figure 1.2), they also evolved the ability to form biofilms that are inherently resistant to many antibiotics. In fact, antimicrobials are 10-1000 times less effective against these cellular structures, and according to the National Institutes of Health, 80% of bacterial infections are biofilm in nature, making bacterial biofilms particularly troubling.[59] Biofilms are characterized by a conglomeration of bacterial cells encapsulated by an exopolysaccharide (EPS) matrix that is comprised of oligosaccharides, proteins, etc. The shift toward biofilm formation occurs following the attachment of a single planktonic cell.[60,61] Mucosal surfaces, such as the gut, nasal, vaginal, and

oral cavities, provide ideal surfaces for attachment, leading to high biofilm colonization.[62] Notably, the first biofilm described in the literature was formed by the oral pathogen, *Streptococcus mutans*. This species is highly prevalent in the mouth, a niche primed for biofilm formation and in turn a hotspot for biofilm-mediated diseases. The second half of this introduction will focus on oral disease, with an emphasis on the Gram-positive biofilm model organism, *S. mutans.*

1.4 Introduction to oral disease

The oral cavity is a complex, dynamic system that is inhabited by over 700 different bacterial species and is constantly experiencing a flux of nutrients. Under normal conditions, these bacterial communities live in symbiosis without causing harm to the host. However, a change in environment or a stress signal can tip the equilibrium toward pathogenic bacteria leading to oral diseases, such as dental caries, gingivitis, and periodontitis.[63,64] In 2000, the US Surgeon General classified oral diseases as a "silent epidemic."[65] Almost 20 years later, 3.5 billion people are still affected each year, with dental caries being a primary culprit.[66] Furthermore, many infections and diseases spanning the human body have been linked to oral pathogens. For example, bacteria residing in the oral cavity have been implicated in endocarditis and diabetes.[67–70] In addition to the health-crisis caused by oral bacteria, they also contribute to a large portion of medical costs. According to the "Global Economic Impact of Dental Diseases," the indirect and direct costs of dental diseases totaled $442 billion worldwide in 2010, providing global financial incentive to improve dental care.[71]

Many hypotheses have been developed to best characterize the etiology and pathology of oral diseases. In the 1970s, the "specific plaque hypothesis" emerged and claimed that only a few specific pathogens were responsible for disease.[72] However, subsequent studies proved that disease could occur in the absence of these specific microbes, suggesting an alternative explanation. The "non-specific plaque hypothesis" was reported a decade later.[73] This view suggested the classification of plaque as a polymicrobial community and proposed that an

enrichment in pathogenic bacteria occurs, and these species work collectively to induce disease. However, this hypothesis does not account for how the enrichment occurs. As a result, Phillip Marsh proposed “the ecological plaque hypothesis,” which states that “disease is the result of an imbalance in the total microflora due to ecological stress, resulting in an enrichment of some “oral pathogens” or “disease-micro-organisms.”[74] Dental caries for example are caused first by a change in diet, usually an influx of sugar, which leads to increased attachment, biofilm formation, and acid production. This stress results in a shift toward a low pH environment, ultimately leading to the enrichment of pathogenic bacteria and subsequent enamel erosion. Effectively this hypothesis acknowledges that the previous hypotheses are not necessarily incorrect, but instead represent part of the story (Figure 1.9). As such, focusing on the fundamental biology and the inhibition of specific pathogens enriched in plaque remains a critical area of research for treating oral disease and advancing our understanding of bacterial pathogenesis.

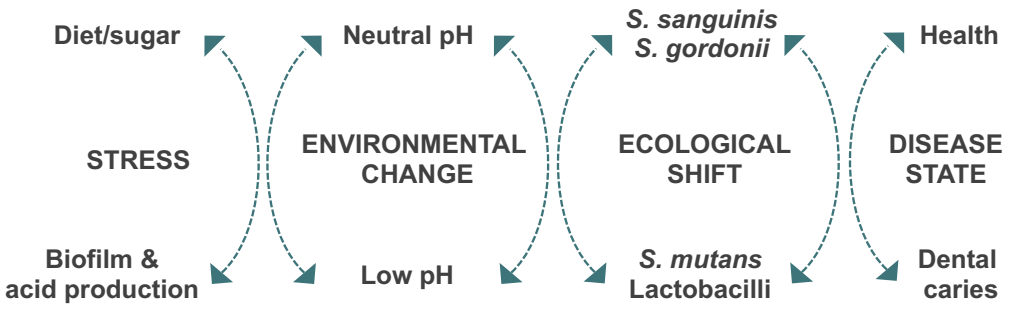

Figure 1.9 Ecological plaque hypothesis

1.5 Oral biofilms

One constant theme through these hypotheses is that oral diseases are mediated by dental plaque, which is a polymicrobial community encased in a biofilm matrix. The formation of an oral biofilm begins with the attachment of a single planktonic cell to the tooth pellicle (Figure 1.10). Following initial attachment, the primary colonizers, such as *Streptococcus, Actinomyces, Haemophilus, Neisseria, Veillonella, Streptococcus mutans*, either auto-aggregate (attachment

between the same species) or co-aggregate (attachment between different species).[75] The degree of biofilm formation depends on the similarity and attraction between bacterial species. During this attachment phase, metabolic activity is low. Secretion of an exopolymeric substance, containing polysaccharides, proteins, and DNA, results in the envelopment of the bacterial cells, forming the biofilm matrix. The microcolony phase, or rapid growth phase, is followed by the adherence of secondary colonizers, comprising of anaerobic Gram-negative bacteria, such as *Porphyromonas gingivalis*. Bacteria trapped within a biofilm typically slow their growth, become completely dormant, or in some cases even show signs of cell death due to a lack of nutrient. Concomitant with this steady state phase is the dispersal of biofilm back to their planktonic state. Dispersed cells either form a new biofilm at a different attachment site or enter the blood stream. Alternatively, biofilms can develop into mature structures that are highly resistant to the innate host immune system and antibiotic treatment.[59,75,76] The decrease in antibiotic susceptibility is because of the decreased metabolic activity within biofilms and thus the decreased expression and activity of traditional antibacterial targets. This provides further credence to the need for novel biofilm targets and inhibitors.

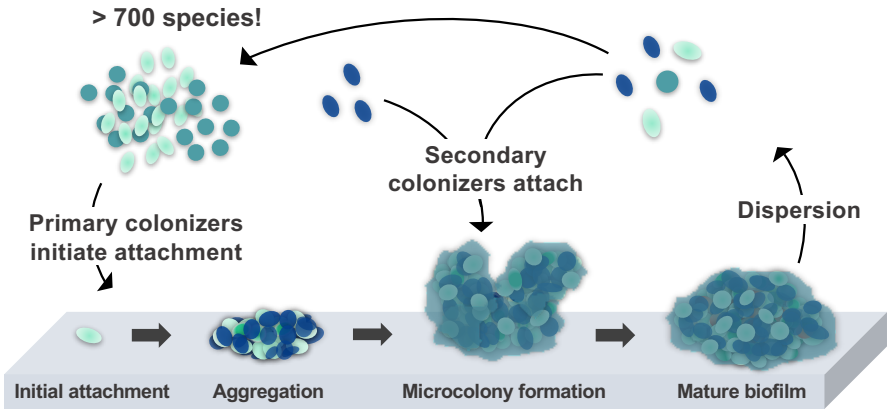

Figure 1.10 Oral biofilm formation

1.6 Streptococcus mutans

Dental caries, or cavities, is an example of a biofilm-mediated disease that has detrimental impacts on society. Over half of the world's population is afflicted by dental caries, with a disproportionate effect on low income and marginalized communities. [65,71,77] Although the overall cause is dysbiosis, *Streptococcus mutans* is the predominant pathogenic species (Figure 1.11). A reduction or elimination of *S. mutans* has been proven to prevent or lessen caries progression[78] This bacterium has also been implicated in infective endocarditis.[79]

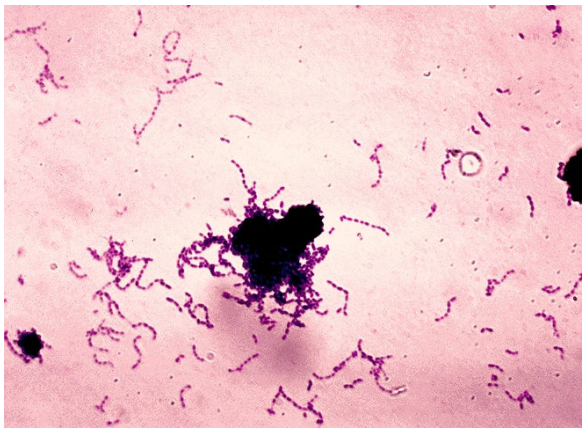

Figure 1.11 *Streptococcus mutans* (CDC, Public Health Image Library)

This facultative Gram-positive bacterium was originally discovered by J. Kilian Clarke in 1924.[80] He thought the cells looked like mutants of other cocci cells leading him to the name *Streptococcus mutans.* This strain has a relatively small genome with around 1500 genes and has a GC content less than 40%. *S. mutans* shares mechanism of gene regulation and metabolic pathways with other Gram-positive bacteria with small genomes, such as *S. pneumoniae*, *S. alagactiae*, and *S. pyogenes*. This strain has emerged as a model organism because of its competence, amenability to genetic analysis, and biofilm lifestyle.[81]

1.6.1 *S. mutans* pathogenicity

S. mutans causes disease through biofilm formation, acid production and acid tolerance. The transition from planktonic cells to biofilm can proceed through a sucrose independent or sucrose-dependent mechanism (Figure 1.12). In the independent pathway, *S. mutans* binds to salivary pellicles on the teeth through cell surface adhesins (antigen I/II, SpaP, and Gbps).[82,83] When exposed to sucrose, the bacterium begins synthesizing long polymer glycan chains via glucosyltransferases (Gtfs). Adherence to the tooth is mediated by the newly synthesized glucans, as well as glucan binding proteins.[84,85] GtfB synthesizes primarily insoluble glucans (α-1,3 glycosidic linkages), GtfC makes both insoluble and soluble glucans (α-1,6 glycosidic linkages), and GtfD produces soluble glucans. These glucans provide additional binding sites for planktonic cells and build the architecture of the growing biofilm. As the cells accumulate and excrete EPS, microcolonies form, eventually developing into mature biofilms.

In sucrose-independent mediated attachment, sortase A (SrtA), facilities the covalent attachment of surface proteins to the cell wall (Figure 1.12).[86–88] Sortase recognizes the motif LPXTG in the substrate protein and cleaves between the threonine and glycine. The resulting free carboxy terminus on threonine is then attached to the cell wall. *S. mutans* encoded for a single sortase belonging to the SrtA subfamily, and six proteins (AgI/II, FruA, WapA, WapE, GbpC, and DexA) containing the LPXTG sequence.[86–89] The inability of a sortase A mutant to adhere and colonize the oral cavity showcases the importance of this enzyme in *S. mutans* biofilm formation and cariogenicity. For this reason, small molecules targeting sortase A have been widely studied.

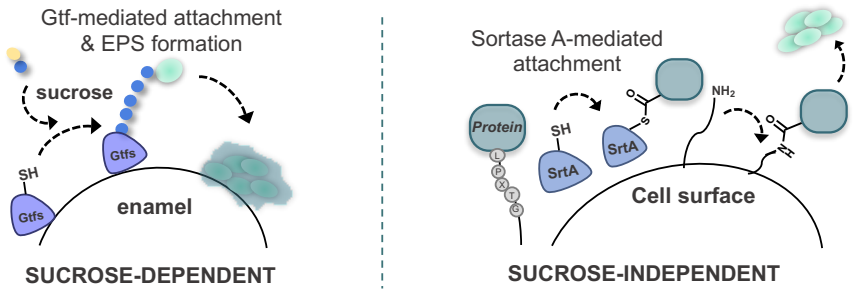

Figure 1.12 Sucrose-dependent and independent biofilm formation

1.6.2 Acidogenicity

Dental caries is ultimately defined by enamel erosion which occurs when organic acids are trapped at the surface of the tooth pellicle within the biofilm matrix. The association between dental caries and sugar derives from the acidification caused by acidogenic (acid-producing) bacterium, such as *S. mutans*. An influx of dietary sugars upregulates glycolysis resulting in increased production of lactic acid (Figure 1.13). Advanced methods to study this acid production have been developed. For example, the design of pH-sensitive fluorescent dyes and fluorescent protein assays enabled spatiomapping of the pH landscape within a biofilm.[90–92] Application of these dyes in single and multi-species biofilms have provided a clearer understanding of the 3D assembly of oral bacteria. These studies demonstrated that the pH environment within a biofilm is heterogenous. Acidification occurs first in microcolonies prior to a global environmental pH shift. Even within these premature biofilm structures, the pH was non-uniform implying that metabolic activity varies at different locations. This acid production leads to the proliferation of acid-tolerant and acidogenic bacteria since commensals cannot withstand this stress.[93]

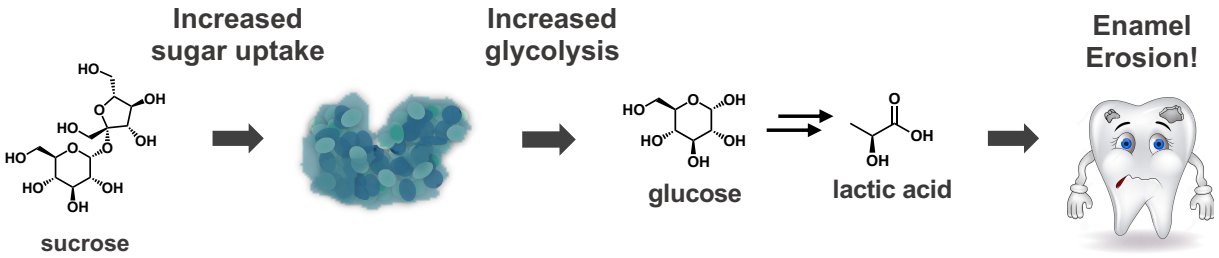

Figure 1.13 Acid production

1.6.3 Acid tolerance response (ATR)

S. mutans biofilm cells have evolved an advanced acid tolerance response (ATR) that promotes their survival under these harsh growth condition through constitutive and acid-induced mechanisms (Figure 1.14). Planktonic cells have also demonstrated an acid tolerance response both when grown in acidic conditions and when pre-exposed to acidic media prior to incubation

at neutral pH. Numerous pathways are employed or affected to provide multiple levels of protection.[93–95] For example, changes in expression of glycolysis play a substantial role in the ATR due its control over lactic acid biosynthesis.[94] As such, sugar uptake and carbon utilization are critical pathways. Additionally, acidification prompts *S. mutans* to alter its membrane composition by increasing the length of the fatty acid chains and shifting toward monounsaturated fatty acids. Changes in the membrane alter the uptake of potassium, which shifts the membrane from anionic to cationic, making them an unattractive pathway for protons to transverse. Another way cells alter proton concentration is through the constitutive membrane bound F_1F_0-ATPase which extrudes protons and has been shown to rapidly regulate the local pH within a dynamic biofilm.[91] Neutralization of protons is another mechanism of the ATR, which is facilitated by the arginine deaminase system (AgDS) produces ammonium (NH_3) and carbon dioxide (CO_2) to neutralize the acidic environment and produce ATP which can in turn fuel the proton pumps. Finally, attachment and EPS matrix production both induce the ATR and provide protection from extracellular protons.

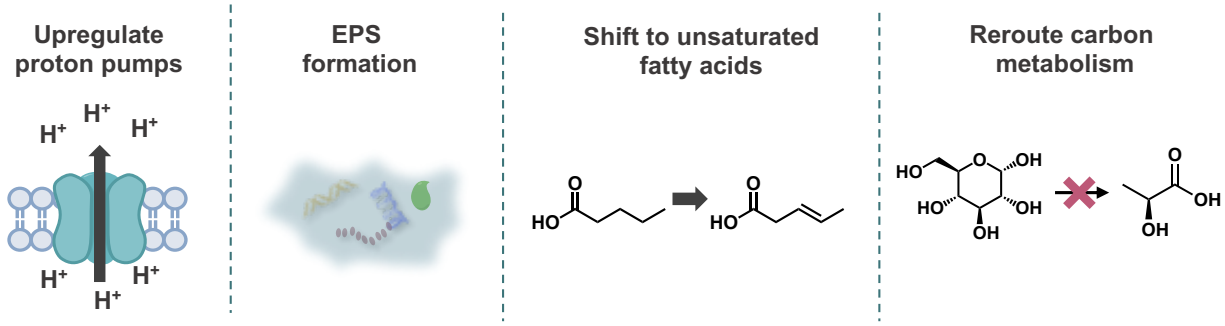

Figure 1.14 Acid tolerance mechanisms

1.6.4 Two-component systems (TCS)

Many of the acid tolerance response mechanism are regulated through two-component systems (TCS). These systems are typically comprised of a membrane histidine kinase sensor protein that senses the environmental cue, and a cytoplasmic response regulator that facilitates

the cellular response through regulation of gene expression (Figure 1.15). When the histidine kinase senses a cue, it phosphorylates the cognate receptor, which triggers dimerization. The dimer can then bind a conserved DNA motif that controls expression of important virulence factors. *S. mutans* encodes 14 TCS, including VicRK, LiaFSR, ComDE, and LevRS. Crosstalk between these systems has been observed. VicRK is the only essential TCS, presumably due to its regulatory role of the essential putative peptidoglycan hydrolase, glucan binding protein B (GbpB).[96] Moreover, VicRK plays fundamental roles in both acid production and acid tolerance.[97]

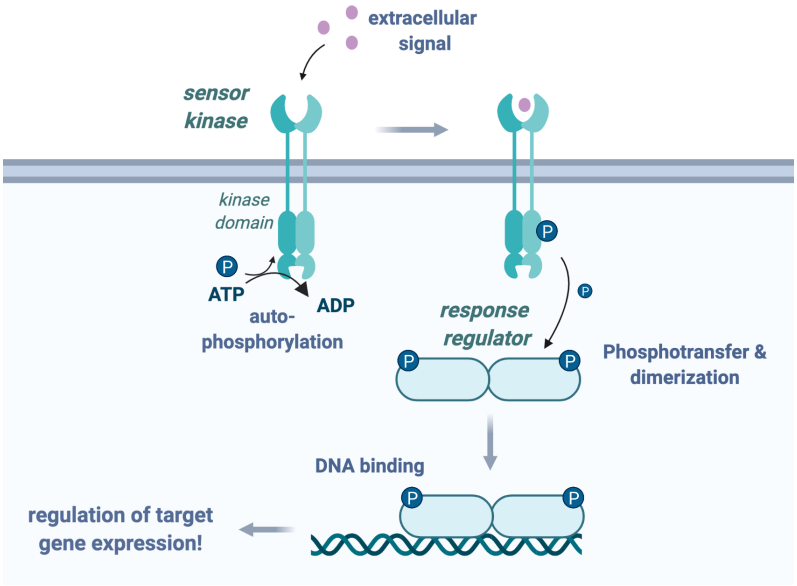

Figure 1.15 Two-component system regulatory mechanism

1.6.5 Quorum sensing

Bacteria have evolved complex methods of communication using small molecules. In response to an environmental signal, such as nutrient availability, or cell density, bacteria produce molecules such as peptide pheromones, which function as signals to surrounding cells.[98] *S. mutans* evolved QS systems that regulate bacteriocin production, which are involved in defense and in competence of the cell. These systems are regulated by the two component systems ComDE and ComRS and mediated through the competence stimulating peptide (CSP) and the

peptide pheromone, XIP (comX- or sigx- inducing peptide), in a complex interconnected system.[93–95] *S. mutans* also use the auto inducer-2 (AI-2) QS system that includes a group of furanones formed as a by-product of LuxS regulation. AI-2 signaling molecules function as a universal messenger among bacterial species. In *S. mutans* specifically, these molecules appear to be involved in acid tolerance, oxidative stress, and biofilm formation.

1.6.6 Prevention methods

S. mutans uses several physiologic adaptations to endure stresses present in the oral cavity - including a propensity for biofilm formation, acid production, and acid tolerance - that provide competitive advantages over non-cariogenic commensals. These capabilities promote the establishment and progression of caries and also cause *S. mutans* to be 100-1000 times more resistant to antibiotics.[4,5] Compounds that can either specifically target cells within a developing biofilm or weaken the biofilm integrity would provide significant advances on two fronts: (1) as tools to explore the complex signaling that underpins community behaviors, and (2) as starting points for narrow-spectrum therapeutics and prophylactics to combat oral disease.

Multiple methods of prevention have been used to limit carries formation. Mechanical methods such as brushing and flossing are used to remove the cariogenic bacteria that colonize the enamel, but relies on human compliance to adequately control dental plaque buildup.[99,100] Meanwhile fluoride treatments reinforce the enamel and protect the teeth from dental plaque acidification.[101] However, when sucrose intake is high and frequent, fluoride is unable to fully prevent demineralization.[102] A newer method of prevention replaces sugars in the diet with xylitol, a noncariogenic and anti-cariogenic sugar substitute, to stop acidification in the oral cavity. Although useful, this method of replacing cariogenic sugars with xylitol has not gained widespread attention.[103] During mechanical removal, mouthwashes and toothpastes containing active antimicrobial agents are generally used. Common small molecule agents such as chlorohexidine or cetylpyridinium chloride are used to remove acidogenic bacteria from the oral cavity but they

do not act via species specific or biofilm specific mechanisms.[104–106] For that reason, the broad-spectrum activity disrupts the microbiome and causes many undesirable side effects, such as staining of the mouth and tongue.[107] Alternative treatments include metal salts, enzymes, quaternary ammonium compounds and essential oils.[108]

1.6.7 Selective inhibition of *S. mutans* biofilm formation

The continuation of this health crisis and the adverse side-effects of current treatments proves the need for therapeutics that can selectively target *S. mutans* biofilm. Small molecules and natural products are a rich source for such compounds.[109] Given the prominence of biofilms in infectious diseases, there has been an increased effort toward the development of compounds that will modulate bacterial biofilm development and maintenance. Groups have taken various approaches to find these active molecules, such as screening large chemical libraries, screening natural products for biofilm activity or using synthesis to develop analogs of interesting lead structures.[110–114] The main mechanisms to prevent *S. mutans* biofilm formation and molecules that work via these mechanisms are described briefly below.

Selective inhibition of *S. mutans* biofilm occurs via two primary mechanisms, anti-adhesion, and signal interreference. Anti-adhesion mechanisms can be sucrose-dependent, such as blocking the formation of the biofilm polymer chains, or sucrose-independent, by blocking the surface protein attachment function of sortase A. By weakening the attachment and undermining the overall stability of the biofilm, this inhibition strategy could potentiate current fluoride and mechanical removal strategies. Molecules that affect *S. mutans* glucosyltransferases (GtfBCD) have been the focus of many studies.[115–117] These enzymes are essential for attachment, biofilm formation, and virulence when sucrose is available in its growth conditions. Obstructing adhesion of planktonic cells will reduce biofilm formation or weaken the biofilm architecture enabling easier removal. The GTF inhibitors generally fall into two categories, polyphenols, such as piceatannol **1.20**), or molecules with high heteroatom density, particularly nitrogen, as shown in **1.21** (Figure

1.16). Michael acceptor moieties, hydrogen bond donor and acceptor moieties were also common features of these molecules, demonstrating the importance of these interactions for enzyme binding.

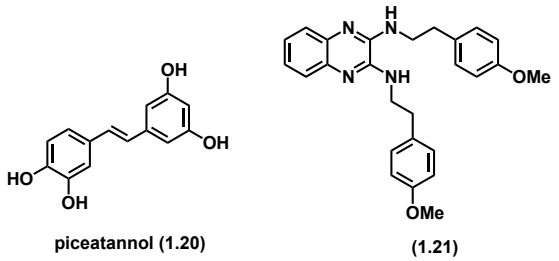

Figure 1.16 Glucosyltransferase inhibitors

Small molecules that inhibit sucrose-independent adhesion have also been explored and typically work by binding surface proteins and disrupting the cell's ability to aggregate. The primary target in this mechanism is the surface protein sortase A, which facilitates the attachment of other proteins to the cell wall. The structural diversity present in the sucrose-independent inhibitors mirrors that of the sucrose-dependent (Figure 1.17). Michael acceptors as seen in trans-chalcone **1.22** were represented, as well as polyphenols such as in **1.23**, and molecules with high heteroatom density as seen in **1.26**. A glycosylated compound (**1.25**) was also identified as a potential inhibitor, but along with **1.26**, *in vitro* confirmation is required. Surface proteins are highly associated with cell hydrophobicity, which is speculated to mediate attachment to the tooth pellicle.[118–120] The test agent **1.24** reduced the hydrophobicity by more than half and is proposed to work via an anti-adhesion mechanism.[119] Further studies are needed to fully understand the mechanisms underlying sucrose-independent anti-adhesion mechanism, but this strategy is promising for the potentiation of current prevention and treatment methods.

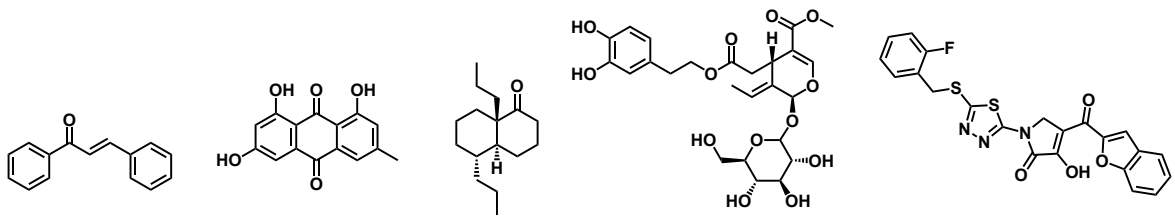

Figure 1.17 Inhibitors of sucrose-independent attachment

The second mechanism, signaling interference, is directed toward quorum sensing and two component systems. Quorum sensing signals are often modulated by two-component systems, making their inhibition tightly connected.[121,122] A benefit of this strategy is the minimal required concentration needed to impede signals initiating biofilm formation, without disrupting growth and survival. In theory, selective pressure will be bypassed, and resistance development is reduced.[123,124] Brominated furanones, such as furanone C30 (**1.27**) have garnered much attention for their biofilm activity via quorum sensing mechanisms (Figure 1.18). The 2-aminoimidazole-based alkaloid, oroidin is a well-studied biofilm inhibitor and numerous analogs have been developed based on its structure.[125,126] Hodnik et al. combined this compound with the idea that indoles are known to affect biofilm formation to develop novel S. mutans biofilm quorum sensing inhibitor, **1.28.**[127,128]

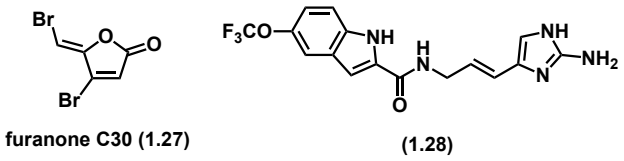

Figure 1.18 Quorum sensing inhibitors

Inhibitors of two-component systems have also been widely explored, including in the Wuest lab, but our contributions will be discussed in the following section. Walkmycin C (**1.29**) is an inhibitor of the two-component system WalK/WalR in *Bacillus subtilis,* that has also been found to disrupt biofilm formation through the homologous system in *S. mutans*, VicRK (Figure 1.19).[129]

Epigallocatechin-3-gallate (**1.30**) is another biofilm inhibitor that works via inhibition of AguD and subsequent energy starvation and disruption of the pH gradient.[130,131] The instability and poor bioavailability of this compound led to the synthesis of a lipophilic derivative, epigallocatechin-3-gallate-stearate (**1.31**), though this modification led to less potent activity.[132] Developing inhibitors of cellular signaling pathways has been successful for some compounds, but there are general drawbacks that limit the amount of success. One of the largest hurdles for discovering or developing these structures is untangling the intricate signaling networks that exist within *S. mutans* and other microorganisms.

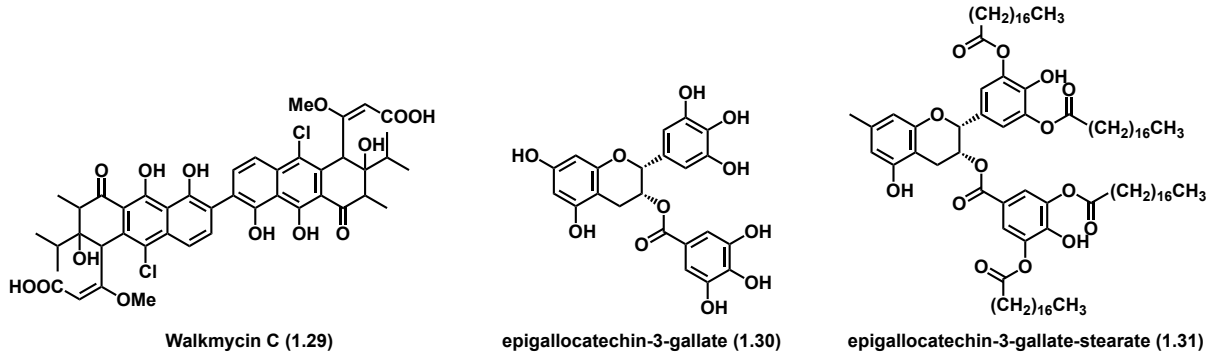

Figure 1.19 TCS inhibitors

The prevention of dental caries is not trivial. The diverse habitats in the oral cavity and the complex factors regulating disease makes designing and testing small molecules with desirable activity quite challenging. Despite these challenges, many small molecules have been discovered from natural sources, or accessed synthetically with specific biofilm activity through inhibition and dispersal mechanisms. Often, these mechanisms result in weakened, or less pathogenic biofilms that are more easily removed via mechanical measures, but this can have negative effects, including further colonization on other mucosal surfaces and even sepsis. Future efforts need to refocus on the important concepts of preventing *S. mutans* biofilm formation rather than only weakening an existing biofilm structure. Developing tools that can specifically modulate biofilm formation can facilitate a better understanding of the molecular biology involved in this process,

which will in turn drastically improve our understanding of biofilm-mediated infections as well as inform the design of biofilm-specific inhibitors to prevent or treat dental caries and other Gram-positive, biofilm-mediated infections.

1.7 Looking ahead

Between 1981 and 2019, 37% of clinically approved drugs were natural products or originated from natural product scaffolds (Figure 1.20).[109] Antibiotic development is even more dependent on these complex scaffolds with 90% of approved antibacterials having been derived from these secondary metabolites. Natural products contain "privileged scaffolds" which impart specific binding interactions with therapeutically relevant protein targets necessary for drug development. However, these chemical structures are also plagued by numerous challenges, such as toxicity, bioavailability, and accessibility (ease of synthesis and/or fermentation), all of which limit further biological analysis and clinical utility.[133] Small molecules also contribute greatly to drug development, and more specifically, antibiotic development. In both categories, small molecules account for approximately 36% of the approved drugs.[109] Small molecules offer some advantages over natural products, including their cell permeability and often more synthetically accessible structure. However, they also come with disadvantages. Due to their size, they can often interact with more than one biological target, resulting in negative side effects.

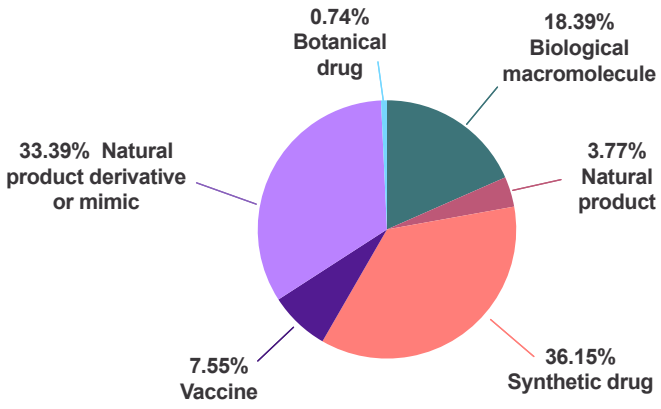

Figure 1.20 Origin of approved drugs from 1991-2019

To overcome challenges plaguing both natural product and small molecule development, many have been motivated to develop synthetic strategies to leverage the advantages of natural products in biological settings.[134] Examples include biology-oriented synthesis (BOS),[135–138] diverted total synthesis (DTS), diversity-oriented synthesis (DOS), complexity to diversity (CtD), and natural product simplification.[139–142] These approaches facilitate the construction of small molecule and natural product inspired libraries to probe biological activity and identify novel mechanisms of action. Such chemical platforms have enabled the design of chemical probes, identification of unexplored targets, and the development of antibiotics that circumvent resistance.[141,143–147]

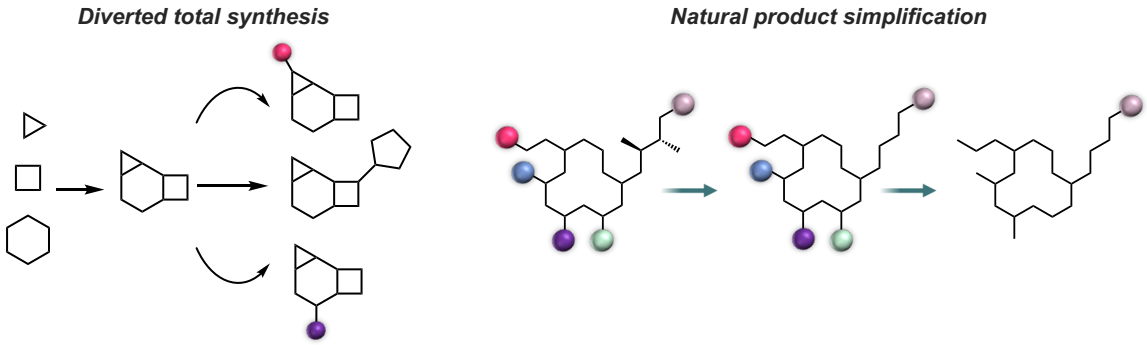

Figure 1.21 Diverted total synthesis and natural product simplification

This thesis leverages these platforms to develop new anti-infectives and tool compounds. using natural product total synthesis, DTS, natural product simplification, and small molecule derivatization to tackle *S. mutans* biofilm formation, as well as inhibition of other pathogenic bacteria (Figure 1.21). Through this work, I have aided in the development of new tool compounds and more potent antibacterials that primarily target the cell membrane.

1.8 References

(1) Williams, K. J. The Introduction of “chemotherapy” Using Arsphenamine - the First Magic Bullet. *J R Soc Med* **2009**, *102* (8), 343–348. https://doi.org/10.1258/jrsm.2009.09k036.

(2) Pasteur Lister, Joseph, L. *Germ Theory and Its Applications to Medicine & on the Antiseptic Principle of the Practice of Surgery*; Prometheus Books: Amherst, N.Y., 1996.
(3) Fleming, A. On the Antibacterial Action of Cultures of a Penicillium, with Special Reference to Their Use in the Isolation of B. Influenzæ. *Br J Exp Pathol* **1929**, *10* (3), 226–236.
(4) World Health Organization. *Antibacterial Agents in Preclinical Development: An Open Access Database*; World Health Organization, 2019.
(5) Organization, W. H. 2019 Antibacterial Agents in Clinical Development: An Analysis of the Antibacterial Clinical Development Pipeline. **2019**.
(6) Chen, B.; Han, J.; Dai, H.; Jia, P. Biocide-Tolerance and Antibiotic-Resistance in Community Environments and Risk of Direct Transfers to Humans: Unintended Consequences of Community-Wide Surface Disinfecting during COVID-19? *Environmental Pollution* **2021**, *283*, 117074. https://doi.org/https://doi.org/10.1016/j.envpol.2021.117074.
(7) Mayer, S.; Boos, M.; Beyer, A.; Fluit, A. C.; Schmitz, F.-J. Distribution of the Antiseptic Resistance Genes QacA, QacB and QacC in 497 Methicillin-Resistant and -Susceptible European Isolates of Staphylococcus Aureus. *Journal of Antimicrobial Chemotherapy* **2001**, *47* (6), 896–897. https://doi.org/10.1093/jac/47.6.896.
(8) Sandegren, L. Selection of Antibiotic Resistance at Very Low Antibiotic Concentrations. *Upsala Journal of Medical Sciences* **2014**, *119* (2), 103–107. https://doi.org/10.3109/03009734.2014.904457.
(9) Ignak, S.; Nakipoglu, Y.; Gurler, B. Frequency of Antiseptic Resistance Genes in Clinical Staphycocci and Enterococci Isolates in Turkey. *Antimicrobial Resistance & Infection Control* **2017**, *6* (1), 88. https://doi.org/10.1186/s13756-017-0244-6.
(10) Campbell, E. A.; Korzheva, N.; Mustaev, A.; Murakami, K.; Nair, S.; Goldfarb, A.; Darst, S. A. Structural Mechanism for Rifampicin Inhibition of Bacterial RNA Polymerase. *Cell* **2001**, *104* (6), 901–912. https://doi.org/https://doi.org/10.1016/S0092-8674(01)00286-0.
(11) Mosaei, H.; Molodtsov, V.; Kepplinger, B.; Harbottle, J.; Moon, C. W.; Jeeves, R. E.; Ceccaroni, L.; Shin, Y.; Morton-Laing, S.; Marrs, E. C. L.; Wills, C.; Clegg, W.; Yuzenkova, Y.; Perry, J. D.; Bacon, J.; Errington, J.; Allenby, N. E. E.; Hall, M. J.; Murakami, K. S.; Zenkin, N. Mode of Action of Kanglemycin A, an Ansamycin Natural Product That Is Active against Rifampicin-Resistant Mycobacterium Tuberculosis. *Mol Cell* **2018**, *72* (2), 263-274.e5. https://doi.org/10.1016/j.molcel.2018.08.028.
(12) Floss, H. G.; Yu, T.-W. RifamycinMode of Action, Resistance, and Biosynthesis. *Chemical Reviews* **2005**, *105* (2), 621–632. https://doi.org/10.1021/cr030112j.
(13) Hooper, D. C.; Jacoby, G. A. Mechanisms of Drug Resistance: Quinolone Resistance. *Ann N Y Acad Sci* **2015**, *1354* (1), 12–31. https://doi.org/10.1111/nyas.12830.
(14) Aldred, K. J.; Kerns, R. J.; Osheroff, N. Mechanism of Quinolone Action and Resistance. *Biochemistry* **2014**, *53* (10), 1565–1574. https://doi.org/10.1021/bi5000564.
(15) Wilson, D. N. Ribosome-Targeting Antibiotics and Mechanisms of Bacterial Resistance. *Nature Reviews Microbiology* **2014**, *12* (1), 35–48. https://doi.org/10.1038/nrmicro3155.
(16) Menninger, J. R. Functional Consequences of Binding Macrolides to Ribosomes. *J Antimicrob Chemother* **1985**, *16 Suppl A*, 23–34.
(17) Gaynor, M.; Mankin, A. S. Macrolide Antibiotics : Binding Site , Mechanism of Action , Resistance. *Current Topics in Medicinal Chemistry* **2003**, *3*, 1–12. https://doi.org/10.2174/1568026033452159.
(18) Tenson, T.; Lovmar, M.; Ehrenberg, M. The Mechanism of Action of Macrolides, Lincosamides and Streptogramin B Reveals the Nascent Peptide Exit Path in the Ribosome. *Journal of Molecular Biology* **2003**, *330* (5), 1005–1014. https://doi.org/https://doi.org/10.1016/S0022-2836(03)00662-4.

(19) Roberts, M. C. Resistance to Macrolide, Lincosamide, Streptogramin, Ketolide, and Oxazolidinone Antibiotics. *Molecular Biotechnology* **2004**, *28* (1), 47. https://doi.org/10.1385/MB:28:1:47.

(20) Allen, N. E. Macrolide Resistance in Staphylococcus Aureus: Inducers of Macrolide Resistance. *Antimicrob Agents Chemother* **1977**, *11* (4), 669–674.

(21) Lina, G.; Quaglia, A.; Reverdy, M. E.; Leclercq, R.; Vandenesch, F.; Etienne, J. Distribution of Genes Encoding Resistance to Macrolides, Lincosamides, and Streptogramins among Staphylococci. *Antimicrobial Agents and Chemotherapy* **1999**, *43* (5), 1062–1066.

(22) Schroeder, M. R.; Stephens, D. S. Macrolide Resistance in Streptococcus Pneumoniae. *Frontiers in Cellular and Infection Microbiology* **2016**, *6*. https://doi.org/10.3389/fcimb.2016.00098.

(23) Leclercq, R. Mechanisms of Resistance to Macrolides and Lincosamides: Nature of the Resistance Elements and Their Clinical Implications. *Clinical Infectious Diseases* **2002**, *34* (4), 482–492.

(24) Garza-Ramos, G.; Xiong, L.; Zhong, P.; Mankin, A. Binding Site of Macrolide Antibiotics on the Ribosome: New Resistance Mutation Identifies a Specific Interaction of Ketolides with RRNA. *Journal of Bacteriology* **2001**, *183* (23), 6898–6907. https://doi.org/10.1128/JB.183.23.6898-6907.2001.

(25) Chopra, I.; Hawkey, P. M.; Hinton, M. Tetracyclines, Molecular and Clinical Aspects. *Journal of Antimicrobial Chemotherapy* **1992**, *29* (3), 245–277. https://doi.org/10.1093/jac/29.3.245.

(26) Chopra, I.; Roberts, M. Tetracycline Antibiotics: Mode of Action, Applications, Molecular Biology, and Epidemiology of Bacterial Resistance. *Microbiol Mol Biol Rev* **2001**, *65* (2), 232–260. https://doi.org/10.1128/MMBR.65.2.232-260.2001.

(27) Krause, K. M.; Serio, A. W.; Kane, T. R.; Connolly, L. E. Aminoglycosides: An Overview. *Cold Spring Harb Perspect Med* **2016**, *6* (6), a027029. https://doi.org/10.1101/cshperspect.a027029.

(28) P., K. L.; Jalal, H.; Shahriar, M. Aminoglycosides: Perspectives on Mechanisms of Action and Resistance and Strategies to Counter Resistance. *Antimicrobial Agents and Chemotherapy* **2000**, *44* (12), 3249–3256. https://doi.org/10.1128/AAC.44.12.3249-3256.2000.

(29) Miller, W. R.; Bayer, A. S.; Arias, C. A. Mechanism of Action and Resistance to Daptomycin in Staphylococcus Aureus and Enterococci. *Cold Spring Harb Perspect Med* **2016**, *6* (11), a026997. https://doi.org/10.1101/cshperspect.a026997.

(30) Yin, J.; Meng, Q.; Cheng, D.; Fu, J.; Luo, Q.; Liu, Y.; Yu, Z. Mechanisms of Bactericidal Action and Resistance of Polymyxins for Gram-Positive Bacteria. *Applied Microbiology and Biotechnology* **2020**, *104* (9), 3771–3780. https://doi.org/10.1007/s00253-020-10525-y.

(31) Deris, Z. Z.; Akter, J.; Sivanesan, S.; Roberts, K. D.; Thompson, P. E.; Nation, R. L.; Li, J.; Velkov, T. A Secondary Mode of Action of Polymyxins against Gram-Negative Bacteria Involves the Inhibition of NADH-Quinone Oxidoreductase Activity. *The Journal of Antibiotics* **2014**, *67* (2), 147–151. https://doi.org/10.1038/ja.2013.111.

(32) Gray, D. A.; Wenzel, M. More Than a Pore: A Current Perspective on the In Vivo Mode of Action of the Lipopeptide Antibiotic Daptomycin. *Antibiotics* . 2020. https://doi.org/10.3390/antibiotics9010017.

(33) Chen, Y.-F.; Sun, T.-L.; Sun, Y.; Huang, H. W. Interaction of Daptomycin with Lipid Bilayers: A Lipid Extracting Effect. *Biochemistry* **2014**, *53* (33), 5384–5392. https://doi.org/10.1021/bi500779g.

(34) A., S. J.; G., P. N.; M., S. H. Correlation of Daptomycin Bactericidal Activity and Membrane Depolarization in Staphylococcus Aureus. *Antimicrobial Agents and Chemotherapy* **2003**, *47* (8), 2538–2544. https://doi.org/10.1128/AAC.47.8.2538-2544.2003.

(35) Joe, P.; Nicolas, P.; A., S. J. Daptomycin-Mediated Reorganization of Membrane Architecture Causes Mislocalization of Essential Cell Division Proteins. *Journal of Bacteriology* **2012**, *194* (17), 4494–4504. https://doi.org/10.1128/JB.00011-12.

(36) Silverman, J. A.; Oliver, N.; Andrew, T.; Li, T. Resistance Studies with Daptomycin. *Antimicrobial Agents and Chemotherapy* **2001**, *45* (6), 1799–1802. https://doi.org/10.1128/AAC.45.6.1799-1802.2001.

(37) Martin, N. I.; Breukink, E. The Expanding Role of Lipid II as a Target for Lantibiotics. *Future Microbiology* **2007**, *2* (5), 513–525. https://doi.org/10.2217/17460913.2.5.513.

(38) Schneider, T.; Sahl, H.-G. An Oldie but a Goodie – Cell Wall Biosynthesis as Antibiotic Target Pathway. *International Journal of Medical Microbiology* **2010**, *300* (2), 161–169. https://doi.org/https://doi.org/10.1016/j.ijmm.2009.10.005.

(39) Sarkar, P.; Yarlagadda, V.; Ghosh, C.; Haldar, J. A Review on Cell Wall Synthesis Inhibitors with an Emphasis on Glycopeptide Antibiotics. *Medchemcomm* **2017**, *8* (3), 516–533. https://doi.org/10.1039/c6md00585c.

(40) Gaynes, R. The Discovery of Penicillin—New Insights After More Than 75 Years of Clinical Use. *Emerging Infectious Diseases* **2017**, *23* (5), 849–853. https://doi.org/10.3201/eid2305.161556.

(41) Lobanovska, M.; Pilla, G. Penicillin's Discovery and Antibiotic Resistance: Lessons for the Future? *Yale J Biol Med* **2017**, *90* (1), 135–145.

(42) Rolinson, G. N.; Chain, E. B.; Stoeckel, H. Bacterial Resistance to Penicillins and Cephalosporins. *Proceedings of the Royal Society of London. Series B. Biological Sciences* **1971**, *179* (1057), 403–410. https://doi.org/10.1098/rspb.1971.0105.

(43) Spratt, B. G. The Mechanism of Action of Penicillin. *Science Progress (1933-)* **1978**, *65* (257), 101–128.

(44) Zeng, D.; Debabov, D.; Hartsell, T. L.; Cano, R. J.; Adams, S.; Schuyler, J. A.; McMillan, R.; Pace, J. L. Approved Glycopeptide Antibacterial Drugs: Mechanism of Action and Resistance. *Cold Spring Harb Perspect Med* **2016**, *6* (12), a026989. https://doi.org/10.1101/cshperspect.a026989.

(45) Stogios, P. J.; Savchenko, A. Molecular Mechanisms of Vancomycin Resistance. *Protein Science* **2020**, *29* (3), 654–669. https://doi.org/https://doi.org/10.1002/pro.3819.

(46) Süssmuth, R. D. Vancomycin Resistance: Small Molecule Approaches Targeting the Bacterial Cell Wall Biosynthesis. *ChemBioChem* **2002**, *3* (4), 295–298. https://doi.org/https://doi.org/10.1002/1439-7633(20020402)3:4<295::AID-CBIC295>3.0.CO;2-G.

(47) van Kraaij, C.; M. de Vos, W.; J. Siezen, R.; P. Kuipers, O. Lantibiotics: Biosynthesis, Mode of Action and Applications. *Natural Product Reports* **1999**, *16* (5), 575–587. https://doi.org/10.1039/A804531C.

(48) McAuliffe, O.; Ross, R. P.; Hill, C. Lantibiotics: Structure, Biosynthesis and Mode of Action. *FEMS Microbiology Reviews* **2001**, *25* (3), 285–308. https://doi.org/10.1111/j.1574-6976.2001.tb00579.x.

(49) A., D. L.; D., C. P.; Colin, H.; Paul, R. R. Lantibiotic Resistance. *Microbiology and Molecular Biology Reviews* **2022**, *79* (2), 171–191. https://doi.org/10.1128/MMBR.00051-14.

(50) Müller, A.; Münch, D.; Schmidt, Y.; Reder-Christ, K.; Schiffer, G.; Bendas, G.; Gross, H.; Sahl, H.-G.; Schneider, T.; Brötz-Oesterhelt, H. Lipodepsipeptide Empedopeptin Inhibits Cell Wall Biosynthesis through Ca^{2+}-Dependent Complex Formation with Peptidoglycan Precursors * . *Journal of Biological Chemistry* **2012**, *287* (24), 20270–20280. https://doi.org/10.1074/jbc.M112.369561.

(51) Epand, R. M.; Walker, C.; Epand, R. F.; Magarvey, N. A. Molecular Mechanisms of Membrane Targeting Antibiotics. *Biochimica et Biophysica Acta (BBA) - Biomembranes* **2016**, *1858* (5), 980–987. https://doi.org/https://doi.org/10.1016/j.bbamem.2015.10.018.

(52) Oliva, B.; Maiese, W. M.; Greenstein, M.; Borders, D. B.; Chopra, I. Mode of Action of the Cyclic Depsipeptide Antibiotic LL-AO34β1 and Partial Characterization of a Staphylococcus Aureus Mutant Resistant to the Antibiotic. *Journal of Antimicrobial Chemotherapy* **1993**, *32* (6), 817–830. https://doi.org/10.1093/jac/32.6.817.

(53) J., E. N.; Simon, C.; J., L. P. High-Resolution Crystal Structure Reveals Molecular Details of Target Recognition by Bacitracin. *Proceedings of the National Academy of Sciences* **2013**, *110* (35), 14207–14212. https://doi.org/10.1073/pnas.1308268110.

(54) Stone, K. J.; Strominger, J. L. Mechanism of Action of Bacitracin: Complexation with Metal Ion and C_{55}-Isoprenyl Pyrophosphate. *Proc Natl Acad Sci U S A* **1971**, *68* (12), 3223–3227.

(55) Sugimoto, A.; Maeda, A.; Itto, K.; Arimoto, H. Deciphering the Mode of Action of Cell Wall-Inhibiting Antibiotics Using Metabolic Labeling of Growing Peptidoglycan in Streptococcus Pyogenes. *Scientific Reports* **2017**, *7* (1), 1129. https://doi.org/10.1038/s41598-017-01267-5.

(56) Minato, Y.; Dawadi, S.; Kordus, S. L.; Sivanandam, A.; Aldrich, C. C.; Baughn, A. D. Mutual Potentiation Drives Synergy between Trimethoprim and Sulfamethoxazole. *Nature Communications* **2018**, *9* (1), 1003. https://doi.org/10.1038/s41467-018-03447-x.

(57) Bushby, S. R.; Hitchings, G. H. Trimethoprim, a Sulphonamide Potentiator. *Br J Pharmacol Chemother* **1968**, *33* (1), 72–90. https://doi.org/10.1111/j.1476-5381.1968.tb00475.x.

(58) Huovinen, P.; Sundström, L.; Swedberg, G.; Skr□ld, O. Trimethoprim and Sulfonamide Resistance. *Antimicrobial Agents and Chemotherapy* **1995**, *39*, 279–289.

(59) Davies, D. Understanding Biofilm Resistance to Antibacterial Agents. *Nature Reviews Drug Discovery* **2003**, *2*, 114.

(60) Aas, J. A.; Griffen, A. L.; Dardis, S. R.; Lee, A. M.; Olsen, I.; Dewhirst, F. E.; Leys, E. J.; Paster, B. J. Bacteria of Dental Caries in Primary and Permanent Teeth in Children and Young Adults. *Journal of Clinical Microbiology* **2008**, *46* (4), 1407–1417. https://doi.org/10.1128/JCM.01410-07.

(61) Yadav, K.; Prakash, S. Dental Caries: A Microbiological Approach. *Journal of Clinical Infectious Diseases & Practice* **2017**, *2* (1), 1–15. https://doi.org/10.4172/2476-213X.1000118.

(62) Donlan, R. M. Biofilms: Microbial Life on Surfaces. *Emerging Infectious Diseases* **2002**, *8* (9), 881–890. https://doi.org/10.3201/eid0809.020063.

(63) Kilian, M.; Chapple, I. L. C.; Hannig, M.; Marsh, P. D.; Meuric, V.; Pedersen, A. M. L.; Tonetti, M. S.; Wade, W. G.; Zaura, E. The Oral Microbiome - An Update for Oral Healthcare Professionals. *British Dental Journal* **2016**, *221*, 657. https://doi.org/10.1038/sj.bdj.2016.865.

(64) Avila, M.; Ojcius, D. M.; Yilmaz, Ö. The Oral Microbiota: Living with a Permanent Guest. *DNA and Cell Biology* **2009**, *28* (8), 405–411. https://doi.org/10.1089/dna.2009.0874.

(65) U.S Department of Health and Human Services. *Oral Health in America: A Report of the Surgeon General*; 2000. https://doi.org/10.1089/pop.2013.0038.

(66) GBD 2017 Disease and Injury Incidence and Prevalence Collaborators. Global, Regional, and National Incidence, Prevalence, and Years Lived with Disability for 354 Diseases and Injuries for 195 Countries and Territories, 1990–2017: A Systematic Analysis for the Global Burden of Disease Study 2017. *The Lancet* **2018**, *392* (10159), 1789–1858. https://doi.org/https://doi.org/10.1016/S0140-6736(18)32279-7.

(67) Li, X.; Kolltveit, K. M.; Tronstad, L.; Olsen, I. Systemic Diseases Caused by Oral Infection. *Clin Microbiol Rev* **2000**, *13* (4), 547–558.

(68) Nakano, K.; Nomura, R.; Ooshima, T. Streptococcus Mutans and Cardiovascular Diseases. *Japanese Dental Science Review* **2008**, *44* (1), 29–37. https://doi.org/10.1016/j.jdsr.2007.09.001.
(69) McGhie, D.; Hutchison, J. G.; Nye, F.; Ball, A. P. Infective Endocarditis Caused by Streptococcus Mutans. *Br Heart J* **1977**, *39* (4), 456–458.
(70) Long, J.; Cai, Q.; Steinwandel, M.; Hargreaves, M. K.; Bordenstein, S. R.; Blot, W. J.; Zheng, W.; Shu, X. O. Association of Oral Microbiome with Type 2 Diabetes Risk. *Journal of Periodontal Research* **2017**, *52* (3), 636–643. https://doi.org/10.1111/jre.12432.
(71) Listl, S.; Galloway, J.; Mossey, P. A.; Marcenes, W. Global Economic Impact of Dental Diseases. *Journal of Dental Research* **2015**, *94* (10), 1355–1361. https://doi.org/10.1177/0022034515602879.
(72) Loesche, W. J. Chemotherapy of Dental Plaque Infections. *Oral Sci Rev* **1976**, *9*, 65–107.
(73) Theilade, E. The Non-Specific Theory in Microbial Etiology of Inflammatory Periodontal Diseases. *Journal of Clinical Periodontology* **1986**, *13* (10), 905–911. https://doi.org/https://doi.org/10.1111/j.1600-051X.1986.tb01425.x.
(74) Marsh, P. D. Microbial Ecology of Dental Plaque and Its Significance in Health and Disease. *Adv Dent Res* **1994**, *8*, 267–271. https://doi.org/10.1177/08959374940080022001.
(75) Kolenbrander, P. E. Oral Microbial Communities: Biofilms, Interactions, and Genetic Systems. *Annual Review of Microbiology* **2000**, *54* (413), 437. https://doi.org/10.1146/annurev.micro.54.1.413.
(76) Huang, R.; Li, M.; Gregory, R. L. Bacterial Interactions in Dental Biofilm. *Virulence* **2011**, *2* (5), 435–444. https://doi.org/10.4161/viru.2.5.16140.
(77) Petersen, P. E. The World Oral Health Report 2003: Continuous Improvement of Oral Health in the 21st Century - The Approach of the WHO Global Oral Health Programme. *Community Dentistry and Oral Epidemiology* **2003**. https://doi.org/10.1046/j..2003.com122.x.
(78) Zhan, L. Rebalancing the Caries Microbiome Dysbiosis: Targeted Treatment and Sugar Alcohols. *Advances in Dental Research* **2018**, *29*, 10–116. https://doi.org/10.1177/0022034517736498.
(79) Ryota, N.; Saaya, M.; Masatoshi, O.; Takahiro, K.; Noboru, T.; Kazuhiko, N.; E., F. N. Contribution of Severe Dental Caries Induced by Streptococcus Mutans to the Pathogenicity of Infective Endocarditis. *Infection and Immunity* **2022**, *88* (7), e00897-19. https://doi.org/10.1128/IAI.00897-19.
(80) Clarke, J. K. On the Bacterial Factor in the Aetiology of Dental Caries. *Br J Exp Pathol* **1924**, *5* (3), 141.
(81) Lemos, J. A.; Quivey, R. G.; Koo, H.; Abranches, J. Streptococcus Mutans: A New Gram-Positive Paradigm? *Microbiology (N Y)* **2013**, *159* (Pt 3), 436–445. https://doi.org/10.1099/mic.0.066134-0.
(82) Krzyściak, W.; Jurczak, A.; Kościelniak, D.; Bystrowska, B.; Skalniak, A. The Virulence of Streptococcus Mutans and the Ability to Form Biofilms. *European Journal of Clinical Microbiology and Infectious Diseases* **2014**, *33*, 499–515. https://doi.org/10.1007/s10096-013-1993-7.
(83) Matsumoto-Nakano, M. Role of Streptococcus Mutans Surface Proteins for Biofilm Formation. *Japanese Dental Science Review* **2018**, *54* (1), 22–29. https://doi.org/10.1016/j.jdsr.2017.08.002.
(84) Banas, J. A.; Vickerman, M. M. Glucan-Binding Proteins of the Oral Streptococci. *Critical Reviews in Oral Biology and Medicine* **2003**, *14* (2), 89–99. https://doi.org/10.1177/154411130301400203.

(85) TOSHIHIKO KOGA, HIDEHARU ASAKAWA, N. O. A. S. H. Sucrose-Dependent Cell Adherence and Cariogenicity of Serotype c Streptococcus Mutans. *Microbiology (N Y)* **1986**, *132* (10), 2873–2883. https://doi.org/10.1099/00221287-132-10-2873.

(86) Lévesque, C. M.; Voronejskaia, E.; Huang, Y. C. C.; Mair, R. W.; Ellen, R. P.; Cvitkovitch, D. G. Involvement of Sortase Anchoring of Cell Wall Proteins in Biofilm Formation by Streptococcus Mutans. *Infection and Immunity* **2005**, *73* (6), 3773–3777. https://doi.org/10.1128/IAI.73.6.3773-3777.2005.

(87) Igarashi, T.; Asaga, E.; Goto, N. The Sortase of Streptococcus Mutans Mediates Cell Wall Anchoring of a Surface Protein Antigen. *Oral Microbiology and Immunology* **2003**, *18* (4), 266–269. https://doi.org/10.1034/j.1399-302X.2003.00076.x.

(88) Lee, S. F.; Boran, T. L. Roles of Sortase in Surface Expression of the Major Protein Adhesin P1, Saliva-Induced Aggregation and Adherence, and Cariogenicity of Streptococcus Mutans. *Infect Immun* **2003**, *71* (2), 676–681. https://doi.org/10.1128/IAI.71.2.676-681.2003.

(89) Igarashi, T.; Asaga, E.; Goto, N. Roles of Streptococcus Mutans Dextranase Anchored to the Cell Wall by Sortase. *Oral Microbiology and Immunology* **2004**, *19* (2), 102–105. https://doi.org/10.1046/j.0902-0055.2003.00123.x.

(90) Guo, L.; Hu, W.; He, X.; Lux, R.; McLean, J.; Shi, W. Investigating Acid Production by Streptococcus Mutans with a Surface-Displayed PH-Sensitive Green Fluorescent Protein. *PLoS One* **2013**, *8* (2), e57182–e57182. https://doi.org/10.1371/journal.pone.0057182.

(91) Hwang, G.; Liu, Y.; Kim, D.; Sun, V.; Aviles-Reyes, A.; Kajfasz, J. K.; Lemos, J. A.; Koo, H. Simultaneous Spatiotemporal Mapping of in Situ PH and Bacterial Activity within an Intact 3D Microcolony Structure. *Scientific Reports* **2016**, *6* (1), 32841. https://doi.org/10.1038/srep32841.

(92) Kim, D.; Barraza, J. P.; Arthur, R. A.; Hara, A.; Lewis, K.; Liu, Y.; Scisci, E. L.; Hajishengallis, E.; Whiteley, M.; Koo, H. Spatial Mapping of Polymicrobial Communities Reveals a Precise Biogeography Associated with Human Dental Caries. *Proc Natl Acad Sci U S A* **2020**, *117*, 12375–12386. https://doi.org/10.1073/pnas.1919099117.

(93) Matsui, R.; Cvitkovitch, D. Acid Tolerance Mechanisms Utilized by Streptococcus Mutans. *Future Microbiology* **2010**, *5* (3), 403–417. https://doi.org/10.2217/fmb.09.129.

(94) Hamilton, I. R.; Buckley, N. D. Adaptation by Streptococcus Mutans to Acid Tolerance. *Oral Microbiology and Immunology* **1991**, *6* (2), 65–71. https://doi.org/10.1111/j.1399-302X.1991.tb00453.x.

(95) Welin-Neilands, J.; Svensäter, G. Acid Tolerance of Biofilm Cells of Streptococcus Mutans. *Appl Environ Microbiol* **2007**, *73* (17), 5633–5638. https://doi.org/10.1128/AEM.01049-07.

(96) Duque, C.; Stipp, R. N.; Wang, B.; Smith, D. J.; Höfling, J. F.; Kuramitsu, H. K.; Duncan, M. J.; Mattos-Graner, R. O. Downregulation of GbpB, a Component of the VicRK Regulon, Affects Biofilm Formation and Cell Surface Characteristics of Streptococcus Mutans. *Infection and Immunity* **2011**, *79*, 786–796. https://doi.org/10.1128/IAI.00725-10.

(97) Senadheera, M. D.; Guggenheim, B.; Spatafora, G. A.; Huang, Y. C. C.; Choi, J.; Hung, D. C. I.; Treglown, J. S.; Goodman, S. D.; Ellen, R. P.; Cvitkovitch, D. G. A VicRK Signal Transduction System in Streptococcus Mutans Affects GtfBCD, GbpB, and Ftf Expression, Biofilm Formation, and Genetic Competence Development. *Journal of Bacteriology* **2005**, *187* (12), 4064–4076. https://doi.org/10.1128/JB.187.12.4064-4076.2005.

(98) Mukherjee, S.; Bassler, B. L. Bacterial Quorum Sensing in Complex and Dynamically Changing Environments. *Nature Reviews Microbiology* **2019**, *17* (6), 371–382. https://doi.org/10.1038/s41579-019-0186-5.

(99) Zero, D. T.; Fontana, M.; Martinez-Mier, E. A.; Ferreira-Zandona, A.; Ando, M.; Gonzalez-Cabezas, C.; Bayne, S. The Biology, Prevention, Diagnosis and Treatment of Dental

Caries Scientific Advances in the United States. *Journal of the American Dental Association* **2009**, *140*, 25S-34S. https://doi.org/10.14219/JADA.ARCHIVE.2009.0355.

(100) Lee, Y. Diagnosis and Prevention Strategies for Dental Caries. *J Lifestyle Med* **2013**, *3*, 107–109.

(101) Petersen, P. E.; Ogawa, H. Prevention of Dental Caries through the Use of Fluoride – the WHO Approach. *Community Dental Health* **2016**, *33*, 66–68. https://doi.org/10.1922/CDH_Petersen03.

(102) Ccahuana-Vásquez, R. A.; Tabchoury, C. P. M.; Tenuta, L. M. A.; del Bel Cury, A. A.; Vale, G. C.; Cury, J. A. Effect of Frequency of Sucrose Exposure on Dental Biofilm Composition and Enamel Demineralization in the Presence of Fluoride. *Caries Research* **2007**, *41* (1), 9–15. https://doi.org/10.1159/000096100.

(103) Milgrom, P.; Rothen, M.; Milgrom, L. Developing Public Health Interventions with Xylitol for the US and US-Associated Territories and States. *Suomen hammaslaakarilehti = Finlands tandlakartidning / [HT]* **2006**, *13*, 2–11.

(104) Masadeh, Majed M., Gharaibeh, Shadi F., Alzoubi, Karem H., Al-Azzam, Sayer I., Obeidat, W. M. Antimicrobial Activity of Common Mouthwash Solutions on Multidrug-Resistance Bacterial Biofilms. *Journal of Clinical Medicine Research* **2013**, *5*, 389–394. https://doi.org/10.4021/jocmr1535w.

(105) Walsh, T.; Oliveira-Neto, J. M.; Moore, D. Chlorhexidine Treatment for the Prevention of Dental Caries in Children and Adolescents. *Cochrane Database of Systematic Reviews* **2015**, *4*, 1–57. https://doi.org/10.1002/14651858.CD008457.pub2.

(106) Joanna Asadoorian, AAS(DH), BScD(DH), MSc and Karen B Williams, RDH, P. Cetylpyridinium Chloride Mouth Rinse on Gingivitis and Plaque. *Journal of Dental Hygeine* **2008**, *82*, 1–5.

(107) Flötra L, Gjermo P, Rölla G, W. J. Side Effects of Chlorhexidine Mouth Washes. *European Journal of Oral Sciences* **1971**, *79* (2), 119–125. https://doi.org/10.1111/j.1600-0722.1971.tb02001.x.

(108) Marsh, P. D. Controlling the Oral Biofilm with Antimicrobials. *Journal of Dentistry* **2010**, *38*, S11-15. https://doi.org/10.1016/S0300-5712(10)70005-1.

(109) Newman, D. J.; Cragg, G. M. Natural Products as Sources of New Drugs over the Nearly Four Decades from 01/1981 to 09/2019. *Journal of Natural Products* **2020**, *83* (3), 770–803. https://doi.org/10.1021/acs.jnatprod.9b01285.

(110) Paytubi, S.; de La Cruz, M. L.; Tormo, J. R.; Martín, J.; González, I.; González-Menendez, V.; Genilloud, O.; Reyes, F.; Vicente, F.; Madrid, C.; Balsalobre, C. A High-Throughput Screening Platform of Microbial Natural Products for the Discovery of Molecules with Antibiofilm Properties against Salmonella. *Frontiers in Microbiology* **2017**, *8*, 1–13. https://doi.org/10.3389/fmicb.2017.00326.

(111) Junker, L. M.; Clardy, J. High-Throughput Screens for Small-Molecule Inhibitors of Pseudomonas Aeruginosa Biofilm Development. *Antimicrobial Agents and Chemotherapy* **2007**, *51* (10), 3582–3590. https://doi.org/10.1128/AAC.00506-07.

(112) Townsley, L.; Shank, E. A. Natural-Product Antibiotics: Cues for Modulating Bacterial Biofilm Formation. *Trends in Microbiology* **2017**, *25* (12), 1016–1026. https://doi.org/10.1016/j.tim.2017.06.003.

(113) Park, S. R.; Tripathi, A.; Wu, J.; Schultz, P. J.; Yim, I.; McQuade, T. J.; Yu, F.; Arevang, C. J.; Mensah, A. Y.; Tamayo-Castillo, G.; Xi, C.; Sherman, D. H. Discovery of Cahuitamycins as Biofilm Inhibitors Derived from a Convergent Biosynthetic Pathway. *Nature Communications* **2016**, *7*, 1–11. https://doi.org/10.1038/ncomms10710.

(114) Rabin, N.; Zheng, Y.; Opoku-Temeng, C.; Du, Y.; Bonsu, E.; Sintim, H. O. Agents That Inhibit Bacterial Biofilm Formation. *Future Medicinal Chemistry* **2015**, *7* (5), 647–671. https://doi.org/10.4155/fmc.15.7.

(115) Yoo, S.; Murata, R. M.; Duarte, S. Antimicrobial Traits of Tea- and Cranberry-Derived Polyphenols against Streptococcus Mutans. *Caries Research* **2011**, *45* (4), 327–335. https://doi.org/10.1159/000329181.

(116) Ferrazzano, G. F.; Amato, I.; Ingenito, A.; Zarrelli, A.; Pinto, G.; Pollio, A. Plant Polyphenols and Their Anti-Cariogenic Properties: A Review. *Molecules* **2011**, *16* (2), 1486–1507. https://doi.org/10.3390/molecules16021486.

(117) Palombo, E. A. Traditional Medicinal Plant Extracts and Natural Products with Activity against Oral Bacteria: Potential Application in the Prevention and Treatment of Oral Diseases. *Evidence-based Complementary and Alternative Medicine* **2011**, *2011*, 1–15. https://doi.org/10.1093/ecam/nep067.

(118) Zhao, W.; Cross, A. R.; Crowe-McAuliffe, C.; Weigert-Munoz, A.; Csatary, E. E.; Solinski, A. E.; Krysiak, J.; Goldberg, J. B.; Wilson, D. N.; Medina, E.; Wuest, W. M.; Sieber, S. A. The Natural Product Elegaphenone Potentiates Antibiotic Effects against Pseudomonas Aeruginosa. *Angewandte Chemie - International Edition* **2019**, *58*, 8581–8584. https://doi.org/10.1002/anie.201903472.

(119) Khan, R.; Zakir, M.; Khanam, Z.; Shakil, S.; Khan, A. U. Novel Compound from Trachyspermum Ammi (Ajowan Caraway) Seeds with Antibiofilm and Antiadherence Activities against Streptococcus Mutans: A Potential Chemotherapeutic Agent against Dental Caries. *Journal of Applied Microbiology* **2010**, *109* (6), 2151–2159. https://doi.org/10.1111/j.1365-2672.2010.04847.x.

(120) Weiss, E.; Rosenberg, M.; Judes, H.; Rosenberg, E. Cell-Surface Hydrophobicity of Adherent Oral Bacteria. *Current Microbiology* **1982**, *7* (2), 125–128. https://doi.org/10.1007/BF01568427.

(121) Beier, D.; Gross, R. Regulation of Bacterial Virulence by Two-Component Systems. *Current Opinion in Microbiology* **2006**, *9* (2), 143–152. https://doi.org/10.1016/j.mib.2006.01.005.

(122) Cvitkovitch, D. G.; Li, Y. H.; Ellen, R. P. Quorum Sensing and Biofilm Formation in Streptococcal Infections. *Journal of Clinical Investigation* **2003**, *112* (11), 1626–1632. https://doi.org/10.1172/JCI200320430.

(123) K. Bhardwaj, A.; Vinothkumar, K.; Rajpara, N. Bacterial Quorum Sensing Inhibitors: Attractive Alternatives for Control of Infectious Pathogens Showing Multiple Drug Resistance. *Recent Patents on Anti-Infective Drug Discovery* **2013**, *8* (1), 68–83. https://doi.org/10.2174/157489113805290809.

(124) Gerdt, J. P.; Blackwell, H. E. Competition Studies Confirm Two Major Barriers That Can Preclude the Spread of Resistance to Quorum-Sensing Inhibitors in Bacteria. *ACS Chemical Biology* **2014**, *9* (10), 2291–2299. https://doi.org/10.1021/cb5004288.

(125) Ballard, T. E.; Richards, J. J.; Wolfe, A. L.; Melander, C. Synthesis and Antibiofilm Activity of a Second-Generation Reverse-Amide Oroidin Library: A Structure–Activity Relationship Study. *Chemistry – A European Journal* **2008**, *14* (34), 10745–10761. https://doi.org/10.1002/chem.200801419.

(126) AleŠ Žula, Danijel Kikelj, J. Ilaš. 2-Aminoimidazoles in Medicinal Chemistry. *Mini-Reviews in Medicinal Chemistry* **2013**, *13* (13), 1921–1943. https://doi.org/http://dx.doi.org/10.2174/1389557511313130007.

(127) Hu, M.; Zhang, C.; Mu, Y.; Shen, Q.; Feng, Y. Indole Affects Biofilm Formation in Bacteria. *Indian Journal of Microbiology* **2011**, *50* (4), 362–868. https://doi.org/10.1007/s12088-011-0142-1.

(128) Hodnik, Ž.; Łoś, J. M.; Žula, A.; Zidar, N.; Jakopin, Ž.; Łoś, M.; Sollner Dolenc, M.; Ilaš, J.; Węgrzyn, G.; Peterlin Mašič, L.; Kikelj, D. Inhibition of Biofilm Formation by Conformationally Constrained Indole-Based Analogues of the Marine Alkaloid Oroidin. *Bioorganic and Medicinal Chemistry Letters* **2014**, *24* (11), 2530–2534. https://doi.org/10.1016/j.bmcl.2014.03.094.

(129) Eguchi, Y.; Kubo, N.; Matsunaga, H.; Igarashi, M.; Utsumi, R. Development of an Antivirulence Drug against Streptococcus Mutans: Repression of Biofilm Formation, Acid Tolerance, and Competence by a Histidine Kinase Inhibitor, Walkmycin C. *Antimicrobial Agents and Chemotherapy* **2011**, *55* (4), 1475–1484. https://doi.org/10.1128/AAC.01646-10.

(130) Xu, X.; Zhou, X. D.; Wu, C. D. Tea Catechin Epigallocatechin Gallate Inhibits Streptococcus Mutans Biofilm Formation by Suppressing Gtf Genes. *Archives of Oral Biology* **2012**, *57* (6), 678–683. https://doi.org/10.1016/j.archoralbio.2011.10.021.

(131) Xu, X.; Zhou, X. D.; Wu, C. D. The Tea Catechin Epigallocatechin Gallate Suppresses Cariogenic Virulence Factors of Streptococcus Mutans. *Antimicrobial Agents and Chemotherapy* **2011**, *55* (3), 1229–1236. https://doi.org/10.1128/AAC.01016-10.

(132) Melok, A.; Lee, L.; Mohamed Yussof, S.; Chu, T. Green Tea Polyphenol Epigallocatechin-3-Gallate-Stearate Inhibits the Growth of Streptococcus Mutans: A Promising New Approach in Caries Prevention. *Dentistry Journal* **2018**, *6* (3), 1–8. https://doi.org/10.3390/dj6030038.

(133) Atanasov, A. G.; Zotchev, S. B.; Dirsch, V. M.; Orhan, I. E.; Banach, M.; Rollinger, J. M.; Barreca, D.; Weckwerth, W.; Bauer, R.; Bayer, E. A.; Majeed, M.; Bishayee, A.; Bochkov, V.; Bonn, G. K.; Braidy, N.; Bucar, F.; Cifuentes, A.; D'Onofrio, G.; Bodkin, M.; Diederich, M.; Dinkova-Kostova, A. T.; Efferth, T.; el Bairi, K.; Arkells, N.; Fan, T.-P.; Fiebich, B. L.; Freissmuth, M.; Georgiev, M. I.; Gibbons, S.; Godfrey, K. M.; Gruber, C. W.; Heer, J.; Huber, L. A.; Ibanez, E.; Kijjoa, A.; Kiss, A. K.; Lu, A.; Macias, F. A.; Miller, M. J. S.; Mocan, A.; Müller, R.; Nicoletti, F.; Perry, G.; Pittalà, V.; Rastrelli, L.; Ristow, M.; Russo, G. L.; Silva, A. S.; Schuster, D.; Sheridan, H.; Skalicka-Woźniak, K.; Skaltsounis, L.; Sobarzo-Sánchez, E.; Bredt, D. S.; Stuppner, H.; Sureda, A.; Tzvetkov, N. T.; Vacca, R. A.; Aggarwal, B. B.; Battino, M.; Giampieri, F.; Wink, M.; Wolfender, J.-L.; Xiao, J.; Yeung, A. W. K.; Lizard, G.; Popp, M. A.; Heinrich, M.; Berindan-Neagoe, I.; Stadler, M.; Daglia, M.; Verpoorte, R.; Supuran, C. T.; Taskforce, the I. N. P. S. Natural Products in Drug Discovery: Advances and Opportunities. *Nature Reviews Drug Discovery* **2021**, *20* (3), 200–216. https://doi.org/10.1038/s41573-020-00114-z.

(134) Rossiter, S. E.; Fletcher, M. H.; Wuest, W. M. Natural Products as Platforms to Overcome Antibiotic Resistance. *Chemical Reviews* **2017**, *117*, 12415–12474. https://doi.org/10.1021/acs.chemrev.7b00283.

(135) Karageorgis, G.; Waldmann, H. Guided by Evolution: Biology-Oriented Synthesis of Bioactive Compound Classes. *Synthesis (Stuttg)* **2019**, *51* (01), 55–66.

(136) Wetzel, S.; Bon, R. S.; Kumar, K.; Waldmann, H. Biology-Oriented Synthesis. *Angewandte Chemie International Edition* **2011**, *50* (46), 10800–10826. https://doi.org/https://doi.org/10.1002/anie.201007004.

(137) L., S. S. Target-Oriented and Diversity-Oriented Organic Synthesis in Drug Discovery. *Science (1979)* **2000**, *287* (5460), 1964–1969. https://doi.org/10.1126/science.287.5460.1964.

(138) O' Connor, C. J.; Beckmann, H. S. G.; Spring, D. R. Diversity-Oriented Synthesis: Producing Chemical Tools for Dissecting Biology. *Chemical Society Reviews* **2012**, *41* (12), 4444–4456. https://doi.org/10.1039/C2CS35023H.

(139) Milani, G.; Cavalluzzi, M. M.; Solidoro, R.; Salvagno, L.; Quintieri, L.; di Somma, A.; Rosato, A.; Corbo, F.; Franchini, C.; Duilio, A.; Caputo, L.; Habtemariam, S.; Lentini, G. Molecular Simplification of Natural Products: Synthesis, Antibacterial Activity, and Molecular Docking Studies of Berberine Open Models. *Biomedicines* . 2021. https://doi.org/10.3390/biomedicines9050452.

(140) Wang, S.; Dong, G.; Sheng, C. Structural Simplification of Natural Products. *Chemical Reviews* **2019**, *119* (6), 4180–4220. https://doi.org/10.1021/acs.chemrev.8b00504.

(141) Wang, S.; Dong, G.; Sheng, C. Structural Simplification: An Efficient Strategy in Lead Optimization. *Acta Pharmaceutica Sinica B* **2019**, *9* (5), 880–901. https://doi.org/https://doi.org/10.1016/j.apsb.2019.05.004.

(142) Szpilman, A. M.; Carreira, E. M. Probing the Biology of Natural Products: Molecular Editing by Diverted Total Synthesis. *Angewandte Chemie International Edition* **2010**, *49* (50), 9592–9628. https://doi.org/https://doi.org/10.1002/anie.200904761.

(143) Basu, S.; Ellinger, B.; Rizzo, S.; Deraeve, C.; Schürmann, M.; Preut, H.; Arndt, H.-D.; Waldmann, H. Biology-Oriented Synthesis of a Natural-Product Inspired Oxepane Collection Yields a Small-Molecule Activator of the Wnt-Pathway. *Proceedings of the National Academy of Sciences* **2011**, *108* (17), 6805 LP – 6810. https://doi.org/10.1073/pnas.1015269108.

(144) Galloway, W. R. J. D.; Isidro-Llobet, A.; Spring, D. R. Diversity-Oriented Synthesis as a Tool for the Discovery of Novel Biologically Active Small Molecules. *Nature Communications* **2010**, *1* (1), 80. https://doi.org/10.1038/ncomms1081.

(145) Staub, I.; Sieber, S. A. β-Lactams as Selective Chemical Probes for the in Vivo Labeling of Bacterial Enzymes Involved in Cell Wall Biosynthesis, Antibiotic Resistance, and Virulence. *J Am Chem Soc* **2008**, *130* (40), 13400–13409. https://doi.org/10.1021/ja803349j.

(146) Li, Q.; Pellegrino, J.; Lee, D. J.; Tran, A. A.; Chaires, H. A.; Wang, R.; Park, J. E.; Ji, K.; Chow, D.; Zhang, N.; Brilot, A. F.; Biel, J. T.; van Zundert, G.; Borrelli, K.; Shinabarger, D.; Wolfe, C.; Murray, B.; Jacobson, M. P.; Mühle, E.; Chesneau, O.; Fraser, J. S.; Seiple, I. B. Synthetic Group A Streptogramin Antibiotics That Overcome Vat Resistance. *Nature* **2020**, *586* (7827), 145–150. https://doi.org/10.1038/s41586-020-2761-3.

(147) Mitcheltree, M. J.; Pisipati, A.; Syroegin, E. A.; Silvestre, K. J.; Klepacki, D.; Mason, J. D.; Terwilliger, D. W.; Testolin, G.; Pote, A. R.; Wu, K. J. Y.; Ladley, R. P.; Chatman, K.; Mankin, A. S.; Polikanov, Y. S.; Myers, A. G. A Synthetic Antibiotic Class Overcoming Bacterial Multidrug Resistance. *Nature* **2021**, *599* (7885), 507–512. https://doi.org/10.1038/s41586-021-04045-6.

2 Carolacton – inspiration for cancer inhibitors & SMU biofilm inhibitors

Sections 2.3-2.6 have been adapted with permission from (Solinski, A. E.; Scharnow, A. M.; Fraboni, A. J.; Wuest, W. M. Synthetic Simplification of Carolacton Enables Chemical Genetic Studies in Streptococcus mutans. *ACS Infect. Dis.* **2019**. https://doi.org/10.1021/acsinfecdis.9b00213.).

2.1 Carolacton Introduction

2.1.1 Isolation and bioactivity of carolacton

Myxobacteria are natural product machines. The secondary metabolites produced by myxobacteria are rich in diversity and complexity as a result of their larger genomes, with *Sorangium cellulosum* having one of the largest genomes reported.[148] Carolacton (**2.1**) is a natural product produced by *S. cellulosum* strain So ce960 that was first isolated in 1998 (Figure 2.1).[149] It wasn't until carolacton was found to have interesting bioactivity in 2010, that the complex structure, containing numerous functional groups and a decorated 14-membered macrolactone, was elucidated.[150] Over the last decade, carolacton has been the focus of numerous total synthesis, mechanism of action, and target identification investigations.

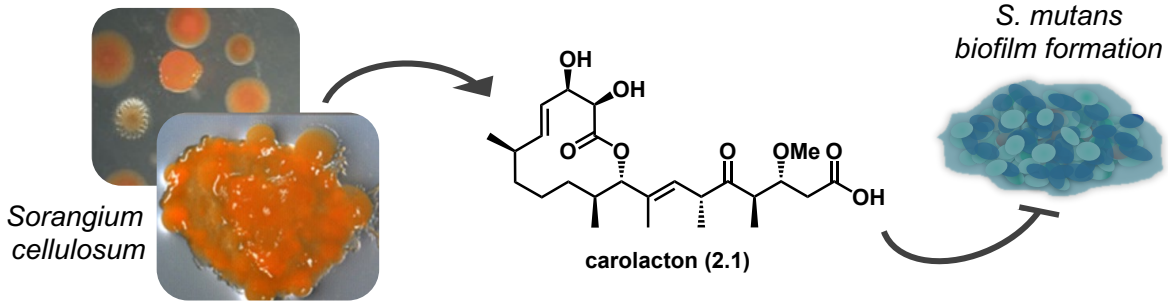

Figure 2.1 Natural product carolacton

Prior to 2010, carolacton found to inhibit an efflux mutant of *E. coli*, however it showed little activity against other strains up to 80 μM, and minor activity against fungi, resulting in a decade hiatus on carolacton research. Subsequent analysis found that carolacton potently killed *S. mutans* cells that were transitioning into a biofilm, but did not impact planktonic growth, which

bodes well for conservation of the commensal oral microbiome. As mentioned previously, many approved antibiotics display decreased effects on organisms in biofilms,[151,152] hindering both their utility as pharmacological agents and as tools to probe these complex systems, making carolacton an attractive target for the development of anti-biofilm compounds as a tool to better understand *S. mutans* biology.

Additional investigation by Muller and co-workers found that at 0.005 μg/mL (10 nM) 35% of cells were non-viable, and at 0.025 μg/mL (50 nM) 66% were non-viable.[153] Using LIVE/DEAD staining and confocal laser microscopy (CLMS), they analyzed the morphology and viability of carolacton treated biofilms. At both concentrations, biofilms exhibited weakened morphologies, as well as elongated and bulged cells. Subsequent studies into carolacton's mechanism of action demonstrated an acid dependent mechanism. In biofilm cells that endogenously produce acid, carolacton is active, but if this culture is buffered, carolacton loses activity. If planktonic cells are pre-cultured in acidic media prior to carolacton treatment, the natural product is active against the planktonic culture. Under typical, neutral planktonic conditions, carolacton is inactive. Studies with the methyl ester of carolacton found that it maintained activity, suggesting that the pH dependence of carolacton is not due to the carboxylic acid itself or the structural activation of the carboxylic acid. Subsequent work demonstrated that *in situ* hydrolysis occurs, revealing the acid likely via an extracellular enzyme, demonstrating the importance of this motif.[154] Wagner-Dobler and co-workers also found that carolacton causes leakage of the cytoplasmic content in cells growing at low pH. Finally, they noted that carolacton's activity plateaus rapidly, suggesting that the target is present in low copy number.[153]

2.1.2 Investigations into the mechanism and target of carolacton

Many groups have contributed to the carolacton story through a variety of methods, including transcriptional analysis, whole proteome analysis, gene knockouts, and phenotypic analysis. Transcriptional analysis on carolacton treated cells implicated CodY (global regulator of

amino acid metabolism), CcpA (carbon catabolite repression), VicR (TCS), and CysR (cysteine metabolism regulator) as major players in carolacton's mechanism.[155] CodY is responsible for branched chain amino acid metabolism, which could contribute to the ATR. CcpA is responsible for carbon utilization and two specific phosphotransferase systems (PTS) under its control were affected by carolacton treatment, including *ptnAB*. Another system that was drastically affected was pyrimidine metabolism. Specifically, the genes responsible for UMP and UDP were upregulated, which can lead to pools of UDP-N-acetylglucosamine, a precursor for cell wall peptidoglycan. Glutamine transporters were also upregulated, which could also contribute to replenishing the cell wall pools. CysR is a cysteine metabolism regulator that was one of the most affected networks. Members of the CysR regulon that were affected included SMU.609 (a putative peptidoglycan hydrolase), SMU. 246 (glycosyltransferase-N-acetylglucosaminyltransferase), and SMU.984 (an uncharacterized autolysin), all of which are tied to cell wall homeostasis. *RgpG* was another member of the CysR regulon that was affected by carolacton, and this protein is part of the rhamnose-glucose polymer biosynthesis pathway and plays a critical role in localization of the cell wall divisome. Small effects were also observed with MurMN and MbrC, which are involved in stem peptide modification and branched chain amino acid synthesis.

Proteomic analysis reinforced many of these results.[156] SMU.609 was similarly upregulated. Cell wall biosynthesis proteins were greatly influenced in the same direction, including two enzymes involved in glutamine biosynthesis. Finally, pyrimidine metabolism was affected as previously demonstrated.

The anti-biofilm activity of carolacton has the strongest ties to the PknB regulon which has been demonstrated throughout all studies on carolacton. PknB is a serine/threonine protein kinase responsible for regulating a diverse array of pathways, including biofilm formation, competence, and most importantly cell division.[157,158] *S. mutans* employs two cell division models, peripheral and septal, depending on the cell's needs, and PknB is speculated to function as regulatory switch between the two. Biofilm assays against a PknB knockout demonstrated loss

of activity, providing strong evidence that PknB mediates the killing effect of carolacton.[158] The elongated cell structure, and increased septum formation induced by carolacton treatment suggest that carolacton either disrupts the coordination between chromosome separation and septal wall synthesis, or mislocalization of the protein machinery responsible for Z-ring placement. While, PknB appears to mediate this activity, its central regulatory role makes it likely that a downstream protein is the true target.

Looking into the PknB regulon using transcriptional analysis, it was found that carolacton immediately downregulated VicRK, a TCS regulated by PknB. All members of the VicRK regulon were affected, except gbpAB.[155] However, the previously mentioned proteomic analysis reported that GbpB was downregulated by about 2-fold.[156] Notably, SMU.609, a putative murein hydrolase, and SMU.503, were the two genes upregulated most strongly, which supports the previous findings demonstrating upregulation of SMU.609.[155,158] SMU. 503 encodes a folate carrier present which could function as a folate transporter, and as such would be very involved in purine, pyrimidine, and methionine metabolism. Both genes localize at the mid-cell with PknB suggesting they play a role in the divisome.[159] Carolacton also disrupts localization of PknB, resulting in cell wall defects. Other genes under the control of PknB were affected that are involved in cell wall metabolism and the phosphotransferase system (sugar import).

In 2017, Muller and co-workers returned to the original assay used to discover carolacton using an *E. coli* efflux knockout *(E. coli∆tolC*) that identified carolacton in attempt to identify its molecular target after a report was published stating that carolacton can enter these cells.[160,161] Using an agar-based assay, they evolved carolacton-resistant isolates. Sequencing revealed mutations in a single target, the gene encoding folate dehydrogenase (FolD). This enzyme plays a key role in folate-dependent one-carbon metabolism, in *E. coli*, *Streptococcus pneumoniae*, and the human homolog MTHFD1/MTHFD2. They confirmed this result via an enzymatic inhibition assay with purified FolD from both *E. coli* and through structure determination of the FolD-carolacton complex. Additionally, they confirmed the inhibitory results against *S. pneumoniae*

derived FolD, since carolacton has inhibitory activity against this Gram-positive bacterium.[162] However, these results cannot account for the acid dependence exhibited by carolacton. The previous connection to SMU.503, the putative folate transporter, could point toward an explanation, but further investigation is required.[158]

Collectively, carolacton most strongly affects carbon utilization, cell wall biosynthesis and amino acid biosynthesis. The primary mechanism is likely through disruption of cell wall synthesis and division as this is the intersecting node between the three most affected areas. The cell membrane damage and cytoplasmic leakage are likely a secondary mechanism that results from a weakened membrane in the presence of acid. Normally, *S. mutans* can alter its membrane to protect from its own acid production, but if resources are diverted toward cell wall homeostasis, there are less resources available to mediate the ATR. Despite this cannon of work, the connection between FolD and carolacton's mechanism of action remains unclear. Clarification of this connection will enable more specific and robust analog design and provide a better understanding of *S. mutans* biology. Moreover, identification of the molecular target will hopefully unveil a new antibiotic target.

2.1.3 Total and biological investigation by the Wuest lab

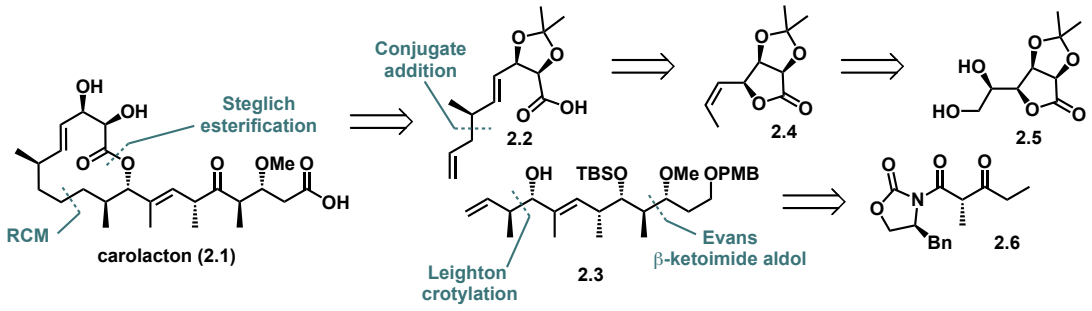

Figure 2.2 The Wuest lab's retrosynthetic analysis

Following the structure elucidation of carolacton, three total syntheses and four partial syntheses were reported of this complex structure. Prior to me joining the lab, the Wuest group

began their initial investigation into carolacton with a total synthesis in collaboration with the Phillips lab at Yale University.[163] They recognized that they could construct the macrocycle through a Steglich esterification and ring-closing metathesis from late-stage intermediates **2.2** and **2.3** (Figure 2.2). The acid fragment (**2.2**) can be accessed through an organocuprate-mediated conjugate addition from lactone **2.4** which they envisioned preparing through an oxidative cleavage/Wittig sequence from **2.5**. The southern sidechain fragment **2.3** can be accessed through a Leighton crotylation and Evans β-ketoimide aldol from Evan's auxiliary **2.6**. In collaboration with the Phillips lab, they conducted a 14 longest-linear step synthesis in an overall yield of 8%.

Subsequent biological analysis confirmed that carolacton induced an anti-biofilm effect (Figure 2.3). Further, they identified a novel phenotype caused by CD1 **2.7** (Figure 2.3). They quickly recognized that studying carolacton comes with many limitations. Firstly, the stereochemically complex sidechain is synthetically limiting. Additionally, because carolacton lacks a quantifiable inhibition, LIVE/DEAD^{TM} staining and confocal microscopy, or viability assays using colony forming unit (CFU/mL) counts are required to determine activity changes. The former is cost prohibitive and subjective, and both methods are laborious and unable to detect subtle changes in activity.

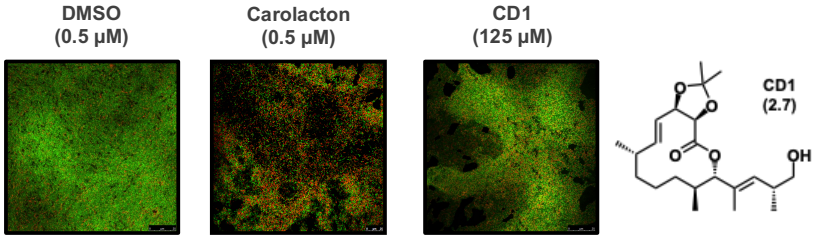

Figure 2.3 Confocal images of compound-treated biofilms

2.1.4 Diverted total synthesis of carolacton

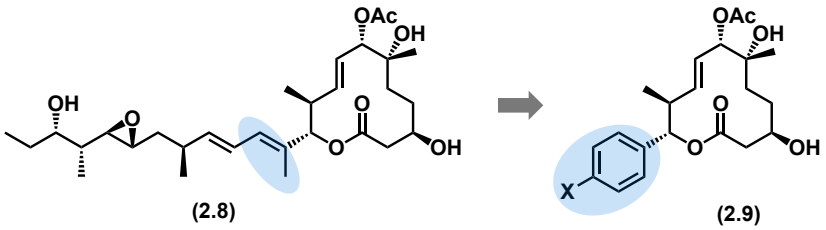

Figure 2.4 Inspiration for 1st generation of analogs

The complexity of carolacton's synthesis inspired the Wuest lab to explore simplified scaffolds via diverted total synthesis (DTS). Previous graduate student, Rich Brzozowski recognized a similar trisubstituted alkene in the natural product pladienolide (**2.8**) that was replaced by an aryl ring without altering cancer activity (Figure 2.4).[164]

Additionally, computational modeling confirmed that the orientation of the sidechain would be retained in the simplified, aryl analogs. They envisioned leveraging the previous synthesis of carolacton using the late-stage acid intermediate **2.2** to rapidly couple in different sidechains (Figure 2.5). The aryl sidechain **2.11** could be accessed through an Rousch crotylation from **2.12**. They intended to access aldehyde **2.12** from a Suzuki coupling between aryl bromide **2.14** and terminal alkenes of various lengths as shown in **2.13**. This route included ten fewer steps than the total synthesis of carolacton and provided an easy handle for sidechain diversification.

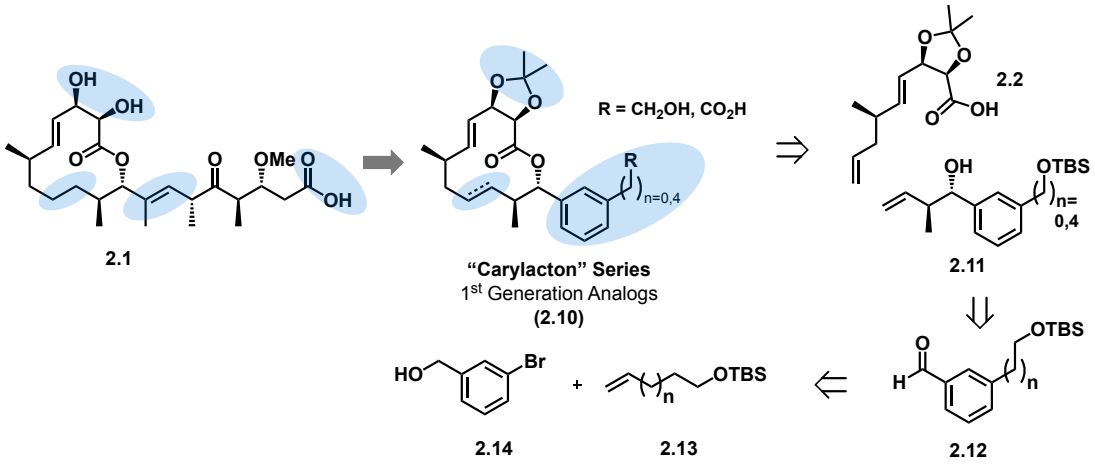

Figure 2.5 Design of 1st generation carolacton analogs via DTS

Following the successful synthesis of this library, they investigated the effects of these analogs on biofilm formation via CLMS.[165] The carolacton mimic, carylacton (**2.15**), induced a similar phenotype to the natural product at 500 nM (Figure 2.6). Both compounds weaken the architecture and reduce the viability of the biofilm. Interestingly, they observed new phenotypes with the truncated analogs. As shown by the representative analog D2 (**2.16**), a microcolony phenotype was observed wherein the biofilm cells were prevented from forming a mature biofilm. This phenotype presents a potential platform for potentiation of current treatments. The activity relationships between the carolacton and the various analogs remains unclear. Additional investigation into this relationship is ongoing by graduate student, Christian Sanchez.

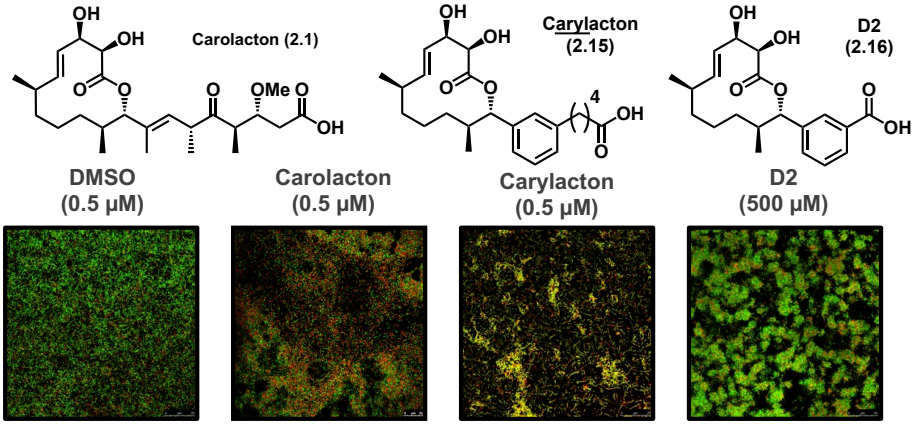

Figure 2.6 CLMS of Carylacton series

2.2 Carolacton-inspired cancer inhibitors

2.2.1 Background

As previously discussed in section 2.1.2, carolacton (**2.1**) has inhibitory activity against the enzyme FolD. In this work, the authors also conducted computational modeling. They superimposed the FolD-carolacton structure onto the human ortholog, MTHFD2, which was crystalized with $NADP^+$ and a substrate analog.[160] From this they found that carolacton would prevent binding of both compounds. Additional docking was done with the aryl analog synthesized by our lab, carylacton (**2.15**). They found that this derivative could form better hydrophobic interactions than the natural product (**2.1**). The authors also noted that truncating the methylene by one carbon would induce a better fit. Stefan Kubicek's lab at the Research Center for Molecular Medicine at the Austrian Academy of Sciences reached out to us because they were interested in exploring the aryl mimic of carolacton against this potential cancer target.

2.2.2 MTHFD1 & MTHFD2 as cancer targets

These proteins are involved in mitochondrial folate one-carbon metabolism. MTHFD1 is a trifunctional enzyme that has three domains: methylenetetrahydrofolate dehydrogenase, cyclohydrolase, and formyltetrahydrofolate synthetase domains. Collectively, these domains

convert CH_2-THF to 10-formyl-tetrahydrofolate. In the mitochondria, MTHFD2 and MTHFD2L carry out these reactions. Recently, the role these proteins in the cancer proliferation has garnered much interest. MTHFD1 has been implicated in colon cancer progression.[166] MTHFD2 is upregulated in various cancers, is associated with poor disease outcomes, and depletion of this protein can mitigate aggressive phenotypes and kill cancer cells.[167]

2.2.3 Synthesis of carylacton

As such, I set out to synthesize **2.15** to send out for biological analysis (Scheme 2.1). I subjected the acid fragment (**2.2**) that I prepared to EDC coupling conditions with the alcohol containing sidechain (**2.17**) made by a previous graduate student and accessed **2.18** in 88% yield. Ring closing metathesis (RCM) of **2.18** was then carried out in 98% yield, followed by a selective hydrogenation, yielding **2.20** in 58% yield**.** Subsequent treatment with tetrabutylammomnium fluoride (TBAF) provided alcohol **2.21** in 54% yield. The original synthesis employed in the 1st generation DTS analogs used a two-step oxidation sequence via a Pinnick and a Swern reaction to yield the terminal carboxylic acid in **2.22**. Instead, I opted for a one-step TEMPO/bleach oxidation that afforded the terminal carboxylic acid in 62% yield. Final deprotection of the acetonide protecting group was carried out with HF•pyridine to provide carylacton (**2.15**) in 7% yield. The low yield on the late-stage reactions resulted from purification difficulties. Fortunately, I was able to send approximately 2 mg to the Kubicek lab for testing.

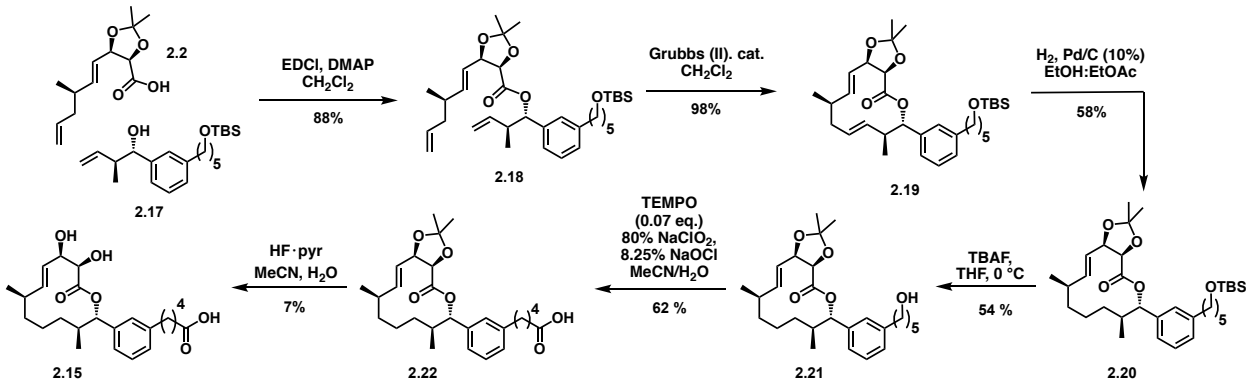

Scheme 2.1 Carylacton synthesis

2.2.4 Evaluation of carylacton as MTHFD1 inhibitor

The Kubicek lab conducted the biological analysis of carylacton (**2.15**) via two assays. The first employed reporter for epigenetic drug screening (REDS) cell lines that induce the expression of mCherry when the protein of interest is inhibited, providing an easy readout for inhibition.[168] They developed a system with MTHFD1 and tested the effects of carylacton treatment. No inhibition was observed at 1 μM and 3 μM carylacton (**2.15**) in comparison to the positive control JQ1, a known inhibitor (Figure 2.8a). The second assay they conducted was a growth rescue assay based on the idea that when MTHFD1 is knocked out, the HAP1 leukemia cells will experience growth rescue in dialyzed media by adenine and derivatives.[169] Thus, they would expect MTFHD1 inhibition to undergo a similar growth rescue under the same conditions. Unfortunately, this effect was not recapitulated in carylacton treated WT cells at 10 μM, but they did observe appreciable toxicity to the cells (Figure 2.8b). For these reasons, we did not pursue the cancer inhibitors further.

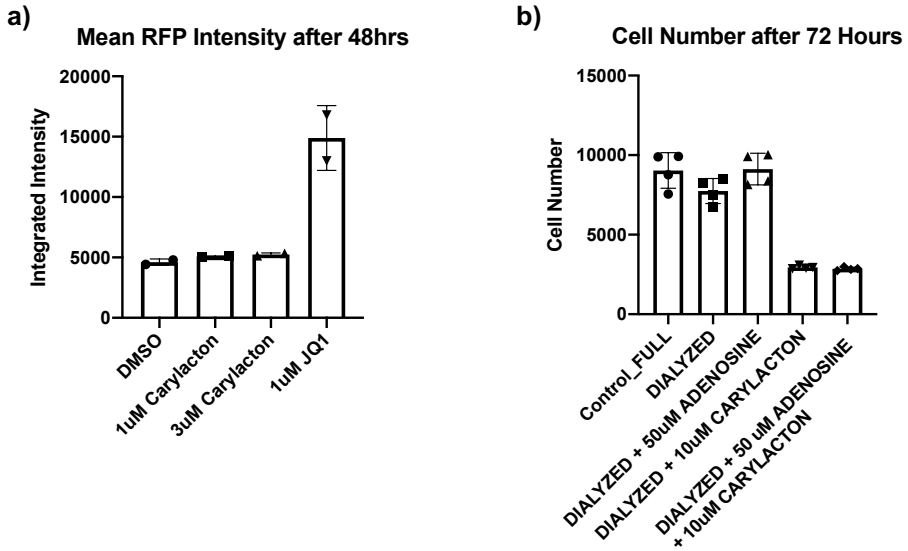

Figure 2.8 MTHD1 inhibition and knockout rescue assays

2.3 Synthetic simplification enables chemical genetic studies

2.3.1 Second-generation design

The previous generation of carolacton analogs validated the aryl group as a bioisostere for a tri-substituted alkene and demonstrated that the polar functionalities, apart from the terminal acid, are not necessary for activity. When I joined the lab, we wondered how further simplifying the sidechain would affect the activity. Would removing the rigidity of the sidechain permit new conformations that could enhance activity? Removal of the aryl ring would impart great flexibility, potentially promoting new binding interactions *in vivo*. To this end, we set out to make n = 5, 8, and 9 analogs. Due to challenges faced along the synthetic route (described below), we prioritized the natural sidechain length resulting on us both carrying out the synthesis of the n=9 analogs simultaneously. Amy Solinski synthesized a panel of n=5 analogs while I prepared n=8 analogs (Figure 2.9). All yields shown are from reactions that I conducted myself. All biological experiments described in the subsequent sections were done by both Amy Solinski and myself.

2.3.2 Simplified analog synthesis

Leveraging the same diverted total synthesis as the previous library we could rapidly access a diverse set of analogs with a simplified alkyl sidechain (**2.23**) (Figure 2.9). To improve the synthesis, we devised a new sidechain synthesis that would reduce the synthesis by one step and avoid harsh oxidation conditions on late-stage macrocycle material. In this route, the macrocycle would be constructed from benzyl ester **2.24** rather than TBS ether **2.25**, which provides the correct oxidation state at the terminal carbon prior to macrocycle formation (Figure 2.9).

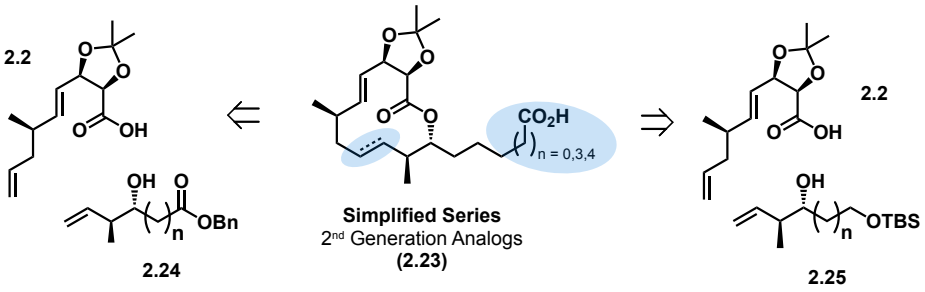

Figure 2.9 Retrosynthetic strategy for the 2nd generation of analogs

In route to the alkyl analogs, a mono-TBS protection of 1,8-octanediol (**2.26**) was carried out in 52% yield, followed by a TEMPO-catalyzed oxidation that yielded carboxylic acid **2.28** in 95% yield (Scheme 2.2). Benzyl protection, and TBS removal primed the scaffold for a Parikh-Doering oxidation from alcohol **2.30** to aldehyde **2.31** in 90 % yield. A stereoselective Rousch crotylation set the two sidechain stereocenters, providing alcohol **2.32** in 65% yield. The synthesis then converges with the previously reported acid fragment **2.2** in an EDC coupling furnishing **2.33**. Subjection to an RCM provided macrocycle **2.34** in 91% yield. A selective hydrogenation was attempted with H_2 (*g*) and Pd/C (10 mol %) in a 1:1 solution of EtOAc:EtOH. This reaction gave a 9:1 ratio of the desired product (**2.35**) to the oversaturated product (**2.37**).

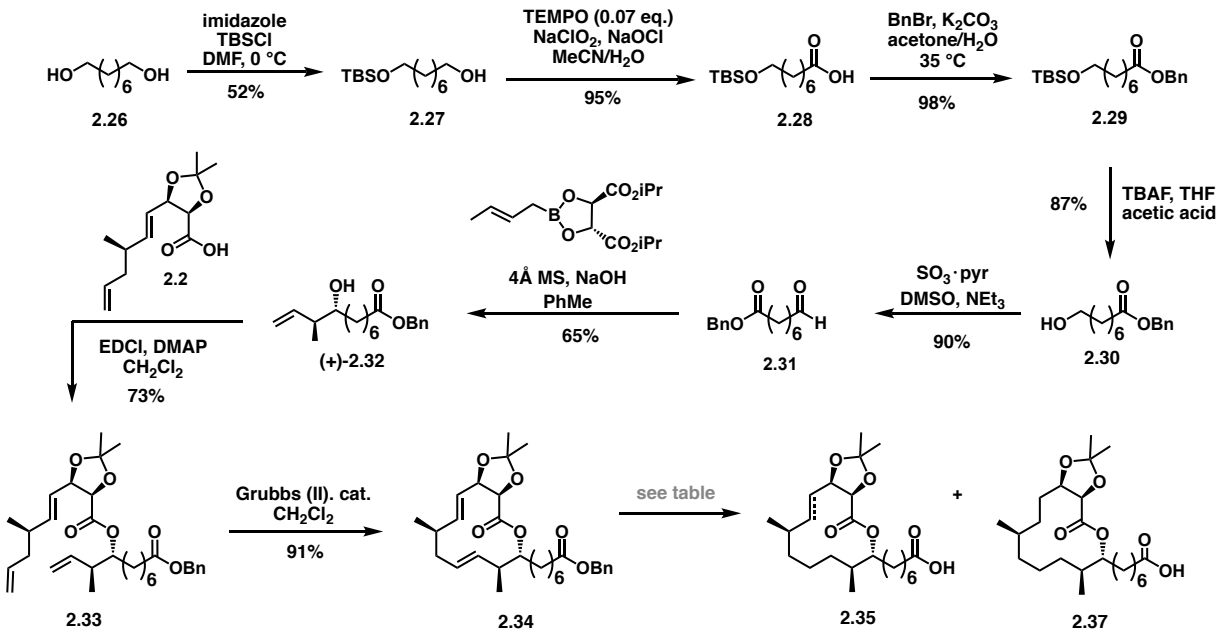

Scheme 2.2 Benzyl ester route to truncated simplified analogs

We attempted a series of purification methods to isolate the desired saturation level. HPLC and mass guided-HPLC-MS were explored, but unfortunately, solubility issues prevented successful use of these methods. Finally, we attempted purification via silver-impregnated silica, which can be used as the solid phase in liquid chromatography for the separation of compounds with different levels of saturation.[170,171] However, these attempts were unsuccessful. For this reason, we reverted to the synthesis published in 2017 aryl series (Scheme 2.1) to probe whether the ester was altering the selectivity of the hydrogenation.[165] This approach would proceed from a late-stage intermediate, such as the OTBS macrocycle **2.41**, or the OH-macrocycle **2.42** (Scheme 2.3), as had been observed in the carolacton synthesis and 1st generation of analogs.

This route proceeds via the same mono-TBS protection yielding **2.27**, followed by a Parikh-Doering oxidation, which afforded aldehyde **2.38** in 69% yield (Scheme 2.3). Akin to the benzyl ester, a Rousch crotylation, EDC coupling, and RCM provided TBS-protected macrocycle **2.40**. The TBS group was removed using TBAF in 83% yield. At this point, we attempted the

selective hydrogenation of the macrocycle, which is discussed following discussion of the n=9 scaffold.

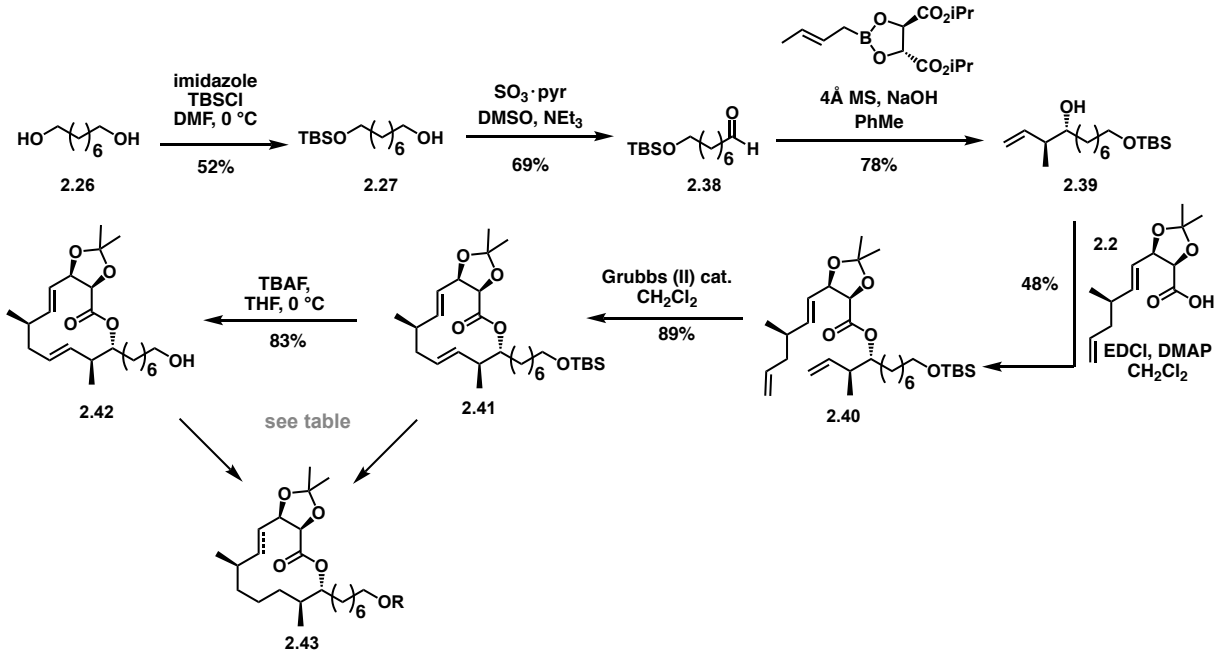

Scheme 2.3 Silyl ether route to truncated simplified analogs

Simultaneously, I synthesized the natural sidechain length analogs using the original silyl ether route (Scheme 2.4). The monoprotected diol (**2.45**) was afforded in 49% yield. A Pinnick oxidation yielded aldehyde **2.46** in 98% yield. The sidechain synthesis was completed via a stereoselective Roush crotylation in 75% yield. An EDC coupling between alcohol **2.47** and the acid fragment **2.2** afforded **2.48** in 75% yield. The macrocycle scaffold (**2.49**) was accessed in 98% yield. TBS removal, followed by a TEMPO oxidation of the terminal alcohol provided the unsaturated macrocycle (**2.51**). HF•pyridine treatment facilitated the removal of the acetonide furnishing **2.52** (yield is not including because it was conducted by Amy Solinski). Hydrogenation from silyl ether **2.49** and alcohol **2.50** are discussed below.

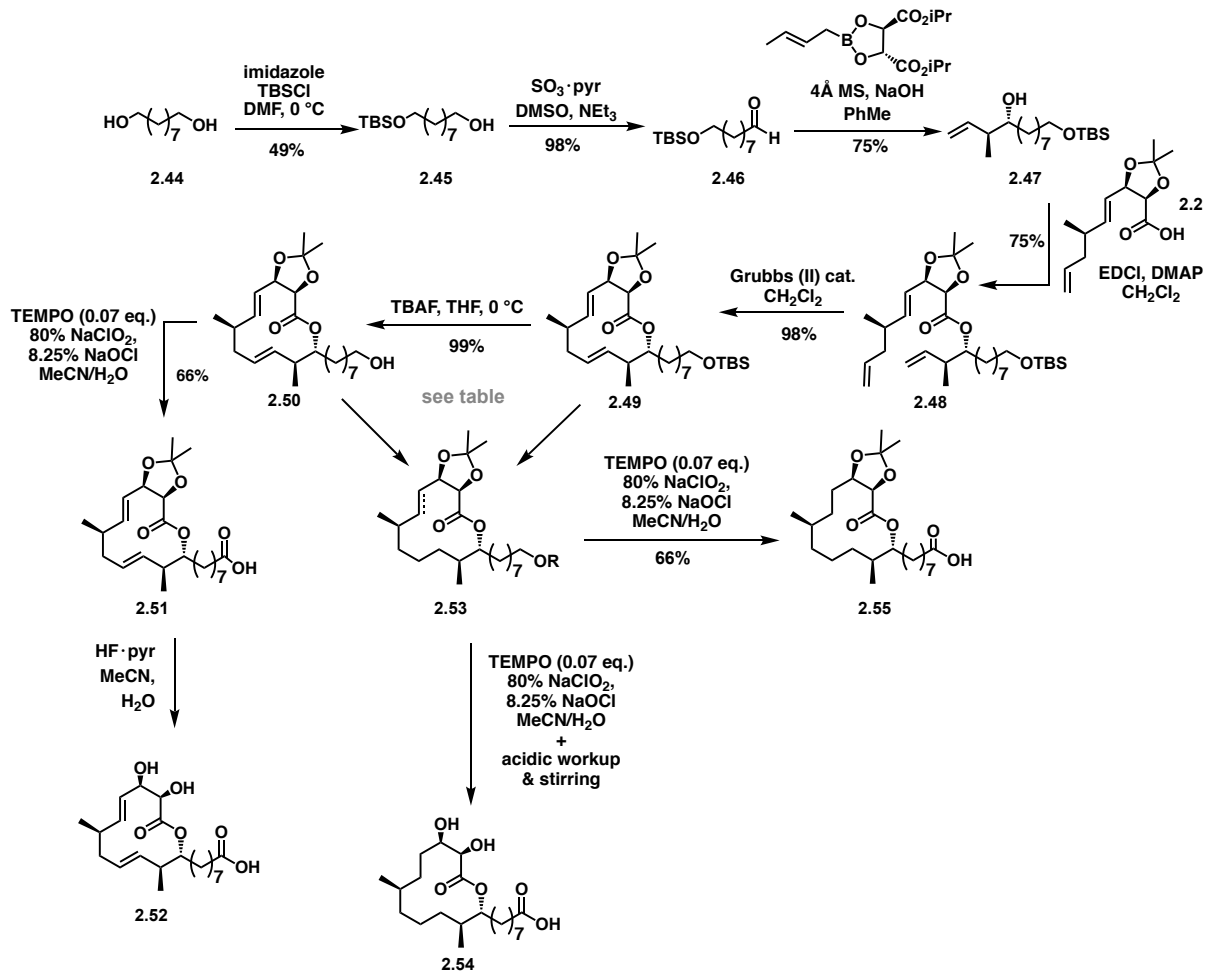

Scheme 2.4 Silyl ether route to natural sidechain length analogs

As previously mentioned, hydrogenation using the terminal benzyl ester provided high selectivity, but the resulting products were inseparable. Therefore, we attempted the selective hydrogenation using the terminal silyl ether macrocycle, as was done in the carolacton and aryl syntheses. Additionally, we attempted this reaction with the terminal alcohol as well. We screened different catalysts, solvent combinations, and reaction times (Table 2.1). In one case, we attempted using ammonium formate as the hydrogen source, but under these conditions only 9% of product was observed after 48 hours. Under most condition, we observed high selectivity for the monosaturated macrocycle (**2.56**) with all three sidechains, but formation of the oversaturated scaffold (**2.57**) was also observed in all cases. We attempted the previously discussed purification

methods, but the similarity in polarity and insolubility in various eluents hindered successful purification. With an excess of partially saturated material in hand, we decided to push the material to the fully saturated macrocycle (**2.57**).

We hypothesize that the loss in selectivity likely arises from the increased flexibility in the sidechain. Molecular docking of the aryl series placed the sidechain out in space away from the macrocycle. This would prevent any intramolecular interactions with the macrocycle core ensuring that the more accessible, lower alkene is free from any hindrance. We postulate that the alkyl sidechain is flexible enough to fold onto the macrocycle and transiently block the catalyst from the lower alkene through the formation of a secondary macrocycle structure. This would provide more time for the catalyst to access the more sterically hindered alkene.

To access the oversaturated acids, the benzyl ester route was used for the truncated series (n = 8) (Scheme 2.2). The natural sidechain length was accessed from the silyl ether route (Scheme 2.4). In the final oxidation step, an acidic workup is required to protonate the terminal carboxylate, which provided the oversaturated diol (**2.54**) when allowed to stir for 30 min (Scheme 2.4). This reduced the need for an additional deprotection step. We then proceeded to biological investigation of our simplified analogs.

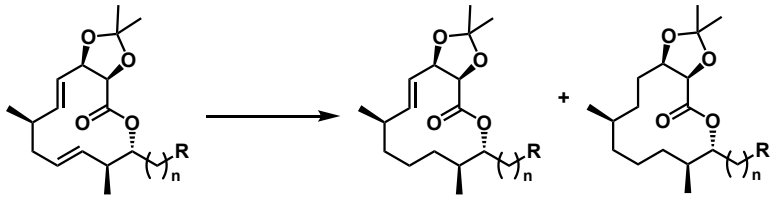

R	Catalyst	Catalyst Load	Solvent	Time	Conversion (SM:A:B)
-CO_2Bn	Pd/C (10%)	7 mol %	EtOAc	20 hrs	NR
	Pd/C (10%)	20 mol %	EtOH	45 min	0:54:46
	Pd/C (10%)	7 mol %	EtOH	10 min	NR
	Pd/C (10%)	10 mol %	EtOAc:MeOH (1:1)	45 min	0:67:33
	Pd/C (10%)	26 mol %	EtOAc:MeOH (1:1)	30 min	0:75:25
	Pd/C (10%)	20 mol %	MeOH:EtOH (1:1)	60 min	NR
	Pd/C (10%)	10 mol %	EtOAc:EtOH (1:1)	10 min	0:90:10
	Pd/C (10%)	20 mol %	EtOAc:EtOH (3:1)	30 min	0:90:10
-CO_2H	Pd/C (10%)	10 mol %	EtOAc:EtOH (1:1)	20 min	90:2.5:2.5
-CH_2OTBS	Pd/C (10%)	7 mol %	EtOAc	60 min	NR
	Pd/C (10%)	7 mol %	EtOH	90 min	0:0:100
	Pd/C (10%)	7 mol %	EtOH	90 min	NR
	Pd/C (10%)	7 mol %	EtOAc:EtOH (1:1)	60 min	0:70:30
	Pd/C (10%)	13 mol %	EtOAc:EtOH (1:1)	60 min	0:84:16
-CH_2OH	Pd/C (10%)	13 mol %	EtOAc:EtOH (1:1)	30 min	0:0:100
	Pd/C (10%)	13 mol %	EtOAc:EtOH (1:1)	20 min	0:77:33
	Pd/C (10%) w/ HCO_2NH_4	8 mol %	EtOAc:MeOH (1:1)	48 hrs	91:9:0
	Wilkinson Cat.	10 mol %	EtOAc	10 min	NR
	Wilkinson Cat.	10 mol %	EtOAc	24 hrs	NR
	Wilkinson Cat.	20 mol %	EtOH:THF (2:1)	24 hrs	84:16:0
	Wilkinson Cat.	20 mol %	EtOH:THF (2:1)	48 hrs	43:25:7
	Wilkinson Cat.	20 mol %	PhH	24 hrs	67:21:12
	Pt/C (10 %)	10 mol %	MeOH	30 min	NR
	Pt/C (10 %)	10 mol %	MeOH:EtOAc (1:1)	30 min	81:14:5
-CH_2OPMB	Pd/C (10%)	7mol %	EtOH	1.5 hrs	0:71:29

Table 2.1 Selective hydrogenation screen

2.4 Preliminary biological investigation

Amy Solinski and I pooled our analogs and collaborated on biological testing to discern whether further simplification of the sidechain and oversaturation of the macrocycle would affect activity. Analogs were tested *S. mutans* in both planktonic conditions (Todd-Hewitt Broth, THB) and biofilm conditions (THB + 0.1% sucrose, THBS). Under planktonic and biofilm conditions, all the truncated analogs (n=5,8) slightly inhibited growth at high concentrations in a similar fashion to carolacton (Figure 2.10). To our surprise, the oversaturated analog **2.55 (Analog 2, A2)** exhibited a minimum inhibitory concentration (MIC) of 250 μM, and an IC_{50} (concentration at which bacterial growth is inhibited to 50%) of 148 μM.

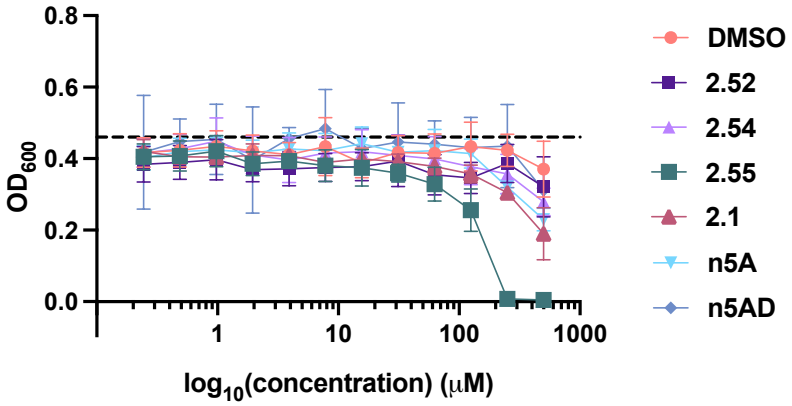

Figure 2.10 Growth inhibition under planktonic conditions

Notably, compound **2.55** exhibited more potent activity against biofilm formation, as demonstrated by its IC_{50} of 77 μM (Figure 2.11). This drastic increase in potency suggests a mechanism of action specific to biofilm, or the low pH characteristic of biofilms, akin to carolacton. Crystal violet analysis showed an increase in biomass at the concentration one dilution below the MIC. This phenomenon has been observed previously at sub-MICs of antibiotics and has even been applied as a tool for identifying bioactive compounds.[172]

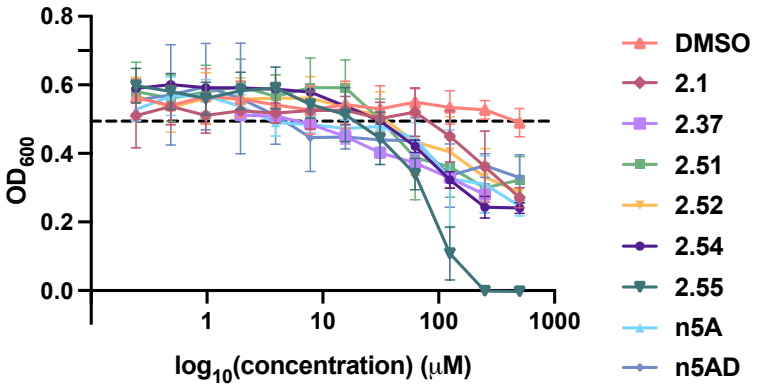

Figure 2.11 Growth inhibition under biofilm conditions

To probe the killing effect of **2.55** relative to carolacton (**2.1**), we conducted colony-forming unit (CFU) assays (Figure 2.12). This assay entails incubating cells overnight in the presence of compound, followed by a serial dilution of the cells in phosphate buffer solution (PBS), and plating them on agar. After 24 hours of incubation, the cells can be enumerated and the number of CFU calculated. **2.55** decreased viability of cells by 96% at 125 μM and 58% at 32 μM compared to DMSO. Carolacton did not induce a killing effect at these concentrations under our assay conditions. Between 62 nM and 2 μM, viability was reduced by 75% and 93%, respectively. Carolacton (**2.1**) reduced viability by 30% and 78% at these concentrations.

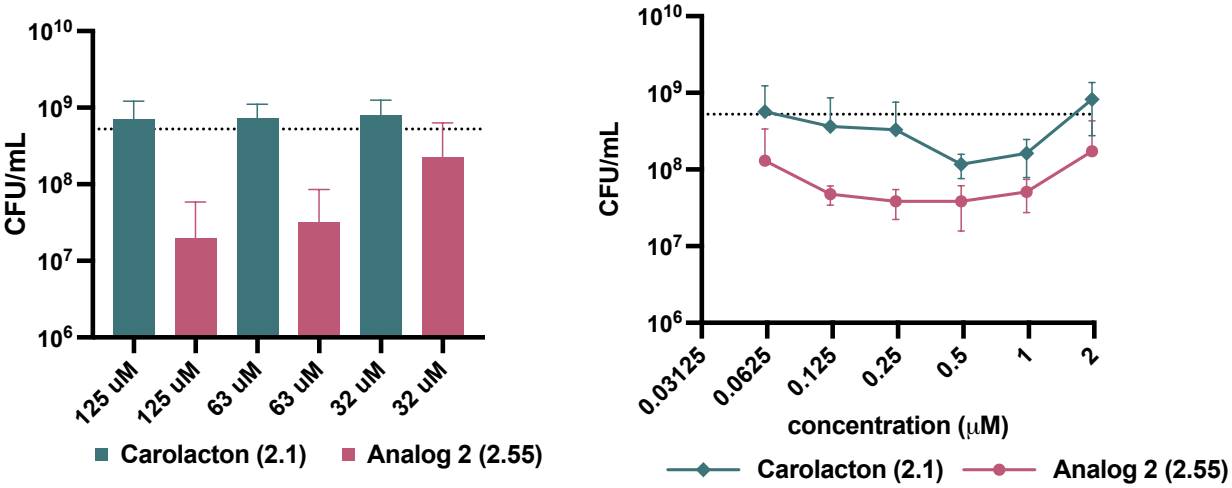

Figure 2.12 Colony forming units assay

To visualize the effects on biofilm morphology, we turned to confocal imaging and LIVE/DEAD straining to analyze the morphological effects. For confocal analysis, we grew *S. mutans* biofilm in glass bottom plates to promote biofilm adherence and growth since glass mimics the tooth pellicle. The promotion of biofilm formation led to an improvement in activity with an IC_{50} of 44 μM. We imaged compound treated biofilm at concentrations ranging from 500 μM to 16 μM. Images of biofilm at 125 and 63 μM show that the increased biomass consisted of cells with severe membrane damage, with only 76% viable cells at 63 μM and 76% at 63 μM (Figure 2.13). At 16 μM, compound **2.55** causes defects to biofilms cells that resembles the microcolony phenotype observed with our first generation of analogs.

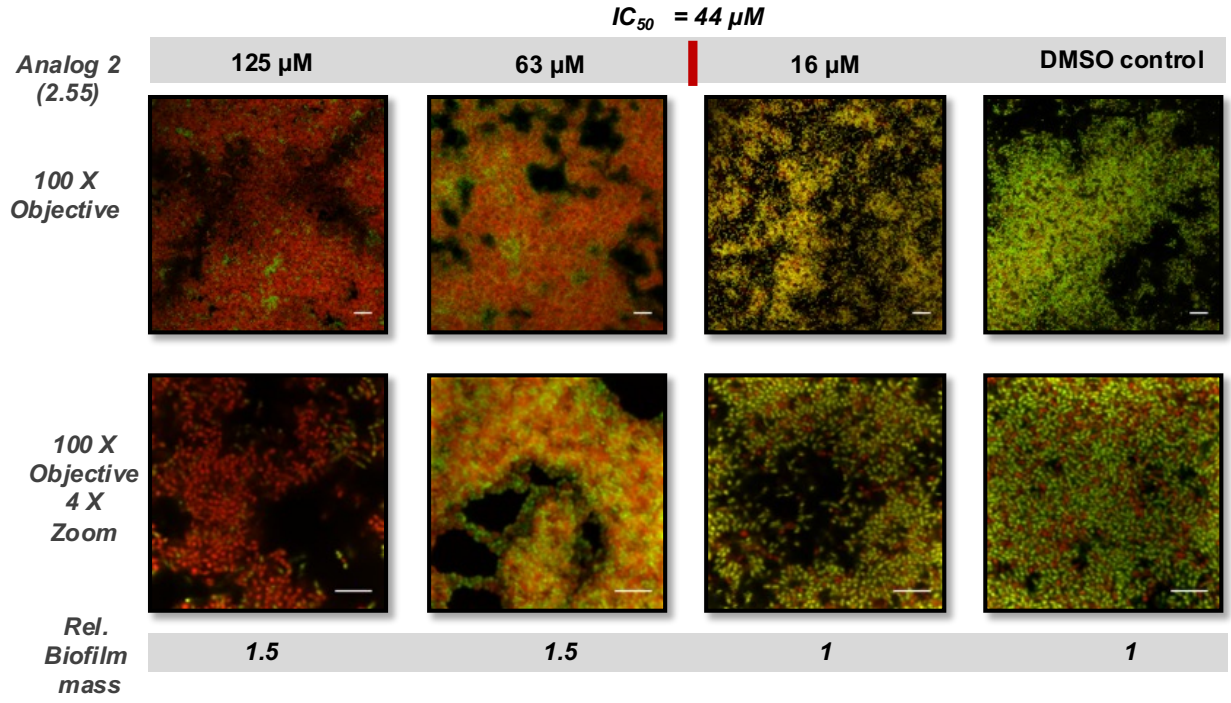

Figure 2.13 CLMS of biofilms treated with 2.55

Carolacton has been shown to possess activity at lower concentrations, encouraging us to image the effects of **2.55** at similar concentrations. Both compounds cause biofilm defects at 0.5 μM, but they induce slightly different phenotypic responses (Figure 2.14). Carolacton (**2.1**) treatment resulted in a sparse biofilm with impaired viability as indicated by the yellow color of the

cells. **2.55** treated cells on the other hand formed hazy microcolonies, as if there was excess cellular membrane material in the EPS. It is possible that the increased hydrophobicity of **2.55** could promote aggregation resulting in more microcolony formation. In the 4X zoom, both compounds induce longer chains of cells, with **2.55** treated cells forming bridging chains between clustered colonies. The longer chain cells caused by carolacton are less densely packed. Collectively, these results suggest that carolacton (**2.1**) and **2.55** likely affect similar pathways.

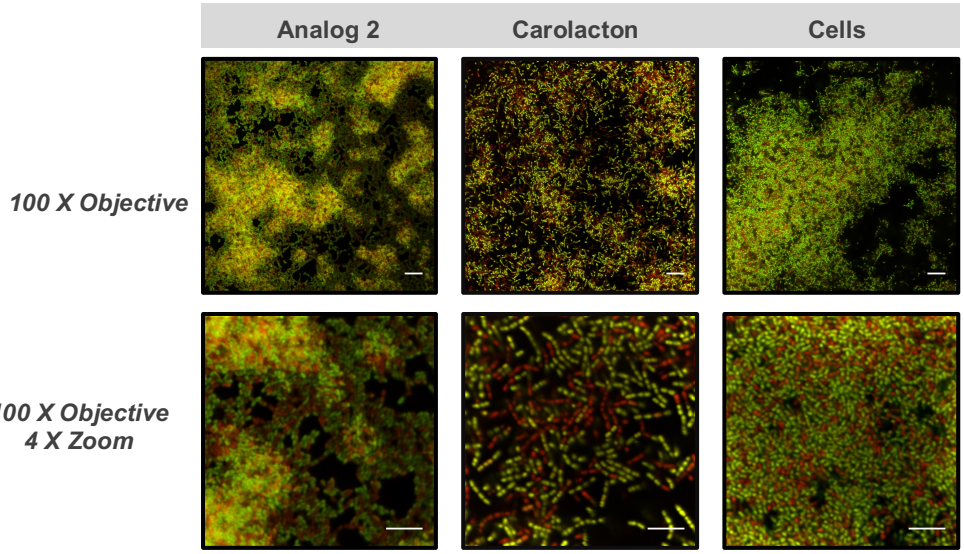

Figure 2.14 Confocal images at low concentrations

2.5 Mechanism of action studies

We were interested in investigating whether this effect was truly a biofilm dependence and not a dependence on the acid tolerance response associated with biofilm formation. Carolacton has been shown to kill planktonic cells to a similar degree when tested against cultures that were pre-acidified with pH 5.5. It has also been demonstrated that pre-exposed cells will induce an acid tolerance response that is retained even when recultivated in neutral media. Carolacton is postulated to depend on the acid produced by *S. mutans* biofilms, encouraging us to investigate whether **2.55** maintains this dependence. Thus, to further confirm the biofilm specificity of **2.55**,

we induced an acid tolerance response in planktonic *S. mutans* cultures by growing them in THB media at pH 5.5. This pH was chosen because it has been shown that the effects of carolacton were not induced until *S. mutans* reached this pH. Interestingly, compound treatment exhibited a parabola dose-dependent response (Figure 2.15). The MIC is 8 μM, but growth begins to increase against at this inflection point, suggesting at these higher concentrations compound treatment induces cell growth. When zooming in on the concentrations below 32 μM, the IC_{50} is 1 μM. It is important to note that DMSO displayed a slight inhibitory effect under these conditions at higher concentrations.

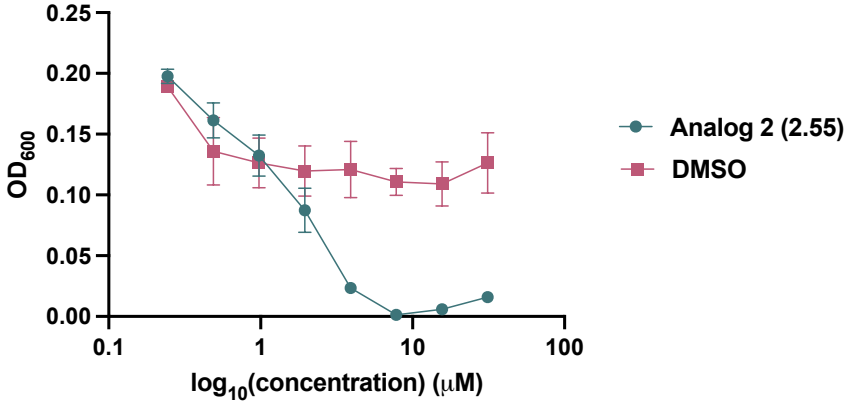

Figure 2.15 Growth inhibition at pH = 5.5

A similar parabola effect was observed with **2.37** via CLMS analysis (Figure 2.16). This effect was a killing effect rather than an inhibitory effect. The lower density biofilm at lower concentrations (32 μM and 2 μM) and higher concentrations (500 μM) relative to the middle concentrations suggest that there is a concentration window where this compound induces growth rather than disrupts. Interestingly, there is a stark difference in viable cells at 63 μM. This result was consistent across three biological trials. These growth induction effects could be a product of the oversaturated macrocyclic core. Additional work is needed to clarify these results.

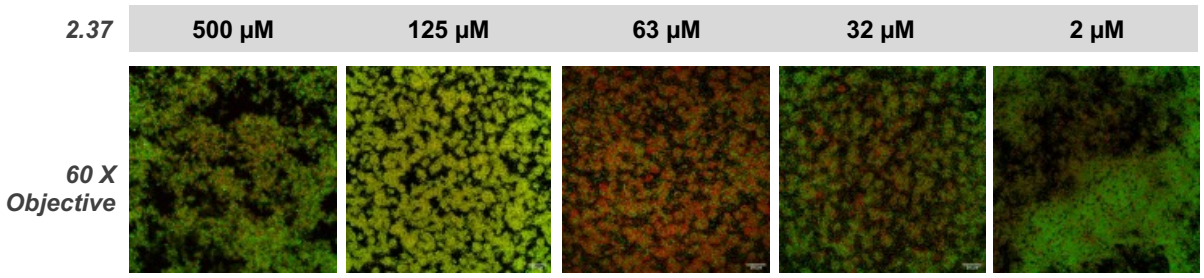

Figure 2.16 CLMS analysis of 2.37. Scale bar is 20µM

The quantitative inhibitory activity exhibited by **2.55** enabled us to perform additional mechanism of action studies previously inaccessible to carolacton, such as a chemical genetic knockout screen. The hypothesis is that removal of the molecular target should result in resistance to compound treatment. We obtained a library of *S. mutans* protein knockouts from Professor Robert Quivey at the University of Rochester. This library contained 17 strains lacking proteins that had previously been tied to carolacton's activity or have been heavily implicated in biofilm formation and acid tolerance (Table 2.2).

OralgenID	SMU locus	Gene	Description
210	SMU.232	*ilvH*	acetolactate synthase, small subunit
328	SMU.363	*glnR*	transcriptional regulator glutamine synthetase repressor
438	SMU.438	*pknB*	Serine/threonine protein kinase
491	SMU.540	*dpr*	peroxide resistance protein
555	SMU.609	*bsp*	putative 40K cell wall protein precursor
556	SMU.610	*spaP*	Cell surface antigen SpaP
846	SMU.933	*atmA*	putative amino acid ABC transporter, periplasmic amino
847	SMU.934	-	putative amino acid ABC transporter, permease protein
914	SMU.914	*gtfB*	glucosyltransferase-I
918	SMU.1008	*ilrG*	Putative response regulator
947	SMU.1038c	*vicR*	Putative histidine kinase
1092	SMU.1193	*yhcF*	Putative transcriptional regulator
1158	SMU.1266	*hisH*	Putative glutamine amidotransferase
1166	SMU.1276c	*ezrA*	Putative septation ring formation regulator
1446	SMU.1591	*ccpA*	Catabolite protein A
1591	SMU.1745c	-	Putative transcriptional regulator
1779	SMU.1930c	*levE*	putative PTS system, mannose-specific IIB component

Table 2.2 *S. mutans* knockout mutant strains

Growth inhibition assays were conducted with each mutant strain. We observed an insensitive phenotype for compound **2.55** when tested against the SMU.1591 mutant compared to the parent UA159 strain, indicating that this gene is involved in the inhibitory activity of **2.55** (Figure 2.17). SMU.1591 lacks the gene that encodes for carbon catabolite protein A (CcpA) that regulates carbon metabolism and is involved in acid tolerance, providing substantial evidence that targets CcpA or a downstream gene. CcpA functions primarily as a negative transcriptional regulator through binding to a promoter motif present in its substrates. As such, it is highly plausible that **2.55** does not directly target CcpA, but a downstream target or pathway that is shut down in the knockout. Notably, carolacton treatment was found to downregulate transcriptional changes to CcpA and its regulon, including genes involved in the phosphotransferase system (*ptnAB*/*manLM* and 3 ABC transporters). We also observed an enhanced effect against two knockout strains,

ΔPknB and ΔEzrA. The former protein and its regulon are highly associated with carolacton's mechanism, as described in section 2.1.2. Collectively, this evidence points toward an effect on cell wall homeostasis, like carolacton (**2.1**), but further investigation is needed to identify the protein target.

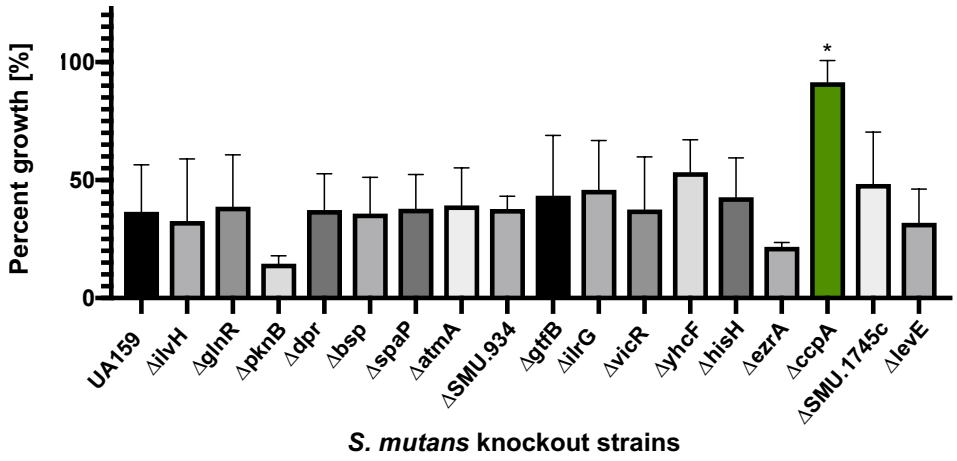

Figure 2.17 Percent growth after treatment with 2.55 (125 μM)

2.6 Conclusion and future work

Natural products offer immense therapeutic potential with their expansive chemical diversity and their evolutionary tuning for specific target engagement. However, synthetic accessibility can limit their usage in target identification and further utilization in clinical applications. Carolacton, a natural product produced by *Sorangium cellulosum*, is one such example of a privileged scaffold with unique acid-mediated activity against *Streptococcus mutans* biofilms but whose stereochemically-rich structure has impeded target elucidation due to synthetic limitations. The unique biological activity of carolacton and its previously disputed mechanism of action motivated our lab to engage a synthetic campaign starting with a concise total synthesis of the natural product and culminating in the identification of a simplified chemical probe that expedited our biological investigation.

Comparative analysis of the second-generation library, which focused on reducing the molecular and stereochemical complexity of the natural product by introducing a simplified alkyl sidechain, revealed **2.55** as the first carolacton-inspired analog with a minimum inhibitory concentration (MIC) against *S. mutans* in both planktonic and biofilm cultures (250 μM), and an enhanced killing effect relative to carolacton. **2.55** maintained carolacton's acid-mediated phenotype that trends with the onset and strength of the acid tolerance response (ATR), evidenced by increasing activity as cultures acidify (i.e., planktonic IC_{50} = 144 μM, biofilm IC_{50} = 77 μM, pre-acidified planktonic cultures MIC = 10 μM).

The quantifiable inhibitory activity motivated a forward chemical genetic screen (previously incompatible with carolacton) that included a panel of gene deletions involved in biofilm formation and acid tolerance. This screen revealed that **2.55** activity was completely abolished in a strain lacking carbon catabolite protein A (CcpA), which regulates carbon metabolism, and was potentiated against two strains, ΔPknB and ΔEzrA. The former strain is lacking PknB, a serine/threonine kinase, that regulates cell division, and the latter is lacking EzrA, a membrane protein that is also involved in cell division. PknB has been shown to negatively regulate CcpA *in Staphylococcus aureus* and is purported to be the most prominent regulator of the divisome, highlighting an intersecting node between these three proteins that has yet to be demonstrated in *S. mutans.*[173] Identification of these proteins as players in the mechanism of **2.55** tied its activity to the natural product, but their roles as master regulators likely preclude them from being the molecular target. Prompted by the preliminary success of our chemical probe, we set out to fully elucidate the biological target(s) of **2.55** and clarify its connection to the parent molecule, carolacton. This work is discussed in Chapter 3.

2.7 References

(148) Diez, J.; Martinez, J. P.; Mestres, J.; Sasse, F.; Frank, R.; Meyerhans, A. Myxobacteria: Natural Pharmaceutical Factories. *Microb Cell Fact* **2012**, *11*, 52. https://doi.org/10.1186/1475-2859-11-52.

(149) Höfle, G. Isolation, Structure Elucidation and Chemical Modification of New Biologically Active Secondary Metabolites. *Scientific Annual Report of the GBF* **1998**, *101*.
(150) Jansen, R.; Irschik, H.; Huch, V.; Schummer, D.; Steinmetz, H.; Bock, M.; Schmidt, T.; Kirschning, A.; Müller, R. Carolacton - A Macrolide Ketocarbonic Acid That Reduces Biofilm Formation by the Caries- and Endocarditis-Associated Bacterium Streptococcus Mutans. *European Journal of Organic Chemistry* **2010**, *7*, 1284–1289. https://doi.org/10.1002/ejoc.200901126.
(151) Stewart, P. S.; Costerton, J. W. Antibiotic Resistance of Bacteria in Biofilms. *Lancet* **2001**, *358*, 135–138. https://doi.org/10.1016/S0140-6736(01)05321-1.
(152) Worthington, R. J.; Richards, J. J.; Melander, C. Small Molecule Control of Bacterial Biofilms. *Organic and Biomolecular Chemistry*. **2012**.
(153) Kunze, B.; Reck, M.; Dötsch, A.; Lemme, A.; Schummer, D.; Irschik, H.; Steinmetz, H.; Wagner-Döbler, I. Damage of Streptococcus Mutans Biofilms by Carolacton, a Secondary Metabolite from the Myxobacterium Sorangium Cellulosum. *BMC Microbiology* **2010**, *10*, 1–13. https://doi.org/10.1186/1471-2180-10-199.
(154) Stumpp, N.; Premnath, P.; Schmidt, T.; Ammermann, J.; Dräger, G.; Reck, M.; Jansen, R.; Stiesch, M.; Wagner-Döbler, I.; Kirschning, A. Synthesis of New Carolacton Derivatives and Their Activity against Biofilms of Oral Bacteria. *Organic and Biomolecular Chemistry* **2015**, *13* (20), 5765–5774. https://doi.org/10.1039/c5ob00460h.
(155) Sudhakar, P.; Reck, M.; Wang, W.; He, F. Q.; Dobler, I. W.; Zeng, A.-P. Construction and Verification of the Transcriptional Regulatory Response Network of Streptococcus Mutansupon Treatment with the Biofilm Inhibitor Carolacton. *BMC Genomics* **2014**, *15* (1), 362. https://doi.org/10.1186/1471-2164-15-362.
(156) Li, J.; Wang, W.; Wang, Y.; Zeng, A. P. Two-Dimensional Gel-Based Proteomic of the Caries Causative Bacterium Streptococcus Mutans UA159 and Insight into the Inhibitory Effect of Carolacton. *Proteomics* **2013**. https://doi.org/10.1002/pmic.201300077.
(157) Banu, L. D.; Conrads, G.; Rehrauer, H.; Hussain, H.; Allan, E.; van der Ploeg, J. R. The Streptococcus Mutans Serine/Threonine Kinase, PknB, Regulates Competence Development, Bacteriocin Production, and Cell Wall Metabolism. *Infect Immun* **2010**, *78* (5), 2209–2220. https://doi.org/10.1128/IAI.01167-09.
(158) Reck, M.; Rutz, K.; Kunze, B.; Tomasch, J.; Surapaneni, S. K.; Schulz, S.; Wagner-Döbler, I. The Biofilm Inhibitor Carolacton Disturbs Membrane Integrity and Cell Division of Streptococcus Mutans through the Serine/Threonine Protein Kinase PknB. *J Bacteriol* **2011**, *193* (20), 5692–5706. https://doi.org/10.1128/JB.05424-11.
(159) Reck, M.; Wagner-Döbler, I. Carolacton Treatment Causes Delocalization of the Cell Division Proteins PknB and DivIVa in Streptococcus Mutans in Vivo. *Frontiers in Microbiology* **2016**, *7*, 684. https://doi.org/10.3389/fmicb.2016.00684.
(160) Fu, C.; Sikandar, A.; Donner, J.; Zaburannyi, N.; Herrmann, J.; Reck, M.; Wagner-Döbler, I.; Koehnke, J.; Müller, R. The Natural Product Carolacton Inhibits Folate-Dependent C1 Metabolism by Targeting FolD/MTHFD. *Nature Communications* **2017**, *8* (1), 1529. https://doi.org/10.1038/s41467-017-01671-5.
(161) Donner, J.; Reck, M.; Bunk, B.; Jarek, M.; App, C. B.; Meier-Kolthoff, J. P.; Overmann, J.; Müller, R.; Kirschning, A.; Wagner-Döbler, I. The Biofilm Inhibitor Carolacton Enters Gram-Negative Cells: Studies Using a TolC-Deficient Strain of Escherichia Coli . *mSphere* **2017**. https://doi.org/10.1128/mspheredirect.00375-17.
(162) Donner, J.; Reck, M.; Bergmann, S.; Kirschning, A.; Müller, R.; Wagner-Döbler, I. The Biofilm Inhibitor Carolacton Inhibits Planktonic Growth of Virulent Pneumococci via a Conserved Target. *Scientific Reports* **2016**, *6*, 29677.
(163) Hallside, M. S.; Brzozowski, R. S.; Wuest, W. M.; Phillips, A. J. A Concise Synthesis of Carolacton. *Organic Letters* **2014**, *16* (4), 1148–1151. https://doi.org/10.1021/ol500004k.

(164) Kumar, V. P.; Chandrasekhar, S. Enantioselective Synthesis of Pladienolide B and Truncated Analogues as New Anticancer Agents. *Organic Letters* **2013**, *15*, 3610–3613. https://doi.org/10.1021/ol401458d.
(165) Solinski, A. E.; Koval, A. B.; Brzozowski, R. S.; Morrison, K. R.; Fraboni, A. J.; Carson, C. E.; Eshraghi, A. R.; Zhou, G.; Quivey, R. G.; Voelz, V. A.; Buttaro, B. A.; Wuest, W. M. Diverted Total Synthesis of Carolacton-Inspired Analogs Yields Three Distinct Phenotypes in Streptococcus Mutans Biofilms. *J Am Chem Soc* **2017**, *139* (21), 7188–7191. https://doi.org/10.1021/jacs.7b03879.
(166) Agarwal, S.; Behring, M.; Hale, K.; al Diffalha, S.; Wang, K.; Manne, U.; Varambally, S. MTHFD1L, A Folate Cycle Enzyme, Is Involved in Progression of Colorectal Cancer. *Translational Oncology* **2019**, *12* (11), 1461–1467. https://doi.org/https://doi.org/10.1016/j.tranon.2019.07.011.
(167) Zhu, Z.; Leung, G. K. K. More Than a Metabolic Enzyme: MTHFD2 as a Novel Target for Anticancer Therapy? . *Frontiers in Oncology* . 2020.
(168) Sdelci, S.; Rendeiro, A. F.; Rathert, P.; You, W.; Lin, J.-M. G.; Ringler, A.; Hofstätter, G.; Moll, H. P.; Gürtl, B.; Farlik, M.; Schick, S.; Klepsch, F.; Oldach, M.; Buphamalai, P.; Schischlik, F.; Májek, P.; Parapatics, K.; Schmidl, C.; Schuster, M.; Penz, T.; Buckley, D. L.; Hudecz, O.; Imre, R.; Wang, S.-Y.; Maric, H. M.; Kralovics, R.; Bennett, K. L.; Müller, A. C.; Mechtler, K.; Menche, J.; Bradner, J. E.; Winter, G. E.; Klavins, K.; Casanova, E.; Bock, C.; Zuber, J.; Kubicek, S. MTHFD1 Interaction with BRD4 Links Folate Metabolism to Transcriptional Regulation. *Nature Genetics* **2019**, *51* (6), 990–998. https://doi.org/10.1038/s41588-019-0413-z.
(169) Zheng, Y.; Lin, T.-Y.; Lee, G.; Paddock, M. N.; Momb, J.; Cheng, Z.; Li, Q.; Fei, D. L.; Stein, B. D.; Ramsamooj, S.; Zhang, G.; Blenis, J.; Cantley, L. C. Mitochondrial One-Carbon Pathway Supports Cytosolic Folate Integrity in Cancer Cells. *Cell* **2018**, *175* (6), 1546-1560.e17. https://doi.org/https://doi.org/10.1016/j.cell.2018.09.041.
(170) Morris, L. J. Separations of Lipids by Silver Ion Chromatography. *Journal of Lipid Research* **1966**, *7* (6), 717–732. https://doi.org/https://doi.org/10.1016/S0022-2275(20)38948-3.
(171) Lawrence, B. M. The Use of Silver Nitrate Impregnated Silica Gel Layers in the Separation of Monoterpene Hydrocarbons. *Journal of Chromatography A* **1968**, *38*, 535–537. https://doi.org/https://doi.org/10.1016/0021-9673(68)85084-8.
(172) Coles, V. E.; Darveau, P.; Zhang, X.; Harvey, H.; Henriksbo, B. D.; Yang, A.; Schertzer, J. D.; Magolan, J.; Burrows, L. L. Exploration of BAY 11-7082 as a Potential Antibiotic. *ACS Infectious Diseases* **2022**, *8* (1), 170–182. https://doi.org/10.1021/acsinfecdis.1c00522.
(173) Leiba, J.; Hartmann, T.; Cluzel, M.-E.; Cohen-Gonsaud, M.; Delolme, F.; Bischoff, M.; Molle, V. A Novel Mode of Regulation of the Staphylococcus Aureus Catabolite Control Protein A (CcpA) Mediated by Stk1 Protein Phosphorylation. *J Biol Chem* **2012**, *287* (52), 43607–43619. https://doi.org/10.1074/jbc.M112.418913.

3 Natural Product simplification yields first inhibitor of an essential streptococcal cell wall hydrolase

A manuscript detailing the following work is in progress.

3.1 Introduction:

Prompted by the preliminary success of our chemical probe, we set out to fully elucidate the biological target(s) of **2.55** (referred to as **A2** going forward) and clarify its connection to the parent molecule, carolacton (**2.1**). Leveraging the simplified scaffold, we designed a photoaffinity probe for affinity-based protein profiling (AfBPP) which identified a small subset of potential protein targets. Using a combination of target validation approaches, we uncovered glucan binding protein B (GbpB), a putative peptidoglycan hydrolase, as the target of **A2**. GbpB plays an essential role in cell wall septal division and is highly conserved across the *Streptococcus* genus, providing a novel strategy to prevent pathogenic streptococcal infections. We report the discovery of a first in class inhibitor of the essential peptidoglycan hydrolase, GbpB/PcsB, establishing the foundation for further antibacterial development and elucidation of its role in cell division and pathogenicity.

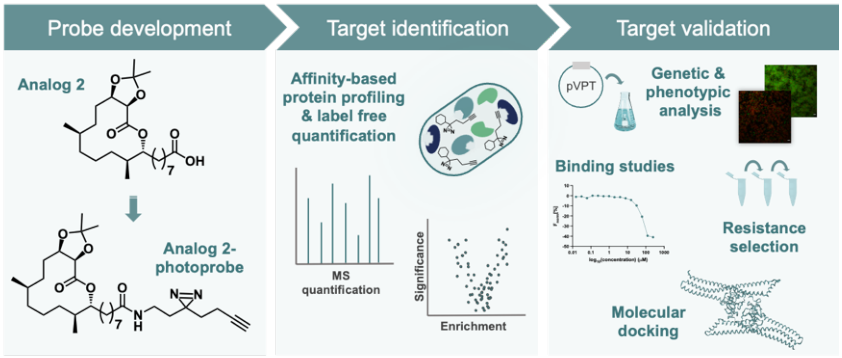

Figure 3.1 Overview of chapter 3

3.2 Ruling out folate dehydrogenase

Müller and co-workers previously reported that carolacton targets folate dehydrogenase (FolD) after selecting for a resistant mutation in this gene using *E. coliΔtolC*, an efflux knockout. They also reported that carolacton exhibited inhibitory activity against recombinant enzyme purified from both *E. coli* and *S. pneumoniae.* purified enzyme. We were interested in connecting these results to the mechanism of carolacton against *S. mutans* biofilm cultures and determining whether **A2** maintained the same activity profile. To this end, bacterial growth assays and confocal laser microscopy (CLMS) were conducted using an *S. mutans* FolD knockout strain and a WT strain. The effect of **A2** on bacterial growth and biofilm morphology was unchanged between the two strains, which likely excluded FolD from this observed mechanism (Figure 3.2).

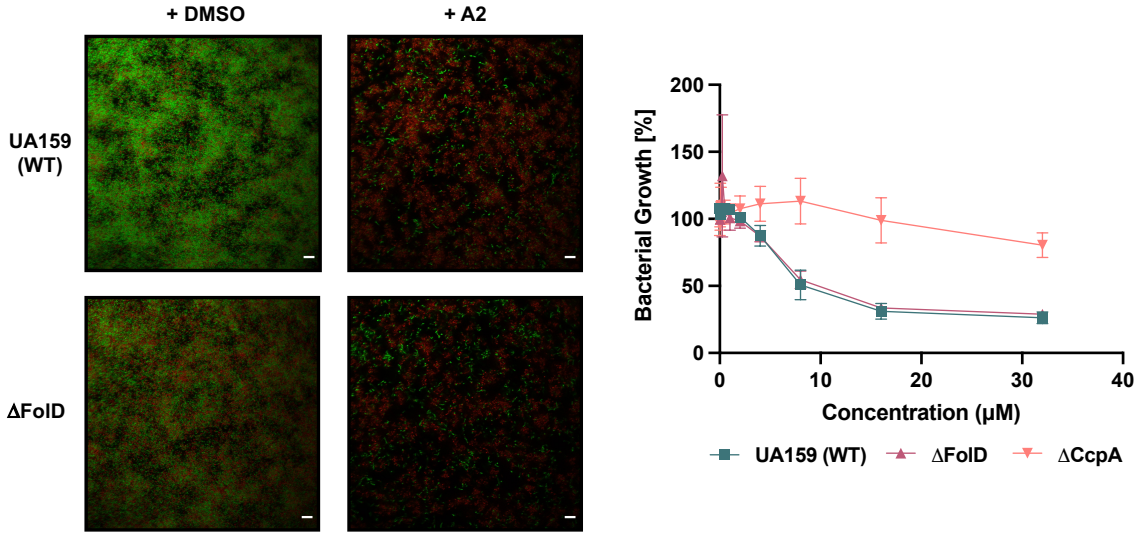

Figure 3.2 Growth assay and CLMS with ΔFolD

To rule out an effect on recombinant FolD, we conducted a previously described dehydrogenase assay using purified *E. coli* FolD.[13] In our assay conditions, carolacton exhibited an IC_{50} value of 94 nM, whereas **A2** was inactive up to 10 μM (Figure 3.3). Collectively, this evidence demonstrates that the acid-mediated effect imparted by the carolacton pharmacophore

is not related to FolD inhibition, and that unlike **A2**, carolacton may exhibit polypharmacology with respect to its killing ability in *S. mutans* and requires further investigation. Future work includes testing carolacton against the FolD mutant.

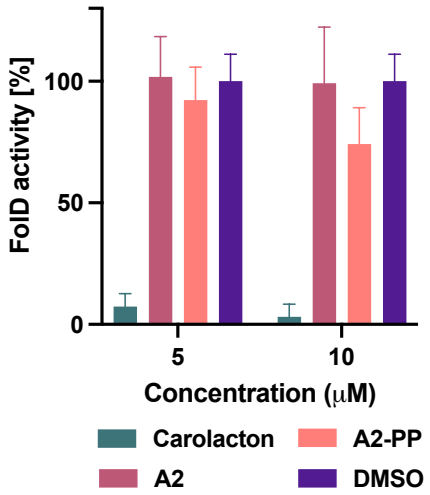

Figure 3.3 FolD enzyme inhibition assay

3.3 Label-free affinity-based protein profiling

To identify the protein target of **A2**, we took advantage of its synthetic accessibility and carbonyl functionality to install a photocrosslinking moiety for use in affinity-based protein profiling (AfBPP) experiments.[174–176] AfBPP is ideal for target identification in cases where covalent inhibition is unlikely. This technique requires a multi-functional biorthogonal probe bearing a photoreactive moiety to induce crosslinking (diazirine) and a handle (alkyne) to facilitate enrichment of the crosslinked proteins without affecting the biological activity. Diazirines form a reactive carbene when irradiated with ultraviolet (UV) light that can insert into any C-H bond within 3 Å. Other functional groups have also been successfully employed as crosslinking handles, including benzophenones and aryl azides, but the diazirine has garnered recent attention for its small size. Subsequent cell lysis and a Huisgen cycloaddition click reaction primes the crosslinked proteins for enrichment or direct MS analysis.

Quantification using MS-based methods can be accomplished using a mass tag labelling approach or using a label free quantification (LFQ) approach. The former uses isobaric mass tags that include stable isotopes. [177,178] This works is done by using reacting the labelled protein with an azide containing tag bearing a terminal amine. This terminal amine of the azide tag is subsequently used as a handle for isobaric tagging (Figure 3.4), installing a tag that facilitates enrichment. The compound treated samples are then treated with formaldehyde ("heavy" label) and the control samples are treated with deuterated formaldehyde ("light" label). The terminal amine reacts with the aldehyde to form an imine, which is then reduced by sodium cyanoborohydride to yield a more reactive amine. This reactive amine undergoes a second methylation sequence to furnish the dimethylated proteins. The reducing agent can also be used as an isobaric label instead of or in addition to formaldehyde. Pooling the samples and subjecting them to MS analysis allows for evaluation of the signal intensity ratios of differentially labelled proteins to determine relative enrichment.

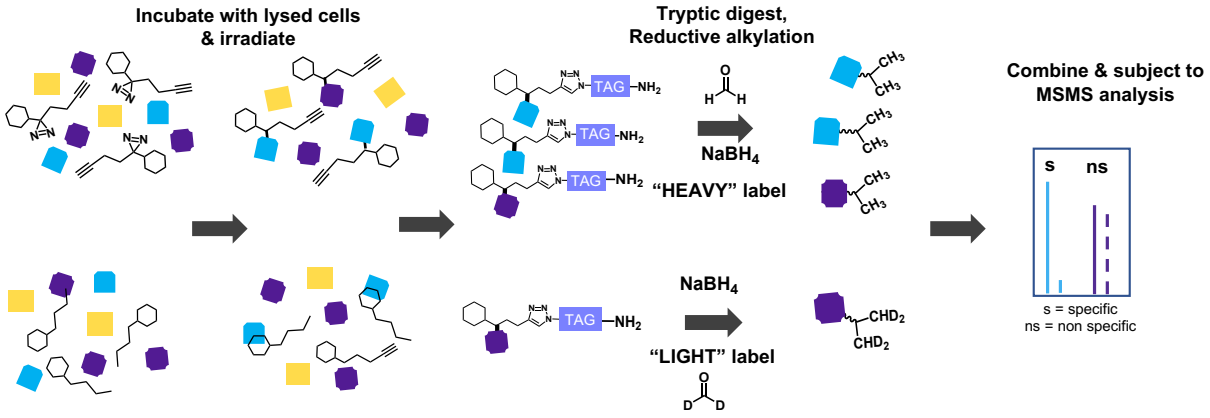

Figure 3.4 Isobaric labeling method

While the labeling reaction is often quick and has proven successful over the years, LFQ methods have emerged that offers many advantages.[175,176,179,180] These include less chemical manipulation of your protein samples (reducing error), less expensive reagents, less complex data analysis, and improved peptide identification rates.[180] LFQ can be based on either the

precursor ion intensity (peak area or height) or on spectral counting (total number of spectra identified for a specific protein).[179]

To carry out label free AfBPP, probe incubation and crosslinking are conducted as previously described. Following cell lysis, crosslinking can be visualized using TAMRA azide (Tetramethylrhodamine 5-Carboxamido-(6-Azidohexanyl), a protein detection reagent, followed by SDS-PAGE and in-gel fluorescence scanning, or processed for quantification analysis (Figure 3.5). Biotin-azide is reacted with the alkyne labelled-protein and the product is enriched on Streptavidin beads. Proteolytical digestion preps the samples for LFQ liquid chromatography/mass spectrometry-mass spectrometry (LC/MS-MS) analysis. In contrast, the gel-free method provides higher resolution, higher sensitivity, and direct identification of crosslinked proteins. However, this method is also more time consuming. As such, they are often used in combination.[176]

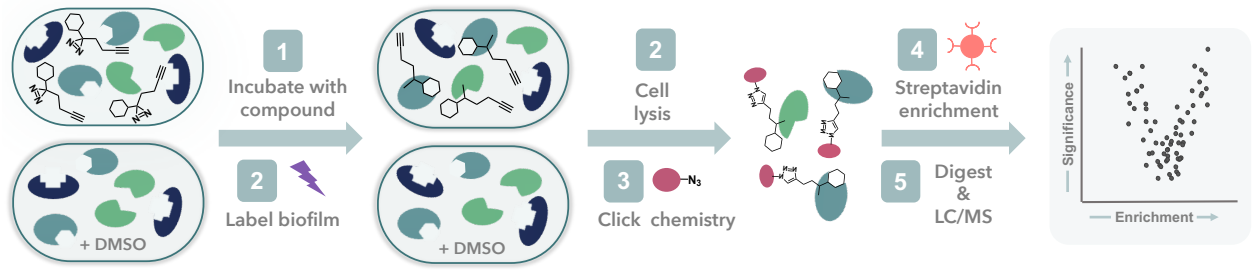

Figure 3.5 Affinity-based protein profiling (AfBPP) workflow

3.3.1 Probe development

The Yao group reported the design of minimalist photoprobes that bear these moieties connected via a short linker to an amine handle for conjugation to the probe molecule.[181] Our groups (S.A.S. and W.M.W.) have previously implemented these minimalist probes successfully in the target identification of two natural products, promysalin and xanthocillin.[182,183] When designing **A2-PP**, we were limited to the terminal carboxylic acid handle for structural modification, needing to maintain its required Bronsted acid properties (Scheme 3.1). We chose the amine variant of the linker to preserve the necessary hydrogen-bond donor character and the correct

oxidation state at the carbonyl carbon. **A2** was coupled to the diazirine containing amine under standard conditions affording **A2-PP** in 61% yield (Scheme 3.1). This reaction was conducted by Amy Solinski, and we collaborated on the synthetic characterization and biological characterization.

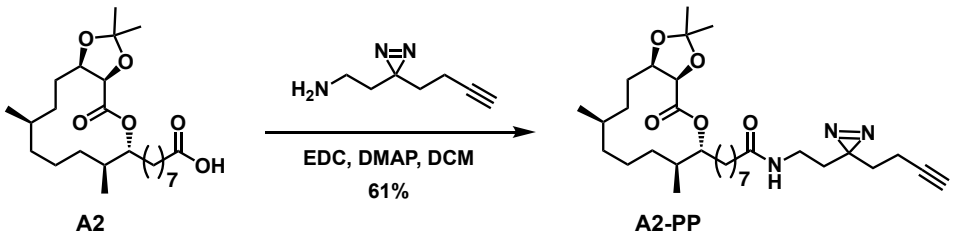

Scheme 3.1 Synthesis of A2-PP

A2-PP was tested against *S. mutans* biofilm cultures to confirm retention of activity. The growth assay showed promotion of growth at high concentrations, but an effect on biofilm was observed using confocal laser microscopy (CLMS (Figure 3.6 and 3.7).

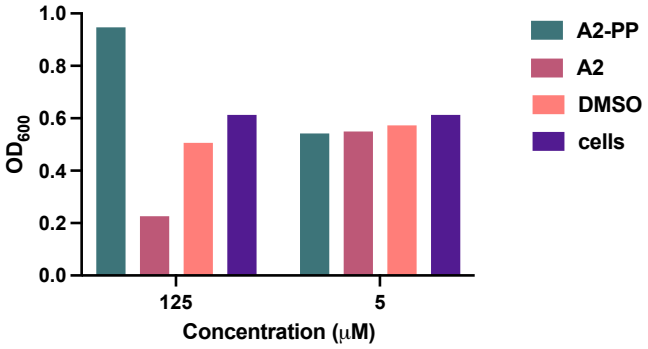

Figure 3.6 Growth assay under biofilm conditions

A2-PP treated cells formed hazy microcolonies, a phenotype observed in **A2**-treated cell as well. Interestingly, high concentrations of **A2-PP** resulted in localized spots of super saturated cells stained with SYTOX green. Since SYTOX Green labels cell membranes, I hypothesize that these spots are indicative of increased damaged membranes, without complete lysis. SYTOX green is a membrane permeable dye that is activated by intracellular esterases. Propidium iodide on the other hand is a membrane impermeable dye that can only stain cells with substantial

membrane damage. As such, damaged membranes could allow for the release of esterases and increased entry of SYTOX green resulting in an enhanced signal. Alternatively, these bright spots could be extremely densely packed microcolonies. All in all, we felt comfortable proceeding with **A2-PP** as a starting point for protein target identification due to the retention of a biofilm effect as observed by CLMS.

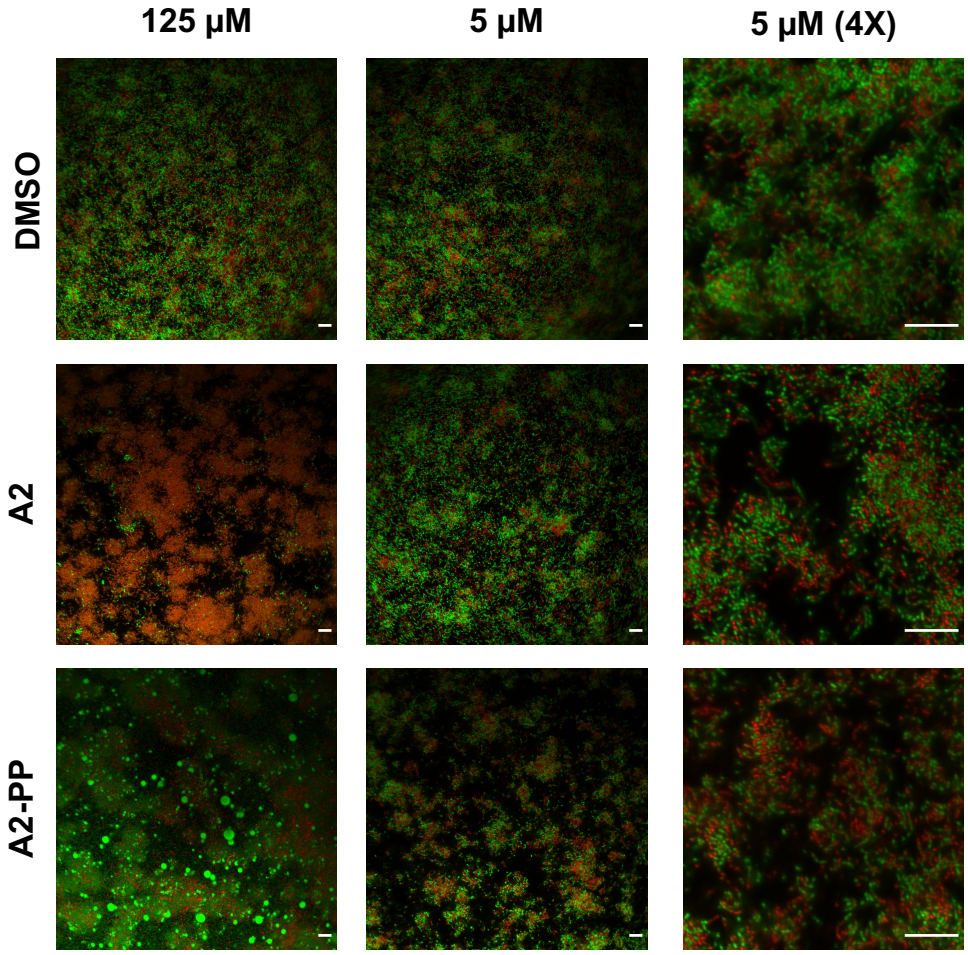

Figure 3.7 CLMS of A2 and A2-PP

3.3.2 AfBPP assay optimization

Amy Solinski travelled to Munich, Germany to work in Stephan Sieber's lab under the guidance of Ines Hübner. During this time, we spoke frequently to troubleshoot the experiments.

AfBPP has been successfully conducted against pre-formed biofilms, but photolabeling in actively growing biofilms, a requirement for **A2** activity, has been underexplored.[24] To control for

this, we conducted two qualitative AfBPP experiments and subsequent gel-based analysis. First, *S. mutans* biofilm cells were dosed with a range of **A2-PP** concentrations (1 μM, 5 μM, and 10 μM) at the start of culture incubation, allowed to incubate for 24 h, then irradiated, lysed, and subjected to a Huisgen cycloaddition "click reaction" with rhodium-biotin azide (pre-treated) (Figure 3.8). In the second experiment, **A2-PP** was dosed after mature biofilm formation and subsequently processed in the same manner as the previous samples (post-treated).

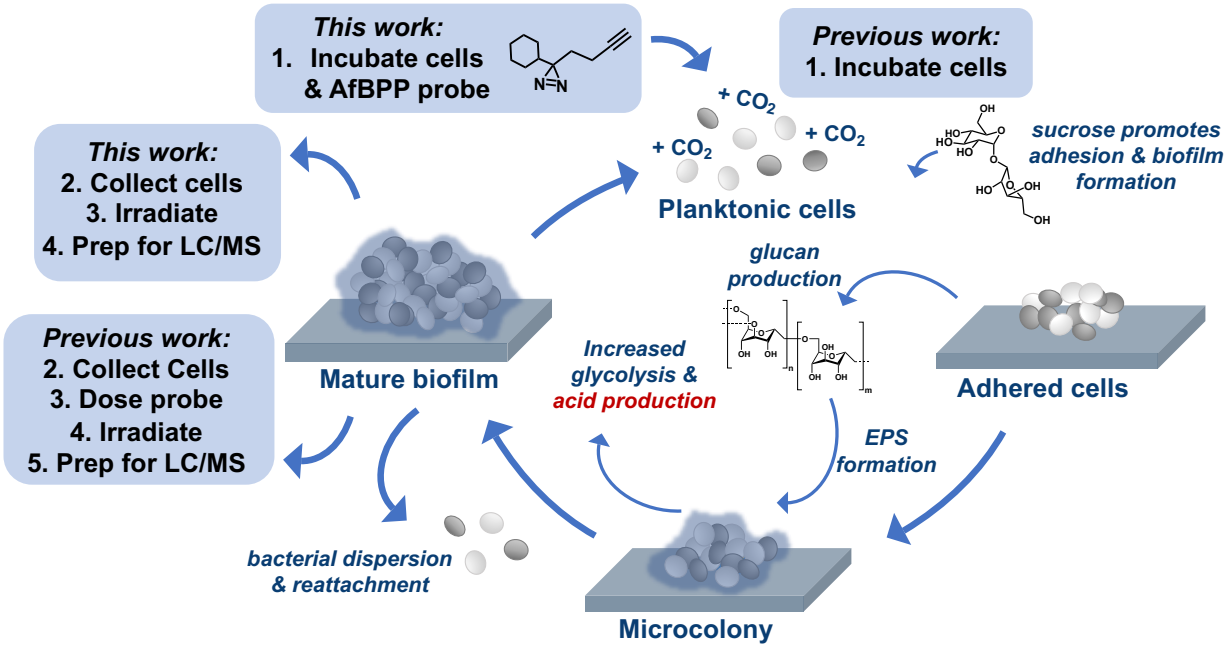

Figure 3.8 AfBPP pre and post treated workflows

Gel-based analysis revealed dose-dependent protein crosslinking in the cultures pre-dosed with **A2-PP**, with optimal concentrations at 1 μM and 5 μM, and no protein crosslinking in the post-treated samples (Figure 3.9).

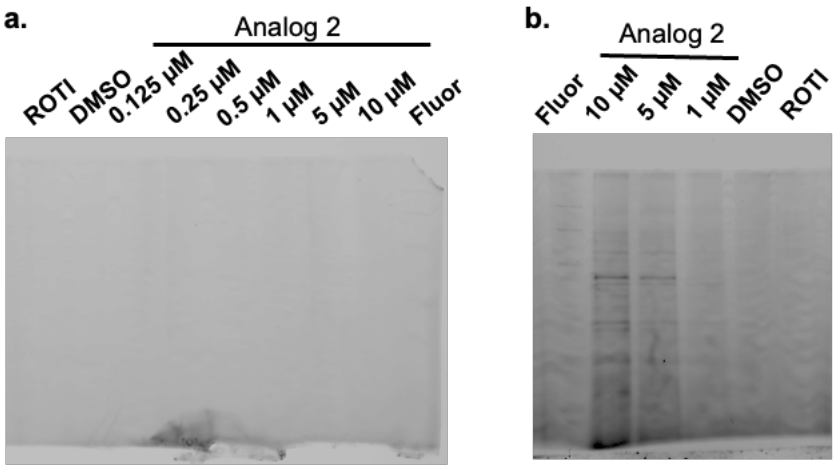

Figure 3.9 Qualitative gel based AfBPP analysis

3.3.3 Protein target identification via AfBPP with label-free quantification

Using our optimized conditions, we sought to identify proteins with a dose-dependent interaction with **A2-PP** via label-free AfBPP analysis rationalizing that these were the most likely involved in direct engagement with **A2**. Following crosslinking and lysis as previously described, samples were reacted with biotin-azide, enriched on streptavidin beads, and prepared for liquid chromatography–tandem mass spectrometry (LC–MS/MS)) with label-free quantification (LFQ) analysis (Figure 3.5). As expected from the gel-based analysis, **A2-PP** exhibited a dose-dependent response with an increase in protein targets from 1 μM to 5 μM. Seven proteins exhibited high enrichment ratios ($-\log_2>2$) and confidences ($p<0.01$) at 1 μM: SMU.1208c (uncharacterized protein), dextranase (DexT), two cell division proteins (FtsA and FtsX), glucan binding protein B (GbpB), a putative ABC transporter (SMU.1068c), and ferrous iron transport protein B (FeoB) (Figure 3.10). A few proteins that almost made the cut off were biofilm regulatory

protein A (BrpA) and the mannose specific IID component of the phosphotransferase system (PTS).

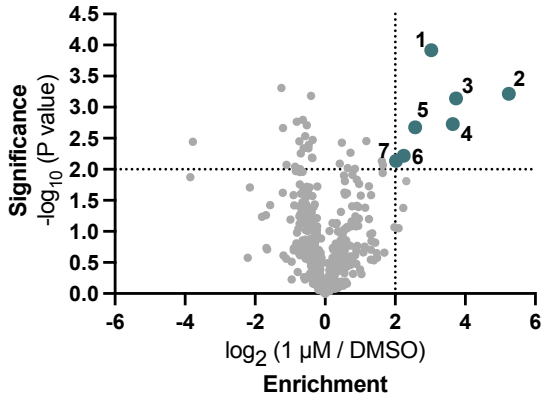

#	UniprotID	Gene	Protein name
1	Q54443	*dexT*	Dextranase
2	Q8DTL1	*ftsX*	Cell division FtsX
3	Q8DVE0	*ftsA*	Cell division FtsA
4	Q8DTW2	*SMU_1208c*	Uncharacterized protein
5	Q8DWM3	*gbpB*	Glucan binding protein B (putative peptidoglycan hydrolase)
6	Q8DU79	*SMU_1068c*	Putative ABC transporter, ATP-binding protein
7	Q8DVC4	*feoA*	Ferrous iron transport protein B

Figure 3.10 Enrichment at 1 µM

At 5 µM, peripheral proteins were crosslinked as a likely result of the indiscriminatory off-target labeling (Figure 3.11), but five of the seven most enriched proteins at 1 µM were among the most enriched at 5 µM, including SMU.1208c (uncharacterized protein), DexT, FtsA, FtsX, and GbpB. The latter three proteins are reported to function as members of the divisome, a large multi-protein complex that facilitates cell wall cleavage. FtsE works with FtsX as an ATP-binding cassette (ABC) transporter. This protein was enriched ($-\log_2>3$), but it did not meet the p-value cutoff. The mannose specific IID component of the phosphotransferase system (PTS) almost

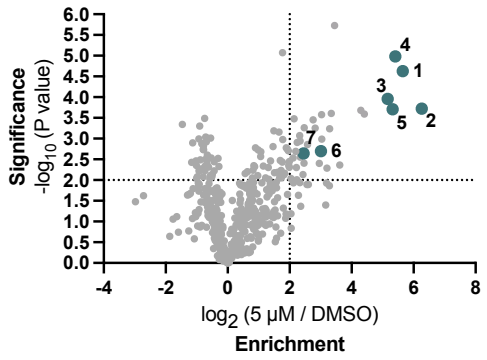

#	UniprotID	Gene	Protein name
1	Q54443	*dexT*	Dextranase
2	Q8DTL1	*ftsX*	Cell division FtsX
3	Q8DVE0	*ftsA*	Cell division FtsA
4	Q8DTW2	*SMU_1208c*	Uncharacterized protein
5	Q8DWM3	*gbpB*	Glucan binding protein B (putative peptidoglycan hydrolase)

Figure 3.11 Enrichment at 5 µM

made the cutoff as well, which we found interesting due to our previous connections to CcpA, and its connections to the PTS system.

To prioritize the potential protein target leads, we analyzed the LFQ intensity dose-dependent response from the untreated samples to 1 μM to 5 μM (Figure 3.12) The proteins that were enriched at 1 μM and exhibited significant dose-dependent responses were DexT, FtsX, FtsA, SMU.1208c, and GbpB. We decided to include BrpA in the follow up studies because it just barely missed the cutoff for significance (p~0.016) at 1 μM and exhibited a good dose-dependent response. The most prominent enrichment and highest overall LFQ intensity was observed with GbpB.

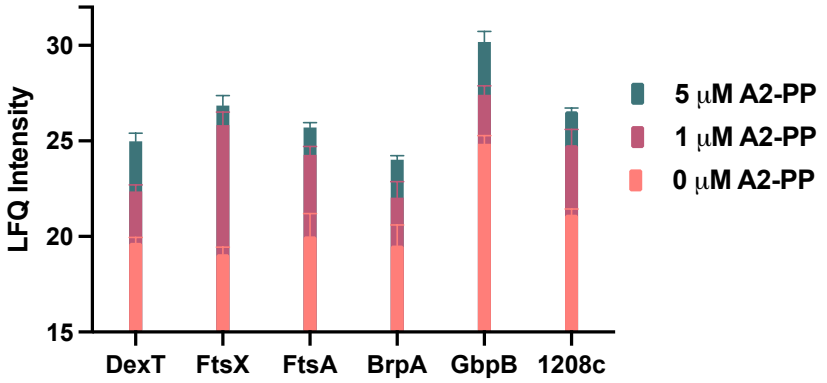

Figure 3.12 Dose-dependent LFQ intensity

We were interested in seeing if competition experiments with **A2** and carolacton would rule out any of these targets. Unfortunately, the excess amount of compound required to outcompete the **A2-PP** (10x) resulted in protein levels that were too low for LCMS analysis due to cell lysis. As a result, alternative validation methods were explored.

If we were to conduct the competition experiments again, there are a few experimental changes that could promote a successful outcome. First, we could use less than 10x excess to see if competition is still observed. Additionally, it is possible that the concentrations of DMSO when a 10 mM stock are used for the excess compound are toxic and adding to the lysis effect.

Thus, using a more concentrated stock of compound would reduce the amount of DMSO added to the cell culture and potentially reduce cell lysis. We could also alter the experimental conditions to optimize activity and thus use less compound and in turn less DMSO (i.e., acidic media).

3.4 Narrowing down targets

The experiments described in this section were carried out jointly by AES and AMS.

We were interested in further exploring the role of the most notable six proteins (FtsA, FtsX, DexT, SMU.1208c, GbpB) in the mechanism of **A2** with chemical genetics and phenotypic analysis using single deletion mutants corresponding to each protein lead.[25] However, the essentiality of GbpB precludes its analysis via gene deletion strategies, requiring the development of new methods to determine its interaction with **A2** (discussed below).

Growth assays with the protein knockout strains were conducted using acidic media to conserve compound since we have previously demonstrated more potent activity in these conditions. The FtsX deletion strain was tested under biofilm promoting conditions (Todd Hewitt Broth + 0.1% sucrose (w/v)) because it does not grow well in acidic media. We would expect decreased susceptibility to compound treatment if the deleted protein mediates the inhibitory activity of **A2**. ΔCcpA was used as a positive control and WT cells were used as a negative control.

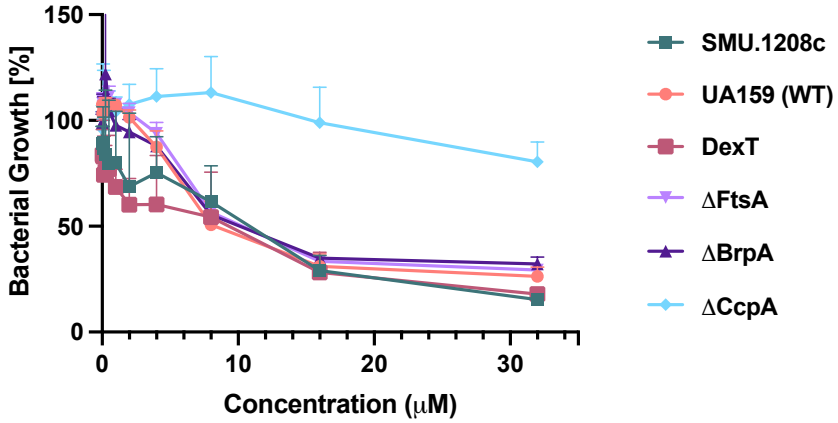

Figure 3.13 Mutant growth assay under acidic conditions

ΔFtsA, ΔDexT, and ΔSMU.1208c were equally susceptible to **A2** as WT cultures, thereby excluding their involvement (Figure 3.13). Against the FtsX knockout, inhibitory activity up to 125 μM was retained, but was slightly less effective at 250 μM (Figure 3.14).

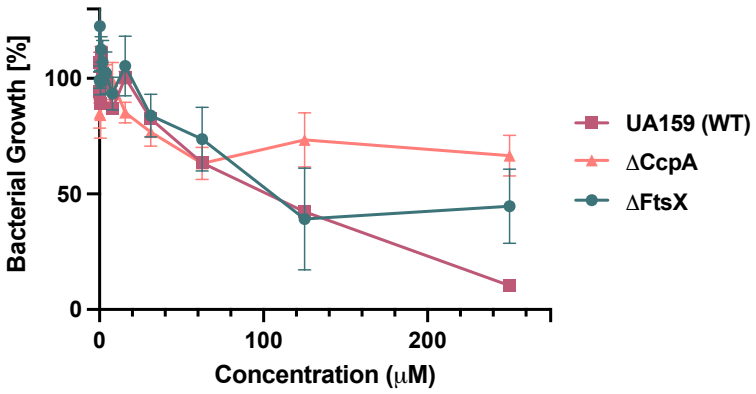

Figure 3.14 Mutant growth assay under biofilm conditions

Confocal analysis was conducted with all the mutants under biofilm promoting conditions and using a glass plate to ensure attachment and further promote biofilm growth. The effect against the FtsA knockout mirrored the WT phenotype (Figure 3.15) supporting the growth assay results. **A2** had a more potent effect on biofilm reduction in the BrpA mutant relative to WT, but this is likely due to the reduced viability of the ΔBrpA cells even in the absence of compound. Imaging of the remaining two mutants, ΔDexT and ΔSMU.1208c, is in progress as we just recently received the mutants.

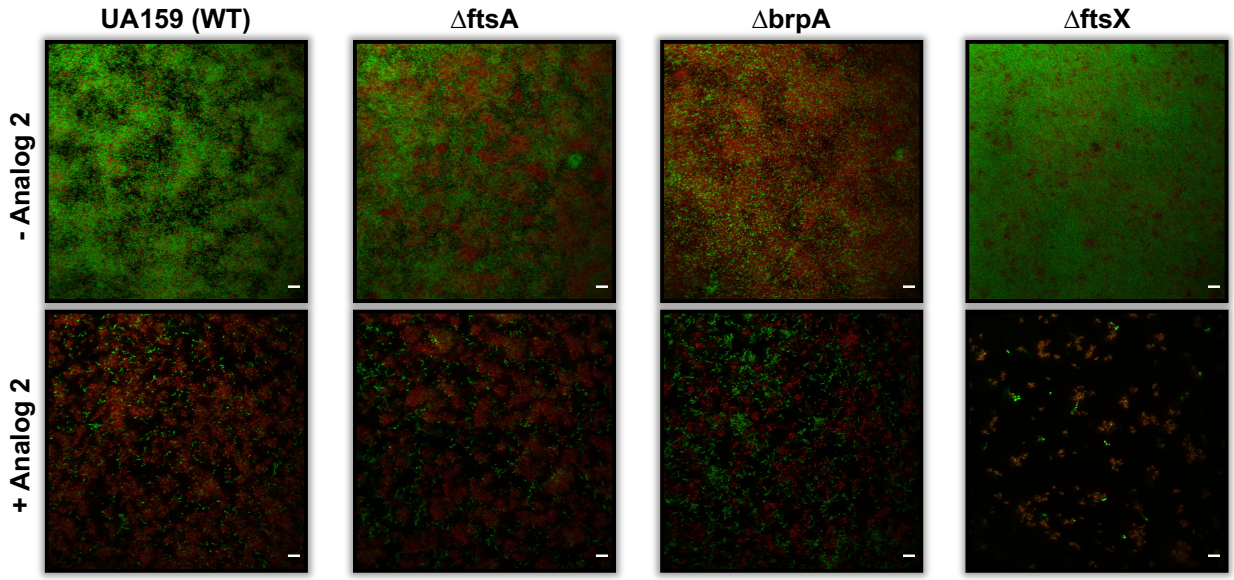

63 μM analog 2; scale bar 10 um

Figure 3.15 CLMS images of A2-treated knockouts

Interestingly, **A2**-treated biofilms (63 μM) stained with LIVE/DEAD™ displayed a more potent effect against ΔFtsX than WT (Figure 3.15). The effect is even more drastic considering the untreated ΔFtsX strain formed a more robust biofilm. The reduced effect at high concentrations and enhanced effect at sub-MIC levels suggest that FtsX plays a secondary role in the biological activity of **A2**. Further, the decreased fitness of the FtsX knockout in acidic media points to a weakened defense against acidification that occurs upon disruption of this complex. FtsX is purported to activate GbpB through a direct protein-protein interaction (PPI), providing additional credence to exploring the remaining AfBPP lead as **A2**'s target.

3.5 Exploring GbpB as the target

The experiments in this section were carried out by AMS unless otherwise stated.

3.5.1 Glucan binding protein B

GbpB is a putative hydrolase that is essential for growth in *S. mutans*, and despite being the subject of numerous studies, its role in biofilm formation, competitive fitness, and the divisome in both secreted and cell-associated forms is still unclear.[15,20,29–31] Its essentiality is likely due to its role in cell wall septum cleavage. The hydrolase activity of GbpB has high homology with the essential peptidoglycan hydrolase, PcsB, in *Streptococcus pneumoniae* (Figure 3.16).[21,32–35] Disruption of either GbpB or PcsB leads to cells with aberrant cell morphologies and mislocalized septa, pointing to crucial rules in cross wall septal splitting.

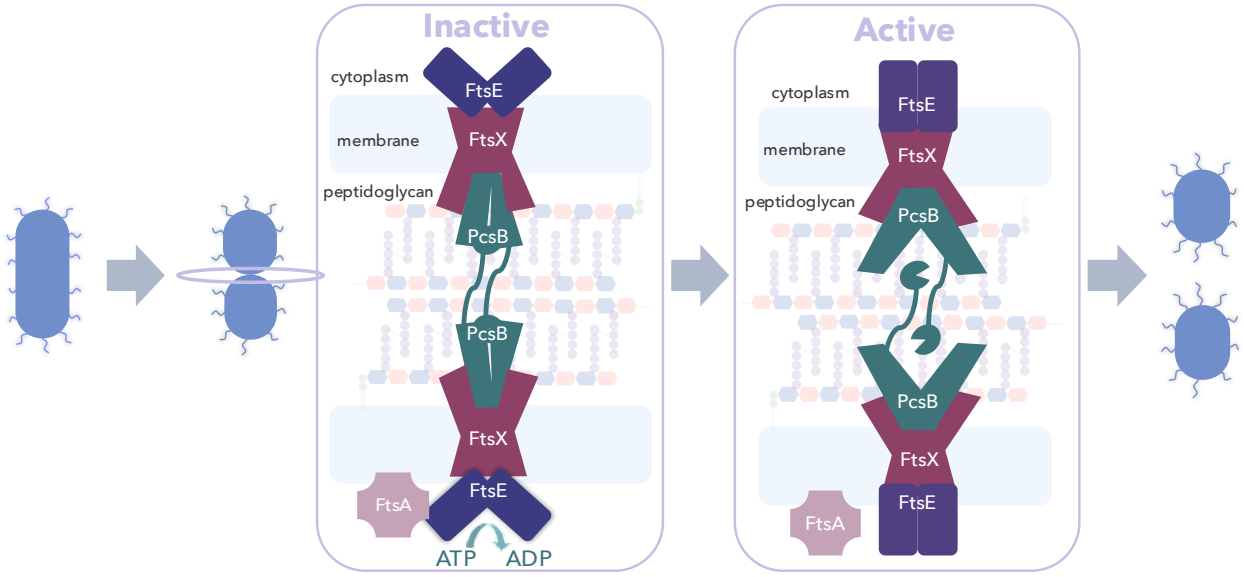

Figure 3.16 Cross wall septal cleavage by the FtsEX-PcsB complex

PcsB-mediated cell separation purportedly occurs by recruitment of PcsB to the septum by the transmembrane FtsEX complex, followed by allosteric activation resulting in “unzipping” of the two daughter cells (Figure 3.16). FtsEX are known to interact with FtsA in the divisome as well. The presence of FtsX and FtsA as top leads, in addition to FtsE almost making the cutoff provides strong support that we are targeting this complex. Similar complexes have been identified in other species including *E. coli and Bacilli.*

Beyond the AfBPP results, carolacton has numerous connections to GbpB. Most notably, the expression of *gbpB* is under the control of the TCS, VicRK, which is directly regulated by PknB. This TCS is also the first to respond to carolacton treatment. Moreover, if GbpB is an essential enzyme in cross wall splitting, then disrupting its function would disrupt cell wall homeostasis requiring changes in the production of the cell wall, carbon utilization, and amino acid utilization, all processes that carolacton are most strongly tied to.

Unlike the other AfBPP leads, GbpB does not have a viable mutant in *S. mutans.* There is a *Streptococcus* strain, *S. sobrinus* strain 3SSA1, that does not produce GbpB.[184] I attempted to secure this strain, but the lab has since shut down and the strains were not saved. As such, we turned to alternative methods for target validation, including resistance selection, chemical-chemical genetics via synergy, overexpression, followed by binding studies.

3.5.2 Resistance selection

Due to the essential role GbpB plays in the cell, we were interested in whether evolution of a resistant mutation in this target was possible. Furthermore, resistance selection has been previously used to validate proteomic experiments.[22] To this end, we serial passaged increasing concentrations of **A2** starting at 5 μM and ending with 100 μM against *S. mutans* biofilm cells over 24 days. Following isolation of single colonies, we tested these strains for their susceptibility to **A2** and found that we evolved three cell lines, with a 1.2-2.0-fold increase in IC_{50} values, and no change in MIC (Table 3.1). We then sent isolated colonies to Professor Daria Van Tyne for sequencing.

Whole-genome sequencing revealed a mutation in *pknB*, a serine/threonine protein kinase in one strain, and in another, a mutation was observed in its negative regulator, the serine/threonine phosphatase, *pppL* (Table 3.1). An identical point mutation in the gene *fbp,* that encodes for the putative fibronectin binding protein, was present in two of the resistant strains. In addition, two strains displayed identical insertions upstream of *ptnA*, the gene encoding for

enzyme II mannose-specific transporter (phosphotransferase; PTS system). Notably, this enzyme is part of the same pathway as the PTS protein discussed in the AfBPP results. Finally, mutations were observed in the putative tagatose regulator and the putative glutamine ABC transporter, *glnP*.

Strain	IC_{50} (μM)	Fold increase	Mutation	Uniprot ID	Locus	Gene	Functional Class
1	139	1.8	His10Tyr	Q8DTA9	SMU.1449	*fbp; pavA*	Fibronectin/fibrinogen binding protein
			Glu226Asp	Q8DWE9	SMU.112c	--	Tagatose utilization transcriptional regulator (RpiR family)
2	93	1.2	Glu238Lys	Q8DVM0	SMU.460	--	Putative amino acid ABC transporter, permease protein
			His41Tyr	Q8DVK2	SMU.483	*pppL*	Putative phosphoprotein phosphatase
			Insertion 150bp upstream of ptnA	Q8DSC4	SMU.1877	*ptnA*	EIIAB-Man, PTS system mannose-specific
3	153	2.0	Met90Ile	Q8DVK1	SMU.484	*pknB*	Ser/Thr protein kinase
			Arg83Cys	Q8DTY2	SMU.1179c	*glnP*	Putative amino acid (glutamine) ABC transporter, permease protein
			His10Tyr	Q8DTA9	SMU.1449	*fbp; pavA*	Fibronectin/fibrinogen-binding protein
			Insertion 150bp upstream of ptnA	Q8DSC4	SMU.1877	*ptnA*	EIIAB-Man, PTS system mannose-specific

Table 3.1 Mutations evolved from serial passaging

The presence of the PknB/PppL regulatory circuit across two of the resistant strains, in addition to the improved potency against the ΔPknB strain reported earlier, strongly implicates this pathway in the mechanism. Notably, previous studies on carolacton speculated that PknB was a potential target. The insertion upstream of *ptnA,* a sugar transporter, likely alters gene expression, which could affect the direct action of this enzyme, or the expression of downstream targets, such as CcpA. Furthermore, changes in sugar availability can alter the glycolytic end products, and the availability for cell wall disaccharide biosynthesis. The tagatose transporter

likely functions in the PTS system specific for tagatose, although many of these PTS transporters have promiscuous activity. Mutations in the fibronectin binding protein could change the outside of the cell which has proven important for localizing cell division proteins. Alternatively, this mutation could alter the biofilm forming abilities. Glutamine is one of the amino acids in the cell wall stem peptide and alterations in its transport could affect the available pools for cell wall biosynthesis. The evolution of these compensatory mutations is likely a result of the sub-MIC concentrations of compound that exerted low selection pressure allowing for compensatory mutations, instead of resistant ones, to emerge.[28] We attempted to induce resistance via stronger selection using an agar-based method. However, these experiments were unsuccessful, suggesting that the fitness cost to mutate GbpB is too high, making it a promising antibiotic target.

3.5.3 Synergy studies

We were then interested in conducting chemical-chemical interaction studies for two reasons: the public health implications and the mechanism of action information that can be deduced. In a recent study by the Department of Veteran Affairs, 82.5% of patients undergoing dental procedures received antibiotic prescriptions for prophylaxis. The two most common prescribed antibiotics were amoxicillin, a β-lactam, and clindamycin, a protein synthesis inhibitor (71.3% and 23.8% of total prescriptions, respectively.[62] For appropriate prophylaxis, the selected antibiotic should be bactericidal and effective against the most common microorganisms that cause infection associated with the procedure.[63] In the oral cavity, the most common microorganisms are streptococci and peptococci (Gram-positive). Ideally, if one can develop a synergistic cocktail that would lower the dosage of these broad-spectrum agents against these pathogens then one could lessen the overall impact of the antibiotics on the patient's microbiome. To date, arguably the most successful approach to antibiotic synergy is through combination with cell envelope-targeting compounds (cell wall or cell membrane).[64] Our lab has had significant success potentiating antibiotics against resistant and persistent gram-positive pathogens.[45,54,65] Further,

the role of GbpB has been shown to be enhanced for cariogenic pathogens as it was initially investigated as a vaccine for oral caries in rates hinting that an inhibitor alone might also be effective as a narrow-spectrum pathogen specific treatment.[68,69]

The second reason we were interested in synergy studies was because a PcsB-deficient strains of *Streptococcus agalactiae* has been shown to be 5x and 40-190x susceptible to clinically approved antibiotics, including β-lactams and protein synthesis inhibitors, presumably due to the defects in the cell wall.[32] Whereas vancomycin was found to have little effect. If we did not see synergy, we wouldn't be that surprised, because contrary results have been seen in *S. mutans* and *S. pneumoniae*, but the clinical benefits were most influential.

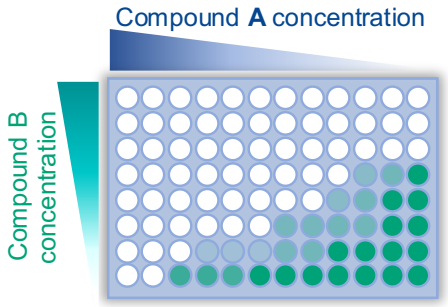

Figure 3.17 Checkerboard assay

Toward this end, we conducted a well-established checkerboard assay to examine synergistic effects using **A2** and the pertinent antibiotics in combination over a range of concentrations (Figure 3.17).[70,71] The fractional inhibitory concentration (FIC) of combinatorial treatment will be determined by the sum of FIC_A (defined as MIC of synergist in combination, divided by MIC of synergist alone) and FIC_B (FIC_A (defined as MIC of the antibiotic in combination, divided by MIC of the antibiotic alone). Synergy correlates to a FIC value of $\leq$0.5, no interaction is characterized by values between 0.5 and 4, and >4.0 is indicative of an antagonistic relationship. These cutoffs require an MIC shift of two dilutions for both compounds to be considered synergistic.

Vancomycin (μM)

Analog 2 (μM)	2	1	0.5	0.25	0.12	0
125	0.0439	0.0445	0.0453	0.0537	0.1418	0.1627
63	0.0444	0.0437	0.0436	0.277	0.2757	0.2431
32	0.0436	0.0446	0.0448	0.2939	0.3302	0.305
16	0.0439	0.0437	0.0439	0.2731	0.3761	0.3487
8	0.0454	0.0458	0.0455	0.3377	0.4026	0.3691
4	0.045	0.0445	0.0442	0.3348	0.4176	0.3853
2	0.0445	0.0454	0.046	0.2458	0.4216	0.3904
0	0.0447	0.0448	0.0463	0.1994	0.4448	0.436

Figure 3.18 Vancomycin checkerboard assay

When vancomycin was tested with **A2**, the FIC was 1, which is indicative of an additive interaction, or no interaction (Figure 3.18). With clindamycin, the FIC is 0.5008. According to the cutoffs, this is additive, or no interaction, but qualitatively, relative to vancomycin, there is more synergy occurring (Figure 3.19).

Clindamycin (μM)

Analog 2 (μM)	0.244	0.122	0.061	0.031	0.015	0.008	0.004	0.002	0.001	0.0005	0.0002	0
125	0.071	0.073	0.078	0.094	0.116	0.107	0.109	0.119	0.129	0.126	0.128	0.147
63	0.061	0.068	0.078	0.152	0.286	0.330	0.344	0.306	0.330	0.317	0.323	0.309
32	0.062	0.069	0.095	0.277	0.388	0.389	0.424	0.396	0.385	0.409	0.363	0.408
16	0.060	0.063	0.077	0.330	0.414	0.405	0.454	0.445	0.450	0.449	0.400	0.395
8	0.057	0.062	0.078	0.399	0.424	0.433	0.513	0.503	0.522	0.494	0.523	0.487
4	0.057	0.064	0.076	0.395	0.478	0.514	0.529	0.550	0.537	0.537	0.550	0.537
2	0.058	0.061	0.086	0.421	0.479	0.509	0.541	0.550	0.546	0.553	0.540	0.486
0	0.057	0.063	0.368	0.464	0.510	0.554	0.556	0.550	0.556	0.559	0.550	0.558

Figure 3.19 Clindamycin checkerboard assay

A similar effect was seen with amoxicillin, but to a lesser degree than clindamycin with an FIC of 0.63 (Figure 3.20). Like **A2** alone, we observed spikes in biomass product at sub-MIC concentrations when the checkerboard assay was analyzed by crystal violet.

Amoxicillin (μM)

Analog 2 (μM)	0.244	0.122	0.061	0.031	0.015	0.008	0.004	0.002	0.001	0.0005	0.0002	0
125	0.070	0.083	0.095	0.089	0.097	0.086	0.088	0.092	0.106	0.094	0.088	0.094
63	0.066	0.077	0.115	0.285	0.287	0.304	0.323	0.298	0.308	0.323	0.267	0.293
32	0.061	0.074	0.339	0.337	0.339	0.320	0.328	0.303	0.325	0.297	0.329	0.343
16	0.059	0.113	0.412	0.473	0.450	0.470	0.460	0.478	0.478	0.440	0.460	0.433
8	0.057	0.278	0.410	0.475	0.477	0.474	0.490	0.496	0.463	0.450	0.450	0.454
4	0.056	0.329	0.491	0.503	0.525	0.531	0.546	0.539	0.532	0.513	0.510	0.522
2	0.056	0.381	0.512	0.552	0.550	0.542	0.554	0.550	0.544	0.572	0.517	0.536
0	0.059	0.382	0.562	0.598	0.596	0.570	0.578	0.570	0.569	0.578	0.580	0.569

Amoxicillin (μM)

Analog 2 (μM)	0.244	0.122	0.061	0.031	0.015	0.008	0.004	0.002	0.001	0.0005	0.0002	0.000
125	0.90	1.40	3.73	4.57	6.79	8.64	10.36	10.01	7.43	11.09	10.80	10.79
63	1.15	2.28	10.19	6.12	7.56	7.03	7.27	7.59	6.78	6.64	7.94	7.51
32	1.13	5.32	6.78	6.97	7.58	7.21	7.55	7.92	6.83	8.04	7.18	6.93
16	1.15	12.15	5.18	3.70	3.49	2.90	3.08	2.30	2.34	2.79	2.77	2.73
8	1.22	8.40	5.49	2.94	2.79	2.62	2.62	2.15	2.46	2.47	2.53	2.69
4	1.41	7.73	3.68	2.25	2.08	1.94	1.83	1.75	1.84	1.98	1.94	2.00
2	1.25	6.32	2.65	1.78	1.75	1.71	1.68	1.57	1.47	1.40	1.51	1.77
0	1.18	6.66	1.68	1.07	1.16	1.09	1.14	1.03	1.07	1.05	1.04	1.16

Figure 3.20 Amoxicillin growth and biofilm checkerboard assay

Overall, the synergy experiments with antibiotics could be improved moving forward by using a linear dilution instead of a serial dilution. The 2-fold changes often represent wide spans of concentrations. As such, subtle changes are often missed, and can result in FIC values like 0.5008. By narrowing in on a more precise MIC, true synergy may be observed.

While the antibiotic synergy studies did not provide any true synergy partners, I had another idea for a potential synergistic pairing. In our initial genetic mutant screen, **A2** was more potent against an *S. mutans* strain where the serine/threonine protein kinase, PknB, is knocked out. This observation inspired a collaboration with Professor Meghan Blackledge at High Point University to find potential synergy partners. Her lab has a library of 22 compounds including, phenanthroline derivatives, carbazole-based compounds, and two FDA approved drugs with activity against the serine/threonine protein kinase (STPK) present in various staphylococcal species.[185] In *S. mutans*, PknB is the only kinase of this kind present, and we were curious if the staphylococcal STPK inhibitors could also have synergistic activity in this strain. Moreover, the identification of a mutation in the *pknB* gene implicated this kinase in the activity of **A2**.

To this end, I conducted preliminary growth assays against WT *S. mutans* under both biofilm and planktonic conditions to determine the baseline MIC for the checkerboard assays. I also tested the PknB knockout to determine whether these compounds exhibited different effects relative to WT, which wasn't expected since PknB is not an essential enzyme. Following this screen, we chose to proceed with only loratadine, the main ingredient in Claritin, for the checkerboard assay. Interestingly, loratadine had an antagonistic relationship with **A2** (Figure 3.21).

Analog 2 (μM) \ Loratadine (μM)	250	125	63	32	16	0
125	0.328	0.2776	0.2536	0.2392	0.2116	0.2191
63	0.3516	0.3113	0.2975	0.2953	0.2835	0.2725
32	0.3763	0.3404	0.3562	0.3166	0.346	0.311
16	0.3269	0.3511	0.399	0.3914	0.3473	0.3967
8	0.2843	0.3603	0.401	0.3893	0.4019	0.4368
4	0.2697	0.3696	0.3836	0.3743	0.4157	0.3597
2	0.2809	0.3851	0.394	0.3915	0.3757	0.4155
0	0.298	0.4159	0.4167	0.4016	0.3996	0.4055

Figure 3.21 Loratadine checkerboard assay

The preliminary understanding in the Blackledge lab is that loratadine binds to the kinase domain in the Staphylcoccal STPK. In *S. pneumoniae*, the PknB homolog was found to regulate the VicRK homolog by a direct protein-protein interaction (PPI), meaning that binding the kinase domain would not alter PknB activation of VicK. However, this activation is presumably activated by ligand binding to the extra cellular PASTA domains in PknB, which triggers a conformational change and induces a binding event between its transmembrane domain and the transmembrane domain in VicK. It is not clear whether loratadine binds in the active site of the kinase domain or at an allosteric site, but either way, if phosphorylation of one amino acid is sufficient to induce a substantial conformation change, it is likely that this binding event would be sufficient as well. If so, a PPI between the two transmembrane domains would result in activation of VicK, and

subsequent upregulation of *gbpB*. A better understanding of how PknB is regulated would greatly increase our understanding of the essential divisome and important virulence traits.

3.5.4 GbpB overexpression in *S. mutans*

We wanted more direct methods of evaluating GbpB as the direct protein target of **A2**. Comparable to knockout studies, overexpression of a molecular target *in vivo* would increase susceptibility to a chemical inhibitor making this approach a viable tool for target identification.[26,27] For this reason, we reached out to our collaborator who works on *S. mutans* microbiology and asked them if they could design this strain for us. A postdoctoral fellow, Dr. Hua Zhang carried out these experiments. A pVPT-GbpB plasmid was constructed and transformed into *S. mutans* UA159 yielding UA159/GbpB and used in bacterial and biofilm inhibition (Figure 3.20). A strain containing an empty vector was also constructed (UA159/pvpt) and used as a negative control. Experiments were completed in two different medias: tryptic soy broth supplemented with 1% yeast extract and 0.5% sucrose (TSBYE-S) and brain heart infusion (BHI-S) supplemented with 0.5% sucrose. At 150 μM, **A2** maintains growth inhibition and anti-biofilm activity against the overexpression strain in both medias (Figure 3.22). However, at 100 μM, cell growth of the strain overexpressing *gbpb* increased 8 to 20-fold compared to that of the WT strain when grown in BHI and TSBYE-S media respectively. The biofilm effect at this concentration was similar, with a 16-fold increase in biofilm formation relative to WT in TSBYE-S and a 10-fold increase in BHI-S. Protection against **A2** inhibition and anti-biofilm activity in the presence of *gbpB* overexpression provides strong evidence that GbpB is responsible for mediating **A2** activity *in vivo*.

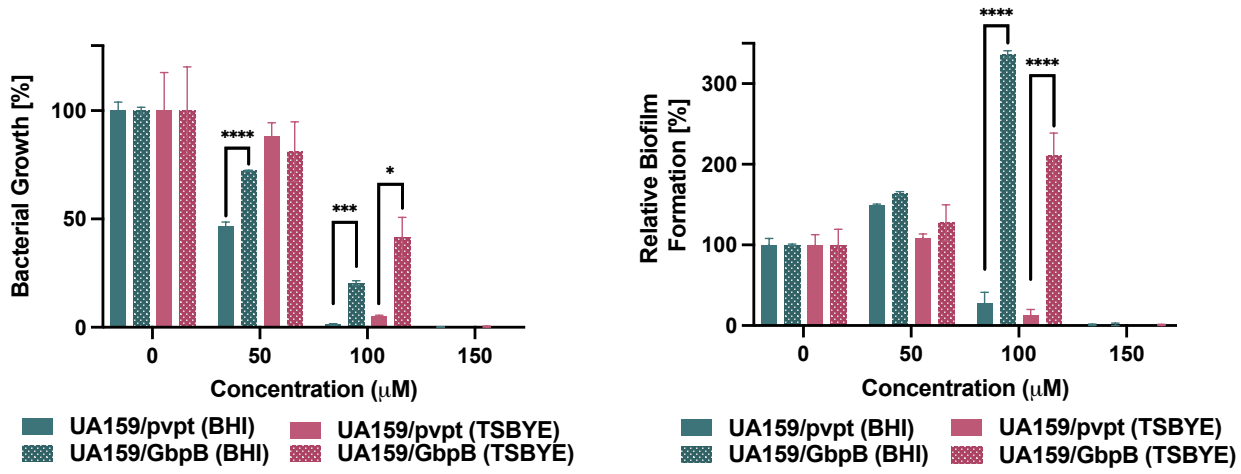

Figure 3.22 Overexpression of GbpB.

left) Percent bacterial growth of WT UA159 and UA159/pVPT-GbpB in TSBYE-S and BHI. Growth was normalized with the OD_{600} of the untreated control being 100% and the OD_{600} of the media was 0%. right) Percent relative biofilm production of WT UA159 and UA159/pVPT-GbpB in TSBYE-S and BHI. Biofilm formation was normalized by dividing OD_{562}/OD_{600} to account for changes in bacterial growth. All data represents three biological replicates (+ s.d.). P value: * < 0.01; ** = < 0.001; * = < 0.0001; **** = < 0.00001; two-tailed Student's t-test.**

3.5.5 Attempts to express and purify GbpB

I initiated a collaboration with the labs of Dan Kahne and Suzanne Walker at Harvard to facilitate my training in the experiments necessary to characterize the interaction between GbpB and **A2.** To start, we were interested in expressing and purifying recombinant GbpB for use in binding studies. I worked with a postdoctoral fellow, Dr. Vadim Baidin for five weeks over the Summer of 2021. We sought to express and purify GbpB using four different constructs (Figure 3.23). Unfortunately, these attempts were unsuccessful. We tried without a fusion partner, and with two different fusion partners, separately. We also switched to a low copy plasmid in case high production of GbpB was detrimental to the cell due potentially due to hydrolase activity, ultimately leading to proteolytic degradation of GbpB. Alternatively, it could be forming inclusion bodies during the isolation procedure.

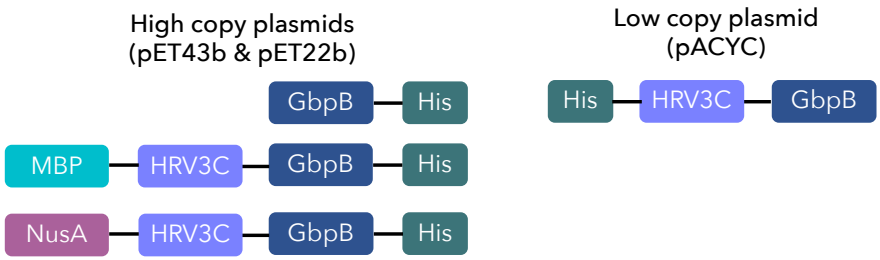

Figure 3.23 GbpB constructs

If I am given the opportunity to attempt this expression again, I would treat the protein samples with a denaturing reagent to solubilize the protein aggregates. I would also make changes in the plasmid design. First, I would move the His tag from the C-terminus to the N-terminus, since I believe that the tag on the C-terminus could be potentially destabilizing. The homolog of GbpB, PcsB has been crystalized and its structure has been resolved. In this structure, PcsB was found to exist as either a dimer or a monomer depending on the concentration of the protein. In both forms, PcsB can exist in two different conformations, an open/activated conformation, and closed/deactivated conformations (Figure 3.16). In the monomeric form, the C-terminus tucks into the coiled-coiled (CC) domain on the N-terminus that makes a V-shape. I confirmed that GbpB would occupy a similar fold using AlphaFold. In either conformation, it's possible that inserting a His-tag could disrupt the stabilizing interactions that promote this closed monomeric conformation, leading to an instable protein.

3.5.6 Expanded bacterial screen

Instead, we elected to express and purify a closely related homolog found *in S. pneumoniae,* PcsB (64% identity), which unlike GbpB has been isolated and characterized biochemically. We first confirmed that **A2** retained activity against *S. pneumoniae* by conducting inhibition assays with two different strains of *S. pneumoniae,* D39 and TIGR4 (Figure 3.24). The former is a virulent, encapsulated serotype 2 strain. Pneumococcal strains are serotyped based on the identity of the capsule that decorates the cell wall. The latter, TIGR4, is also a virulent,

encapsulated strain, but from the serotype 4 family. These assays were done in THB supplemented with 1% yeast extract. The media prior to incubation is neutral, but after incubation, the pH in untreated cells, **A2**-treated cells, and DMSO-treated cells ranges between 5.3 and 5.7, which could explain the improved activity relative to *S. mutans* biofilms (Table 3.2). Alternatively, the impermeability and lowered metabolic rate of biofilm cells could also play a role.

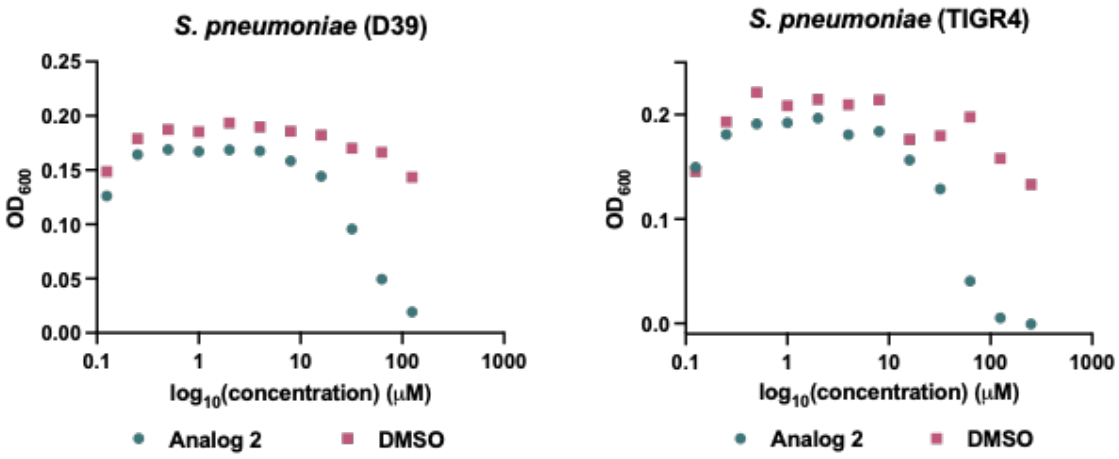

Figure 3.24 Inhibition assays with *S. pneumoniae* strains

A2 exhibited an MIC of 125 μM against both strains. Against the D39 strain, **A2** displayed an IC_{50} of 62 μM. When tested against the TIGR4 strain the IC_{50} was 42 μM. CFU/mL counts were attempted, but the colonies were too small and clustered to count. These strains are notoriously difficult to work with.

A2 was also tested against two other pathogenic streptococci, *S. pyogenes* (Group A Strep, GAS) and *S. alagactiae* (Group B Strep, GBS). **A2** maintained an MIC of 125 μM against all GAS and GBS and IC_{50} values in similar ranges, 30 μM and 38 μM, respectively (Figure 3.25). **A2** also exhibited an MBC of 32 μM (Figure 3.26).

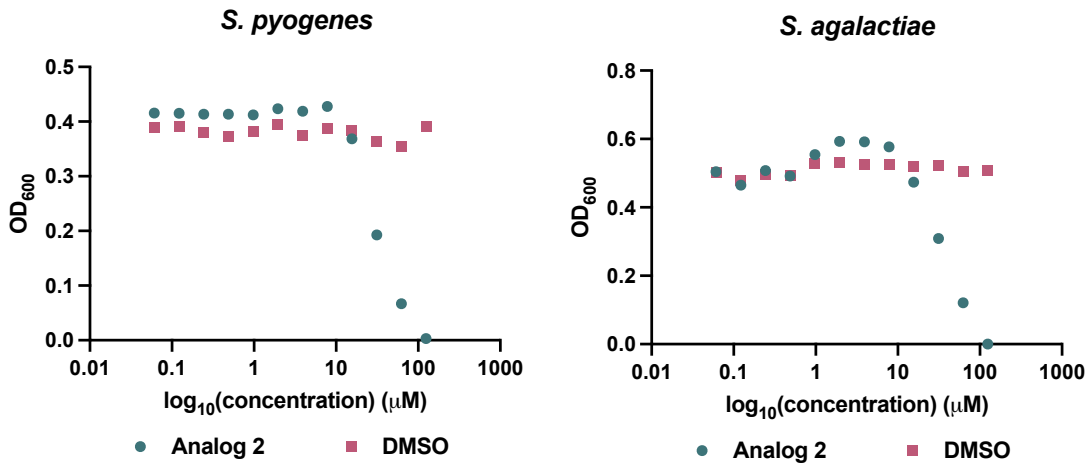

Figure 3.25 Inhibition assay against GAS and GBS

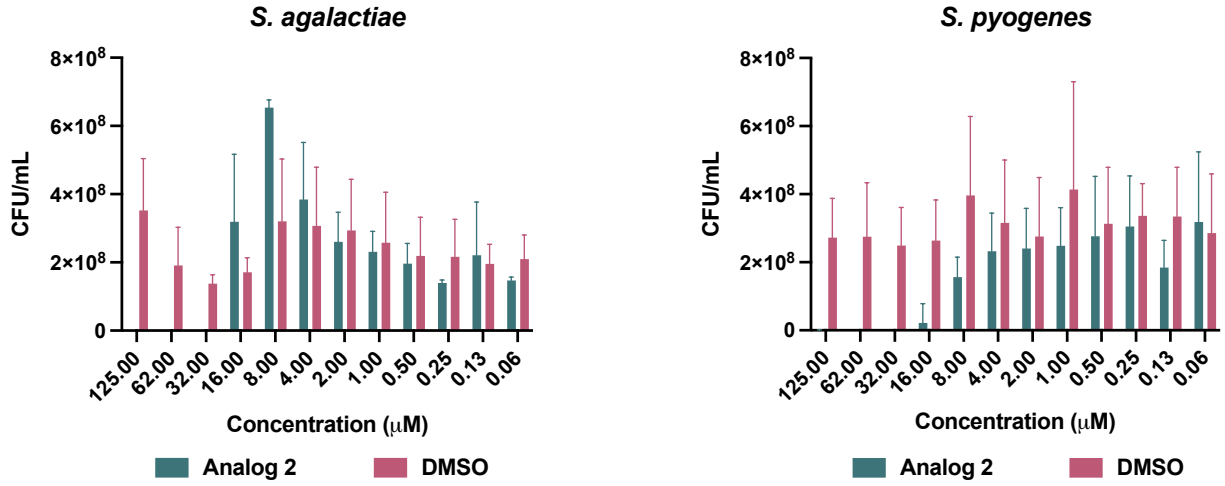

Figure 3.26 CFU/mL assay with GBS and GAS

We then tested **A2** on commensal strains, *S. gordonii* and *S. sanguinis*, to explore the effects this compound would have on the oral microbiome, to probe potential synergism, and/or to deduce additional mechanistic information. These strains were of particular interest because a previous study showed that in a co-culture with *S. gordonii*, *S. sanguinis*, and *S. mutans,* where CcpA was knocked out in all three strains, the commensals were able to outcompete the pathogenic organism. We first conducted planktonic assays to determine whether our compound

would remain biofilm specific, if active at all. **A2** inhibited planktonic growth with IC_{50} values ranging from 29-48 μM (Figure 3.27). Interestingly, the same inhibition activity was observed in the biofilm assay. The lack of specificity for biofilm supports our hypothesis that CcpA regulates the target because these strains rely more heavily on CcpA for carbon metabolism in both their planktonic and biofilm states, unlike *S. mutans*.

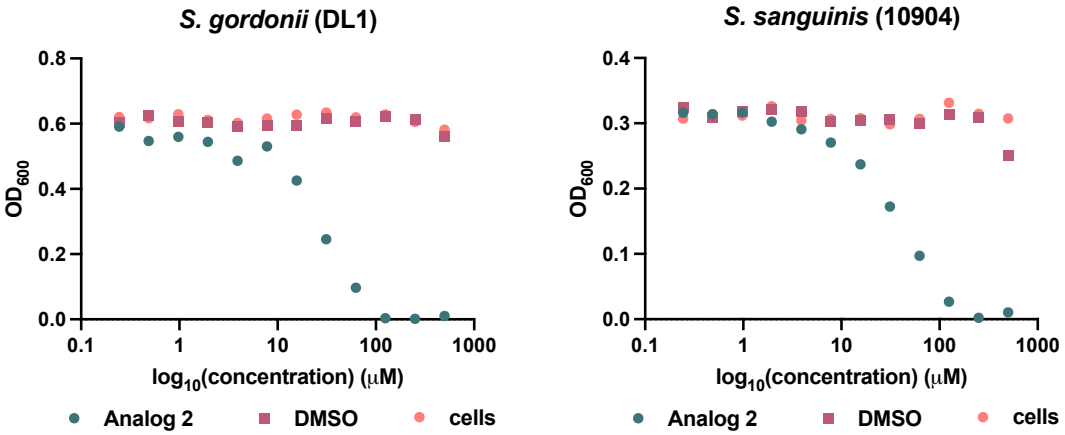

Figure 3.27 Inhibition assays with commensal strains

A summary of the activity of **A2** against the panel of streptococci can be found in Table 3.2. The trends in activity can be explained by the pH of the environment. The conditions where **A2** is most active are in the pre-acidified planktonic *S. mutans* cultures. Since the cells are immediately acid shocked in a homogenous fashion, the ATR would turn on throughout the entire population. In biofilm populations, on the other hand, acid production occurs over time, in a cyclic and heterogenous fashion. As such, it takes longer for the ATR to turn and the environment to be acidified leading to decreased activity. The other streptococci strains seem to fall right in the middle, likely because they acidify their cultures throughout incubation; it isn't instant, nor is it cyclical, thus the ATR onset would fall right in between. This data suggests a conserved target

across the streptococci genus, encouraging us to proceed with characterizing **A2** with PcsB as a GbpB proxy.

Strain	MIC (μM)	IC_{50} (μM)
S. mutans (UA159) - planktonic	125	144
S. mutans (UA159) - biofilm	250	77
S. mutans (UA159) - enhanced biofilm	250	44
S. mutans (UA159) - acidic planktonic	8	1
S. pneumoniae (D39/NCTC 7466)	125	62
S. pneumoniae (TIGR4)	125	42
S. agalactiae (ATCC BAA-1138)	125	38
S. pyogenes (ATCC700294)	125	30
S. gordonii (DL1/ATCC 35105)	125	29
S. sanguinis (NCTC 10904)	125	36

Table 3.2 Summary of streptococcal activity

3.6 PcsB expression and purification

To this end, we designed two PcsB constructs, one with the His(6)-tag on the N-terminus and a second with the His(6)-tag on the C-terminus, to probe if either termini are important for function (Figure 3.28). Both proteins expressed well in a range of buffers at a range of pH values.

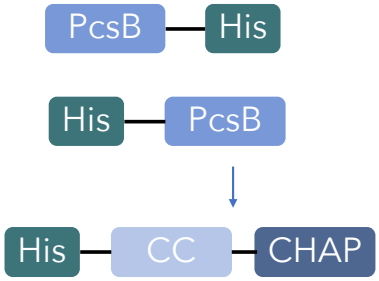

Figure 3.28 PcsB constructs

3.7 Microscale thermophoresis

To evaluate the *in vitro* interaction between **A2** and PcsB, we turned to microscale thermophoresis (MST).[186–188] MST monitors the movement of a fluorescently dyed molecule at a constant concentration through microscopic temperature gradients microliter volumes in the presence of different concentrations of ligand. The thermophoretic response of a protein alone typically differs from the thermophoresis response of a protein-ligand complex, allowing for quantification of a binding affinity.

We then leveraged the nickel (II) nitriloacetate (Ni-NTA)) chelating abilities of the His(6)-tag to facilitate fluorophore attachment using Nanotemper Technologies' His-tag labeling kit. In the MST experiments, the concentration of the labeled PcsB was kept constant (10 nM), while the concentration of the non-labeled binding partner (**A2** or DMSO) was varied between 0.015 μM – 500 μM. After 10 min of incubation, the samples were loaded into Monolith NT.115 Premium Capillaries (NanoTemper Technologies) and the MST measurement was performed using the Monolith NT.115Pico (NanoTemper Technologies) at 20 % LED power and medium MST power. An MST-on time of 1.5 s was used for analysis. We used a conservative definition of outliers, only removing data points where there were irregularities with the absolute fluorescence, the capillary scans, or where the temperature related intensity change (TRIC) traces showed bleaching or aggregation. To determine dissociation constants, we employed the K_d binding model based on the Langmuir binding isotherm that is included in the MO.Affinity Analysis Software provided by

Nanotemper Technologies. We also determined the binding affinities in Prism GraphPad software. We assumed that a specific, one site binding interaction was occurring, and these values agreed with Nanotemper.

The ligands were evaluated for binding in neutral buffer (pH = 7.4). Both PcsB constructs tested with DMSO did not result in a dose-dependent response as evidenced by signal to noise (S:N) ratios less than 5 (Figure 3.29). The top graph shows the MST traces, which represent the changes in relative fluorescence over time. The bottom graphs show the normalized fluorescence, or the ratio of relative fluorescence of the selected region after heating (hot region) and relative initial fluorescence before heating (cold region).

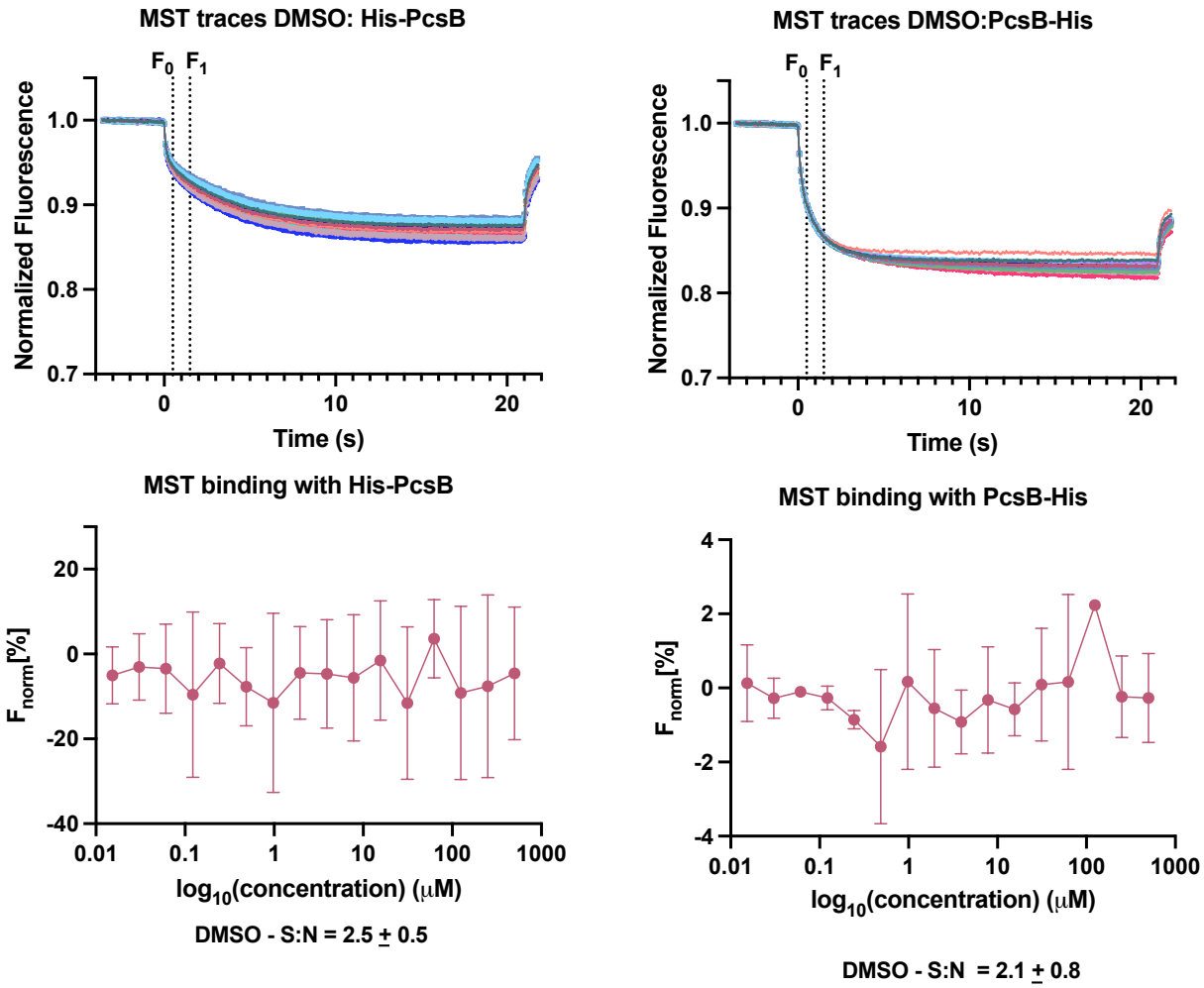

Figure 3.29 MST with DMSO

A2 exhibited a binding interaction at the concentrations tested, with a higher affinity binding to PcsB-His (K_d = 150 ± 51 μM) (Figure 3.31) than to His-PcsB (K_d = 338 ± 51 μM) (Figure 3.30). The signal to noise (S:N) ratio for the former was 29 ± 8, which suggests very good assay conditions and high-quality data. The S:N for the latter was 6.9 ± 0.9, which is acceptable according to manufacturer recommendations, but > 10 is a more generally accepted value. Both binding curves do not reach complete saturation of the target which can result in lower S:N and higher standard deviations in K_d values, but higher concentrations often resulted in aggregation. At the protein concentration (1 mg/mL) used in this assay, PcsB primarily exist in its monomeric

form, wherein the CHAP domain (C terminus) tucks into the CC domain (N terminus) and blocks access to the active site. We postulate that the presence of the His(6)-tag at the C-terminus disrupts the stabilizing interactions between the two domains and creates an entry point for the photoprobe. Alternatively, if **A2** binds at the postulated interface of PcsB and FtsX near the CC domain, the presence of the His(6)-tag at the N-terminus could occlude the residues involved in binding.

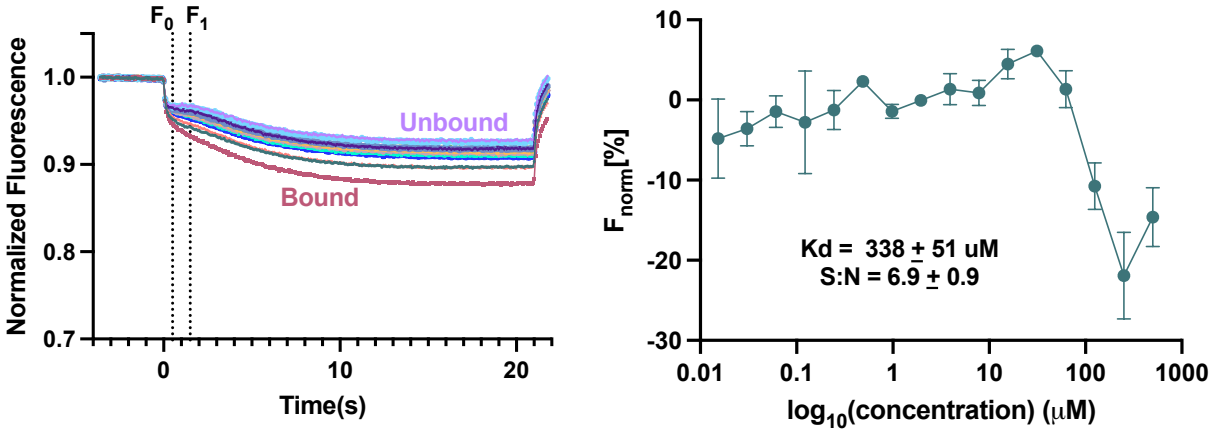

Figure 3.30 MST with A2 and His-PcsB

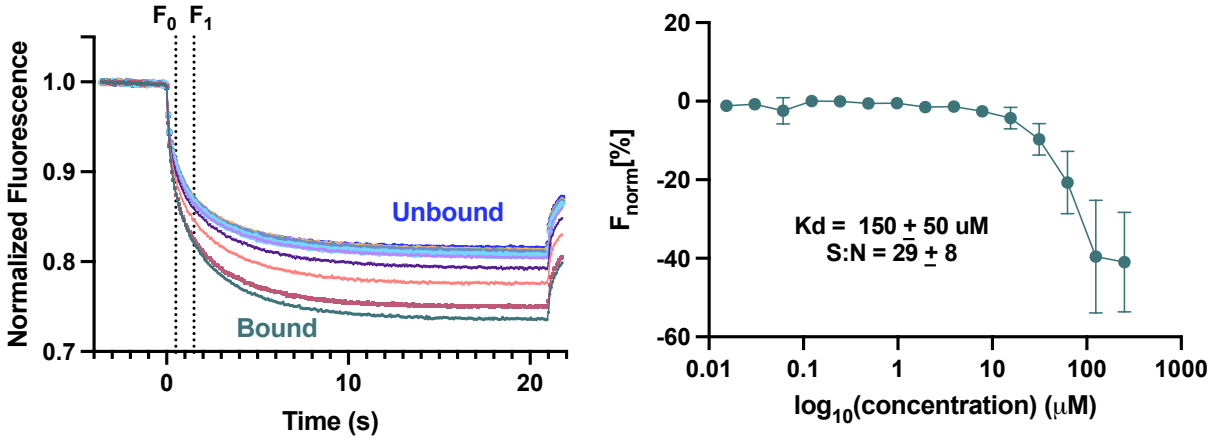

Figure 3.31 MST with A2 and PcsB-His

The acid-dependent mechanism displayed by **A2**, as well as the low isoelectric point (pI) of PcsB, led us to investigate the binding affinities in acidic buffer (pH = 5.4). However, binding was not observed under these conditions (Figure 3.32).

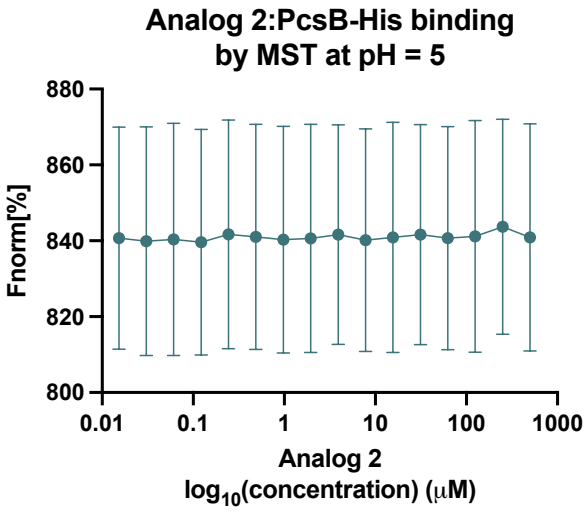

Figure 3.32 MST in acidic buffer

3.8 In vitro crosslinking and molecular docking

With binding confirmation by MST, we were interested in identifying the binding site using *in vitro* crosslinking between recombinant protein and **A2-PP**. First, we sought to confirm a crosslinking event via denatured intact mass spectrometry. **A2-PP** was incubated on ice for 10 minutes with either His-PcsB (25 μM) or PcsB-His (25 μM) followed by 10 minutes of UV irradiation to induce crosslinking. A high concentration (500 μM) of **A2-PP** was chosen to ensure saturation of the binding sites.

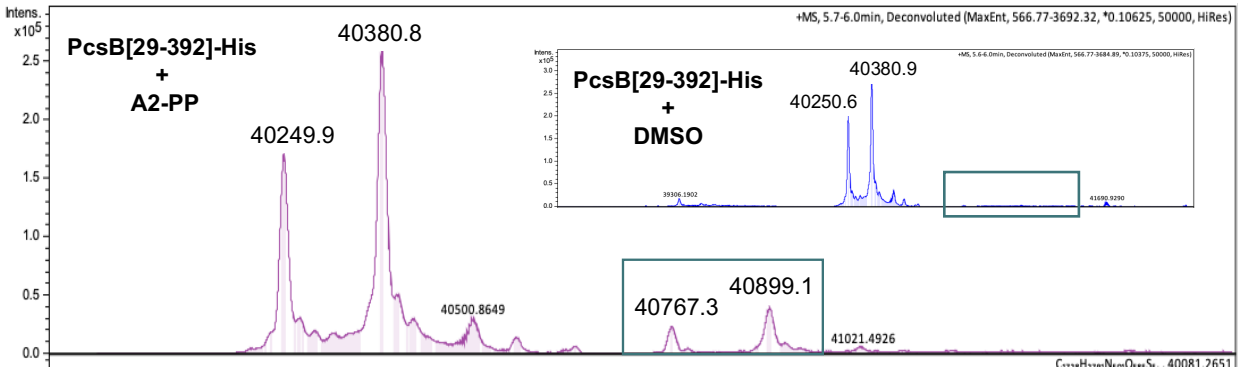

Figure 3.33 In vitro crosslinking with PcsB-His

Samples were submitted directly to the Harvard Center for Mass Spectrometry and analyzed by ESI-qTOF-MS for intact protein analysis to determine the presence of a crosslinked adduct. This analysis identified a crosslink between PcsB-His (Figure 3.33), but not His-PcsB (Figure 3.34), which correlates with the MST results and provides credence toward a selective crosslinking event. For the C-terminal tagged protein, two parent ion peaks were observed, one that contained a terminal methionine, and one that did not. An adduct between **A2-PP** and both parent ions were observed. The labelling efficiency is low, but this could be improved by increasing incubation time or better mixing.

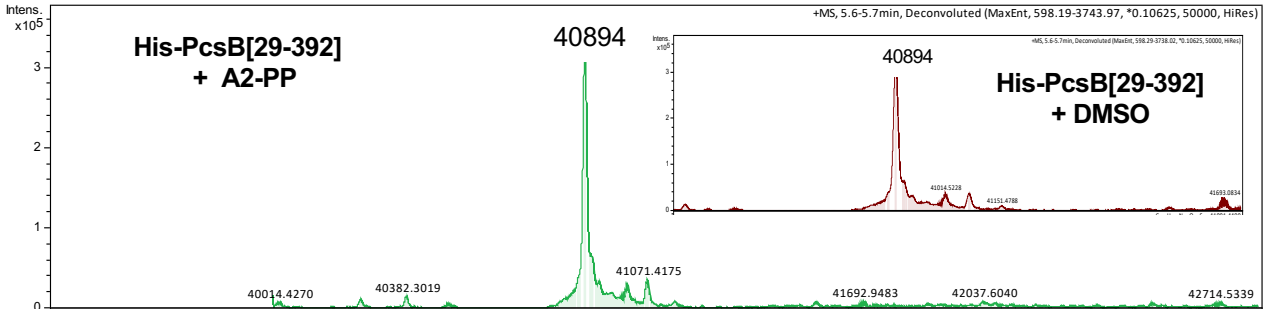

Figure 3.34 In vitro crosslinking with His-PcsB

For binding site mapping, samples were subjected to proteolytic digestion with trypsin and submitted for LC-MS/MS analysis. The spectra obtained from tryptic digest were searched by Sequest HT and Byonic against the known PcsB sequence. As expected, peptide fragments with the correct mass increase were identified in the PcsB-His sample, but not the N-terminally tagged protein. It is important to note that all peptides were medium confidence. To improve this signal of the peptide fragments with a crosslink, our sample can be enriched with the crosslinked adducts. This can be accomplished using biotin azide, which can be coupled to the terminal alkyne in the probe.

Generally, crosslinking was observed near the active site and on the periphery of the active site, which is expected since the probe sidechain is elongated relative to **A2** (Figure 3.35, pink

residues). Another cluster of crosslinking sites (bottom right hand corner Figure 3.35) is in a region containing a hydrophobic leucine zipper, which could attract the hydrophobic macrocycle. Not only does this region play important stabilizing roles for the catalytic domain, but it also plays a role in opening the cavity toward the active conformation; in *vivo*, this is accomplished in concert with FtsX via PPIs.

Molecular docking was investigated to see if the crosslinking sites could be explained, and to explore the potential binding interactions with **A2**. Docking was conducted using the Glide docking module of Maestro (Schrödinger suite) in extra-precision (XP) mode. Docking was limited to the catalytic site based on the cocrystalized PEG ligand, precluding the justification for more peripheral crosslinks. However, the two docking poses with the best XP Glide score can provide some explanation for our results (scores imbedded in figures). The first conformation places the diazirine into the catalytic pocket toward the cluster with the most crosslinking sites. The second conformation places the diazirine facing outward, but in proximity to two of the crosslinking sites, Ser359 and Glu360, the latter residue is part of the catalytic triad.

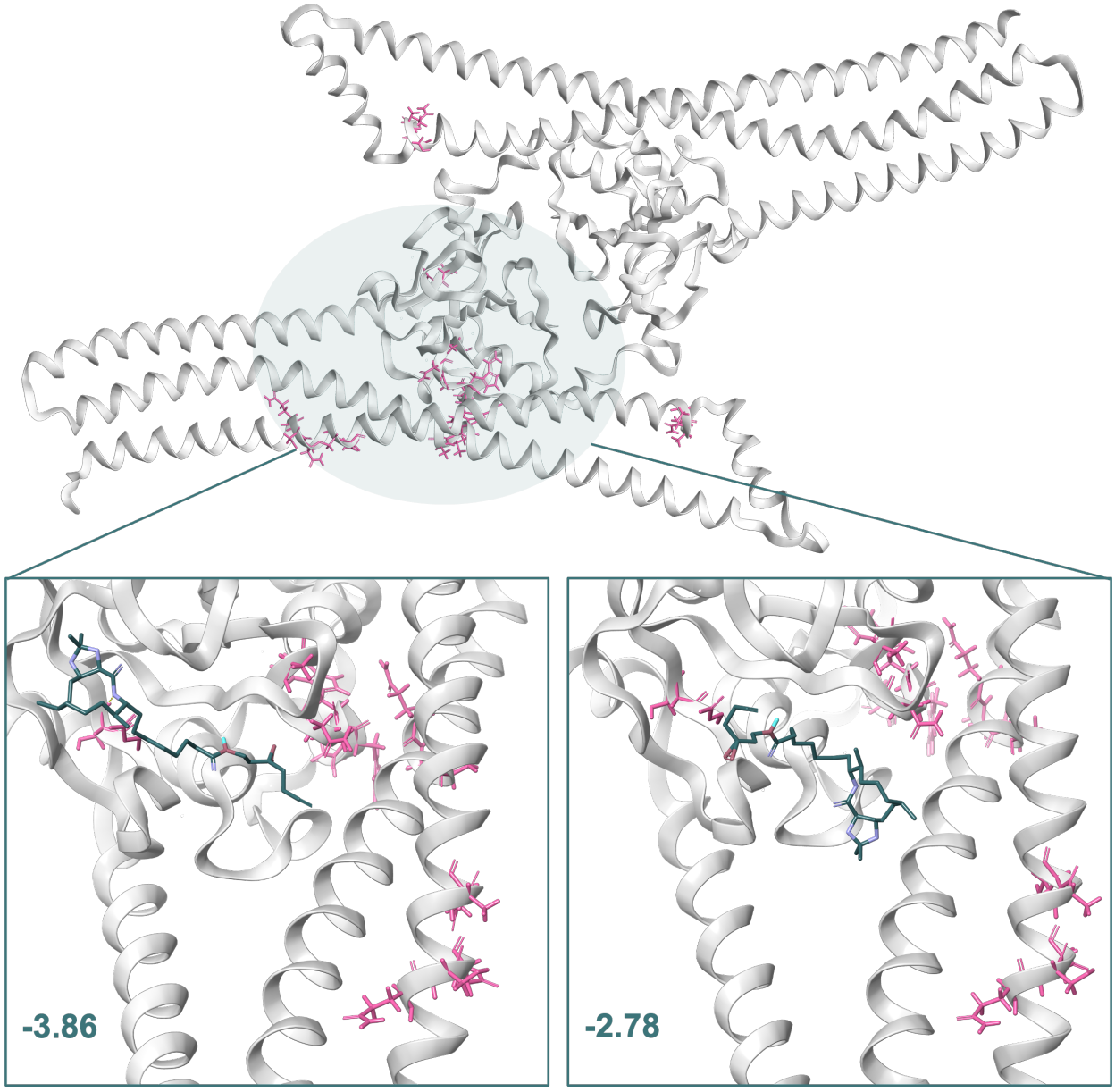

Figure 3.35 Docking and crosslinking site of A2-PP

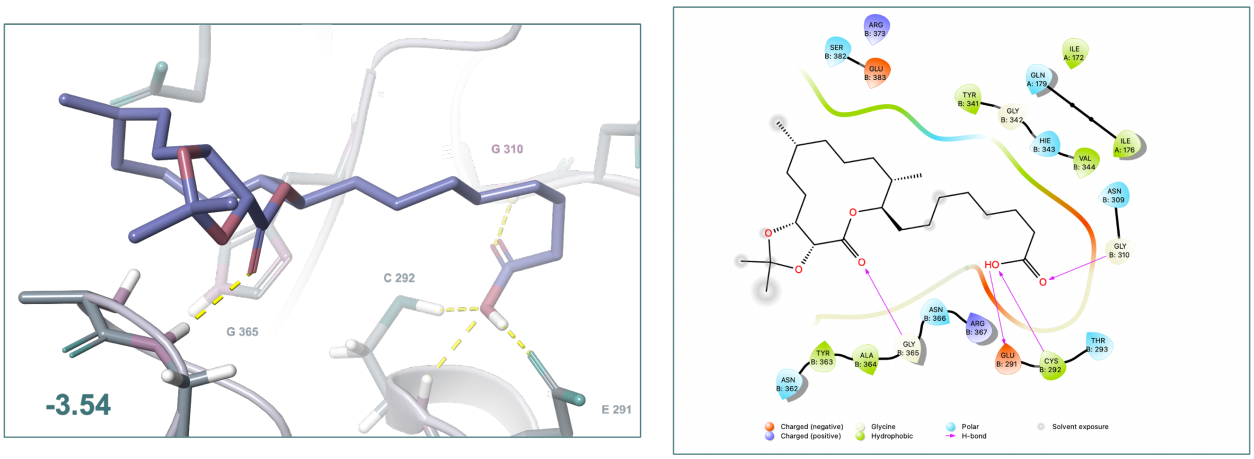

Figure 3.36 Docking with A2

The pose with the best docking score for **A2** places the alkyl chain into the catalytic pocket, priming the terminal carboxylic acid for key hydrogen bonding interactions (Figure 3.36). Key contacts are present between the carbonyl of **A2** and Gly310, the hydroxyl oxygen of **A2** and a Cys292 backbone hydrogen, as well as the hydrogen directly bonded to the catalytic sulfur in Cys292 and the carbonyl of **A2**. Additional contacts are present between Glu291 and the carboxylic acid proton, and the lactone carbonyl and Gly365. A similar binding mode was observed when Chou, et al. examined the docking results with a minimal peptide ligand, L-alanyl-γ-D-glutamyl-mesodiaminopimelic acid (L-Ala-D-Glu-mDAP) and Tse1, a peptidoglycan amidase.[189] Other poses with lower docking scores revealed an alternative binding orientation wherein the macrocyclic lactone is placed near the catalytic C292 (not shown).

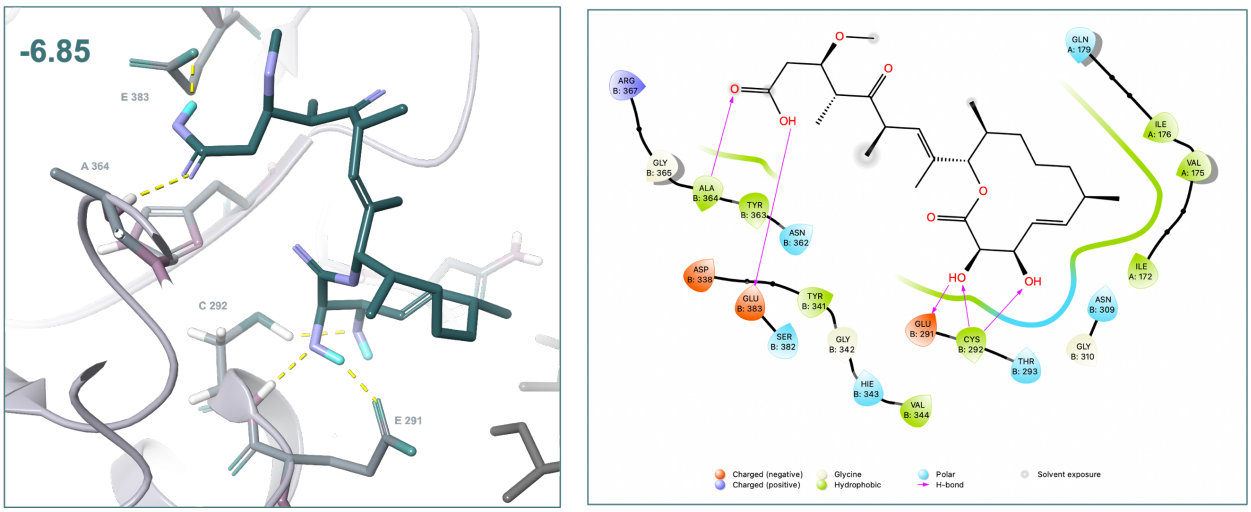

Figure 3.37 Docking with carolacton (pose 1)

A reverse trend was observed for carolacton. The poses with the best XP glide scores place the macrocycle lactone carbonyl in the catalytic pocket near the catalytic Cys292 (Figure 3.37). Another posing with a slightly lower score places the sidechain carbonyl into the pocket, like **A2** (Figure 3.38). Notably, the carolacton poses scored better than A2. This suggests that if both compounds directly interact with GbpB to mediate their activity, other factors must be contributing to A2's enhanced bioactivity, such as the ability to reach the target.

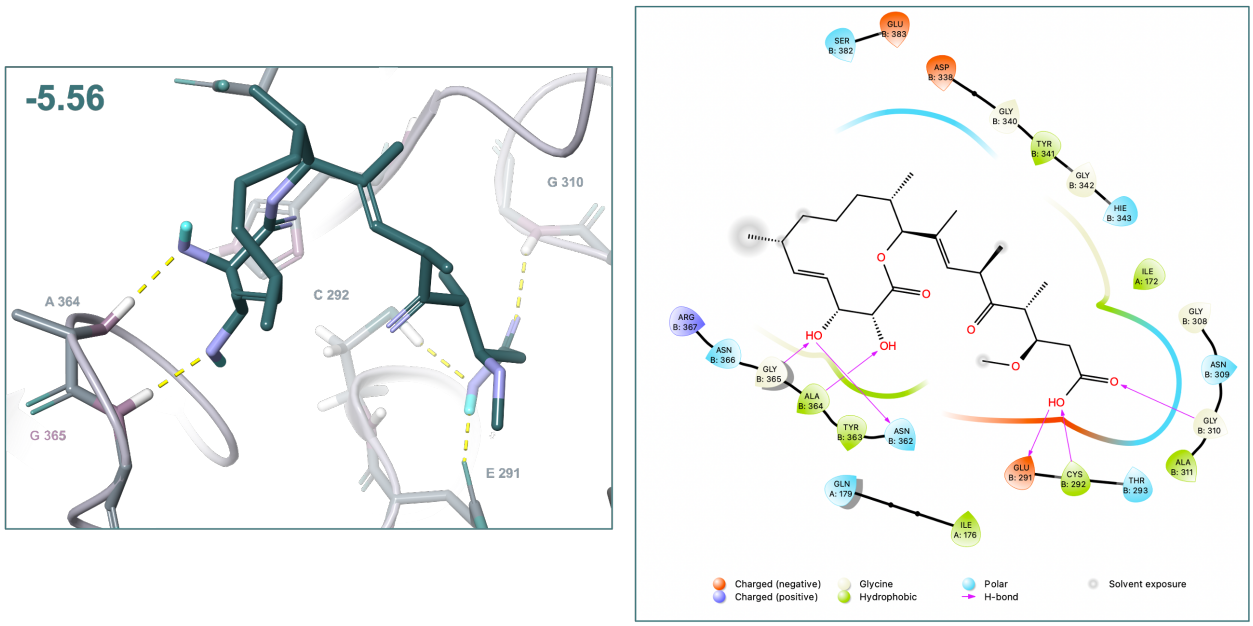

Figure 3.38 Figure 3.38 Docking with carolacton (pose 2)

3.9 Hydrolase assay development

Hydrolase activity has not been demonstrated at all for GbpB and has only been proven for a truncated version of PcsB that only contained the catalytic domain. For the truncated PcsB protein, they used a zymography assay where pneumococcal cells were incorporated into an SDS-PAGE gel.[190] They used for protein separation with either an activate CHAP protein, or a mutated CHAP protein (C292A). They saw clearing zones with the normal truncated protein, but not with the mutated protein. This is good evidence, but zymography assays are often misinterpreted, and are known for false positives.[191] The reason hydrolase activity is only observed in the truncated protein is likely on account of the locked conformation of the monomer wherein the N-terminal coiled-coiled (CC) domain is tucked into the catalytic domain at the C-terminus. They also conducted in solution studies, which would allow more flexibility, but they did not find evidence of muropeptide fragmentation using LCMS analysis. It is possible that the conditions are not conducive to hydrolase activity of this enzyme.

The Walker lab at the Harvard Medical School has designed numerous assays to study cell wall hydrolases which have enabled major advancements in our understanding of cell wall biochemistry. I had the opportunity of working in training under a MD/PhD student, Julia Page, from the Walker lab to begin applying their assays to study PcsB and **A2** inhibition. The first assay relies on pre-labeling the lysine on the side chain with a fluorophore. I had concerns about the fluorophore being placed on the lysine in the stem peptide since PcsB is hypothesized to cleave between the lysine and the glutamic acid residues, and the large size of ATTO488 may hinder this reaction.[190] As such, we simultaneously explored a post-labeling strategy that they had developed previously.

In the pre-labeling assay, they use isolated lipid II that was extracted from *S. pneumoniae* and react it with an N-hydroxysuccinimide ester ligated to ATTO488, a fluorescent molecule (Figure 3.39). Subsequently, the labelled lipid II is polymerized using the glycosyltransferase SgtB, which recognizes a diverse range of stem peptides. Incubation with and without the hydrolase of interest followed by SDS-PAGE analysis allows for fluorescent visualization of proteolytical cleavage.

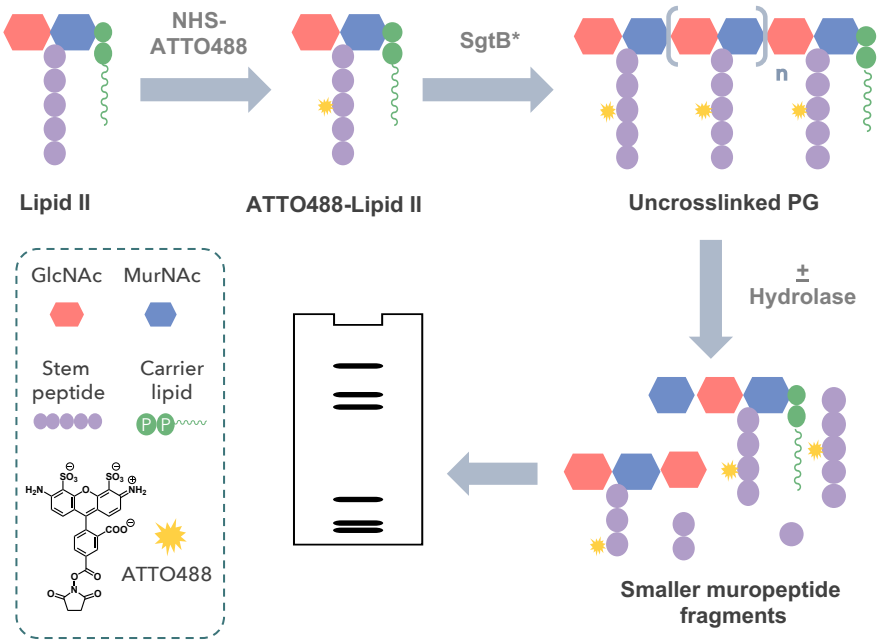

Figure 3.39 ATTO-488 hydrolase assay

Since the metal dependence of PcsB is unknown, we included magnesium, zinc, and calcium. We also conducted the assay using two different pH values, 7.5 and 6.1. Hydrolase activity is represented by the presence of tighter spaced bands with decreased signal intensity, as well as the emergence of a band in the middle of the gel that represents the released stem peptide, as shown with the positive control LytH/ActH (Figure 3.40, lane 3). Under these conditions, we did not observe hydrolase activity with the full-length protein tagged at either termini, or the truncated protein.

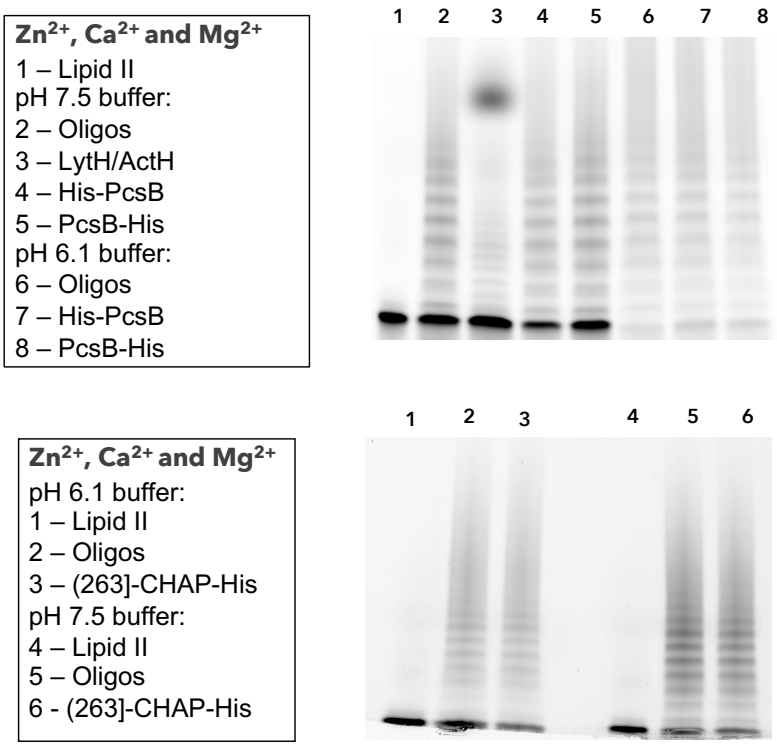

Figure 3.40 ATTO-488 pre-labeling assay with zinc, magnesium, and calcium

We later found literature precedent that zinc can inhibit CHAP domains, so we decided to test for hydrolase activity with either just magnesium or just calcium. In the pre-labeling assay, hydrolase activity was still not observed (Figure 3.41). Julia Page ran this experiment.

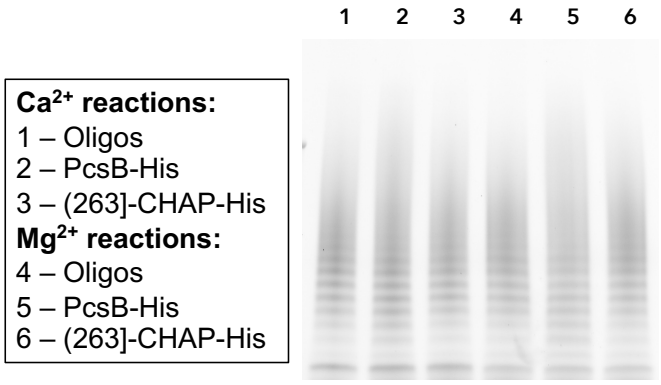

Figure 3.41 ATTO-488 pre-labeling assay with magnesium or calcium

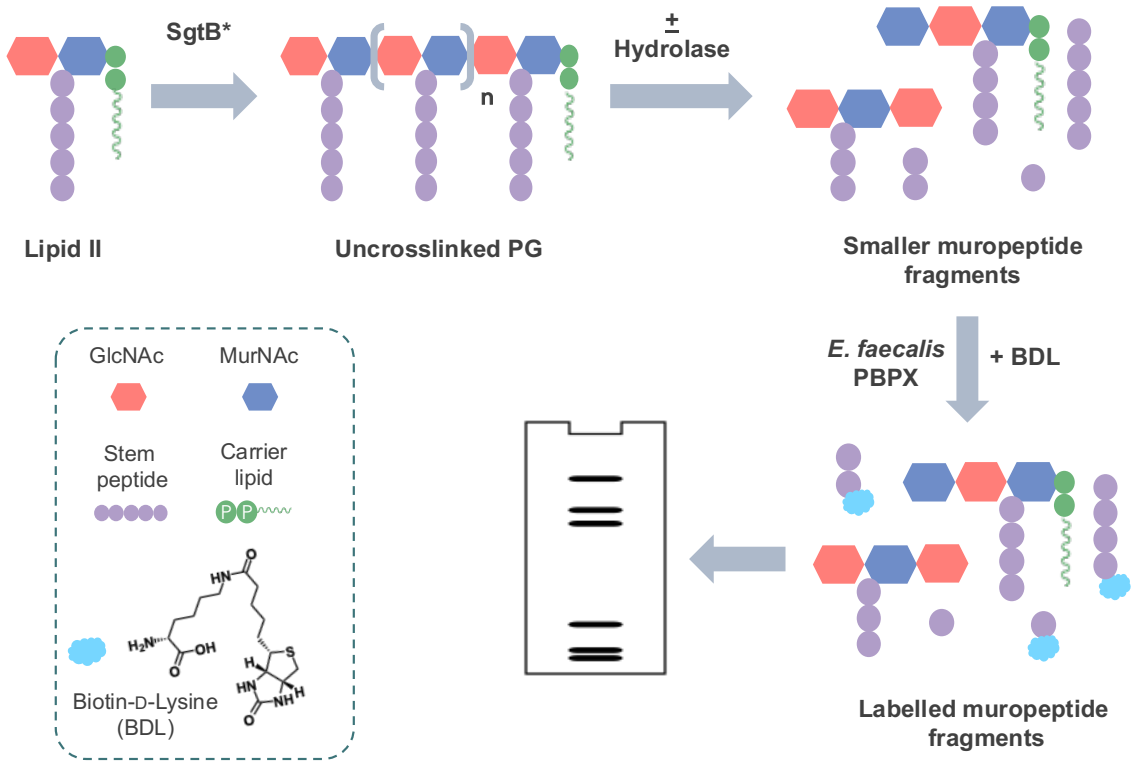

Figure 3.42 BDL hydrolase assay

For the post-labeling assay that we explored, lipid II polymerization is carried out with SgtB, and the samples are incubated with or without the hydrolase of interest (Figure 3.42). Subsequently, the muropeptides are reacted in an amino acid exchange reaction. The Walker lab previously identified a class of penicillin binding protein from *Enterococcus faecalis* was found to catalyze the exchange of the terminal D-alanine on lipid II with biotin-D-lysine, without catalyzing any background reactions. SDS-PAGE and Western blotting allows for visualization of BDL intensity. A reduction in intensity suggests the hydrolase is active.

When tested with all three metals under the post-labeling conditions and found that PcsB in the full-length form nor the truncated form showed catalytic activity (Figure 3.43). Like the pre-labeling assay, the zinc could be inhibiting catalytic activity.

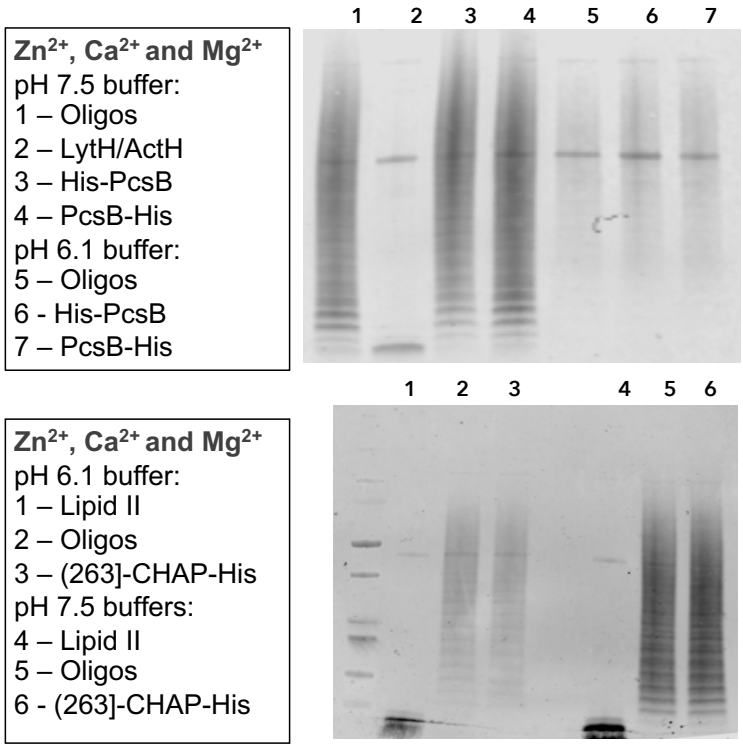

Figure 3.43 BDL post-labeling assay with zinc, magnesium, and calcium

We then ran the assays either calcium or magnesium. To our gratification both the full length and the CHAP domain exhibited hydrolase activity (Figure 3.44), as evidenced by the lighter bands relative to the oligo lanes (lanes 2 & 5) Intriguingly, the full-length protein demonstrated similar activity under both reaction conditions. The CHAP domain also exhibited activity in both, but activity was better in the magnesium reaction. Julia Page conducted the experiments shown in Figure 3.44.

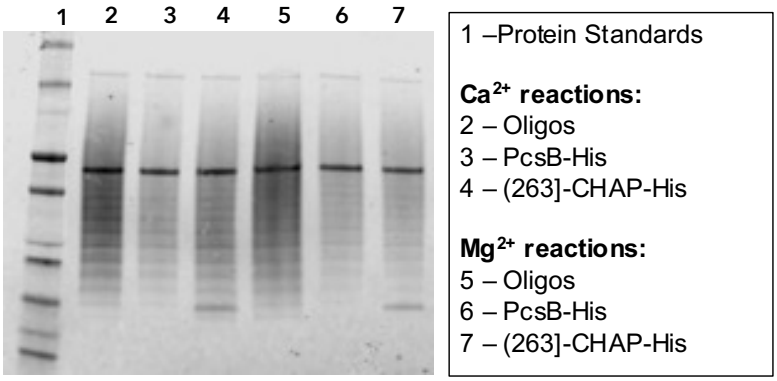

Figure 3.44 BDL post-labeling assay with calcium or magnesium

Interestingly, we would assume that full length hydrolase activity was observed due to the His-tag induced destabilization of the inactive monomer, but we have observed activity for both the N-tagged protein and the C-tagged protein. We are in the process of confirming that these results are valid and not just an artifact using catalytically inactive mutants (C292A). Moreover, since the signal is still low, we are still optimizing this assay by testing different temperatures, times, and exploring crosslinked substrates. The latter area proves more challenging because each strain can vary in their stem peptides and crosslinks, and isolation of lipid II is not trivial. Additionally, finding a compatible enzyme to facilitate lipid II crosslinking can be difficult. We are also exploring time course studies as well as zymography using peptidoglycan sacculi to have crosslinked substrates.

3.10 Conclusions and future work

Herein, I described a multi-faceted approach to elucidating and validating the molecular target of **A2**, a simplified carolacton mimic. Through a comprehensive investigation that I spearheaded, we identified GbpB/PcsB, as the primary cellular target responsible for the activity of this pharmacophore in gram positive streptococci, rendering **A2** as the first inhibitor of an essential bacterial cell wall hydrolase. Furthermore, we demonstrated hydrolase activity with full

length PcsB for the first time. This finding establishes a foundation for screening for novel inhibitors.

Finding the balance between necessary hydrolysis for cell wall elongation and overactive lytic activity is difficult, and bacteria have developed complex regulatory systems to maintain homeostasis. This work highlights the druggability of these complex systems and highlights the untapped potential of bacterial hydrolases as antibiotic targets. This study lays the foundation for additional chemical probe design and investigation into this essential class of cell wall CHAP hydrolases. Application of these tools can illuminate the biochemistry underlying cell wall division in gram positive streptococci and facilitate discovery of methods to circumvent current antibiotic resistance mechanisms.

3.11 References

(174) Sato, S.; Murata, A.; Shirakawa, T.; Uesugi, M. Biochemical Target Isolation for Novices: Affinity-Based Strategies. *Chemistry & Biology* **2010**, *17* (6), 616–623. https://doi.org/https://doi.org/10.1016/j.chembiol.2010.05.015.

(175) Medvedev, A.; Kopylov, A.; Buneeva, O.; Zgoda, V.; Archakov, A. Affinity-Based Proteomic Profiling: Problems and Achievements. *PROTEOMICS* **2012**, *12* (4–5), 621–637. https://doi.org/10.1002/pmic.201100373.

(176) Chen, X.; Wang, Y.; Ma, N.; Tian, J.; Shao, Y.; Zhu, B.; Wong, Y. K.; Liang, Z.; Zou, C.; Wang, J. Target Identification of Natural Medicine with Chemical Proteomics Approach: Probe Synthesis, Target Fishing and Protein Identification. *Signal Transduction and Targeted Therapy* **2020**, *5* (1), 72. https://doi.org/10.1038/s41392-020-0186-y.

(177) Rauniyar, N.; Yates, J. R. Isobaric Labeling-Based Relative Quantification in Shotgun Proteomics. *Journal of Proteome Research* **2014**, *13* (12), 5293–5309. https://doi.org/10.1021/pr500880b.

(178) Hsu, J.-L.; Huang, S.-Y.; Chow, N.-H.; Chen, S.-H. Stable-Isotope Dimethyl Labeling for Quantitative Proteomics. *Analytical Chemistry* **2003**, *75* (24), 6843–6852. https://doi.org/10.1021/ac0348625.

(179) Cox, J.; Hein, M. Y.; Luber, C. A.; Paron, I.; Nagaraj, N.; Mann, M. Accurate Proteome-Wide Label-Free Quantification by Delayed Normalization and Maximal Peptide Ratio Extraction, Termed MaxLFQ. *Mol Cell Proteomics* **2014**, *13* (9), 2513–2526. https://doi.org/10.1074/mcp.M113.031591.

(180) van Rooden, E. J.; Florea, B. I.; Deng, H.; Baggelaar, M. P.; van Esbroeck, A. C. M.; Zhou, J.; Overkleeft, H. S.; van der Stelt, M. Mapping in Vivo Target Interaction Profiles of Covalent Inhibitors Using Chemical Proteomics with Label-Free Quantification. *Nature Protocols* **2018**, *13* (4), 752–767. https://doi.org/10.1038/nprot.2017.159.

(181) Li, Z.; Hao, P.; Li, L.; Tan, C. Y. J.; Cheng, X.; Chen, G. Y. J.; Sze, S. K.; Shen, H.-M.; Yao, S. Q. Design and Synthesis of Minimalist Terminal Alkyne-Containing Diazirine Photo-

Crosslinkers and Their Incorporation into Kinase Inhibitors for Cell- and Tissue-Based Proteome Profiling. *Angewandte Chemie International Edition* **2013**, *52* (33), 8551–8556. https://doi.org/10.1002/anie.201300683.

(182) Keohane, C. E.; Steele, A. D.; Fetzer, C.; Khowsathit, J.; van Tyne, D.; Moynié, L.; Gilmore, M. S.; Karanicolas, J.; Sieber, S. A.; Wuest, W. M. Promysalin Elicits Species-Selective Inhibition of Pseudomonas Aeruginosa by Targeting Succinate Dehydrogenase. *J Am Chem Soc* **2018**, *140* (5), 1774–1782. https://doi.org/10.1021/jacs.7b11212.

(183) Hübner, I.; Shapiro, J. A.; Hoßmann, J.; Drechsel, J.; Hacker, S. M.; Rather, P. N.; Pieper, D. H.; Wuest, W. M.; Sieber, S. A. Broad Spectrum Antibiotic Xanthocillin X Effectively Kills Acinetobacter Baumannii via Dysregulation of Heme Biosynthesis. *ACS Cent Sci* **2021**, *7* (3), 488–498. https://doi.org/10.1021/acscentsci.0c01621.

(184) Mattos-Graner, R. O.; Jin, S.; King, W. F.; Chen, T.; Smith, D. J.; Duncan, M. J. Cloning of the Streptococcus Mutans Gene Encoding Glucan Binding Protein B and Analysis of Genetic Diversity and Protein Production in Clinical Isolates. *Infect Immun* **2001**, *69* (11), 6931–6941. https://doi.org/10.1128/IAI.69.11.6931-6941.2001.

(185) Cutrona, N.; Gillard, K.; Ulrich, R.; Seemann, M.; Miller, H. B.; Blackledge, M. S. From Antihistamine to Anti-Infective: Loratadine Inhibition of Regulatory PASTA Kinases in Staphylococci Reduces Biofilm Formation and Potentiates β-Lactam Antibiotics and Vancomycin in Resistant Strains of Staphylococcus Aureus. *ACS Infectious Diseases* **2019**. https://doi.org/10.1021/acsinfecdis.9b00096.

(186) Scheuermann, T. H.; Padrick, S. B.; Gardner, K. H.; Brautigam, C. A. On the Acquisition and Analysis of Microscale Thermophoresis Data. *Analytical Biochemistry* **2016**, *496*, 79–93. https://doi.org/10.1016/J.AB.2015.12.013.

(187) Jerabek-Willemsen, M.; André, T.; Wanner, R.; Roth, H. M.; Duhr, S.; Baaske, P.; Breitsprecher, D. MicroScale Thermophoresis: Interaction Analysis and Beyond. *Journal of Molecular Structure* **2014**, *1077*, 101–113. https://doi.org/https://doi.org/10.1016/j.molstruc.2014.03.009.

(188) Bartoschik, T.; Galinec, S.; Kleusch, C.; Walkiewicz, K.; Breitsprecher, D.; Weigert, S.; Muller, Y. A.; You, C.; Piehler, J.; Vercruysse, T.; Daelemans, D.; Tschammer, N. Near-Native, Site-Specific and Purification-Free Protein Labeling for Quantitative Protein Interaction Analysis by MicroScale Thermophoresis. *Sci Rep* **2018**, *8* (1), 4977. https://doi.org/10.1038/s41598-018-23154-3.

(189) Chou, S.; Bui, N. K.; Russell, A. B.; Lexa, K. W.; Gardiner, T. E.; LeRoux, M.; Vollmer, W.; Mougous, J. D. Structure of a Peptidoglycan Amidase Effector Targeted to Gram-Negative Bacteria by the Type VI Secretion System. *Cell Reports* **2012**, *1* (6), 656–664. https://doi.org/10.1016/j.celrep.2012.05.016.

(190) Bartual, S. G.; Straume, D.; Stamsås, G. A.; Muñoz, I. G.; Alfonso, C.; Martínez-Ripoll, M.; Håvarstein, L. S.; Hermoso, J. A. Structural Basis of PcsB-Mediated Cell Separation in Streptococcus Pneumoniae. *Nature Communications* **2014**, *5*, 3842. https://doi.org/10.1038/ncomms4842.

(191) Escobar, C. A.; Cross, T. A. False Positives in Using the Zymogram Assay for Identification of Peptidoglycan Hydrolases. *Analytical Biochemistry* **2018**, *543*, 162–166.

4 Progress toward the total synthesis of α-santal-11-en-10-one

4.1 Introduction

4.1.1 Porphyromonas gingivalis

Periodontal disease is a complex oral disease that affects over half of the US population and the leading cause of tooth loss.[192] This disease state is characterized by the inflammatory state of the gingiva caused by dental plaque, or biofilms, ultimately leading to tissue and bone destruction. Further, there is a risk for oral pathogens to enter the bloodstream and cause additional health problems, such as cardiovascular disease. The keystone pathogen associated with periodontal disease is *Porphyromonas gingivalis.*[192,193] This bacterium is a non-motile, Gram-negative, obligate anaerobe that resides in the subgingival niche with a small portion of other species.

4.1.2 *P. gingivalis* pathogenicity

P. gingivalis typically exists in a biofilm and produces an array of virulence factors including metabolites, fimbriae, and proteolytic enzymes. Gingipains, a class of proteolytic enzymes, are the major contributors to pathogenicity.[194,195] With a hand in cellular attachment, nutrient acquisition, and host defense evasion, these enzymes are essential for virulence and biofilm formation, making them potential antibiotic targets. The cysteine active site, like in the enzyme classes above, provide a potential moiety for covalent inhibition. Unlike most bacteria, *P. gingivalis* lacks the machinery to produce siderophores to obtain heme, thereby primarily relying on gingipain activity (Figure 4.1). This bacterium requires heme for growth, and it has been shown that heme is critical in biofilm formation, but this connection remains fragmented.[193,196,197] Targeting this virulence factor is a feasible avenue to explore this important connection and therapeutic development. Additionally, gingipains have been implicated in bacterial attachment to epithelial cells and other bacteria. By disrupting this process, biofilm formation will be perturbed

leading to easier removal. Interestingly, gingipain inhibitors are being examined in Alzheimer's studies.[198]

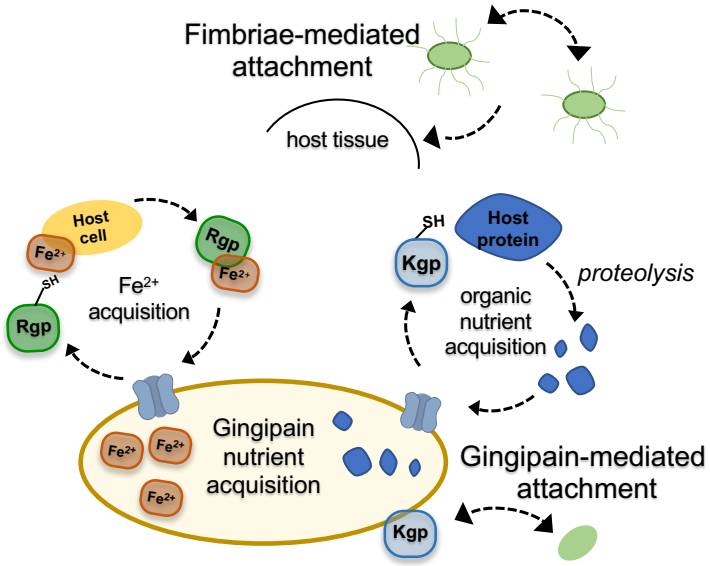

Figure 4.1 *P. gingivalis* virulence

Fimbriae, another virulence factor in *P. gingivalis*, also facilitate attachment and biofilm formation. Additionally, they are involved in cell motility, transport of proteins and DNA, and invasion of host cells.[195,199] These polymers have been shown to work through hydrophobic contacts.[200] Disrupting fimbriae function via hydrophobic interactions is another viable route for inhibiting biofilm formation and *P. gingivalis* virulence.

4.2 Santalene-sesquiterpenoids – isolation and bioactivity

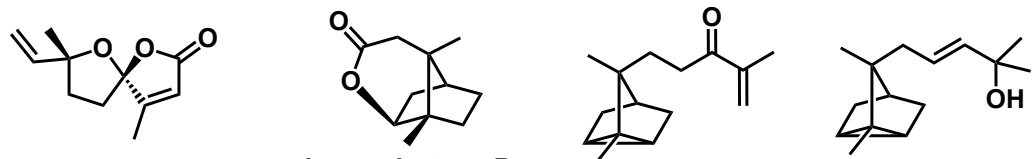

Lanceolactone A (4.1) **Lanceolactone B (4.2)** **4.3** **4.4**

Figure 4.2 Santalene-type sesquiterpenoids isolated from *Illicium lanceolatum*

In 2015, two new santalene-type sesquiterpenoids, Lanceolactone A (**4.1**) and Lanceolactone B (**4.2)** in addition to two known compounds, **4.3** and **4.4**, were isolated from the leaves of *Illicium lanceolatum* (Figure 4.2).[201] The authors carried out a small screen against a panel of oral bacteria, including *S. mutans, P. gingivalis*, *S. mitis, S. oralis,* and *S. sobrinus.* Only **4.3** demonstrated inhibitory activity against two strains, *S. mutans* (20 μg/mL) and *P. gingivalis (*10 μg/mL). The more potent activity against a Gram-negative strain over a Gram-positive strain caught our attention. Also, the fact that **4.3** is inactive against the Gram-positive commensal strains, *S. mitis*, *S. oralis*, and *S. sobrinus* is promising from a preventative and therapeutic standpoint since compound treatment would not decimate the oral flora. Moreover, it suggests a possibly unique mechanism tied to virulence. As many of the enzymes responsible for virulence contain a nucleophilic warhead, the accessible Michael-acceptor in **4.3** could function as an electrophilic trap. The role of the Michael acceptor in the mechanism is reenforced by the inactivity displayed by **4.4**. Covalent inhibition of would enable more direct target identification approaches and could be leveraged for use as a chemical tool. Additionally, because oral bacterial attachment is mediated through hydrophobic contacts it is likely that the highly hydrophobic nature of this tricycle interferes with these important interactions. The relatively simple structure of **4.3**, and the literature precedence for accessing similar scaffolds encouraged us to synthesize a panel of analogs for biological investigation. The goal of this work was to use this natural product scaffold as the foundation for optimizing its activity and using as a tool to study the biology of *P. gingivalis* and *S. mutans.*

4.3 Synthesis

4.3.1 Retrosynthetic plan

When we first looked at the molecule, we recognized the tricycle core that is present in other natural products such as the santalols, a common class used in fragrances (Figure 4.3). We chose to utilize the route most used to access this scaffold as a starting point.[202] This strategy

would include a one-step alkylation from bromotricycle **4.5**, which accessible in four steps from commercially available 3-endo-bromocamphor (**4.6**).

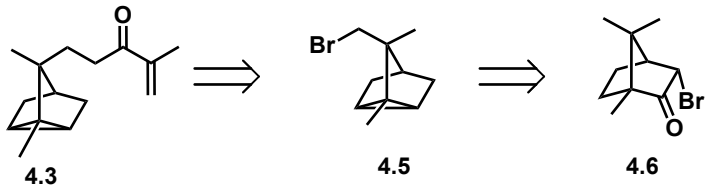

Figure 4.3 Retrosynthetic analysis of 4.3

4.3.2 Accessing the key intermediate

Starting with **4.6,** a bromination reaction yields 3,9-dibromocamphor (**4.7**) in 65% yield (Scheme 4.1). The low yield is due to over bromination at the same carbon. I deviated from Corey's synthesis for the bromine removal to avoid the use of unnecessary corrosive chemicals, like hydrobromic acid in addition to zinc. Instead, I opted to just use zinc, which selectively debrominated the α-bromine in 91% yield affording 9-bromocamphor **4.38**. Treatment with hydrazine under acidic conditions, followed a mercuric oxide catalyzed transformation provides **4.5**. While I have accessed this molecule in 73% over two steps, both steps have proven inconsistent and unreliable. For this reason, I explored alternative methods to form this key bond.

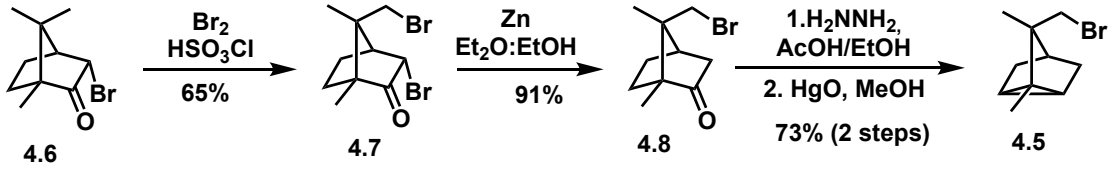

Scheme 4.1 Synthetic route to intermediate 4.5

To this end, I explored two different acid catalysts, Amberlyst 15 and a silica-supported heteropolyacid, namely molybdophosphoric acid (MPA).[203,204] The former catalyst has been shown to efficiently dehydrate tertiary alcohols, which made me wonder whether it could be

applied to the secondary alcohol in isoborneol (**4.9**). I conducted a preliminary solvent screen since solvent plays an important role in these reactions (Table 4.1). The reactions conducted in toluene and CH_2Cl_2 (DCM) produced <1% of product, whereas no product was formed with $CHCl_3$ and acetic acid (AcOH). The second route utilizes a silica-supported molybdophosphoric acid catalyst. I prepared the impregnated catalysis and screened reaction conditions. Notably, this reaction was successfully used on a similar scaffold to that of **4.7**. They found that reaction time and temperature can drastically alter the reaction outcome. When run at room temperature in $CHCl_3$, I observed less than 1% of product, but under all other conditions, no product was formed. Longer reaction times were explored but due to unforeseen circumstances, this route was put on hold. Both acid catalyzed methods demonstrated proof of concept with this scaffold, but additional screening is required to favor formation of the desired tricyclene **4.5.**

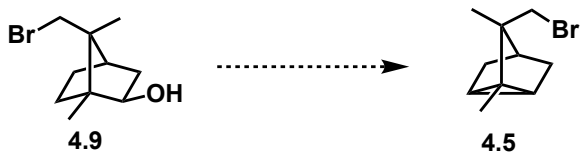

4.9 **4.5**

Entry	Catalyst	Catalyst load	Solvent	Temp (ºC)	Time (h)	Yield
1	Amberlyst 15	1.2 (w/w)	$CHCl_3$	rt	2	0%
2	Amberlyst 15	1.2 (w/w)	Toluene	rt	2	< 1%
3	Amberlyst 15	1.2 (w/w)	CH_2Cl_2	rt	2	<1 %
5	Amberlyst 15	1.2 (w/w)	AcOH	rt	2	0%
6	MPA/S	0.1	$CHCl_3$	rt	72	<1%
7	MPA/S	0.1	$CHCl_3$	reflux	16	0%
8	MPA/S	0.5	$CHCl_3$	rt	16	0%
9	MPA/S	1.0	$CHCl_3$	rt	16	0%
10	MPA/S	1.0	$CHCl_3$	reflux	16	0%
11	MPA/S	0.1	Toluene	rt	16	0%
10	MPA/S	0.1	Toluene	reflux	16	0%
12	MPA/S	1.0	Toluene	reflux	16	0%

Table 4.1 Tricyclene formation attempts

4.3.3 One-step alkylation attempts

I envisioned accessing the target compound in one step from intermediate **4.5**. The most straightforward strategy for this would be a direct carbon-carbon coupling with 3-methyl-3-buten-2-one **4.10** (Table 4.2). The neopentyl electrophile in **4.5** make direct substitution more challenging, but they have been observed with this scaffold. Moreover, the small size of **4.9** could potentially circumvent the steric restraints. I initially screened lithium diisopropylamide (LDA) with DMPU, as it has been successfully used in congested systems.[205] Even when freshly distilled diisopropylamine was used to prepare LDA, the reaction was not successful when a ratio of 1.2 to 1.0 of **4.5** to **4.1** is used. However, when the equivalence of **4.10** is increased to 3.1, I observed 1% of the desired product (**4.3**). Despite this small success, I felt that this method was not viable due to the reactivity of the ketone (**4.10**) and non-reactivity of the bromine (**4.5)**.

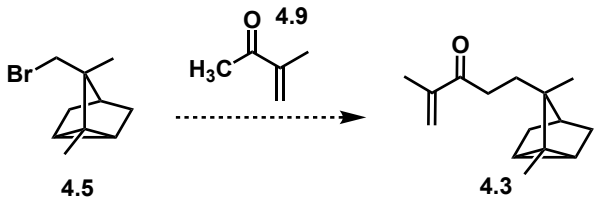

Entry	Base	Ratio of 4.5:4.9	Temp (°C)	Yield
1	LDA + DMPU	1:5	-78 → -50	NR
2	LDA	1.2:1.0	-78 → -10	NR
3	LDA (freshly distilled)	1.2:1.0	-78 → -10	NR
4	LDA (freshly distilled)	1.0:3.1	-78 → -10	<1%

Table 4.2 Enol alkylation routes

Scheme 4.2 Coupling reactions with 3-methyl-3-buten-2-one

To find the balance in reactivity, I switched to the silyl enol ether **4.10** (Table 4.3). They are generally less reactive and have shown great success in reactions that are not amenable to the

enolate. This has been particularly true when used with the lewis acid titanium tetrachloride ($TiCl_4$). This combination has facilitated the direct coupling of tertiary carbons. Unfortunately, none of the $TiCl_4$ mediated reactions were successful. It should be noted that the volatility of the TMS ether **4.10** made these reactions particularly challenging. A small screen of different lewis acid systems only demonstrated success in two instances (entries 4 and 9). When $ZnCl_2$ is activated on an aluminum oxide support and when silver nitrate is used, a small amount of product was formed. While these reactions could be explored further, the inability to yield more than 1% of product suggests that this route is not viable. As such, I sought out two step alkylation methods.

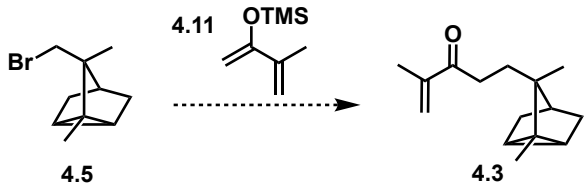

Entry	Lewis acid	Lewis acid equiv.	Solvent	Yield
1	$TiCl_4$	1.1	CH_2Cl_2	NR
2	TiCl4	3.0	CH_2Cl_2	NR
3	$TiCl_4$ (new bottle)	1.0	CH_2Cl_2	NR
4	$ZnCl_2$-Al_2O_3	1.0	N/A	<1%
5	Alumina (acidic)	5.3	CH_2Cl_2	NR
6	$ZnCl_2$ (not activated)	1.0	CH_2Cl_2	NR
7	$AlCl_3$	0.1	CH_2Cl_2	NR
8	Zn (purum)	2.0	DMF	NR
9	$AgNO_3$	0.1	CH_2Cl_2	<1 %

Table 4.3 TMS ether routes

4.3.4 Two-step alkylation routes

While there are numerous ways to access this scaffold in a multi-step way, since the one-step was not successful, I wanted to explore two two-step alkylation sequences. As such, I envisioned proceeding through two known natural products, α-santalol (**4.12)** and a-santalene (**4.13**), particularly since we are interested in their bioactivity as well (Scheme 4.3).[202,206] To

access **4.12**, I first attempted a lithium and triethylamine catalyzed substitution reaction. However, this reaction the crude reaction mixture and TLC contained a large assortment if byproducts. I then proceeded without the triethylamine as was done previously, and this reaction provided **4.12** in 22% yield by crude NMR. Subsequent purification was unsuccessful as there were numerous byproducts. This is likely due to decomposition of the epoxide starting material **4.13,** since the bottle I used was very old. I ordered a new bottle over a year ago, but we still have not received it. For that reason, I chose to pursue natural product **4.14** via a silver-catalyzed allylation reaction. This route allows for either reaction partner to be used as the Grignard. Since 3,3-allylbromide is commercially available, and I must synthesize tricyclene **4.5**, I proceeded with **4.16** as the Grignard. This reaction results in inconsistent ratios of **4.14** and **4.15.** Purification attempts were not very successful due to the similar polarity of these compounds. I was able to access about 2 milligrams to use in a subsequent test reaction.

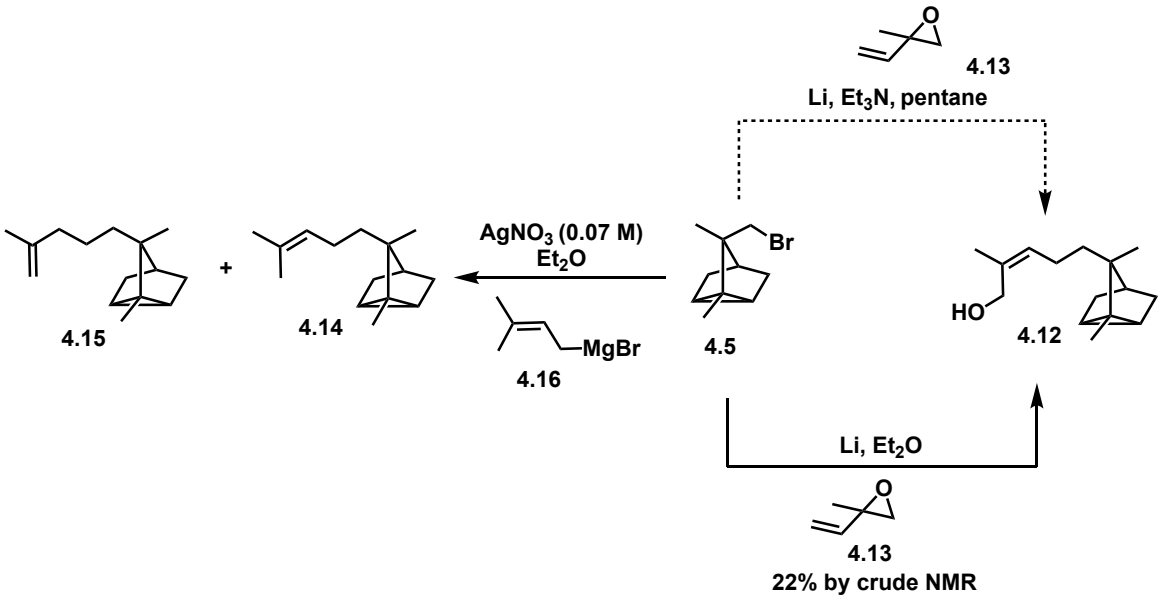

Scheme 4.3 Two-step alkylation routes

The alkene motif in **4.14** closely resembles a scaffold that was used to develop a catalytic oxygenative allylic transposition (Scheme 4.4).[207] Preliminary experiments were unsuccessful, but

it is likely due to incomplete formation of AZADO^{+}BF4^{-}. Optimization of the catalyst synthesis would render this method viable.

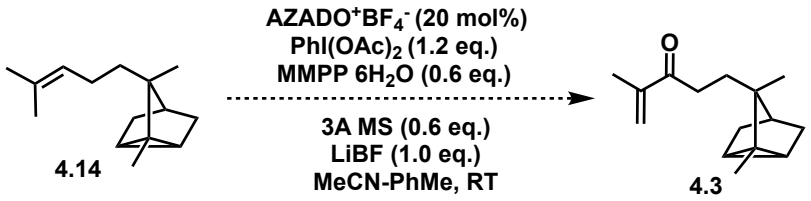

Scheme 4.4 Catalytic oxygenative allylic transposition

4.4 Conclusion and outlook

Herein I described the current progress toward α-santal-11-en-10-one (**4.3**). This molecule inhibits the growth of both *S. mutans* and *P. gingivalis* potentially through a novel mechanism. As such, I sought to synthesize this compound and carry out biological investigation. Though I did not successfully access the target molecule through the one step alkylation route, I believe that the two-step alkylation routes are viable options moving forward. Alternatively, a multistep sequence can be employed to access the target molecule.

4.5 References

(192) How, K. Y.; Song, K. P.; Chan, K. G. Porphyromonas Gingivalis: An Overview of Periodontopathic Pathogen below the Gum Line. *Front Microbiol* **2016**, *7*, 53. https://doi.org/10.3389/fmicb.2016.00053.

(193) Lamont, R. J.; Jenkinson, H. F. Life below the Gum Line: Pathogenic Mechanisms of Porphyromonas Gingivalis. *Microbiol Mol Biol Rev* **1998**, 1244–1263.

(194) Potempa, J.; Sroka, A.; Imamura, T.; Travis, J. Gingipains, the Major Cysteine Proteinases and Virulence Factors of Porphyromonas Gingivalis: Structure, Function and Assembly of Multidomain Protein Complexes. *Current Protein & Peptide Science* **2005**, 397–407. https://doi.org/10.2174/1389203033487036.

(195) Kuboniwa, M.; Amano, A.; Hashino, E.; Yamamoto, Y.; Inaba, H.; Hamada, N.; Nakayama, K.; Tribble, G. D.; Lamont, R. J.; Shizukuishi, S. Distinct Roles of Long/Short Fimbriae and Gingipains in Homotypic Biofilm Development by Porphyromonas Gingivalis. *BMC Microbiology* **2009**, *9* (1), 105. https://doi.org/10.1186/1471-2180-9-105.

(196) Dashper, S. G.; Ang, C. S.; Veith, P. D.; Mitchell, H. L.; Lo, A. W. H.; Seers, C. A.; Walsh, K. A.; Slakeski, N.; Chen, D.; Lissel, J. P.; Butler, C. A.; O'Brien-Simpson, N. M.; Barr, I. G.; Reynolds, E. C. Response of Porphyromonas Gingivalis to Heme Limitation in Continuous Culture. *Journal of Bacteriology* **2009**, *191* (3), 1044–1055. https://doi.org/10.1128/JB.01270-08.

(197) How, K. Y.; Song, K. P.; Chan, K. G. Porphyromonas Gingivalis: An Overview of Periodontopathic Pathogen below the Gum Line. *Frontiers in Microbiology*. 2016, p 53.
(198) Dominy, S. S.; Lynch, C.; Ermini, F.; Benedyk, M.; Marczyk, A.; Konradi, A.; Nguyen, M.; Haditsch, U.; Raha, D.; Griffin, C.; Holsinger, L. J.; Arastu-Kapur, S.; Kaba, S.; Lee, A.; Ryder, M. I.; Potempa, B.; Mydel, P.; Hellvard, A.; Adamowicz, K.; Hasturk, H.; Walker, G. D.; Reynolds, E. C.; Faull, R. L. M.; Curtis, M. A.; Dragunow, M.; Potempa, J. Porphyromonas Gingivalis in Alzheimer's Disease Brains: Evidence for Disease Causation and Treatment with Small-Molecule Inhibitors. *Science Advances* **2019**. https://doi.org/10.1126/sciadv.aau3333.
(199) Enersen, M.; Nakano, K.; Amano, A. Porphyromonas Gingivalis Fimbriae. *J Oral Microbiol* **2013**, *5*, 10.3402/jom.v5i0.20265. https://doi.org/10.3402/jom.v5i0.20265.
(200) Naito, Y.; Tohda, H.; Okuda, K.; Takazoe, I. Adherence and Hydrophobicity of Invasive and Noninvasive Strains of Porphyromonas Gingivalis. *Oral Microbiology and Immunology* **1993**, *8* (4), 195–202. https://doi.org/10.1111/j.1399-302X.1993.tb00559.x.
(201) Kubo, M.; Nishikawa, Y.; Harada, K.; Oda, M.; Huang, J. M.; Domon, H.; Terao, Y.; Fukuyama, Y. Tetranorsesquiterpenoids and Santalane-Type Sesquiterpenoids from Illicium Lanceolatum and Their Antimicrobial Activity against the Oral Pathogen Porphyromonas Gingivalis. *Journal of Natural Products* **2015**, *78* (6), 1446–1449. https://doi.org/10.1021/acs.jnatprod.5b00237.
(202) Corey, E. J.; Chow, S. W.; Scherrer, R. A. The Synthesis of α-Santalene and of Trans-Δ11,12-Iso-α-Santalene. *J Am Chem Soc* **1957**, *79* (21), 5773–5777. https://doi.org/10.1021/ja01578a049.
(203) Vázquez, P.; Pizzio, L.; Cáceres, C.; Blanco, M.; Thomas, H.; Alesso, E.; Finkielsztein, L.; Lantaño, B.; Moltrasio, G.; Aguirre, J. Silica-Supported Heteropolyacids as Catalysts in Alcohol Dehydration Reactions. *Journal of Molecular Catalysis A: Chemical* **2000**, *161* (1), 223–232. https://doi.org/https://doi.org/10.1016/S1381-1169(00)00346-0.
(204) Frija, L. M. T.; Afonso, C. A. M. Amberlyst®-15: A Reusable Heterogeneous Catalyst for the Dehydration of Tertiary Alcohols. *Tetrahedron* **2012**, *68* (36), 7414–7421. https://doi.org/https://doi.org/10.1016/j.tet.2012.06.083.
(205) Snider, B. B.; Kiselgof, J. Y.; Foxman, B. M. Total Syntheses of (±)-Isosteviol and (±)-Beyer-15-Ene-3β,19-Diol by Manganese(III)-Based Oxidative Quadruple Free-Radical Cyclization. *The Journal of Organic Chemistry* **1998**, *63* (22), 7945–7952. https://doi.org/10.1021/jo981238x.
(206) Hasegawa, T.; Izumi, H.; Tajima, Y.; Yamada, H. Structure-Odor Relationships of α-Santalol Derivatives with Modified Side Chains. *Molecules* **2012**, *17* (2), 2259–2270. https://doi.org/10.3390/molecules17022259.
(207) Nagasawa, S.; Sasano, Y.; Iwabuchi, Y. Catalytic Oxygenative Allylic Transposition of Alkenes into Enones with an Azaadamantane-Type Oxoammonium Salt Catalyst. *Chemistry - A European Journal* **2017**. https://doi.org/10.1002/chem.201702512

5 Quaternary Phosphonium Compounds

Chapter 5 has been adapted with permission from Sommers, K. J.; Michaud, M. E.; Hogue, C. E.; Scharnow, A. M.; Amoo, L. E.; Petersen, A. A.; Carden, R. G.; Minbiole, K. P. C.; Wuest, W. M. Quaternary Phosphonium Compounds: An Examination of Non-Nitrogenous Cationic Amphiphiles That Evade Disinfectant Resistance. *ACS Infect. Dis.* **2022**, *8* (2), 387–397. https://doi.org/10.1021/acsinfecdis.1c00611.

5.1 Quaternary ammonium compounds (QACs)

Quaternized antibacterials were discovered by the Rockefeller Institute in 1916 but weren't used as a disinfectant for another few decades.[208] Upon the advent of their use, quaternary ammonium compounds (QACs) rapidly became a staple antiseptic in domestic, agricultural, industrial, and clinical settings, and their popularity has persisted due to their broad-spectrum activity against a variety of microorganisms (bacteria, viruses, etc.).[209] Although these cationic compounds were known to be detrimental to the skin microbiome, its nonspecific mechanism, namely targeting the cell membrane, provided a false promise that this class would evade bacterial resistance development, enabling their continuous use.[210]

The amphiphilic nature of QACs is paramount to its function. The positively charged nitrogen head is electrostatically attracted to the negatively charged membrane surface (Figure 5.1). [211] Subsequent insertion of the nonpolar alkyl tail into the lipid bilayer and concomitant aggregation of the phospholipid bilayer induced by the cationic head results in loss of membrane integrity and cell lysis. [212,213]

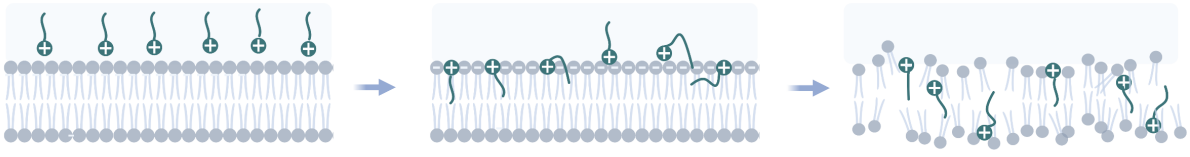

Figure 5.1 QAC mechanism of action

Unfortunately, tolerance was observed only 15 years after widespread usage, and genetic resistance 50 years after.[214,215] Alterations in membrane composition, biofilm formation, and

stimulation of the *qac* efflux systems are responsible for changes in QAC susceptibility. The presence of *qac* resistance genes (*qacAB*) not only confer tolerance to compound treatment, but also, their plasmid origins prime them for horizontal gene transfer (HGT), resulting in further spread of resistance.[216–220] Specifically, the unusually high degree of sequence conservation for *qacC* coupled with its aberrant location between the double-strand replication origin (DSO) and single-strand replication origin (SSO) on rolling-circle (RC) plasmids in the absence of mobilizing genetic elements, suggest that *Staphylococcus* populations may have recently evolved a new mechanism for the efficient horizontal transfer of the *qacC* gene. Moreover, the only other RC-plasmid gene currently suspected to involve a similar transfer mechanism is *lnuA*, a gene conferring resistance to lincosamides in *Staphylococcus* species, leading Wassenarr and coworkers to posit that this novel “DSO-gene-SSO” HGT mechanism may have been selected for through the use of disinfectants and antibiotics.[221] This hypothesis coincides with a multitude of studies investigating evolutionary selection for the spread of QAC resistance genes, as well as QAC-mediated co-resistance to antibiotics.[17,73–75] Furthermore, sub-inhibitory concentrations of QAC treatment have been shown to promote acquisition of both *qac* resistance and resistance genes associated with other antibiotics. Considering the coronavirus pandemic, this is particularly concerning since usage of QAC-based cleaning supplies has skyrocketed. Of the 558 disinfectant products currently listed by the EPA as effective against SARS-CoV-2, 260 (46.6%) list quaternary ammonium compounds (QACs) as an active ingredient.[222,223] As such, synthetic campaigns toward more potent and less toxic QACs are critical. The rapidly growing prevalence of antimicrobial resistance demands for renewed interest in the development of next-generation antibiotics and disinfectants, such as those disclosed herein

5.2 QACs in oral healthcare

Antiseptics including QACs are widely, and recklessly used in the dental industry. The QAC, cetylpyridinium chloride (CPC), is commonly used in mouth washes and toothpastes at low

concentrations.[106,224–226] Moreover, various QAC scaffolds, including the ubiquitous benzalkonium chloride (BAC) (have been used as antibacterials in dental materials.[227–229] When hard tissue needs replacement, composite resin materials are used as a replacement. This hard surface provides additional attachment sites for microbial biofilm formation that pose concern for the health of the oral cavity. To circumvent this problem, materials embedded with antibacterial and antifungal activity have been explored, including immobilized QACs on dental resins and nanoparticles, as well as in dental primers and adhesives.[228,229] These materials would provide a constant supply of low concentrations of active agent, allowing for the selection of resistance. Even more concerning is the coexistence of *qac* resistance genes and multidrug resistant genes on the same plasmid. A consequence of this would be the increased spread of AMR within the oral cavity and in oral biofilms. The biofilm nature poses an additional concern due to its increased propensity for horizontal gene transfer on account of the proximity of the densely packed cells.[230] The effects of this resistance selection are not limited to the oral cavity, since oral bacteria have been implicated in diseases spanning the body.[69,79,231]

To the best of my knowledge, only one study to the best of my knowledge has explored the connection between sub-MIC doses of CPC and other QAC-based materials in dental care and the evolution and spread of AMR.[208,225,228] While this study did not find any significant trends between resistance and CPC exposure on the oral microbiome, the study was limited to six weeks. Our use of dental materials drastically outlasts a six-week experiment. Furthermore, they did not explore phenotypic resistance or hetero-resistance possibilities, which has emerged as a major concern in AMR, particularly with QACs.

5.3 QAC diversification

In hopes of discovering new scaffolds that evade these resistance mechanisms and exhibit improved bioactivity and reduced cytotoxicity. These studies have focused on structure-activity and structure-resistance relationships in QACs, from which insights regarding the number and

ratio of charges, lengths and types of side chains, core structural rigidity, and (most recently) the inclusion of organometallic substituents have all contributed to the advancement of discovering next-generation QAC scaffolds.[210,232,233] Cationic heteroatom-based compounds beyond QACs have also been the subject of numerous studies, albeit far less. Trivalent sulfonium compounds (TSCs) and quaternary phosphonium compounds (QPCs) were recently the subject of a thorough review that detailed the collection of SAR investigations and highlight their promise as a solution to QAC-related resistance and toxicity.

5.4 Quaternary Phosphonium Compounds

Inspired by these previous works, we envisioned employing the knowledge gained from our previous QAC investigations to further probe the underrepresented class of QPCs. QPCs are characterized by their tetravalent phosphorous atom with a positive formal charge. They have served as anti-tumor agents,[234,235] catalysts,[236] and mitochondrial antioxidants[7] Additionally, polymeric QPCs have been utilized as surfactants, water desalination agents, and most importantly, antimicrobials.[237–240] Notably, QPC-based polymers have shown enhancements in activity relative to their nitrogen counterparts.[241–245] Few structure activity relationship investigations have been pursued, but factors such as the number of hydrophobic tails and saturation within the hydrocarbon chain have been explored for some scaffolds. These investigations highlighted the importance of alkyl chain length, as well as the quantity of alkyl ligands. When longer chain lengths are used, less alkyl ligands are necessary, but as you increase the number of alkyl substituents on the phosphorous center, shorter alkyl lengths display improved activity. These results further enforce the notion that optimizing the ratio of polar to nonpolar character is a major determinant of antimicrobial activity of quaternized scaffolds.[246–249] Despite their promising antimicrobial activity, QPCs remain an underexplored class of disinfectants, making them prime candidates for further study. This work focuses on the development of new QPC analogs to discover improved antibacterials that lack QAC-like resistance profiles.

Leveraging our understanding of QAC SAR in conjunction with previous work on QPCs, we set out to synthesize a library of QPC analogs and interrogate their structure-activity and structure-resistance relationships. Through this work, we have revealed bis-cationic quaternary phosphonium compounds (bisQPCs) to be a potent broad-spectrum subclass of disinfectant molecules. Within this subclass, we unveiled a novel bis-QPC (P6P-10,10) with improved activity against both gram-positive and gram-negative species compared to two of the leading commercial QACs. Moreover, this compound was also effective against strains displaying *qpc* resistance, which we purport may arise due to the unique presence of the *qac* family efflux pump, QacC, revealed by bioinformatic analysis.

5.5 Preparation of the QPCs by the Minibole Lab

The Minibole lab was interested in identifying a core phosphine scaffold that could serve as a branching point to access a diverse library using facile alkylations. They envisioned that this may be achieved through quaternization of phenylphosphine compounds such as 1,3-bis(diphenylphosphino)propane (dppp) and triphenylphosphine (TPP). These were promising scaffolds due to their ubiquity in organic synthesis,[250,251] and relative air-stabilities.[252] Furthermore, previous studies have demonstrated promising antimicrobial activity for TPP derivatives against Gram-positive bacteria, although a systematic investigation into TPP-based QPC architectures remains unexplored.[253–257] Additionally, while several of these previously synthesized TPP derivatives have shown low micromolar antimicrobial activities, efflux pump-mediated resistance to TPP-derived QPCs has precluded their widespread utility.[258–260] They then began our investigations with the synthesis of TPP- and dppp-derived QPCs bearing hydrocarbon tails of varying lengths, seeking to interrogate whether increasing the amphiphilic and cationic nature of the QPCs may increase broad-spectrum antimicrobial activity and aid in the evasion of efflux-pump mediated resistance. They successfully accessed 59 synthetic QPCs using a facile alkylation reaction that required little medication and provided the desired products in good yields.

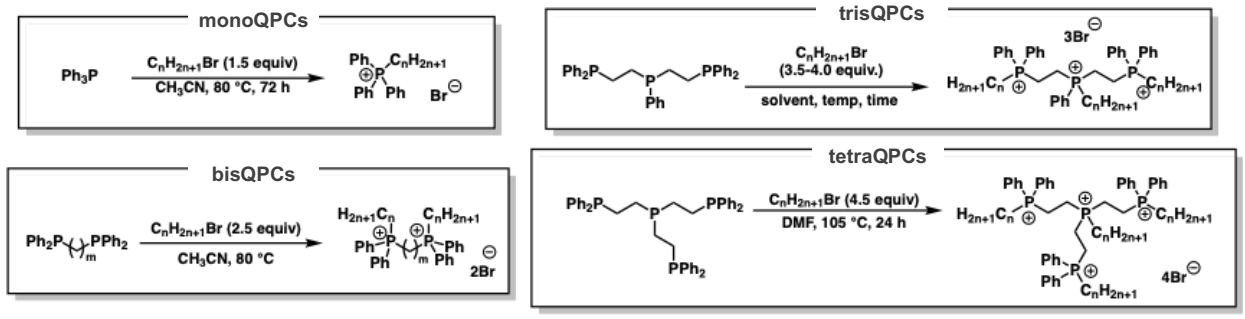

Figure 5.2 Synthetic strategy for the QPCs

5.6 Biological investigation of QPCs

5.6.1 Evaluation of bioactivity and toxicity of the QPC library

Of the 59 QPCs that were synthesized, we focused on assessing the bioactivities of 8 monoQPCs, 29 bisQPCs, 6 trisQPCs, and 3 tetraQPCs. We found that many compounds particularly, QPCs bearing long hydrocarbon tails displayed poor water solubility (Figure 5.3). Following vehicle solubility tests, we found that a 2.5% DMSO carrier concentration was optimal to solubilize the compounds at the highest test concentration (250 μM).

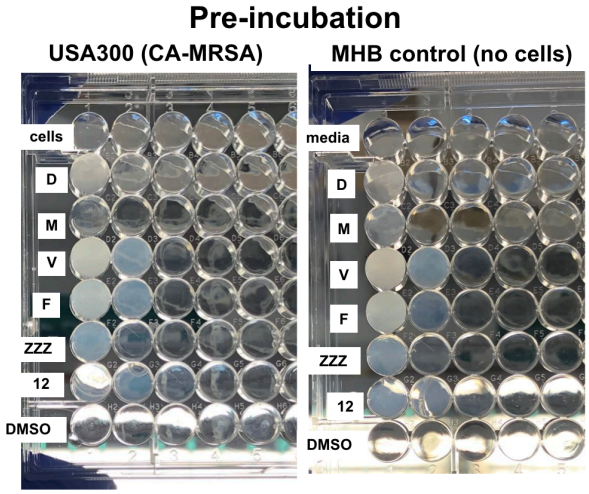

Figure 5.3 Representative example of compound solubility

The antimicrobial activity, as well as toxicity, were assessed for the QPCs, using red blood cell (RBC) lysis as a proxy for the latter. For comparison to commercially employed QACs,

benzalkonium chloride (BAC; 70% benzyldimethyldodecylammonium chloride and 30% benzyldimethyltetradecylammonium chloride) and cetylpyridinium chloride (CPC) were included in the assays. Additionally, **2Pyr-11,11**, a pyridinium-based bis-cationic QAC displaying best-in-class potency out of roughly 650 compounds synthesized to-date by our group, was also included for comparison.[212] The complete set of MIC values against a panel of six bacterial strains [community-acquired methicillin-resistant *S. aureus* (CA-MRSA; USA 300-0114), hospital-acquired methicillin-resistant *S. aureus* (HA-MRSA; ATCC 33591), methicillin-susceptible *S. aureus* (MSSA; SH1000), *Enterococcus faecalis* (OG1RF), *Escherichia coli* (MC4100), and *Pseudomonas aeruginosa* (PAO1)] along with the RBC lysis (represented by $Lysis_{20}$), are presented in Table 5.1. Interestingly, we observed unique phenotypes across many strains, with varying aggregation patterns (Figure 5.4). Marina Michaud is conducting follow up experiments to determine whether these phenotypes are indicative of a resistance mechanism, such as hetero resistance.

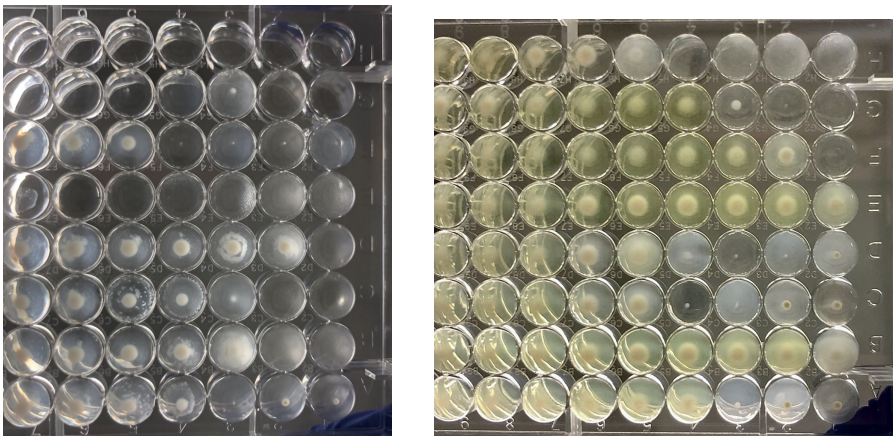

Figure 5.4 Representative example of interesting phenotypes

	Compound	Minimum Inhibitory Concentration (μM)						Lys_{20} (μM)[a]
		MSSA	CA-MRSA	HA-MRSA	*E. faecalis*	*E. coli*	*Pa*[b]	
QACs	BAC	4	4	8	250	63	250	16
	CPC	1	1	2	250	32	250	4
	2Pyr-11,11	1	2	2	8	2	16	4
monoQPCs	TPP-8	4	4	125	>250	>250	>250	63
	TPP-10	1	2	8	250	250	250	16
	TPP-11	1	1	4	125	125	250	16
	TPP-12	0.5	1	2	63	250	63	8
	TPP-13	1	1	2	16	4	32	4
	TPP-14	2	2	2	8	16	16	4
	TPP-16	2	2	4	4	16	16	4
	TPP-18	4	8	8	16	125	125	4
bisQPCs	P2P-8,8	1	0.5	8	250	>250	250	63
	P2P-10,10	1	1	2	8	16	8	4
	P2P-11,11	1	1	2	8	32	16	4
	P2P-12,12	1	2	8	32	63	63	4
	P3P-8,8	1	1	4	250	>250	250	63
	P3P-10,10	2	1	2	4	63	4	2
	P3P-11,11	1	1	16	4	8	16	4
	P3P-12,12	1	1	4	32	125	125	4
	P3P-13,13	2	2	4	63	63	63	4
	P3P-14,14	2	2	8	125	63	>250	2
	P4P-8,8	1	1	4	125	250	125	63
	P4P-10,10	1	2	2	4	16	8	2
	P4P-11,11	1	2	2	4	16	16	2
	P4P-12,12	2	2	4	16	63	>250	1
	P4P-13,13	2	2	8	125	125	>250	2
	P4P-14,14	8	4	4	63	125	>250	1
	P5P-8,8	0.5	1	2	125	250	125	32
	P5P-10,10	1	1	4	2	16	4	2
	P5P-11,11	2	2	4	2	8	16	2
	P5P-12,12	2	2	4	16	32	63	2
	P5P-13,13	4	4	4	63	125	250	2
	P5P-14,14	4	8	8	63	125	>250	1
	P5P-16,16	8	16	16	125	125	250	1
	P6P-8,8	0.5	0.5	2	63	125	63	16
	P6P-10,10	**1**	**1**	**2**	**2**	**8**	**4**	**2**
	P6P-11,11	2	2	4	2	16	16	2
	P6P-12,12	2	2	2	16	32	32	2
	P6P-13,13	4	2	4	32	63	>250	2
	P6P-14,14	4	4	8	63	63	250	2
trisQPCs	P2P2P-8,8,8	2	1	2	250	250	>250	16
	P2P2P-10,10,10	2	2	8	250	32	>250	2
	P2P2P-11,11,11	2	4	4	63	63	>250	1
	P2P2P-12,12,12	2	4	8	125	125	>250	1
	P2P2P-13,13,13	2	4	16	125	125	>250	2
	P2P2P-14,14,14	16	16	32	250	250	>250	1
tetraQPCs	4P-10,10,10,10	16	32	32	250	250	>250	8
	4P-11,11,11,11	16	32	125	125	125	>250	4
	4P-12,12,12,12	16	16	63	250	250	>250	4

Table 5.1 Antimicrobial activity and cytotoxicity.

5.6.2 Elucidation of structure-activity relationships

First, inspection of the bioactivity profiles of the monoQPCs indicated trends that were unique from the multi-cationic species examined herein (Figure 5.5). Compounds bearing 11–13-carbon tail lengths displayed optimal activity against MSSA, CA-MRSA, and HA-MRSA was observed for compounds (MIC = 0.5, 1, and 2 μM, respectively). Furthermore, **TPP-13** displayed the greatest potency amongst the monoQPCs against Gram-negative strains, with a ~63-fold increase in activity compared to its 12-carbon analog against *E. coli* (MIC = 4 μM). Our group has previously seen this trend between bioactivity and tail length.[261] Hydrophobic tails between 12–14 carbons have proven ideal for sufficient disruption of the intermolecular forces of the lipid bilayer in Gram-positive bacteria. At longer chain lengths, activity against *E. faecalis* and *P. aeruginosa* continued to increase, with **TPP-16** resulting in ~63-fold and ~16-fold increases in activity (MIC = 4 and 16 μM, respectively) compared to the commercially available QACs, BAC and CPC.

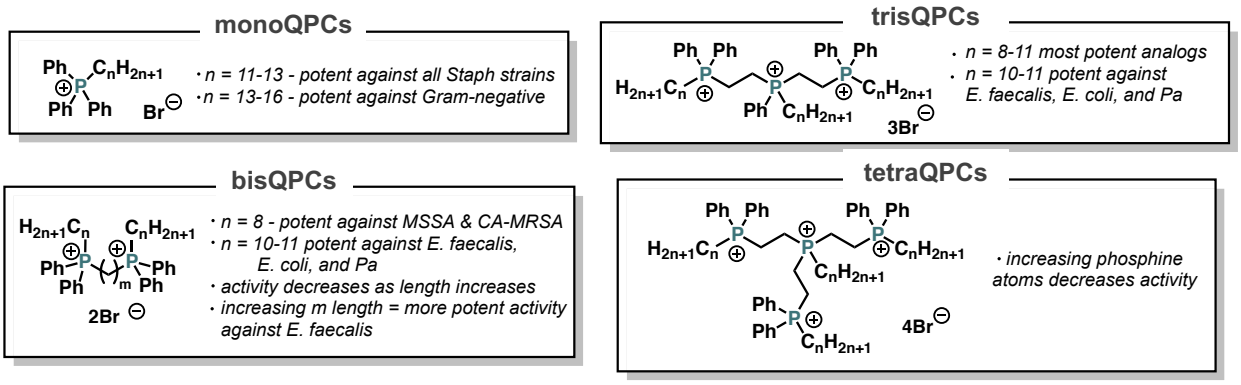

Figure 5.5 Summary of QPC structure-activity relationships

The bisQPCs followed a slightly different pattern in bioactivity relative to their monoQPC counterparts, with compounds bearing shorter tail lengths displaying optimal activities for all strains. Against MSSA and CA-MRSA, compounds with 8-carbon tail lengths displayed the best activities, with **P2P-8,8**, **P5P-8,8**, and **P6P-8,8** each reporting sub-micromolar activity (MIC = 0.5 μM) for at least one of the two strains. In contrast. the alkyl tail length 10 and 11 carbons resulted

in 4-fold and greater enhancements in activity compared to their 8-carbon counterparts against *E. faecalis*, *E. coli*, and *P. aeruginosa*. For all strains, as the hydrocarbon tail length increased beyond 11 carbons, activity across all strains began to decline, with this trend being most evident against *E. faecalis*, *E. coli*, and *P. aeruginosa*. Interestingly, these findings contrast our previous investigations of multiQACs, in which growing chain lengths displayed an improvement in activity, suggesting the interaction between bisQPCs and the cellular membrane may deviate from that of QACs. The effect of varying the alkyl linker separating the two quaternized phosphines led to slight improvement in activity for five of the strains, increasing the alkyl linker length did lead to a noteworthy increase in optimal activity against *E. faecalis*.

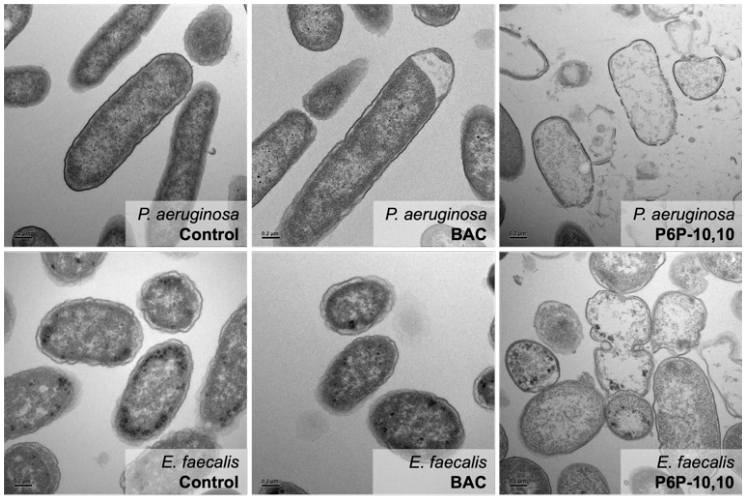

Figure 5.6 TEM images

Notably, **P6P-10,10**, bearing a 6-carbon linker, displayed the greatest broad-spectrum activity of all the prepared QPCs, and exhibited a different resistance profile compared to QACs. Moreover, **P6P-10,10** displayed improved activity compared to both commercial QACs, as well as our best-in-class bis-cationic QAC, **2Pyr-11,11**. To further examine the broad-spectrum efficacy of **P6P-10,10** compared to the leading commercial QAC (BAC) transmission electron microscopy (TEM) imaging was performed by Marina Michaud. A 2.5% DMSO carrier was used. The results of the TEM analysis underscore the distinct efficacy of **P6P-10,10** against both Gram-positive (*E. faecalis)* and Gram-negative (*P. aeruginosa*) pathogens over BAC (Figure 5.6).

Together these results highlight the promise of bisQPCs, namely **P6P-10,10**, as next-generation disinfectant compounds that warrant further investigation.

Lastly, analysis of the multiQPCs revealed no increase in bioactivity corresponding to the additional phosphonium residues. Rather, tris-cationic multiQPCs unveiled a similar trend to that of the bisQPCs, with shorter alkyl tail lengths (8–11 carbons) exhibiting greater potencies. In particular, **P2P2P-8,8,8** illustrated the best activity against the MSSA, CA-MRSA, and HA-MRSA strains (MIC = 2, 1, and 2 μM, respectively). However, in general, increasing the number of phosphonium atoms led to an overall decrease in antimicrobial activity for both tris- and tetra-cationic QPCs compared to their bis-cationic counterparts.

5.6.3 Determination of QPC cytotoxicity

Red blood cell lysis (measured as $Lysis_{20}$), serving as an approximation for cytotoxicity, appeared to parallel alkyl chain length for mono- and bisQPCs. For mono-, bis-, and trisQPCs, 8-carbon species consistently displayed the lowest hemolytic activity, with no compound reporting toxicity greater than BAC ($Lysis_{20}$ ≥ 16 μM). However, increasing the chain length from 8 to 10 carbons had a profound impact on toxicity, leading to at least an 8-fold increase in hemolytic activity for bis- and trisQPCs. For compounds with alkyl chains above 10 carbons, hemolytic activity continued to gradually increase. Additionally, the length of the alkyl linker had a minor impact on the toxicity of bisQPCs, with longer spacers leading to increased hemolytic activity. These results parallel previous studies on antimicrobial and anticancer amphiphiles in which increasing hydrocarbon tail length correlates with increasing cytotoxicity due to membrane disruption. Notably, many compounds exhibited improved therapeutic indices when tested under the original conditions with less DMSO. Since DMSO exhibits lytic effects, the maximal $Lysis_{20}$ value possible was 63 μM, greatly reducing the index.

5.6.4 Elucidation of QPC resistance mechanisms

Comparing the bioactivity across the six strains revealed several interesting trends. As expected, due to their protective outer membrane, Gram-negative species were less susceptible than Gram-positive species to the QPCs.[262] Next, between the Gram-positive *S. aureus* and *E. faecalis* strains examined, *E. faecalis* displayed significantly decreased susceptibility. Typically, *E. faecalis* and MRSA display similar susceptibility profiles, but the recent increase in AMR in enterococci species could explain this deviation.[263,264] The increase in resistance has particularly affected cell-well targeting molecules.

Intriguingly, amongst the *S. aureus* strains a pattern of resistance for HA-MRSA emerged. Specifically, mono- and bisQPCs possessing short to moderate hydrocarbon tail lengths (8–12 carbons) displayed significantly higher MICs against the HA-MRSA strain compared the MSSA and CA-MRSA strains. This result contrasts the previously elucidated QAC resistance panels, in which CA-MRSA typically displays a degree of resistance while MSSA and HA-MRSA display higher susceptibilities. Efflux of similar cationic phosphonium compounds, such as methylTPP has been reported, lending credence to the existence of a distinct efflux pump in HA-MRSA.[264–266]

5.6.5 Implication of SMR family transporters in QPC resistance

To further investigate this hypothesis, Marina Michaud first utilized bioinformatic analysis to identify potential efflux pump-encoding genes in the bacterial genomes. Specifically, she used the Comprehensive Antibiotic Resistance Database (CARD) database and the National Center for Biotechnology Information (NCBI) Basic Local Alignment Search Tool (BLAST) to compare the resistomes of the bacterial panel. Representative resistance-mediating efflux pumps are shown in Table 5.2. All the strains share efflux pumps from four different classes, including the major facilitator superfamily (MFS), resistance/nodulation/cell division (RND), ATP-binding Cassette (ABC), and the multi-drug and toxic compound extrusion family (MATE). The presence

of the Small Multidrug Resistant (SMR) family of efflux pumps in the strains resistant to QPC treatment was quite intriguing. These genes included *qacC* which is present in HA-MRSA*, qacE* from *E. faecalis,* and *emrE,* from the two Gram-negative species. QacC was first identified by Lyon and Skurray in 1987.[258,267] They found that this efflux pump was capable of effluxing quaternary ammonium compounds, as well as two phosphonium compounds, methyltriphenylphosphonium (methylTPP) and tetraphenylphosphonium. Taken together, the unique presence of these Small Multidrug Pump (SMP) class of SMR-family transporters may be responsible for the observed refractory nature of these strains to treatment with QAC and QPC disinfectants.

	Transporter Family	MFS					RND		ABC		MATE		SMR		
	gene	qacA	qacB	norA	norB	tetA	mexB	mtrC	macB	tolC	mepA	mdtG	qacC	qacE	emrE
Strain	MSSA			●	●	●					●	●			
	CA-MRSA			●	●	●					●	●			
	HA-MRSA			●	●	●					●		●		
	E. faecalis					●			●					●	
	E. coli						●	●	●	●	●	●			●
	P. aeruginosa					●	●	●	●						●

Table 5.2 Bioinformatic analysis of resistance-mediating multi-drug efflux pumps

5.6.6 Investigations into efflux-mediated resistance mechanisms

To probe our purported SMR-mediated mechanism of resistance, we hypothesized that an efflux pump inhibitor would potentiate the activities of the QAC and QPC molecules. Therefore, Marina re-evaluated the MICs of QAC and QPC molecules in the presence and absence of carbonyl cyanide m-chlorophenyl hydrazone (CCCP), a protonophore that functions as an inhibitor of the proton-motive force that is necessary for transport in SMR family efflux pumps.[268] She used one commercial QAC (BAC), our best-in-class biscationic QAC (**2Pyr-11,11**), a derivative of the efflux-susceptible methylTPP QPC (**TPP-8**), and our best-in-class biscationic

QPC (**P6P-10,10**) in combination with CCCP. Due to the inherent inhibitory activity of CCCP, the MIC was first evaluated, and then half of this concentration was used for the assay.

Contrary to what we expected, CCCP antagonized the biscationic QAC (**2Pyr-11,11**) and QPC (**P6P-10,10**) molecules against several strains (Table 5.3). CCCP induced membrane depolarization could alter the charge of the bacterial membrane, thus altering the electrostatic interaction that mediates QAC and QPC activity. This effect was most drastic for **P6P-10,10** with greater than four-fold increases in MIC against all strains. We speculate that membrane depolarization may be central in the mechanism by which this QPC exerts its broad-spectrum potency and evades apparent mechanisms of resistance.

	Minimum Inhibitory Concentration (μM)							
	BAC		2Pyr-11,11		P6P-10,10		TPP-8	
	– CCCP	+ CCCP	– CCCP	+ CCCP	– CCCP	+ CCCP	– CCCP	+ CCCP
MSSA	4	4	1	2	1	4	4	4
CA-MRSA	4	4	2	2	1	4	4	4
HA-MRSA	8	4	2	2	2	16	125	125
E. faecalis	250	>250	8	>250	2	>250	>250	>250
E. coli	63	63	2	4	8	125	>250	>250
P. aeruginosa	250	250	16	>250	4	250	>250	>250

Table 5.3 Effects of CCCP co-treatment on the MIC of P6P-10,10

We further investigated the role of membrane depolarization in the mechanism of P6P-10,10 using a fluorescent based assay (Figure 5.7). The fluorecent probe $DiBAC_4(3)$ (bis-(1,3-dibutylbarbituric acid)trimethine oxonol) fluorecense as a result of membrane depolarization and has been used as a reliable readout for this effect. In addition to **P6P-10,10**, we included **TPP-8** to explore the effects on membrane depolarization in MSSA and HA-MRSA because the latter compound displayed significantly decreased potency against HA-MRSA, likely as a result of efflux-mediated resistance. Therefore, we hypothesized that **P6P-10,10** would effect greater memebrane depolarization against HA-MRSA compared to **TPP-8**, as the presence of efflux

pumps in this strain may abate membrane depolarization for TPP-derived moelcules that are susceptible to efflux. The $DiBAC_4$ assay confirmed our hypothesis. **P6P-10,10** treatment lead to a two-fold increase in depolarization compared to **TPP-8** treatment. Furthermore, while **TPP-8** demonstrated initial depolarization of the membrane, membrane repolarization occurred. Collectively, we posit that the enhanced ability of **P6P-10,10** to perturb the membrane through depolarization underlies the mechanism by which this compounds displays improved broad-spectrum potency.

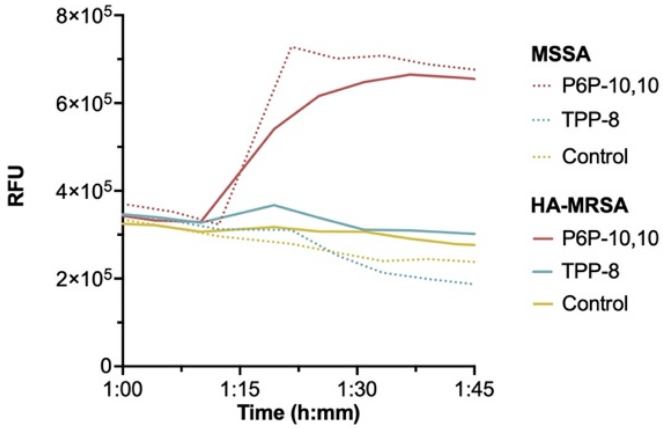

Figure 5.7 DiBAC4(3) depolarization assay

5.7 Conclusions

An overreliance on select quaternary ammonium-based disinfectants and antiseptics has radically promoted antimicrobial resistance. This public health crisis urgently necessitates the development of diverse antimicrobials for sanitization.[4,77] Herein, we have disclosed the synthesis and biological investigation of 59 quaternary phosphonium compounds, unveiling the promise of these underexplored cationic amphiphiles. Through this investigation, we elucidated the SAR between different alkyl chain lengths and cationic phosphine atoms with antibacterial and cytotoxic activity. We found that both monoQPCs with moderate hydrocarbon tail lengths (11–13

carbons) and bisQPCs with shorter tail lengths (8–11 carbons) demonstrated promising antimicrobial activities against a panel of six Gram-positive and Gram-negative bacteria.

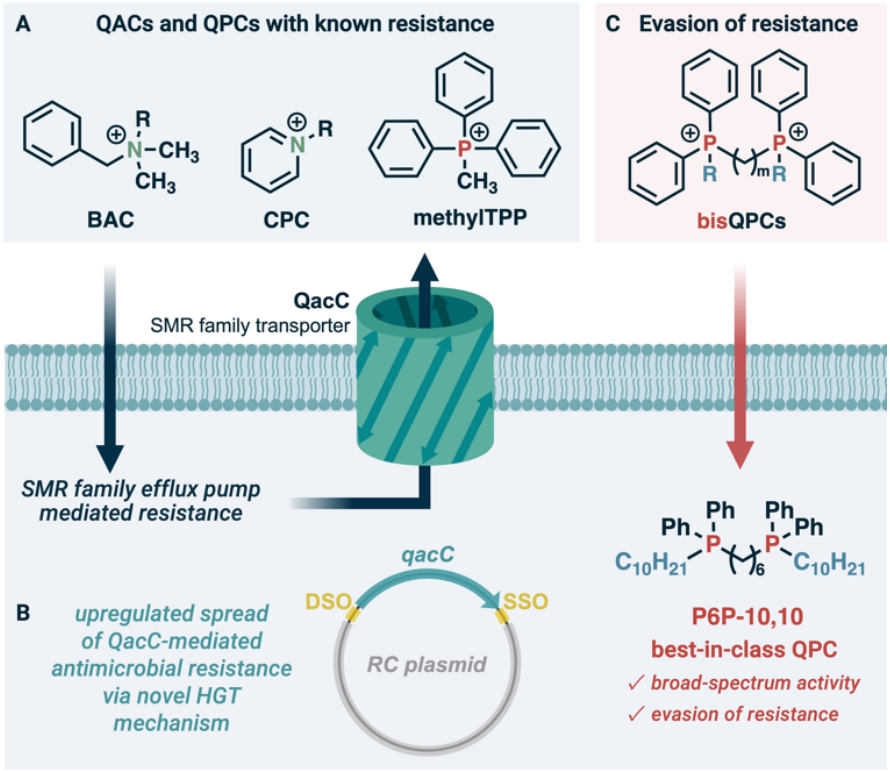

Figure 5.8 Overview of QPC findings

The most promising compound to emerge from this study was **P6P-10,10**, exhibiting comparable cytotoxicity and ≥4-fold increases in activity against Gram-negative species compared to commercial QACs, BAC and CPC (Figure 5.8). Moreover, improved lytic activity relative to commercial QACS, BAC, was observed via TEM imaging. The resistance profile deviated from the other compounds tested, leading to further bioinformatic analysis which revealed the presence of SMR family efflux pumps, such as QacC in HA-MRSA, that likely mediates efflux of these compounds. This potential relationship between disinfectant resistance and QacC is noteworthy, as a study purporting the recent spread of the *qacC* gene through a novel HGT mechanism underscores the need for next-generation disinfectants, such as **P6P-10,10**, that overcome mounting resistance. To further probe this mechanism of resistance, efflux

pump inhibition and membrane depolarization assays were performed, together elucidating the central role of membrane depolarization in the mechanism by which **P6P-10,10** exhibits broad-spectrum potency and evades resistance.

The results of our investigation have provided the impetus for further exploration of QPC architectures, as well as further investigation into the mechanisms of resistance observed with these compounds, both of which are subjects of ongoing collaborative research in our laboratories.

5.8 References

(208) Jacobs, W. A.; Heidelberger, M.; Amoss, H. L. The bactericidal properties of the quaternary salts of hexamethylenetetramine :ii. The relation between constitution and bactericidal action in the substituted benzylhexamethylenetetraminium salts. *Journal of Experimental Medicine* **1916**, *23* (5), 569–576. https://doi.org/10.1084/jem.23.5.569.

(209) Jacobs, W. A.; Heidelberger, M.; Amoss, H. L. The Bactericidal Properties of the Quaternary Salts of Hexamethylenetetramine: II. the Relation between Constitution and Bactericidal Action in the Substituted Benzyliiexamethylenetetraminium Salts. *Journal of Experimental Medicine* **1916**, *23* (5), 569–576. https://doi.org/10.1084/jem.23.5.569.

(210) Minbiole, K. P. C.; Jennings, M. C.; Ator, L. E.; Black, J. W.; Grenier, M. C.; LaDow, J. E.; Caran, K. L.; Seifert, K.; Wuest, W. M. From Antimicrobial Activity to Mechanism of Resistance: The Multifaceted Role of Simple Quaternary Ammonium Compounds in Bacterial Eradication. *Tetrahedron* **2016**, *72* (25), 3559–3566. https://doi.org/https://doi.org/10.1016/j.tet.2016.01.014.

(211) Gilbert, P.; Moore, L. E. Cationic Antiseptics: Diversity of Action under a Common Epithet. *Journal of Applied Microbiology* **2005**, *99* (4), 703–715. https://doi.org/10.1111/j.1365-2672.2005.02664.x.

(212) Al-Khalifa, S. E.; Jennings, M. C.; Wuest, W. M.; Minbiole, K. P. C. The Development of Next-Generation Pyridinium-Based MultiQAC Antiseptics. *ChemMedChem* **2017**, *12* (4), 280–283. https://doi.org/10.1002/cmdc.201600546.

(213) Alkhalifa, S.; Jennings, M. C.; Granata, D.; Klein, M.; Wuest, W. M.; Minbiole, K. P. C.; Carnevale, V. Analysis of the Destabilization of Bacterial Membranes by Quaternary Ammonium Compounds: A Combined Experimental and Computational Study. *ChemBioChem* **2020**, *21* (10), 1510–1516. https://doi.org/10.1002/cbic.201900698.

(214) SOPREY, P. R.; MAXCY, R. B. Tolerance of Bacteria for Quaternary Ammonium Compounds. *Journal of Food Science* **1968**, *33* (5), 536–540. https://doi.org/10.1111/j.1365-2621.1968.tb03669.x.

(215) Tennent, J. M.; Lyon, B. R.; Gillespie, M. T.; May, J. W.; Skurray, R. A. Cloning and Expression of Staphylococcus Aureus Plasmid-Mediated Quaternary Ammonium Resistance in Escherichia Coli. *Antimicrobial Agents and Chemotherapy* **1985**, *27* (1), 79–83. https://doi.org/10.1128/AAC.27.1.79.

(216) Liu, W. J.; Fu, L.; Huang, M.; Zhang, J. P.; Wu, Y.; Zhou, Y. S.; Zeng, J.; Wang, G. X. Frequency of Antiseptic Resistance Genes and Reduced Susceptibility to Biocides in

Carbapenem-Resistant Acinetobacter Baumannii. *Journal of Medical Microbiology* **2017**, *66* (1), 13–17. https://doi.org/10.1099/jmm.0.000403.

(217) Abuzaid, A.; Hamouda, A.; Amyes, S. G. B. Klebsiella Pneumoniae Susceptibility to Biocides and Its Association with CepA, QacΔE and QacE Efflux Pump Genes and Antibiotic Resistance. *Journal of Hospital Infection* **2012**, *81* (2), 87–91. https://doi.org/10.1016/j.jhin.2012.03.003.

(218) Liu, Q.; Liu, M.; Wu, Q.; Li, C.; Zhou, T.; Ni, Y. Sensitivities to Biocides and Distribution of Biocide Resistance Genes in Quaternary Ammonium Compound Tolerant Staphylococcus Aureus Isolated in a Teaching Hospital. *Scandinavian Journal of Infectious Diseases* **2009**, *41* (6–7), 403–409. https://doi.org/10.1080/00365540902856545.

(219) Mayer, S.; Boos, M.; Beyer, A.; Fluit, A. C.; Schmitz, F. J. Distribution of the Antiseptic Resistance Genes QacA, QacB and QacC in 497 Methicillin-Resistant and -Susceptibile European Isolates of Staphylococcus Aureus [4]. *Journal of Antimicrobial Chemotherapy*. Oxford Academic June 1, 2001, pp 896–897. https://doi.org/10.1093/jac/47.6.896.

(220) Ignak, S.; Nakipoglu, Y.; Gurler, B. Frequency of Antiseptic Resistance Genes in Clinical Staphycocci and Enterococci Isolates in Turkey. *Antimicrobial Resistance and Infection Control* **2017**, *6* (1), 1–7. https://doi.org/10.1186/s13756-017-0244-6.

(221) Wassenaar, T. M.; Cabal, A. The Mobile Dso-Gene-Sso Element in Rolling-Circle Plasmids of Staphylococci Reflects the Evolutionary History of Its Resistance Gene. *Letters in Applied Microbiology* **2017**, *65* (3), 192–198. https://doi.org/https://doi.org/10.1111/lam.12767.

(222) Chen, B.; Han, J.; Dai, H.; Jia, P. Biocide-Tolerance and Antibiotic-Resistance in Community Environments and Risk of Direct Transfers to Humans: Unintended Consequences of Community-Wide Surface Disinfecting during COVID-19? *Environmental Pollution* **2021**, *283*, 117074. https://doi.org/10.1016/j.envpol.2021.117074.

(223) United States Environmental Protection Agency. List N: Disinfectants for Coronavirus (COVID-19) https://www.epa.gov/coronavirus/about-list-n-disinfectants-coronavirus-covid-19-0 (accessed 2021 -06 -19).

(224) Radford, J. R.; Beighton, D.; Nugent, Z.; Jackson, R. J. Effect of Use of 0.05% Cetylpyridinium Chloride Mouthwash on Normal Oral Flora. *Journal of Dentistry* **1997**, *25* (1), 35–40. https://doi.org/https://doi.org/10.1016/S0300-5712(95)00116-6.

(225) Mao, X.; Auer, D. L.; Buchalla, W.; Hiller, K.-A.; Maisch, T.; Hellwig, E.; Al-Ahmad, A.; Cieplik, F. Cetylpyridinium Chloride: Mechanism of Action, Antimicrobial Efficacy in Biofilms, and Potential Risks of Resistance. *Antimicrob Agents Chemother* **2020**, *64* (8), e00576-20. https://doi.org/10.1128/AAC.00576-20.

(226) Latimer, J.; Munday, J. L.; Buzza, K. M.; Forbes, S.; Sreenivasan, P. K.; McBain, A. J. Antibacterial and Anti-Biofilm Activity of Mouthrinses Containing Cetylpyridinium Chloride and Sodium Fluoride. *BMC Microbiology* **2015**. https://doi.org/10.1186/s12866-015-0501-x.

(227) Gilbert, P.; Moore, L. E. Cationic Antiseptics: Diversity of Action under a Common Epithet. *Journal of Applied Microbiology* **2005**, *99* (4), 703–715. https://doi.org/10.1111/j.1365-2672.2005.02664.x.

(228) Makvandi, P.; Jamaledin, R.; Jabbari, M.; Nikfarjam, N.; Borzacchiello, A. Antibacterial Quaternary Ammonium Compounds in Dental Materials: A Systematic Review. *Dental Materials* **2018**, *34* (6), 851–867. https://doi.org/https://doi.org/10.1016/j.dental.2018.03.014.

(229) Cheng, L.; Weir, M. D.; Zhang, K.; Arola, D. D.; Zhou, X.; Xu, H. H. K. Dental Primer and Adhesive Containing a New Antibacterial Quaternary Ammonium Monomer Dimethylaminododecyl Methacrylate. *J Dent* **2013**, *41* (4), 345–355.

(230) Roberts, A. P.; Mullany, P. Oral Biofilms: A Reservoir of Transferable, Bacterial, Antimicrobial Resistance. *Expert Review of Anti-infective Therapy* **2010**, *8* (12), 1441–1450. https://doi.org/10.1586/eri.10.106.
(231) Robbins, N.; Szilagyi, G.; Tanowitz, H. B.; Luftschein, S.; Baum, S. G. Infective Endocarditis Caused by Streptococcus Mutans: A Complication of Idiopathic Hypertrophic Subaortic Stenosis. *Archives of Internal Medicine* **1977**, *137* (9), 1171–1174. https://doi.org/10.1001/archinte.1977.03630210045014.
(232) Al-Khalifa, S. E.; Jennings, M. C.; Wuest, W. M.; Minbiole, K. P. C. The Development of Next-Generation Pyridinium-Based MultiQAC Antiseptics. *ChemMedChem* **2017**, *12* (4), 280–283. https://doi.org/10.1002/cmdc.201600546.
(233) Carden, R. G.; Sommers, K. J.; Schrank, C. L.; Leitgeb, A. J.; Feliciano, J. A.; Wuest, W. M.; Minbiole, K. P. C. Advancements in the Development of Non-Nitrogen-Based Amphiphilic Antiseptics to Overcome Pathogenic Bacterial Resistance. *ChemMedChem* **2020**, *15* (21), 1974–1984. https://doi.org/10.1002/cmdc.202000612.
(234) Kumar, V.; Malhotra, S. V. Study on the Potential Anti-Cancer Activity of Phosphonium and Ammonium-Based Ionic Liquids. *Bioorganic and Medicinal Chemistry Letters* **2009**, *19* (16), 4643–4646. https://doi.org/10.1016/j.bmcl.2009.06.086.
(235) Iksanova, A. G.; Gabbasova, R. R.; Kupriyanova, T. V.; Akhunzyanov, A. A.; Pugachev, M. V.; Vafiva, R. M.; Shtyrlin, N. V.; Balakin, K. V.; Shtyrlin, Y. G. In-Vitro Antitumor Activity of New Quaternary Phosphonium Salts, Derivatives of 3-Hydroxypyridine. *Anti-Cancer Drugs* **2018**, *29* (7), 682–690. https://doi.org/10.1097/CAD.0000000000000642.
(236) Macarie, L.; Simulescu, V.; Ilia, G. Phosphonium-Based Ionic Liquids Used as Reagents or Catalysts. *ChemistrySelect* **2019**, *4* (32), 9285–9299. https://doi.org/10.1002/slct.201901712.
(237) Muñoz-Bonilla, A.; Fernández-García, M. Polymeric Materials with Antimicrobial Activity. *Progress in Polymer Science* **2012**, *37* (2), 281–339. https://doi.org/10.1016/j.progpolymsci.2011.08.005.
(238) Xue, Y.; Xiao, H. Characterization and Antipathogenic Evaluation of a Novel Quaternary Phosphonium Tripolyacrylamide and Elucidation of the Inactivation Mechanisms. *Journal of Biomedical Materials Research - Part A* **2016**, *104* (3), 747–757. https://doi.org/10.1002/jbm.a.35613.
(239) Xue, Y.; Pan, Y.; Xiao, H.; Zhao, Y. Novel Quaternary Phosphonium-Type Cationic Polyacrylamide and Elucidation of Dual-Functional Antibacterial/Antiviral Activity. *RSC Advances* **2014**, *4* (87), 46887–46895. https://doi.org/10.1039/c4ra08634a.
(240) Xue, Y.; Xiao, H.; Zhang, Y. Antimicrobial Polymeric Materials with Quaternary Ammonium and Phosphonium Salts. *International Journal of Molecular Sciences* **2015**, *16* (2), 3626–3655. https://doi.org/10.3390/ijms16023626.
(241) Kanazawa, A.; Ikeda, T.; Endo, T. Polymeric Phosphonium Salts as a Novel Class of Cationic Biocides. IX. Effect of Side-Chain Length between Main Chain and Active Group on Antibacterial Activity. *Journal of Polymer Science Part A: Polymer Chemistry* **1994**, *32* (10), 1997–2001. https://doi.org/10.1002/pola.1994.080321024.
(242) Kanazawa, A.; Ikeda, T.; Endo, T. Polymeric Phosphonium Salts as a Novel Class of Cationic Biocides. III. Immobilization of Phosphonium Salts by Surface Photografting and Antibacterial Activity of the Surface-treated Polymer Films. *Journal of Polymer Science Part A: Polymer Chemistry* **1993**, *31* (6), 1467–1472. https://doi.org/10.1002/pola.1993.080310615.
(243) Kanazawa, A.; Ikeda, T.; Endo, T. Polymeric Phosphonium Salts as a Novel Class of Cationic Biocides. V. Synthesis and Antibacterial Activity of Polyesters Releasing Phosphonium Biocides. *Journal of Polymer Science Part A: Polymer Chemistry* **1993**, *31* (12), 3003–3011. https://doi.org/10.1002/pola.1993.080311216.

(244) Kanazawa, A.; Ikeda, T.; Endo, T. Polymeric Phosphonium Salts as a Novel Class of Cationic Biocides. VII. Synthesis and Antibacterial Activity of Polymeric Phosphonium Salts and Their Model Compounds Containing Long Alkyl Chains. *Journal of Applied Polymer Science* **1994**, *53* (9), 1237–1244. https://doi.org/10.1002/app.1994.070530910.
(245) Kanazawa, A.; Ikeda, T.; Endo, T. Synthesis and Antimicrobial Activity of Dimethyl- and Trimethyl- Substituted Phosphonium Salts with Alkyl Chains of Various Lengths. *Antimicrobial Agents and Chemotherapy* **1994**, *38* (5), 945–952. https://doi.org/10.1128/AAC.38.5.945.
(246) Carden, R. G.; Sommers, K. J.; Schrank, C. L.; Leitgeb, A. J.; Feliciano, J. A.; Wuest, W. M.; Minbiole, K. P. C. Advancements in the Development of Non-Nitrogen-Based Amphiphilic Antiseptics to Overcome Pathogenic Bacterial Resistance. *ChemMedChem* **2020**, *15* (21), 1974–1984. https://doi.org/10.1002/cmdc.202000612.
(247) Kanazawa, A.; Ikeda, T.; Endo, T. Polymeric Phosphonium Salts as a Novel Class of Cationic Biocides. IX. Effect of Side-chain Length between Main Chain and Active Group on Antibacterial Activity. *Journal of Polymer Science Part A: Polymer Chemistry* **1994**, *32* (10), 1997–2001. https://doi.org/10.1002/pola.1994.080321024.
(248) Lukáč, M.; Devínsky, F.; Pisárčik, M.; Papapetropoulou, A.; Bukovský, M.; Horváth, B. Novel Phospholium-Type Cationic Surfactants: Synthesis, Aggregation Properties and Antimicrobial Activity. *Journal of Surfactants and Detergents* **2017**, *20* (1), 159–171. https://doi.org/10.1007/s11743-016-1908-6.
(249) Terekhova, N. V.; Tatarinov, D. A.; Shaihutdinova, Z. M.; Pashirova, T. N.; Lyubina, A. P.; Voloshina, A. D.; Sapunova, A. S.; Zakharova, L. Y.; Mironov, V. F. Design and Synthesis of Amphiphilic 2-Hydroxybenzylphosphonium Salts with Antimicrobial and Antitumor Dual Action. *Bioorganic and Medicinal Chemistry Letters* **2020**, *30* (13). https://doi.org/10.1016/j.bmcl.2020.127234.
(250) Lao, Z.; Toy, P. H. Catalytic Wittig and Aza-Wittig Reactions. *Beilstein Journal of Organic Chemistry* **2016**, *12* (1), 2577–2587. https://doi.org/10.3762/bjoc.12.253.
(251) Zhao, Y. L.; Li, Y.; Li, Y.; Gao, L. X.; Han, F. S. Aryl Phosphoramides: Useful Electrophiles for Suzuki-Miyaura Coupling Catalyzed by a NiCl2/Dppp System (Dppp=1,3-Bis(Diphenylphosphino) Propane). *Chemistry - A European Journal* **2010**, *16* (17), 4991–4994. https://doi.org/10.1002/chem.201000420.
(252) Stewart, B.; Harriman, A.; Higham, L. J. Predicting the Air Stability of Phosphines. *Organometallics* **2011**, *30* (20), 5338–5343. https://doi.org/10.1021/om200070a.
(253) Pugachev, M. V.; Shtyrlin, N. V.; Sapozhnikov, S. V.; Sysoeva, L. P.; Iksanova, A. G.; Nikitina, E. V.; Musin, R. Z.; Lodochnikova, O. A.; Berdnikov, E. A.; Shtyrlin, Y. G. Bis-Phosphonium Salts of Pyridoxine: The Relationship between Structure and Antibacterial Activity. *Bioorganic and Medicinal Chemistry* **2013**, *21* (23), 7330–7342. https://doi.org/10.1016/j.bmc.2013.09.056.
(254) Pugachev, M. V.; Shtyrlin, N. V.; Sysoeva, L. P.; Nikitina, E. V.; Abdullin, T. I.; Iksanova, A. G.; Ilaeva, A. A.; Musin, R. Z.; Berdnikov, E. A.; Shtyrlin, Y. G. Synthesis and Antibacterial Activity of Novel Phosphonium Salts on the Basis of Pyridoxine. *Bioorganic and Medicinal Chemistry* **2013**, *21* (14), 4388–4395. https://doi.org/10.1016/j.bmc.2013.04.051.
(255) Kayumov, A. R.; Nureeva, A. A.; Trizna, E. Y.; Gazizova, G. R.; Bogachev, M. I.; Shtyrlin, N. V.; Pugachev, M. V.; Sapozhnikov, S. V.; Shtyrlin, Y. G. New Derivatives of Pyridoxine Exhibit High Antibacterial Activity against Biofilm-Embedded Staphylococcus Cells. *BioMed Research International* **2015**, *2015*. https://doi.org/10.1155/2015/890968.
(256) Shtyrlin, N. V.; Vafina, R. M.; Pugachev, M. V.; Khaziev, R. M.; Nikitina, E. V.; Zeldi, M. I.; Iksanova, A. G.; Shtyrlin, Y. G. Synthesis and Biological Activity of Quaternary Phosphonium Salts Based on 3-Hydroxypyridine and 4-Deoxypyridoxine. *Russian Chemical Bulletin* **2016**, *65* (2), 537–545. https://doi.org/10.1007/s11172-016-1334-y.

(257) Tsepaeva, O. V.; Nemtarev, A. V.; Grigor'eva, L. R.; Mironov, V. F. Synthesis of C(28)-Linker Derivatives of Betulinic Acid Bearing Phosphonate Group. *Russian Chemical Bulletin* **2021**, *70* (1), 179–182. https://doi.org/10.1007/s11172-021-3074-x.
(258) Grinius, L. L.; Goldberg, E. B. Bacterial Multidrug Resistance Is Due to a Single Membrane Protein Which Functions as a Drug Pump. *Journal of Biological Chemistry* **1994**, *269* (47), 29998–30004. https://doi.org/10.1016/s0021-9258(18)43980-4.
(259) Costa, S. S.; Junqueira, E.; Palma, C.; Viveiros, M.; Melo-Cristino, J.; Amaral, L.; Couto, I. Resistance to Antimicrobials Mediated by Efflux Pumps in Staphylococcus Aureus. *Antibiotics* **2013**, *2* (1), 83–99. https://doi.org/10.3390/antibiotics2010083.
(260) Ovchinnikov, V.; Stone, T. A.; Deber, C. M.; Karplus, M. Structure of the Emre Multidrug Transporter and Its Use for Inhibitor Peptide Design. *Proc Natl Acad Sci U S A* **2018**, *115* (34), E7932–E7941. https://doi.org/10.1073/pnas.1802177115.
(261) Forman, M. E.; Fletcher, M. H.; Jennings, M. C.; Duggan, S. M.; Minbiole, K. P. C.; Wuest, W. M. Structure-Resistance Relationships: Interrogating Antiseptic Resistance in Bacteria with Multicationic Quaternary Ammonium Dyes. *ChemMedChem* **2016**, *11* (9), 958–962. https://doi.org/10.1002/cmdc.201600095.
(262) Gilbert, P.; Moore, L. E. Cationic Antiseptics: Diversity of Action under a Common Epithet. *Journal of Applied Microbiology* **2005**, *99* (4), 703–715. https://doi.org/10.1111/j.1365-2672.2005.02664.x.
(263) Paniak, T. J.; Jennings, M. C.; Shanahan, P. C.; Joyce, M. D.; Santiago, C. N.; Wuest, W. M.; Minbiole, K. P. C. The Antimicrobial Activity of Mono-, Bis-, Tris-, and Tetracationic Amphiphiles Derived from Simple Polyamine Platforms. *Bioorganic and Medicinal Chemistry Letters* **2014**, *24* (24), 5824–5828. https://doi.org/10.1016/j.bmcl.2014.10.018.
(264) Joyce, M. D.; Jennings, M. C.; Santiago, C. N.; Fletcher, M. H.; Wuest, W. M.; Minbiole, K. P. Natural Product-Derived Quaternary Ammonium Compounds with Potent Antimicrobial Activity. *Journal of Antibiotics* **2016**, *69* (4), 344–347. https://doi.org/10.1038/ja.2015.107.
(265) Paniak, T. J.; Jennings, M. C.; Shanahan, P. C.; Joyce, M. D.; Santiago, C. N.; Wuest, W. M.; Minbiole, K. P. C. The Antimicrobial Activity of Mono-, Bis-, Tris-, and Tetracationic Amphiphiles Derived from Simple Polyamine Platforms. *Bioorganic and Medicinal Chemistry Letters* **2014**, *24* (24), 5824–5828. https://doi.org/10.1016/j.bmcl.2014.10.018.
(266) Forman, M. E.; Fletcher, M. H.; Jennings, M. C.; Duggan, S. M.; Minbiole, K. P. C.; Wuest, W. M. Structure-Resistance Relationships: Interrogating Antiseptic Resistance in Bacteria with Multicationic Quaternary Ammonium Dyes. *ChemMedChem* **2016**, *11* (9), 958–962. https://doi.org/10.1002/cmdc.201600095.
(267) Lyon, B. R.; Skurray, R. Antimicrobial Resistance of Staphylococcus Aureus: Genetic Basis. *Microbiological Reviews* **1987**, *51* (1), 88–134. https://doi.org/10.1128/mmbr.51.1.88-134.1987.
(268) Mombeshora, M.; Mukanganyama, S. Development of an Accumulation Assay and Evaluation of the Effects of Efflux Pump Inhibitors on the Retention of Chlorhexidine Digluconate in Pseudomonas Aeruginosa and Staphylococcus Aureus. *BMC Research Notes* **2017**, *10* (1). https://doi.org/10.1186/s13104-017-2637-2.

6 Experimental

6.1 Supplementary figures

Figure S1. Table of crystal violet biofilm mass data (top). Values shown are the result of (CV OD_{595}/ growth O_{D600}) to demonstrate biofilm formation relative to bacterial growth. Graphical representation of (CV OD_{595}/ growth O_{D600}) (middle). Relative biofilm mass compared to DMSO control (bottom).

	Relative Biomass Compared to DMSO control											
conc (μL)	**500.00**	**250.00**	**125.00**	**63.00**	**32.00**	**16.00**	**8.00**	**4.00**	**2.00**	**1.00**	**0.50**	**0.25**
9	1.00	1.82	1.63	1.72	1.18	0.94	0.90	0.92	0.79	0.92	0.92	0.88
10	1.40	1.85	1.65	1.53	1.16	1.04	0.91	0.84	0.87	0.87	0.95	0.84
2	0.36	0.39	2.32	1.78	1.27	1.08	0.97	0.89	0.89	1.04	0.92	0.99
carolacton	1.44	1.58	1.15	0.98	0.91	0.88	0.86	0.93	0.97	0.94	0.91	1.08

	Average Biomass Trials 1-9											
DMSO	4.69	3.99	4.17	3.96	4.25	4.38	4.47	4.10	4.18	3.97	3.80	3.50
9	4.67	7.26	6.81	6.79	5.01	4.10	4.03	3.75	3.29	3.66	3.50	3.08
10	6.58	7.36	6.88	6.06	4.91	4.54	4.06	3.43	3.62	3.45	3.62	2.95
2	1.70	1.55	9.69	7.04	5.39	4.72	4.36	3.65	3.73	4.13	3.51	3.47
	Average Biomass Trials 1-3											
DMSO	7.28	5.92	6.46	6.43	7.38	7.18	7.59	6.98	6.65	6.75	6.48	5.93
carolacton	10.47	9.32	7.41	6.32	6.75	6.34	6.49	6.48	6.45	6.35	5.92	6.41

Figure S2. *S. mutans* mutants were screened against analog (+)-2. Strains were screened in biological triplicate with compound and with the DMSO vehicle (top). The % growth at 125 mL for all 17 mutants is shown (middle). “% growth” refers to (growth with compound/growth with vehicle*100).

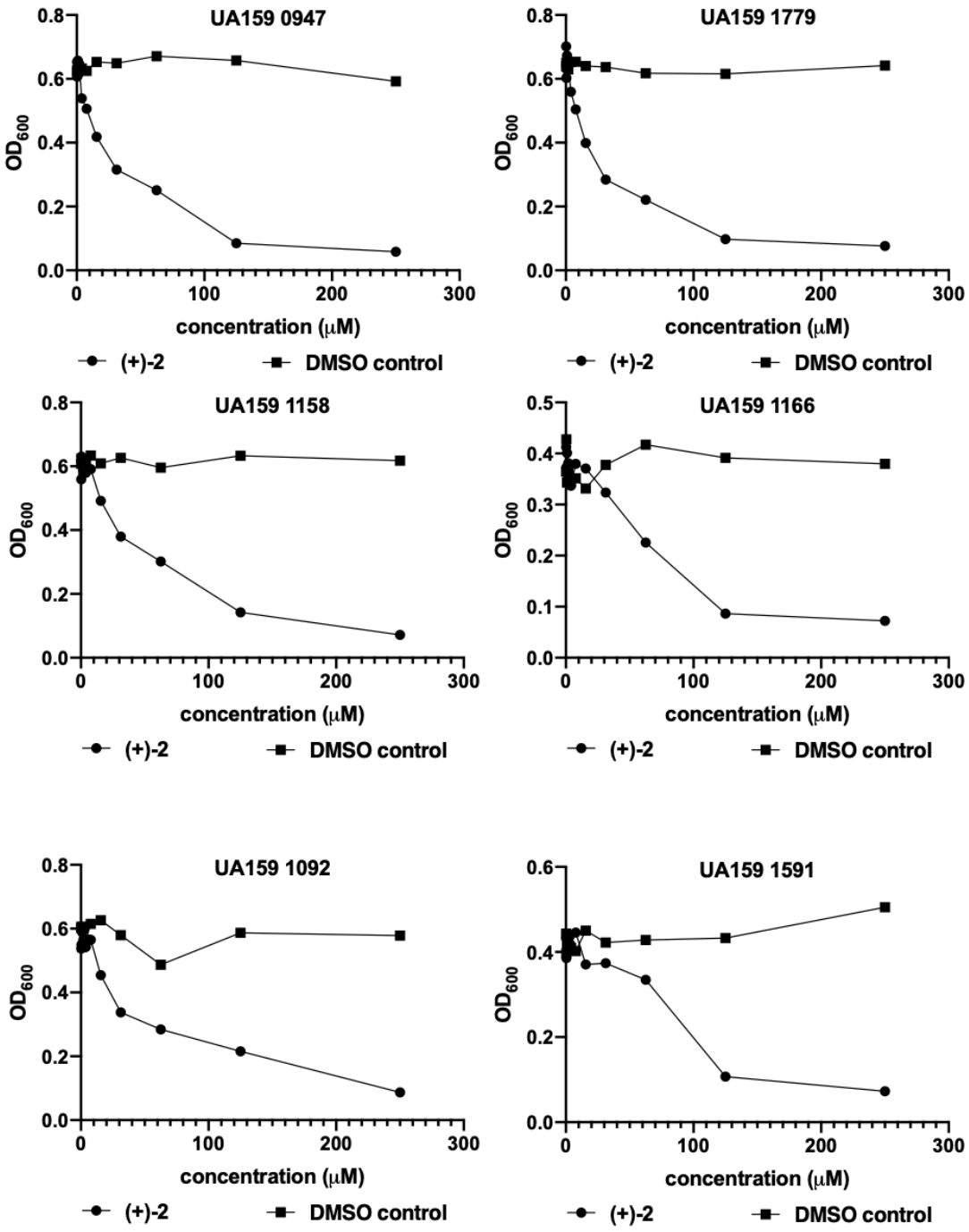

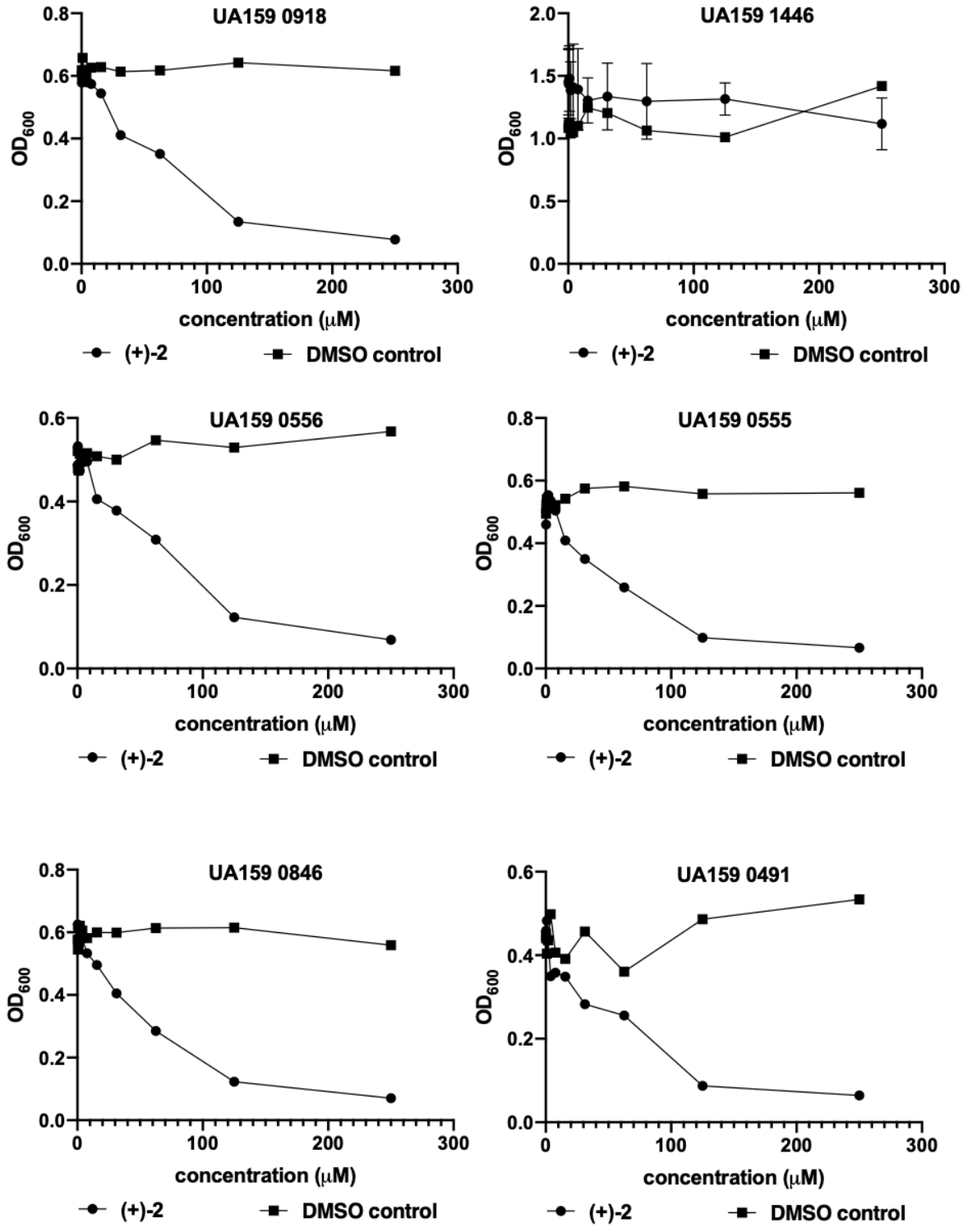
UA159 0918
UA159 1446
UA159 0556
UA159 0555
UA159 0846
UA159 0491
OD600
concentration (μM)
(+)-2
DMSO control

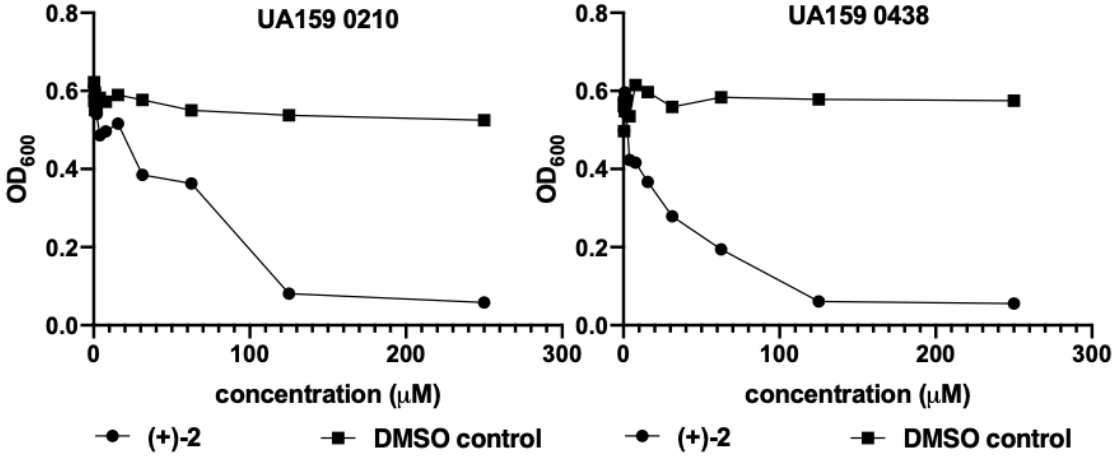
UA159 0210
UA159 0438
OD600
concentration (μM)
(+)-2
DMSO control

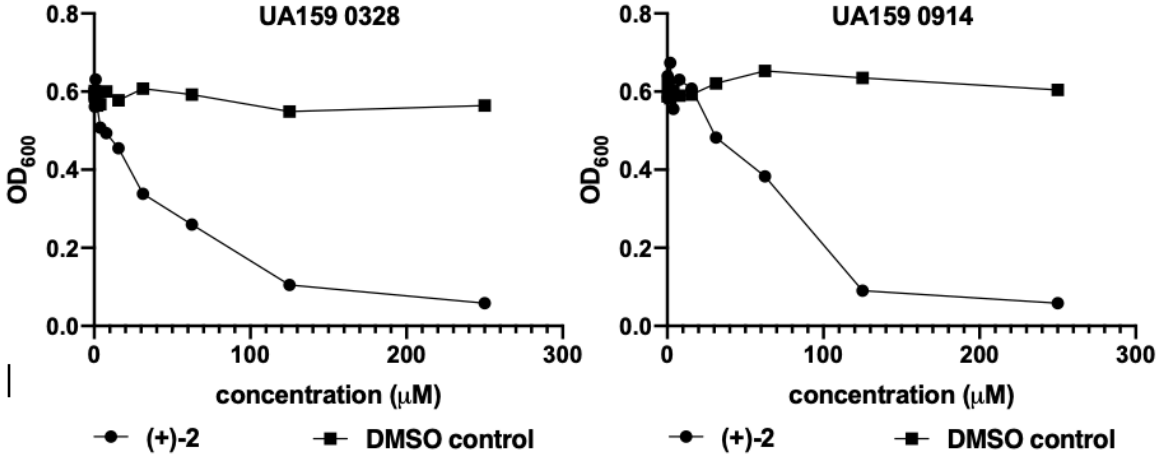
UA159 0328
UA159 0914
OD600
concentration (μM)
(+)-2
DMSO control

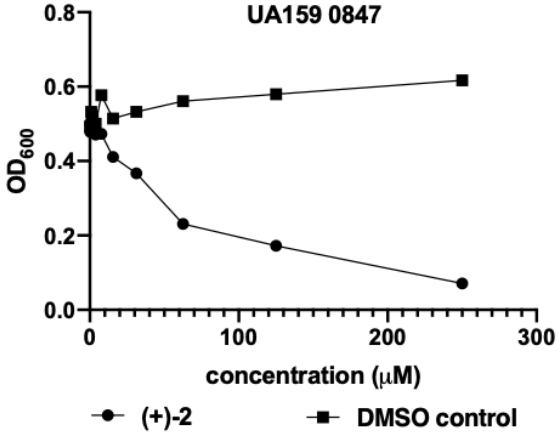
UA159 0847
OD600
concentration (μM)
(+)-2
DMSO control

Figure S3. IC_{50} Curves

All optical density (OD) measurements were performed on a Molecular Devices SpectraMax iD3 plate reader and growth was recorded by OD_{600}. The dotted line refers to the average growth of bacterial strain in that growth condition. IC_{50} curves were calculated with GraphPad Prism using a four-parameter nonlinear regression fit.

Bacteria: *S. mutans* **Growth Conditions:** THB Media **Compound:** carolacton

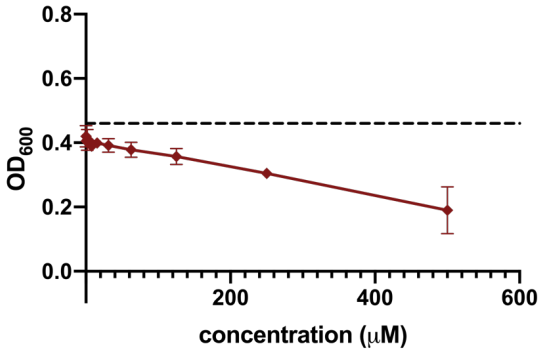

Bacteria: *S. mutans* **Growth Conditions:** THB Media **Compound:** C3

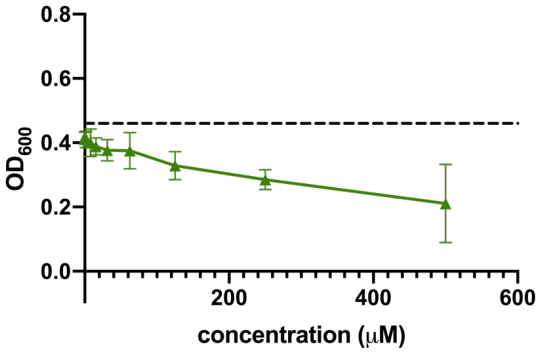

Bacteria: *S. mutans* **Growth Conditions:** THB Media **Compound:** 2.51

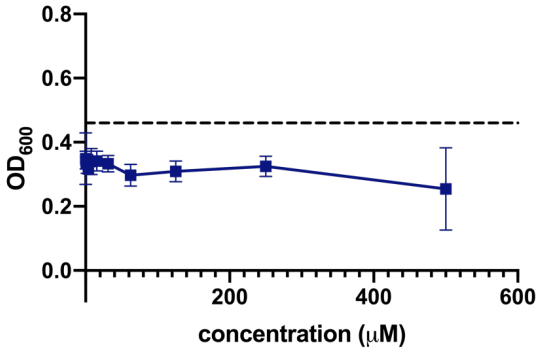

Bacteria: *S. mutans* **Growth Conditions:** THB Media **Compound:** 2.52

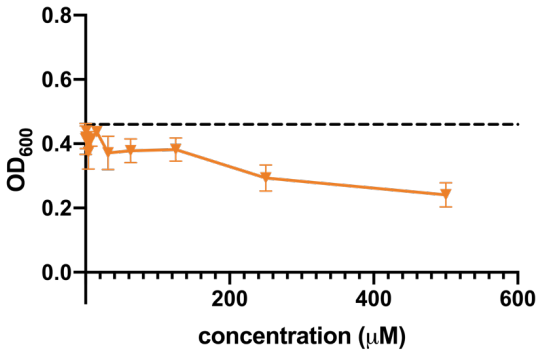

Bacteria: *S. mutans* **Growth Conditions:** THB Media **Compound:** 2.55

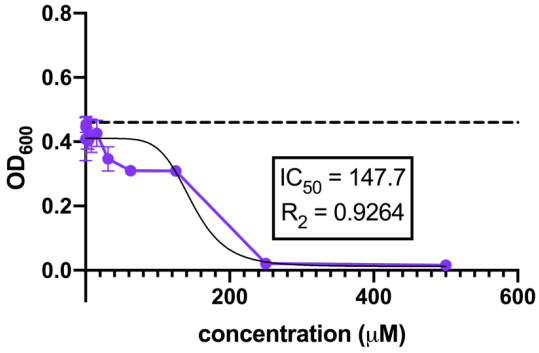

Bacteria: *S. mutans* **Growth Conditions:** THB Media + 0.1% sucrose **Compound:** carolacton

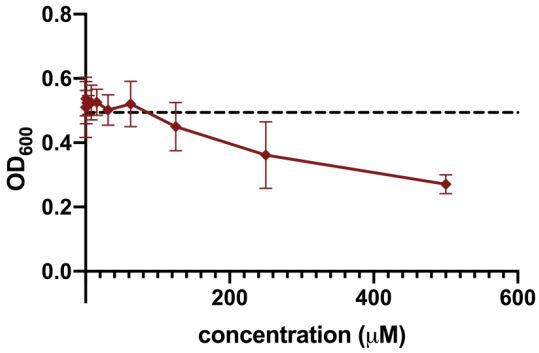

Bacteria: *S. mutans* **Growth Conditions:** THB Media + 0.1% sucrose **Compound:** 2.51

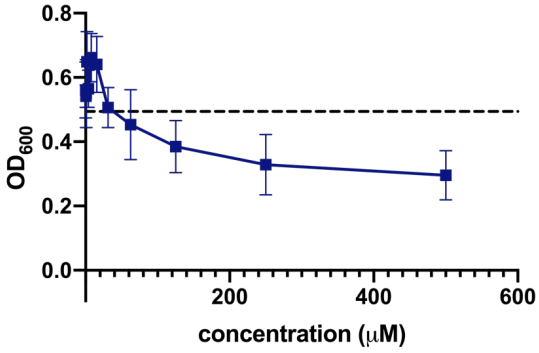

Bacteria: *S. mutans* **Growth Conditions:** THB Media + 0.1% sucrose **Compound:** 2.52

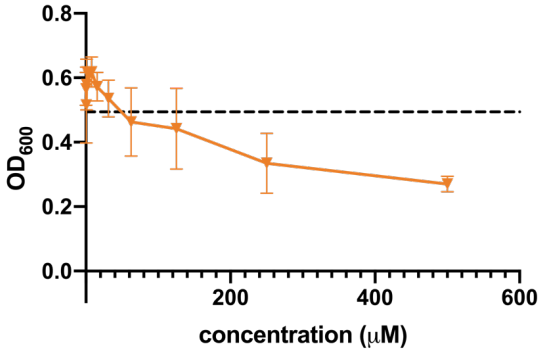

Bacteria: *S. mutans* **Growth Conditions:** THB Media + 0.1% sucrose **Compound:** 2.55

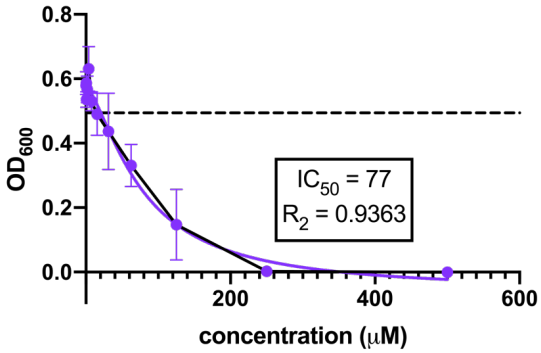

Bacteria: *S. mutans* **Growth Conditions:** THB + 0.1% sucrose + glass bottom 96-well plate **Compound:** carolacton

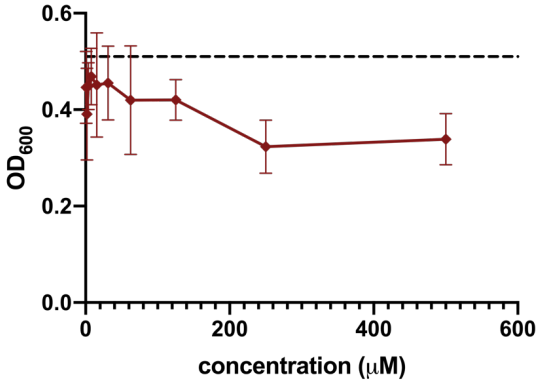

Bacteria: *S. mutans* **Growth Conditions:** THB + 0.1% sucrose + glass bottom 96-well plate **Compound:** 2.51

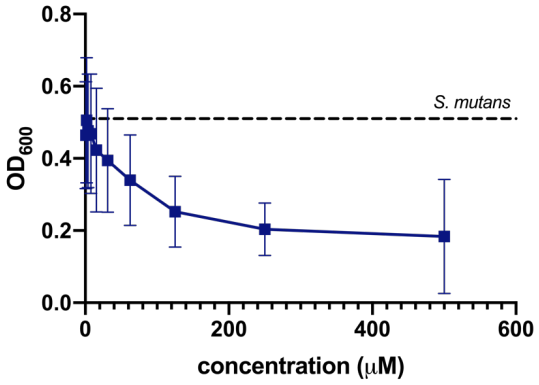

Bacteria: *S. mutans* **Growth Conditions:** THB + 0.1% sucrose + glass bottom 96-well plate

Compound: 2.52

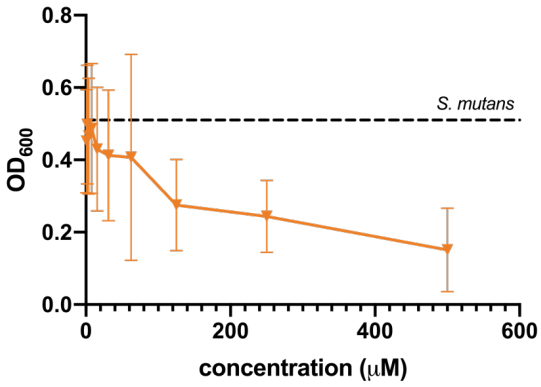

Bacteria: *S. mutans* **Growth Conditions:** THB + 0.1% sucrose + glass bottom 96-well plate

Compound: 2.55

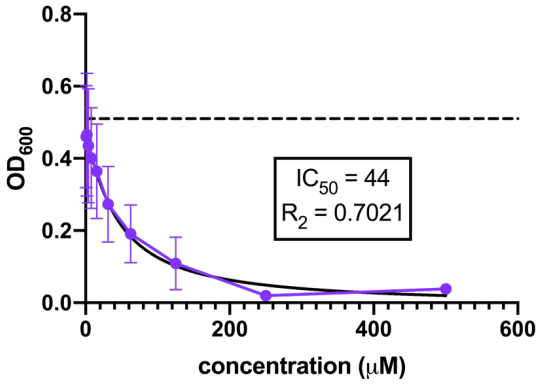

Bacteria: *S. mutans* **Growth Conditions:** THB; pH 5 **Compound:** 2.55

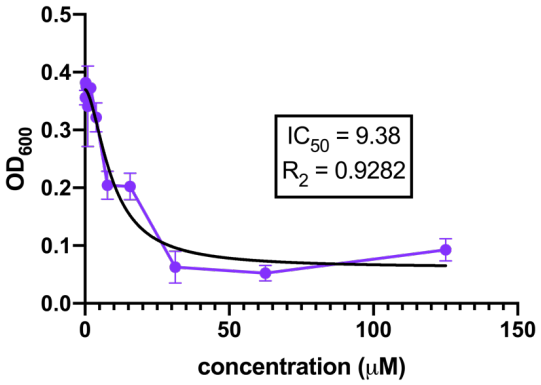

Bacteria: *S. gordonii* **Growth Conditions:** THB **Compound:** 2.55

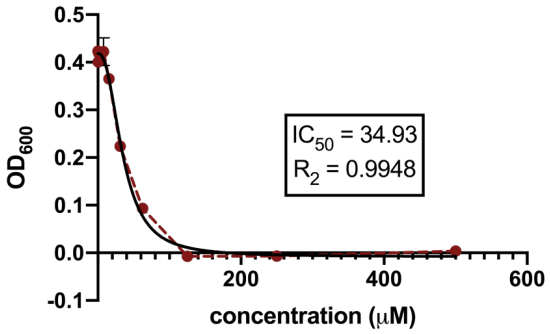

Bacteria: *S. gordonii* **Growth Conditions:** THB + 0.1% sucrose **Compound:** 2.55

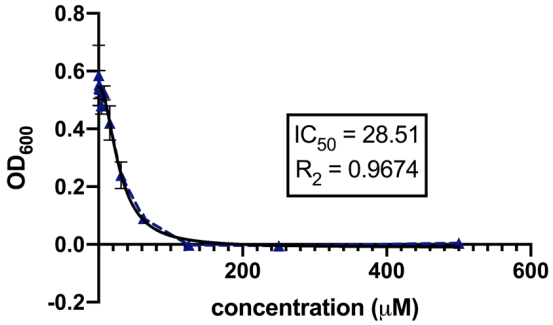

Bacteria: *S. sanguinis* **Growth Conditions:** THB **Compound:** (+)-2

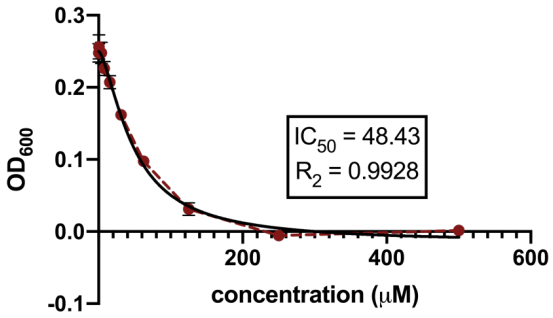

Bacteria: *S. sanguinis* **Growth Conditions:** THB + 0.1% sucrose **Compound:** (+)-2

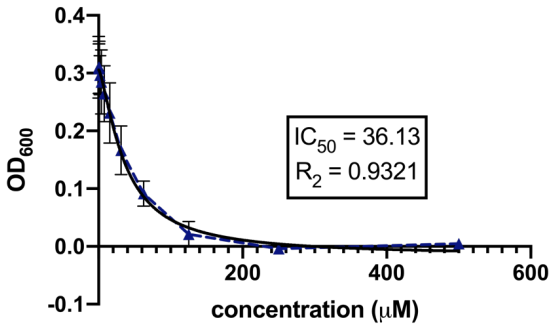

Figure S4. Confocal images of 2.51 and 2.52

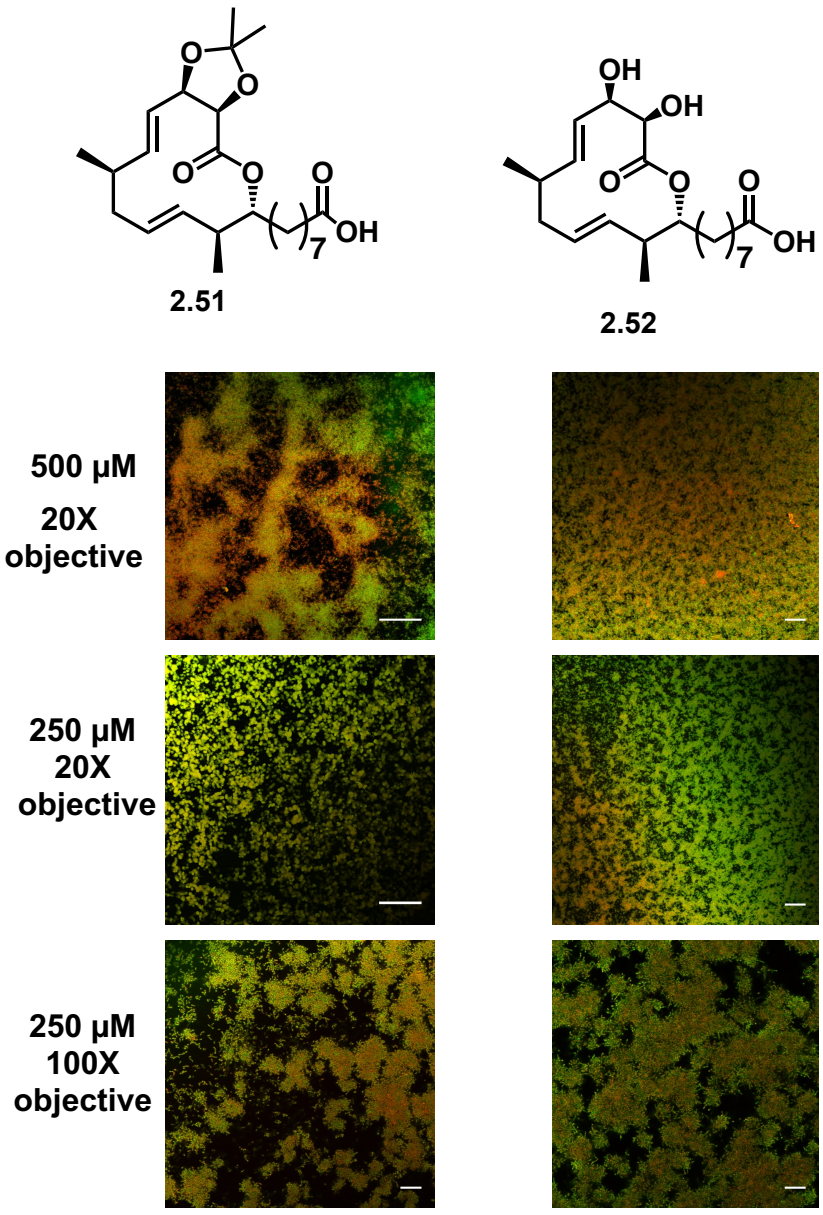

Figure S5. Confocal images of 2.37

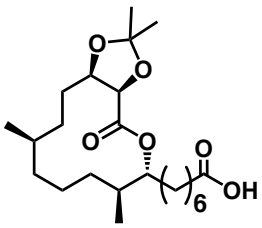

2.37

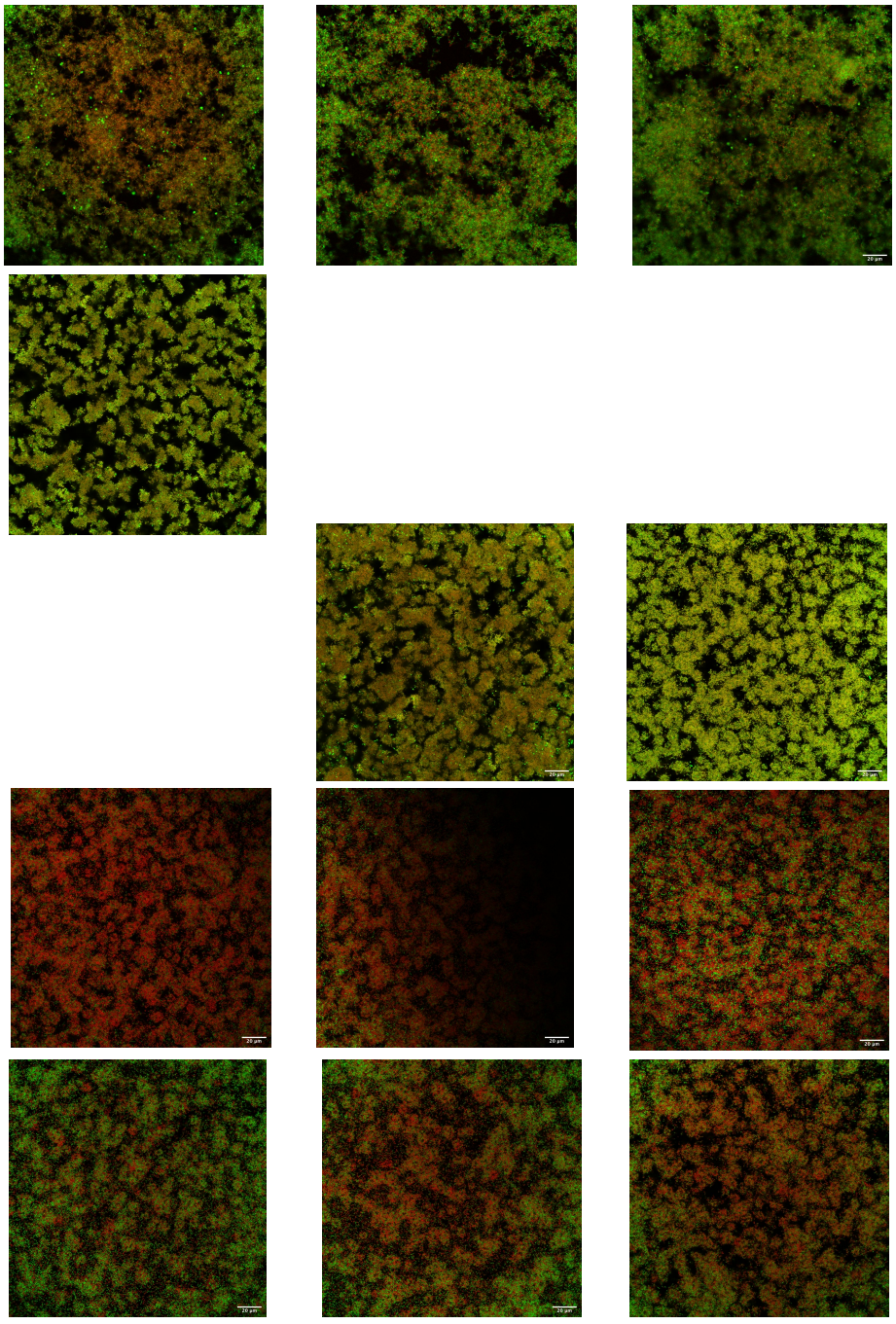

Figure S6. Confocal images of A2 and A2-PP treated cells

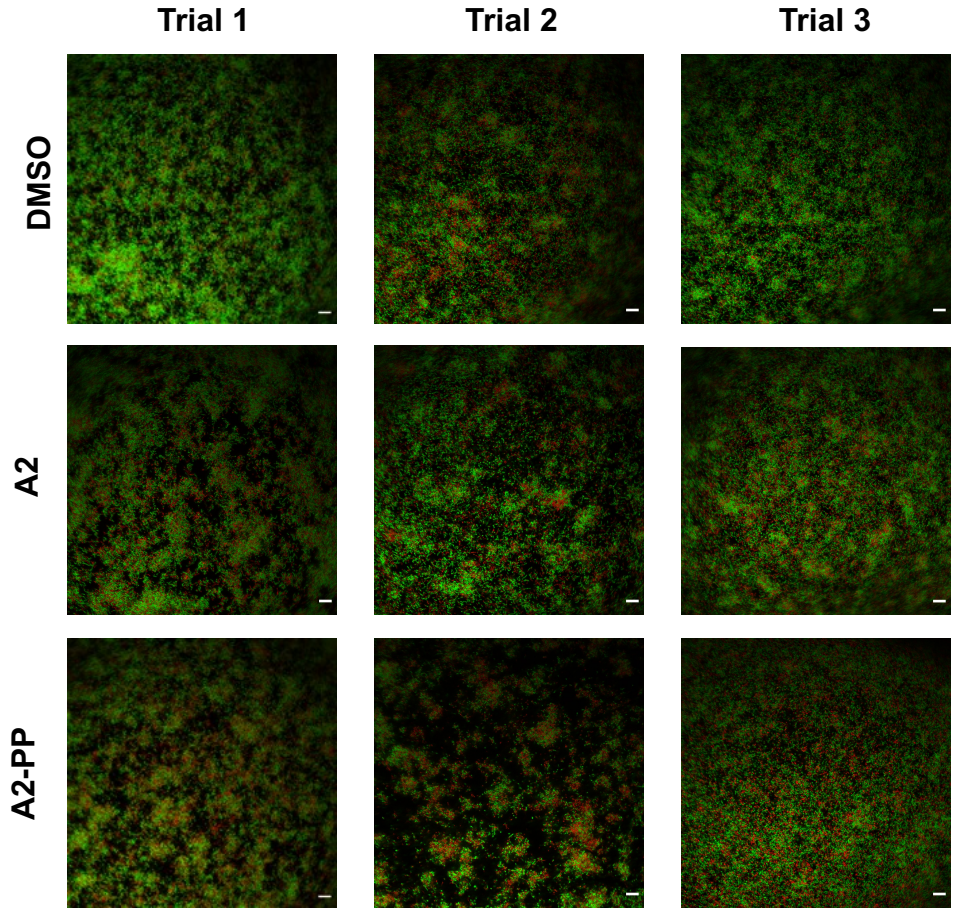

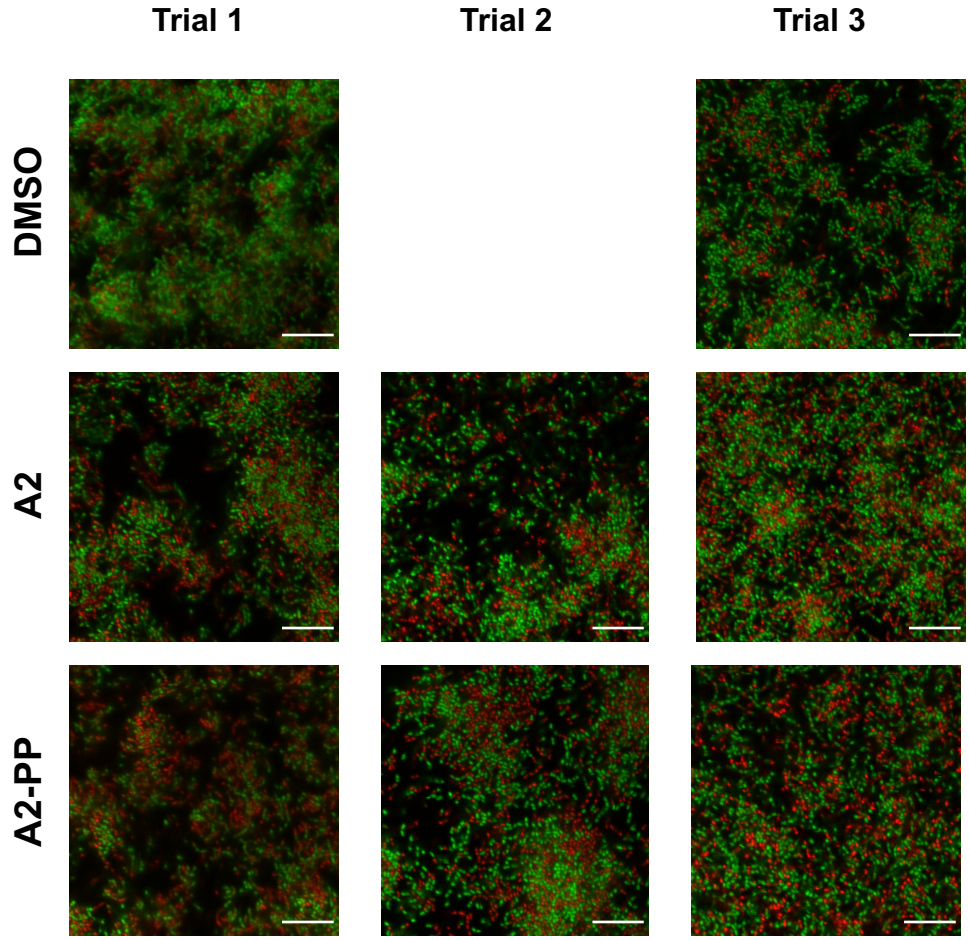
Trial 1
Trial 2
Trial 3
DMSO
A2
A2-PP
5 uM
60X optical lens
(4X ZOOM)
Scale bar 10 nM

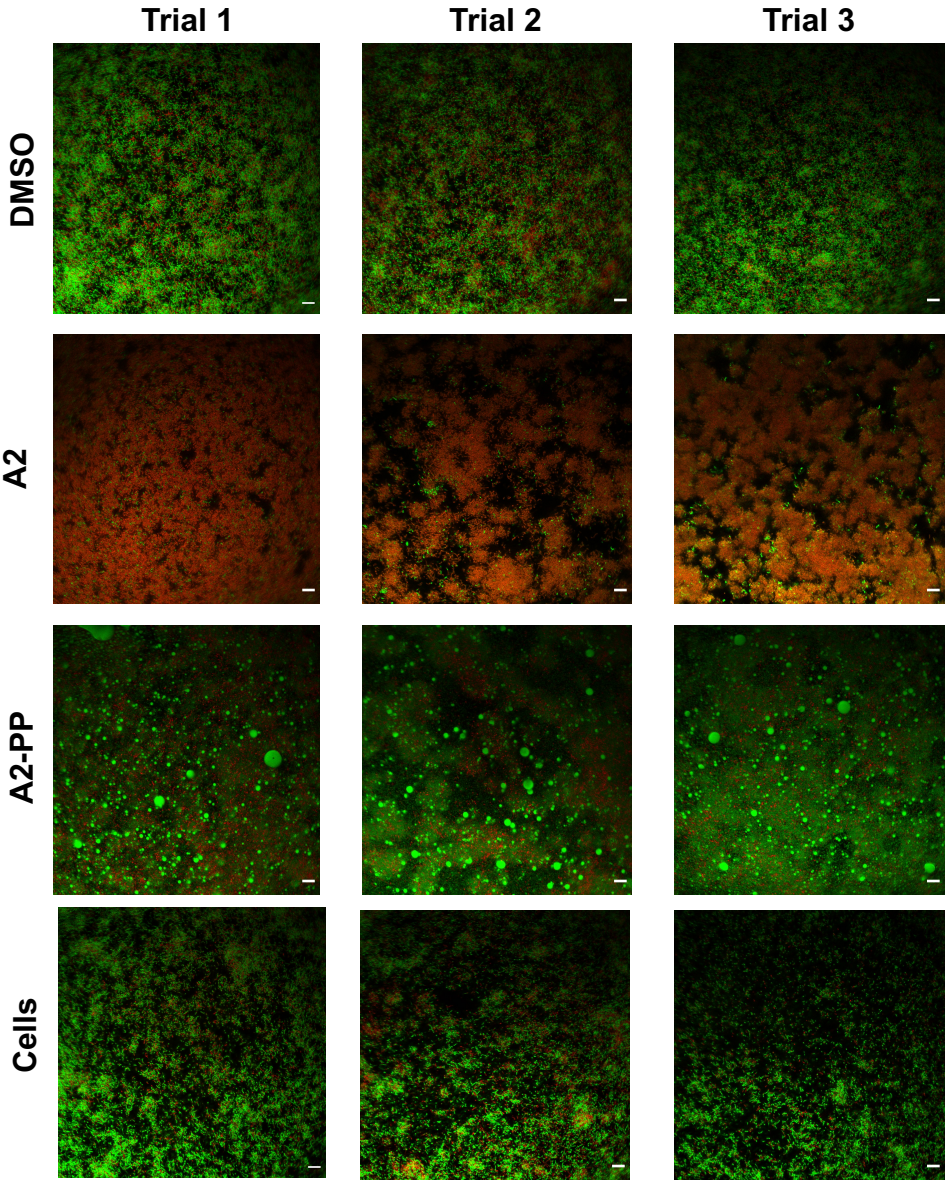
Trial 1
Trial 2
Trial 3
DMSO
A2
A2-PP
Cells
125 uM
60X optical lens
10 nM scale bar

Figure S7. Trial 1 confocal images of AfBPP mutants (63 μM, 100X objective, 10 μM scale bar)

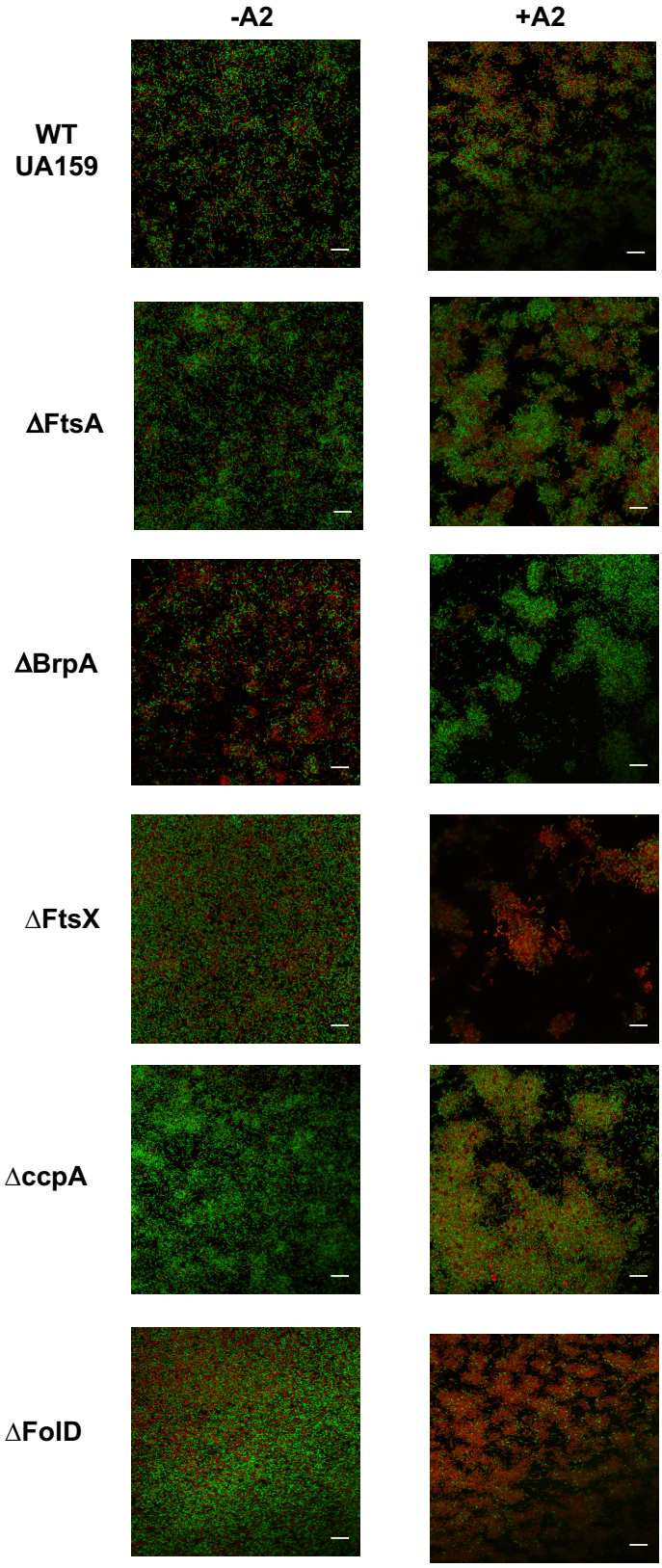

Figure S8. Trial 2 confocal images of AfBPP mutants (63 μM, 60X objective, 10 μM scale bar)

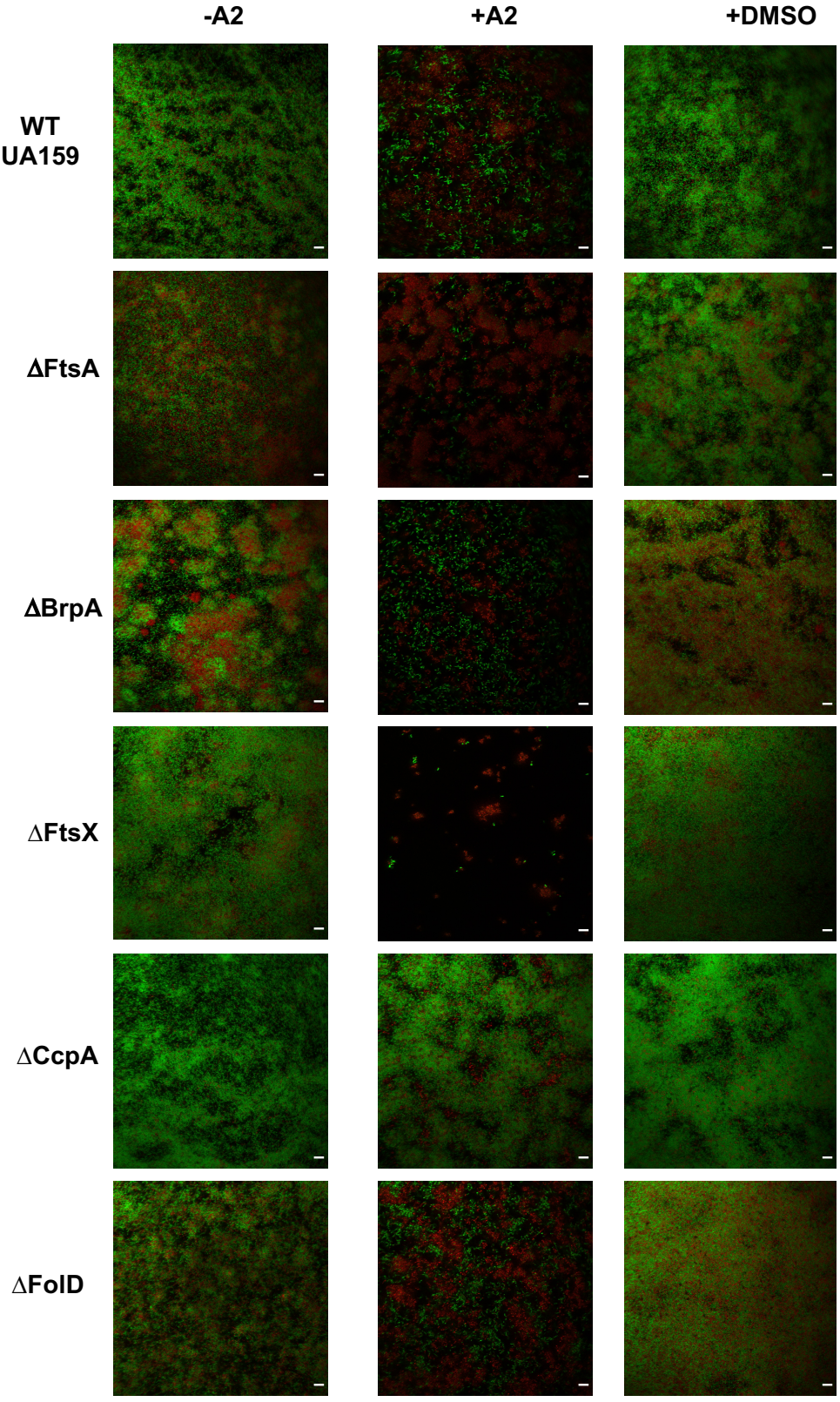

Figure S9. Trial 3 confocal images of AfBPP mutants (63 μM, 60X objective, 10 μM scale bar)

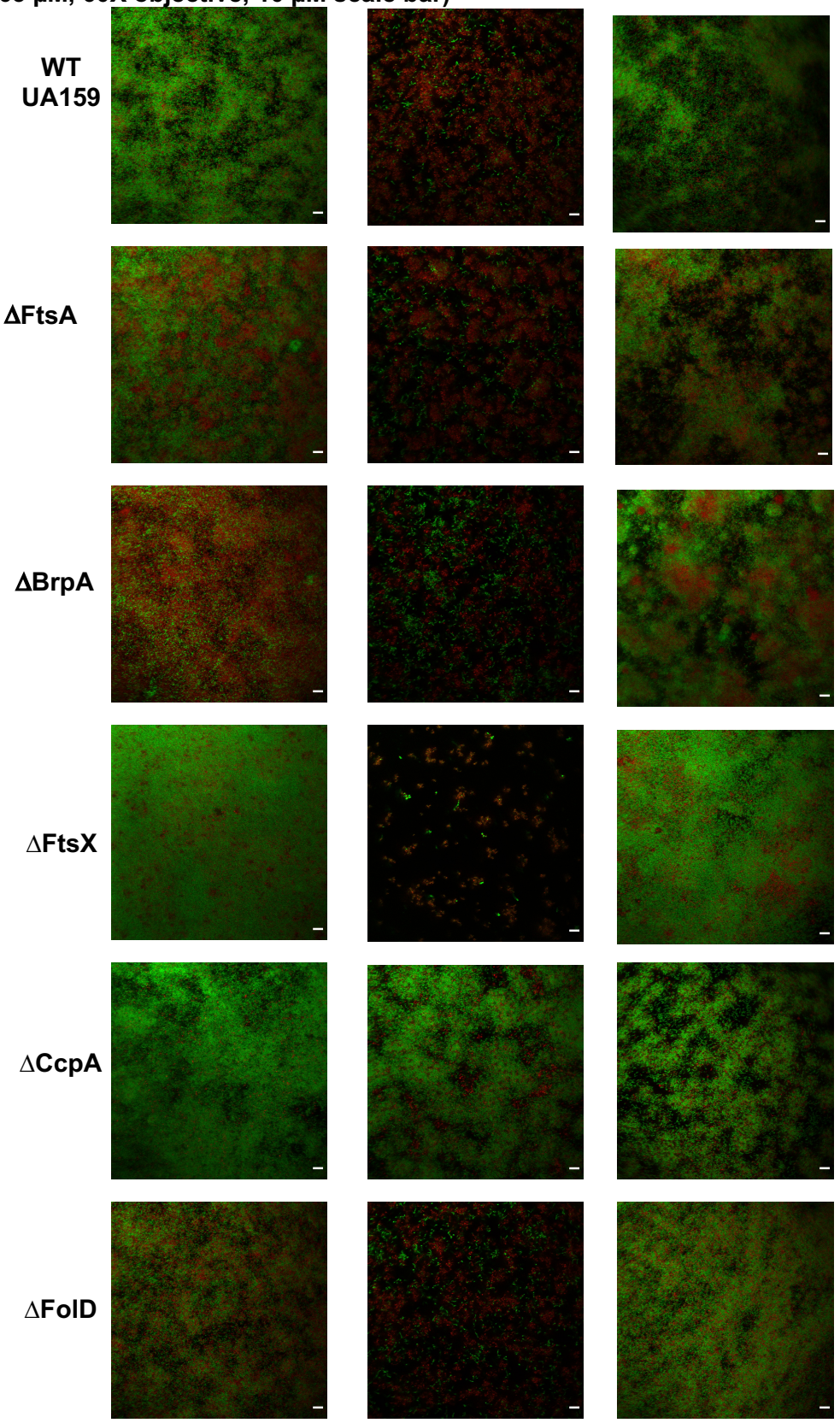

Figure S10. Alignment was computed in T-coffee and the figure was made with ESPript.

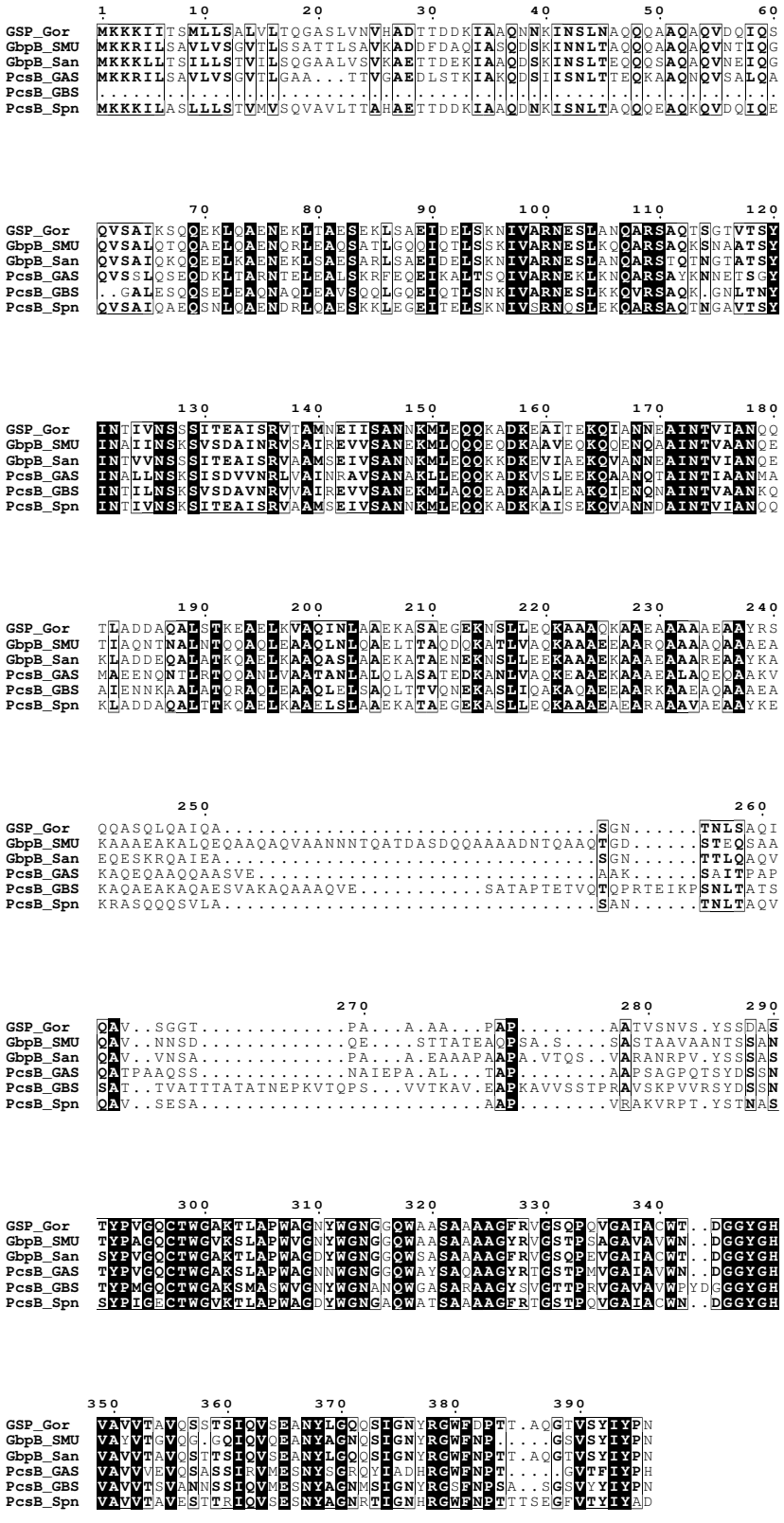

Figure S11 Gels from the expression and purification of His-PcsB

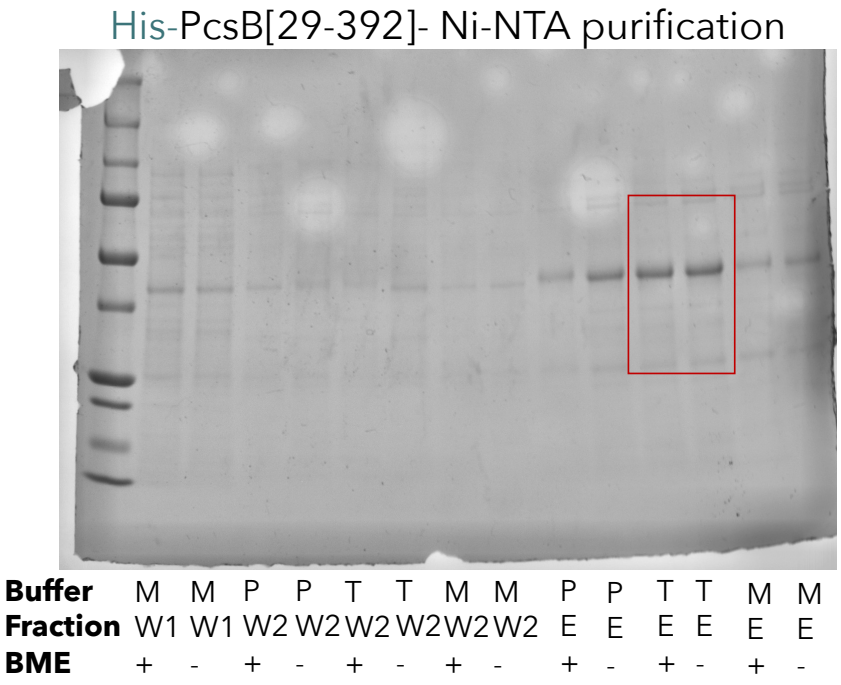

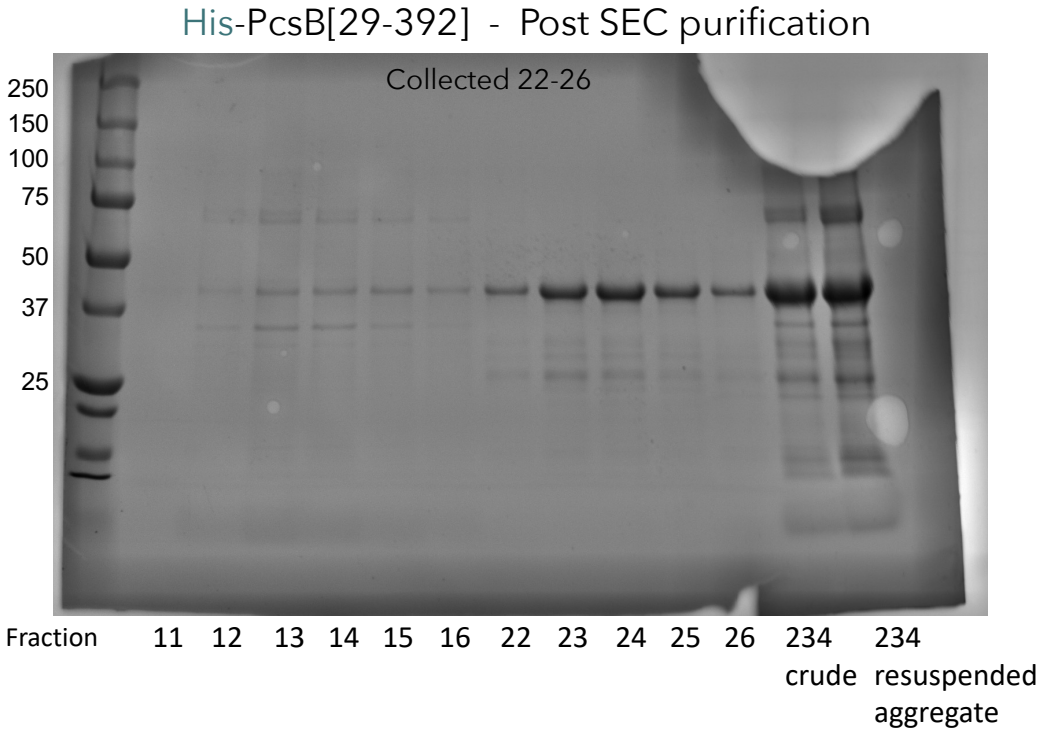

Figure S12 Gels from the expression and purification of PcsB-His

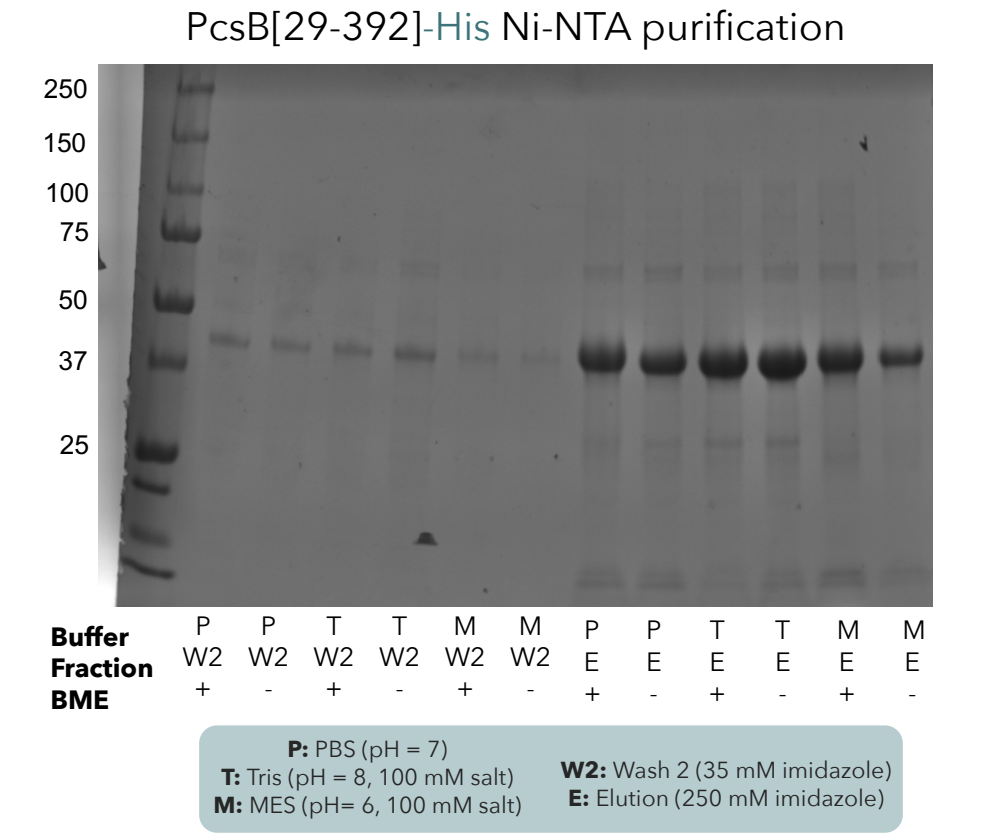

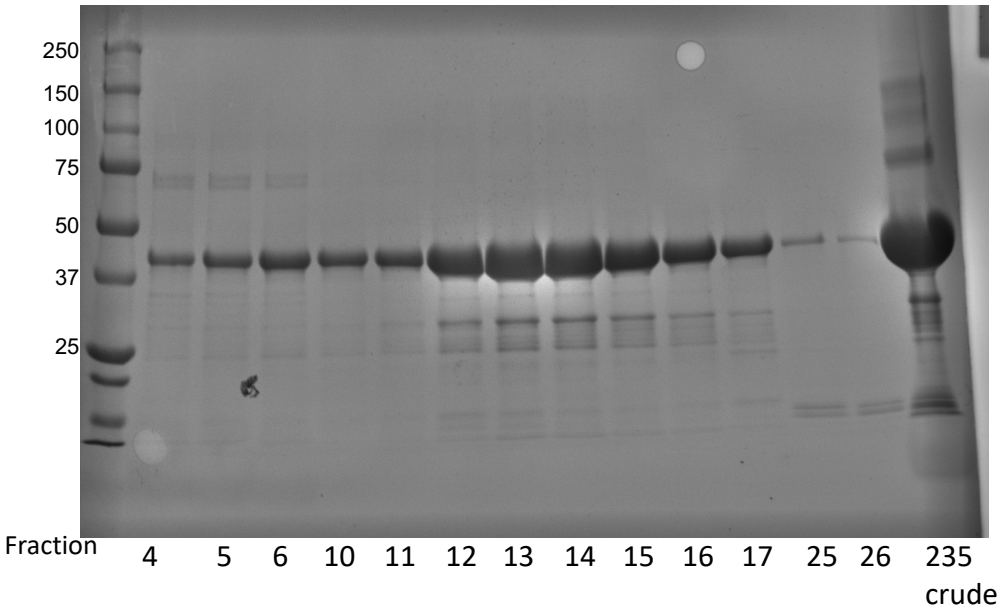

6.2 Biological procedures

6.2.1 General notes

Streptococcus mutans wild-type strain UA159 was used for all bacterial cultures and was provided by Dr. Bettina Buttaro from Temple University Medical School, Philadelphia, PA. Bacteria were routinely maintained in BactoTM Todd-Hewitt (TH) agar plates and liquid cultures were grown in in BactoTM Todd-Hewitt broth (THB). For growth of *S. mutans* biofilms, THB was supplemented with 0.1% sucrose, unless otherwise noted. Incubation was stagnant at 37 °C in a microaerophilic environment (5% CO2). *S. mutans* mutants were provided by Dr. Robert G. Quivey from the Department of Microbiology and Immunology of University of Rochester. Bacterial mutants were maintained in BactoTM Todd-Hewitt broth supplemented with erythromycin. *Streptococcus gordonii* strain DL1 and *Streptococcus sanguinis* strain 10904 were provided by Dr. Robert G. Quivey from University of Rochester Medical School. *Streptococcus pneumoniae* D39 and TIGR4 were provided by Dr. Chris LaRock at Emory University. *Streptococcus pyogenes* (ATCC700294) and *Streptococcus alagactiae* (ATCC BAA-1138) were purchased from ATCC. For all biological assays in Chapter 5, laboratory strains of methicillin-susceptible *Staphylococcus aureus* MSSA (SH1000), *Enterococcus faecalis* (OG1RF), *Escherichia coli* (MC4100), *Pseudomonas aeruginosa* (PAO1), community-acquired methicillin-resistant *Staphylococcus aureus* CA-MRSA (USA300-0114), and hospital-acquired methicillin-resistant *Staphylococcus aureus* HA-MRSA (ATCC 33591) were grown with shaking at 37 ºC overnight from freezer stocks in 5 mL of the indicated media: SH1000, OG1RF, MC4100, USA300-0114 , and PAO1 were grown in BD™ Mueller-Hinton broth (MHB), whereas ATCC 33591 was grown in BD™ tryptic soy broth (TSB). Optical density (OD) measurements were obtained using a SpectraMax iD3 plate reader (Molecular Devices, United States). *E. coli* was grown in Miller lysogeny broth (LB) or on LB with 2% agar at 37°C. Antibiotics were purchased from VWR. Vectors and bacterial strains NovaBlue (DE3) and BL21(DE3) were obtained from Novagen. Oligonucleotide primers for PCR were

purchased from GENEWIZ.

6.2.2 Procedures

S. *mutans* MIC assay

Stock solution of carolacton analogs, 10,000 μM in DMSO, were serial diluted in THB media in flat-bottom 96-well microtiter plates. Mid-exponential phase cell culture was diluted to an OD_{600} of 0.004 and added to the serial diluted compound to reach a final volume of 200 μL. Plates are incubated at 37 °C in 5% CO_2 for 20-24 hours upon which time wells are evaluated visually for bacterial growth and the OD_{600} was recorded with the plate reader. The MIC is determined as the lowest concentration of compound resulting in no bacterial growth visible to the naked eye. The IC_{50} is the concentration of compound needed for 50% growth inhibition. Biological triplicates were performed in three separate experiments to confirm results.

Compound treated *S. mutans* biofilm preparation model

Stock solution of carolacton analogs, 10,000 μM, were serial diluted in THB media with 0.1% sucrose (w/v) in glass flat-bottom 96-well microtiter plates. Mid-exponential phase cell culture was diluted to an OD_{600} of 0.004 and added to the serial diluted compound to reach final volume of 200 μL. Plates were incubated at 37 °C in 5% CO_2 for 24-28 hours (early-stage biofilm) at which time wells were evaluated visually for bacterial growth. OD_{600} measurements of growth was performed after visual inspection. Biological triplicates were performed in three separate experiments to confirm results.

Colony-Forming Units Assay

Compound treated *S. mutans* biofilms were prepared as described above. Plates were incubated at 37 °C in 5% CO_2 for 28 hours (early-stage biofilm) at which time wells were evaluated visually for bacterial growth. OD_{600} measurements of growth was performed after visual inspection, and then emptied by inverting carefully, as to not disturb the biofilm. Wells were washed with 200 μL

of phosphate buffer solution (PBS) or THB media to remove planktonic cells three times. Following the washes, 200 µL of PBS were added, and the biofilm cells were resuspended. Then, the biofilm suspensions were diluted in PBS or THB, in log fashion, and plated on THB agar plates. Plates were incubated for 24-48 hours, and colonies were counted.

***S. mutans* mutant screen**

10,000 µM stock solutions were serial diluted in THB media with 0.1% sucrose (w/v) in glass flat-bottom 96-well microtiter plates. Each mutant was grown with compound, and separately with the DMSO vehicle. Mid-exponential phase cell culture was diluted to an OD_{600} of 0.004 and added to the serial diluted compound or DMSO control to reach final volume of 200 µL. Plates were incubated at 37 °C in 5% CO_2 for 24 hours (early-stage biofilm) at which time wells were evaluated visually for bacterial growth. OD_{600} measurements of growth was performed after visual inspection.

***S. mutans* $MBIC_{50}$ assay**

Biofilms were prepared with above procedure, evaluated visually, OD_{600} of bacterial growth was recorded, and then emptied by inverting carefully, as to not disturb the biofilm. Wells were washed with 200 µL of phosphate buffer solution (PBS) and dried overnight at 37°C. Once dry, plates were incubated for 10 min at room temperature with 200 µL of 1% w/v crystal violet in DI H_2O. Excess crystal violet was removed by aspirating off the liquid and performing DI H_2O rinses until the runoff was colorless. Plates were then inverted and dried overnight at 37°C. Crystal violet-stained biofilm was dissolved with 200 µL of 10% acetic acid in DI H_2O. The crystal violet plate with acetic acid solution was allowed to incubate at room temperature for 10-30 minutes to allow for full dissolution. Then 100 µL was transferred to a fresh flat-bottom 96-well plate for absorbance measurements at 595 nm. DMSO controls corresponding to each test concentration were performed. Crystal violet reading was set relative to bacterial growth (OD_{595}/OD_{600}) to allow for

appropriate comparison of biofilm mass formation. $MBIC_{50}$ refers to the concentration at which biofilm growth is inhibited by 50% compared to the control. Biological triplicates were performed in three separate experiments to confirm results.

Confocal Imaging

Biofilms were prepared with above procedure. To perform efficient imaging, uncoated 96-Well Plates with 5 mm Glass Diameter from MatTek (Part No: P96G-0-5-F) were used for confocal imaging experiments. After incubation, media was removed, and each well was carefully rinsed three times with PBS to remove planktonic cells. Subsequently, 20 µL of BacLight LIVE/DEAD™ stain was added to each well. Excess dye was rinsed off biofilm with PBS. Images of biofilms were then obtained using the Olympus FV1000 inverted microscope in the Integrated Cellular Imaging Core at Emory University.

Resistance development assays

Stock solution of compound, 10,000 µM, were serial diluted in THB media with 0.1% sucrose (w/v) in glass flat-bottom 96-well microtiter plates. Mid-exponential phase cell culture was diluted to an OD_{600} of 0.004 and added to the serial diluted compound to reach final volume of 200 µL. Plates were incubated at 37 °C in 5% CO_2 for 24 hours. Biofilm cultures were serial passaged and exposed to increasing concentrations of **A2** over 24 days.

Checkerboard assay

Synergy was tested by the checkerboard method, a two-dimensional array of serial concentrations of test compounds. The MIC of each antibiotic used was determined under the checkerboard assay conditions prior to determine the concentration ranges to examine. One compound is serial diluted down the plate and the other across the plate. Mid-exponential phase cell culture was diluted to an OD_{600} of 0.004 and added to the serial diluted compound to reach a

final volume of 200 µL. Plates are incubated at 37 °C in 5% CO_2 for 20-24 hours upon which time wells are evaluated visually for bacterial growth and the OD_{600} was recorded with the plate reader.

QPC MIC assay

Compounds were serially diluted two-fold from stock solutions (1.0 mM) to yield twelve 100 µL test concentrations, wherein the starting concentration of DMSO was 2.5%. Overnight *S. aureus, E. faecalis, E. coli, P. aeruginosa,* USA300-0114 (CA-MRSA), and ATCC 33591 (HA-MRSA) cultures were diluted to ca. 106 CFU/mL in MHB or TSB and regrown to mid-exponential phase, as determined by optical density recorded at 600 nm (OD_{600}). All cultures were then diluted again to ca. 106 CFU/mL and 100 µL were inoculated into each well of a U-bottom 96-well plate (Corning, 351177) containing 100 µL of compound solution. Plates were incubated statically at 37 ºC for 72 hours upon which wells were evaluated visually for bacterial growth. The MIC was determined as the lowest concentration of compound resulting in no bacterial growth visible to the naked eye, based on the highest value in three independent experiments. Aqueous DMSO controls were conducted as appropriate for each compound.

Red Blood Cell (RBC) Lysis Assay (Lysis20)

RBC lysis assays were performed on mechanically defibrinated sheep blood (Hemostat Labs: DSB030). An aliquot of 1.5 mL blood was placed into a microcentrifuge tube and centrifuged at 3,800 rpm for ten minutes. The supernatant was removed, and the cells were resuspended with 1 S 2mL of phosphate-buffered saline (PBS). The suspension was centrifuged as described above, the supernatant was removed, and cells were resuspended 4 additional times in 1 mL PBS. The final cell suspension was diluted twentyfold with PBS. Compounds were serially diluted with PBS twofold from stock solutions (1.0 mM) to yield 100 µL of twelve test concentrations on a flat-bottom 96-well plate (Corning, 351172), wherein the starting concentration of DMSO was 2.5%. To each of the wells, 100 µL of the twentyfold suspension dilution was then innoculated.

The concentration of DMSO in the first well was 2.5%, resulting in DMSO-induced lysis at all concentrations >63 μM. TritonX (1% by volume) served as a positive control (100% lysis marker) and sterile PBS served as a negative control (0% lysis marker). Samples were then placed in an incubator at 37 ºC and shaken at 200 rpm. After 1 hour, the samples were centrifuged at 3,800 rpm for ten minutes. The absorbance of the supernatant was measured with a UV spectrometer at a 540 nm wavelength. The concentration inducing 20% RBC lysis was then calculated for each compound based upon the absorbances of the TritonX and PBS controls. Aqueous DMSO controls were conducted as appropriate for each compound.

Whole Genome Sequencing and Analysis

Bacterial genomic DNA was extracted using a DNeasy Blood and Tissue Kit (Qiagen, Germantown, MD) from 1 mL overnight bacterial cultures. Next-generation sequencing libraries were prepared with a Nextera kit (Illumina, San Diego, CA), and libraries were sequenced at the Microbial Genome Sequencing Center (MiGS) on an Illumina NextSeq using 150bp paired-end reads. Single nucleotide polymorphisms (SNPs) were identified in resistant mutant genomes by mapping sequencing reads to the annotated UA159 reference genome (GenBank Accession AE014133, https://pubmed.ncbi.nlm.nih.gov/12397186/) using CLC Genomics Workbench v11.0.1. Each identified SNP had a minimum coverage of 10 reads and a minimum frequency of 80%.

Label-free AfBPP in growing biofilm

5 mL of THB media was inoculated with *S. mutans* (UA159) from freezer stock and grown overnight. The overnight culture was diluted (1:100) and regrown to OD_{600} = 0.4 (exponential phase). To a petri dish, 200 μl of 100X stock solution of **A2-PP** was added to 19.8 mL of THB sucrose 0.1% sucrose (w/v). Petri dishes were incubated at 37 °C in 5% CO_2 for 24 hours. Petri dishes were then immediately irradiated with UV light (280-315 nm). Irradiation cycle was repeated three times (6 minutes irradiation, 6 minutes on cold pack). Then the biofilm supernatant

was removed, and the biofilm was carefully rinsed with PBS three times. Biofilm cells were resuspended with 10 mL of PBS and transferred to 25 mL falcon tubes. Samples were centrifuged for 10 minutes (6000 x g, 4°C), supernatant discarded, and pellet was transferred to Eppendorf tube with 800 µL of PBS. The samples were then again centrifuged for 10 minutes (6,000 g, 4°C), supernatant was disposed, and pellet was resuspended in PBS with 0.4% SDS (4 °C). Bacterial cell lysis was completed with 3 cycles of 30 second sonification at 80% intensity. Samples were then centrifuged at 20,000 x g for 30 minutes (4 °C) thus separating the soluble fraction (supernatant) and the insoluble fraction (pellet). Samples were then processed according to the gel-based AfBPP or the gel-free AfBPP procedure described below.

Gel-based AfBPP

With the soluble fraction, we performed click chemistry with rhodium azide using a freshly prepared “master mix”. Master mix included (per sample) 2 µl of RhN_3 [TAMRA Azide (Tetramethylrhodamine 5-Carboxamido-(6-Azidohexanyl)] (10 mM in DMSO), 2 µl TCEP (52 mM, 15 mg/mL in dd H_2O), and 6 µl TBTA ligand (1.677 M 1 x ligand; 800 uL t-BuOH, 180 µL DMSO, 20 µL 50 x ligand) (50 x ligand = 8.85 mg in 200 uL DMSO). 88 µL of the soluble fraction and 10 µL of the master mix were combined in an Eppendorf and vortexed. Then, 2 µL of 50 mM CuSO4 were added to each sample and vortexed. Samples were incubated for 1 hour at RT in the dark. 100 µl of 2 X SDS loading buffer were added to the samples, vortexed analyzed by SDS-PAGE with fluorescence scanning. Protein loading was visualized by Coomassie-staining of the gels.

Gel-free and label-free AfBPP

Protein concentration was measured with the BCA Assay and samples were adjusted to 0.63 mg/mL using PBS + 0.4% SDS buffer (total volume of 500 µL of each sample). Click chemistry was performed with biotin azide using a freshly prepared “master mix”. Master mix included (per 500 µL sample) 3 µL of biotin azide (10 mM in DMSO), 10 µL TCEP (52 mM, 15 mg/mL in dd H2O), and 30 µL TBTA ligand (1.677 M 1 x ligand; 800 uL t-BuOH, 180 µl DMSO, 20 µL 50 x

ligand) (50 x ligand = 8.85 mg in 200 uL DMSO), and 10 µl of $CuSO_4$ (50 mM stock in dd H_2O). 500 µL of the soluble fraction and 53 µL of the master mix were combined in a 15 mL falcon tube, vortexed and incubated for 1 hour at RT in the dark. Proteins were precipitated by adding 4x volume (2 mL) cold acetone (-80 °C). Samples were then stored at -20 °C overnight). Precipitated proteins were pelletized for 15 minutes at 16900 x g at 4 .C and the supernatants were discarded. Protein pellets were washed twice with 500 µL of cold methanol (-80 °C) and resuspension with sonication (10 seconds, 10% intensity, Sonopuls HD 2070 ultrasonic rod, Bandelin electronic GmbH). Pelletize protein for 15 minutes at 16900 x g at 4 °C, discard supernatant and resuspend protein pellet in 500 µL 0.4% SDS in PBS (at RT) by sonication (10 seconds, 10% intensity, Sonopuls HD 2070 ultrasonic rod, Bandelin electronic GmbH). Protein enrichment was then started by transferring 50 µL of Avidin bead suspension into Protein LoBind Eppendorf tubes with a cropped pipette tip. Beads were washed with 1 mL of 0.4% SDS (MS grade) in PBS three times (3 minutes, 400 x g). Incompletely solubilized protein aggregates were removed with centrifugation, and then 0.5 mL of protein sample was transferred to the LoBind Eppendorf tubes containing the Avidin beads. Samples were incubated at RT with continuous mixing for 1 hour. To remove any bound proteins, beads were then washed three times with 1 mL 0.4% SDS in PBS (MS grade), two times with 1 mL 6 M urea in ddH_2O (MS grade) and three times with 1 mL PBS (MS grade). For quantitative mass spectrometric analyses, avidin agarose beads with bound proteins were resuspended in200 uL of X buffer (7 M urea, 2 M thiourea in 20 mM HEPES buffer pH 7.5). Upon on-bead reduction with TCEP (5 mM) for 1 hour at 37 .C, proteins were alkylated using of iodoacetamide (10 mM) at RT for 30 minutes in the dark and samples were quenched with dithiothreitol (DTT, 10mM9 at RT for 30 min. The protein samples were digested with LysC (1 µL per sample) for 2-4 hours at RT. Samples were then diluted with 600 µL of 50 mM of TEAB, 1.5 µL of 0.5 µg/µL trypsin (sequencing grade, modified, *Promega*) was added and the samples were incubated overnight at 37 °C under continuous shaking (450 rpm). On the next day, digestion was stopped by adding 10 µL of FA to the samples. The pH was checked (3 or below). Samples

were centrifuged to pelletize the beads. Samples were desalted by using 50 mg SepPak C18 columns (Waters) equilibrated with equilibrated with 1 mL of 0.1% TFA. Samples were loaded and the peptides were washed three times with 1 mL 0.1% TFA, and then 500 µL 0.5% FA. Finally, the peptide samples were then eluted off the column with 250 µL 80% MeCN/0.5% FA, three times, lyophilized and stored at -80 °C until further usage.

LCSM analysis

Before MS measurements, the lyophilized peptides were resolved in 25-40 µL 1% FA and filtered through 0.22 µm PVDF filters (*Millipore*), which were equilibrated with 300 µL 1% FA. The filtrates were transferred into MS-vials and stored at –20 °C until the measurements were performed. Samples were analyzed with an UltiMate 3000 nano HPLC system (*Dionex*) using an Acclaim C18 PepMap100 (75 µm ID × 2 cm) trap column and an Acclaim PepMap RSLC C18 (75 µm ID × 50 cm) separation column coupled to a Q Exactive Plus (*Thermo Fisher*) in EASY-spray setting. Samples were loaded on the trap column and washed with 0.1% TFA, then transferred to the analytical column (buffer A: H_2O with 0.1% FA, buffer B: ACN with 0.1% FA, flow 300 nL/min, gradient 5 to 22% buffer B in 115 min, then to 32% buffer B in 10 min, then to 90% buffer B in 10 min and hold 90% buffer B for 10 min, then to 5% buffer B in 0.1 min and hold 5% buffer B for 9.9 min). Q Exactive Plus was operated in a TOP10 data dependent mode. Full scan acquisition was performed in the orbitrap at a resolution of 140,000 and an AGC target of $3e^6$ (maximum injection time of 80 ms) in a scan range of 300−1,500 m/z. Monoisotopic precursor selection as well as dynamic exclusion (exclusion duration: 60 s) was enabled. Precursors with charge states of >1 and intensities greater than $1e^5$ were selected for fragmentation. Isolation was performed in the quadrupole using a window of 1.6 m/z. Precursors were collected to an AGC target of $1e^5$ (maximum injection time of 100 ms) and acquisition was performed at a resolution of 17,500 in a scan range of 200−2,000 m/z. Fragments were generated using higher-energy collisional dissociation (HCD, normalized collision energy: 27%) and detected in the orbitrap.'

MS data analysis

Raw files were analyzed using MaxQuant software (version 1.6.2.10) with the Andromeda search engine. The following settings were applied: fixed modification: carbamidomethylation (cysteine); variable modification: oxidation (methionine), acetylation (*N*-terminus); proteolytic enzyme: trypsin/P; missed cleavages: 2; main search tolerance: 4.5 ppm; MS/MS tolerance: 0.5 Da; false discovery rates: 0.01. The options "LFQ" and "match between runs" (0.7 min match and 20 min alignment time windows) were enabled; "second peptides" was disabled.[2] Searches were performed against the UniProt database for *S. mutants* UA159 (taxid: 210007, 29th July 2019).

Statistical analysis of the data was performed using Perseus (version 1.6.14.0.).[3] Putative contaminants, reverse peptides and peptides only identified by site were deleted. LFQ intensities were $\log_2$-transformed, and data was filtered for three valid values in at least one group and missing value imputation was performed over the total matrix. For statistical evaluation, $-\log_{10}$(*P* values) were obtained by a two-sided two sample Student's *t*-test.

Construction of overexpression strains in *S. mutans* UA159

The full length of GbpB gene was amplified by PCR using primer set GbpB-Sal1-F (TCAGTCGACATGAAAAAAAGAATTTTATCA) and GbpB-Kpn1-R (TCAGGTACCTTAGTTTGGATAGATATAGCT). The amplified PCR fragments were digested with *Sal*I and *Kpn*I, and then ligated into *E. coli*-Streptococcal shuttle vector pVPT (erythromycin resistant) (Zhou, Fives-Taylor et al. 2008), yielding pVPT-GbpB. The resulting plasmid was selected by LB plate with erythromycin resistance and confirmed by sequencing. The pVPT-GbpB was transformed into *S. mutans* UA159 for GbpB overexpression studies. The overexpression strain of BrpA was generated by the same method as GbpB. The full length of BrpA gene was amplified by primer set BrpA-Sal1-F (TCAGTCGACATGAAGATTGGTAAAAAAATT) and BrpA-Kpn1-R (TCAGGTACCTTAATTACCAATTCCCGTTCC), inserted into pVPT vector to generate

pVPT-BrpA. The pVPT-BrpA was transformed into BrpA mutant strain for BrpA overexpression studies.

Biofilm formation assay for overexpression

S. mutans biofilm was grown in Tryptic Soy Broth with 1% Yeast Extract (TSBYE medium) containing 0.5% sucrose or Brain Heart Infusion broth with 0.5% sucrose. Overnight cultures were subcultured into fresh TSBYE, grown to an optical density at 600 nm (OD_{600}) of 0.6. It subsequently diluted at 1:100 to 200uL biofilm medium (TSBYE with 0.5% sucrose) in a polystyrene 96-well plate (Nunc, Thermo Scientific), and grown at 5% CO_2 at 37°C under static conditions The OD_{600} was measured to evaluate growth effects. Biofilm samples were then collected after 16 h and stained with 0.1% crystal violet for 15 min. The well was rinsed 3 times and the crystal violet was solubilized in 200 uL of 30% acetic acid. The OD_{562} was used to measure biofilm formation (Wu, Zeng et al. 2007). Each assay was performed in triplicate and replicated three times.

Protein expression and purification

Plasmids were confirm using Sanger sequencing and transformed into BL-21(DE3). *E. coli* BL21 (DE3) containing the desired expression plasmid was inoculated into LB-Miller broth with the appropriate antibiotic and grown at 37 °C overnight. The overnight culture was diluted 200-fold into LB-Miller broth containing antibiotic, $MgSO_4$ and glycerol. The cells were grown at 37 °C until OD_{600} reached 0.6, and isopropyl-1thio-β-D-galactopyranoside (IPTG) was added to a final concentration of 100 μM and incubated for 4 hours at 30 ºC or overnight at 16 ºC. Following incubation, cells were harvested by centrifugation at 5020 x g for 30 minutes. Cell pellets were washed with 150 mL 20 mM Tris pH 8 containing 100 mM NaCl and flash-frozen with liquid nitrogen, and then thawed. Pellets were resuspended in 1mM PMSF, 1 tablet of Roche cOmplete

protease inhibitor cocktail, 1:100 lysosyme (100 mg/mL) and 1:100 DNAse (50 mg/mL). Cells were homogenized using an Ultraturrax and lysed by three passages through an Avestin EmulsiFlex-C5 disruptor. Cell lysates were clarified by centrifugation at 47,000 x g for 60 minutes. The supernatants were applied to preequilibrated nickel-NTA resin. Protein was eluted with 3 column volumes of 20 mM Tris pH 8 containing 100 mM NaCl. Proteins were concentrated using 30 molecular weight cut-off (MWCO) Amicon Ultra centrifuge filter device (Millipore). The supernatant was purified by size-exclusion chromatography using an ÄKTA-pure (Cytiva) and a Superdex 200 increase column in 20 mM Tris pH 8 containing 100 mM NaCl. The desired protein fractions were collected and concentration to 1 mg/mL. Purified protein concentrations were evaluated by NanoDrop 2000 (ThermoFisher) using the Protein A280 method. Following purification by affinity column and SEC, protein fractions were assayed for purity by separation on SDS-PAGE (sodium dodecyl sulfate - polyacrylamide gel electrophoresis) and either Coomassie staining or Western blot. For Western blotting, the gel was transferred to methanol-activated polyvinylidene fluoride (PVDF) membranes (Bio-Rad Laboratories). The membrane was blocked with 10 mL casein blocking buffer and probed with α-His-HRP (1:5,000, BioLegend). Proteins were detected using the Amersham enhanced chemiluminescence (ECL) reagent and imaged on an Azure c400.

Microscale Thermophoresis (MST)

All His_6-tagged proteins were labeled using the Protein Labeling Kit RED-NHS (NanoTemper Technologies). The labeling reaction was performed according to the manufacturer's instructions. The labeled proteins were adjusted to 10 nM with 50 mM HEPES buffer (150 mM NaCl, pH = 7.4) supplemented with 0.05 % Tween 20 (unless otherwise noted). Ligands were prepared as a DMSO stock from either a 10 mM stock or a 50 mM stock and diluted in 50 mM HEPES buffer (150 mM NaCl, pH = 7.4) supplemented with 0.05 % Tween 20, and a series of 16 1:1 dilutions was prepared using the same buffer, producing ligand concentrations ranging from 0.03 µM to

1000 µM. For the measurement, each ligand dilution was mixed with one volume of labeled protein, which led to a final concentration of protein of 10 nM and final ligand concentrations ranging from 0.015 µM to 500 µM. After 10 min incubation followed by centrifugation at 15 000 × g for 10 min at 4 °C, the samples were loaded into Monolith NT.115 [Premium] Capillaries (NanoTemper Technologies). The MST measurements were performed using a Monolith NT.115 Pico instrument (NanoTemper Technologies) at an ambient temperature of 25 °C. Instrument parameters were adjusted to 20 % LED power and medium MST power.

MST Data Analysis

Data of three (unless otherwise noted) independently pipetted measurements were analyzed (MO.Affinity Analysis software version 2.3, NanoTemper Technologies) using the signal from an MST on time of 1.5 s. We used a conservative definition of outliers, only removing data points where there were irregularities with the absolute fluorescence, capillary scan showed irregularities, MST, or temperature related intensity change (TRIC) traces showed bleaching, or aggregation. The dissociation constants (Kd) were determined using the K_d binding model (Eq. 1), which is based on the Langmuir binding isotherm and is defined as follows: f(c) is the fraction bound at given ligand concentration c. Unbound is defined as the normalized fluorescence signal (Fnorm; MST mode) of the target alone and bound is the normalized fluorescence of the ligand:protein complex. Kd is the dissociation constant or binding affinity, and c(target) is final concentration of the target present in the assay. The concentration used of the target was 10 nM.

$$f(c) = Unbound + \frac{(Bound-Unbound) * c+c(target)+Kd-\sqrt{(c+c(target)+Kd)^2-4c*c(target)}}{2c(target)} \quad \text{Eq. (1)}$$

Data was processed for presentation using two methods outlined by Nanotemper Technologies. The first method is baseline corrected normalized fluorescence ΔF_{norm} [%], wherein the baseline F_{norm} value is subtracted from all data points of the same curve. This value is provided by

MO.Affinity Analysis as the ‘unbound’ value when a fit is performed. In cases where a fit was not successful, the average of capillaries 14-16 was taken and used as the baseline F_{norm} value. The second method is represented as fraction bound vs. ligand concentration. Fraction bound values were calculated by dividing the normalized fluorescence (∆Fnorm [%]) by the amplitude of the curve.

In vitro photocrosslinking

In a 96 well plate, compound (10 μM) or DMSO was added to 100 mL of either His-PcsB or PcsB-His (1 mg/mL) in Tris buffer to give a final concentration of 500 mM to ensure saturation. Samples were incubated for 15 minutes on ice. Photo-crosslinking was performed by using a UVP Blak-Ray B-100AP high-intensity UV lamp with a 100-W spot bulb. The lamp was positioned approximately 6 cm away from the samples and the samples were irradiated for 10 minutes. Samples were then split and transferred to 1.5 mL Eppendorf tubes. Subsequently, samples were either analyzed directly by ESI-qTOF-MS for intact protein analysis or further processed for trypsin digest analysis. Molecular weight determination of intact protein was conducted by direct Electro Spray Ionization (ESI) on the Q-TOF Premier and analyzed by the Harvard Center for Mass Spectrometry Proteomics Center.

Processing for proteolytic digest

To prepare samples for trypsin digest, a methanol-chloroform precipitation procedure was employed. Methanol (50 μL) was added to the sample (50 μL) and vortexed. Chloroform (50 μL) was added, and the sample vortexed. The sample was centrifuged for 2 min at 14000 g, and the top layer aspirated off. Methanol (200 μL) was added, the sample was vortexed, centrifuged for 3 minutes at 14000g, and submitted and analyzed by LCMS/MS by the Harvard Center for Mass Spectrometry Proteomics Center.

Molecular docking

Docking was conducted using the Glide grid-based docking module of Maestro (Schrödinger suite) in extra-precision (XP) mode. The refined structure of PcsB downloaded from the PDB database was optimized in Maestro using the Protein Preparation Wizard (Schrodinger, 2010). Ligands were prepared using the LigPrep module of the Schrodinger suite using the OPLS4 force field. The receptor grid was generated by defining the binding site using the cocrystalized ligand. An outer box of 40 X 40 X 40 Å and an inner box of 10 X 10 X 10 Å was used.

Control peptide test

The control peptide test was conducted like all MST experiments. The control peptide was dyed according to manufacturer instructions. Compound was serially diluted in MST buffer, and a constant concentration of dyed peptide was added. Following 10 min incubation, the samples were loaded into the capillaries and measured.

ATTO-488 hydrolase assay

ATTO488-labeled Lipid II (1.4 μM) was polymerized with 1.8 μM $SgtB^{Y181D}$, a monofunctional peptidoglycan glycosyltransferase with impaired processivity, in either pH 7.5 buffer (10x buffer: 500 mM Hepes pH 7.5, 100 mM $CaCl_2$, 600 μM $Zn(OAc)_2$) or pH 6.1 (10x buffer: 500 mM MES pH 6.1, 100 mM $CaCl_2$) at room temperature for 2 h. The polymerization reaction was heat-quenched at 100 °C for 5 min. After cooling, the digestion reaction was set up by adding 1 μL of enzyme to 9 μL of the polymerization reaction product (total volume 10 μL). After incubating the reaction mixtures at room temperature overnight, the reactions were quenched by adding 10 μL 2x Laemmli sample buffer (Bio-Rad). The samples were then loaded onto a 4-20% Mini-PROTEAN TGX Precast Protein gel (Bio-Rad) and run at 180 V. The gels were imaged using a Typhoon FLA 7000 imager using the 488 setting. For the pH 6.1 reaction with all three metals, zinc was added to reaction rather than the buffer. For the magnesium only reactions, metals were not added to the buffer. For the calcium only reactions, zinc was not added to the buffer.

Biotin-D-lysine (BDL) hydrolase assay

Unlabeled lipid II 1.4 μM) was polymerized with 1.8 μM $SgtB^{Y181D}$, a monofunctional peptidoglycan glycosyltransferase with impaired processivity, in either pH 7.5 buffer (10x buffer: 500 mM Hepes pH 7.5, 100 mM $CaCl_2$, 600 μM $Zn(OAc)_2$) or pH 6.1 (10x buffer: 500 mM MES pH 6.1, 100 mM $CaCl_2$) at room temperature for 2 h. The polymerization reaction was heat-quenched at 100 °C for 5 min. After cooling, the digestion reaction was set up by adding 1 μL of enzyme to 9 μL of the polymerization reaction product (total volume 10 μL). After incubating the reaction mixtures at room temperature overnight, the reaction was heat quenched at 100 ºC for 5 min. Then, BDL (1.5 μL of 20 mM stock) and *E. faecalis* PBPX (1 μL of 40 μM stock) were added to the sample and incubated at RT for 1 h. The reaction was quenched by adding 12.5 μL of 2x SDS loading buffer. The final mixture was loaded onto a 15% SDS polyacrylamide gel. The products were transferred to Immun-Blot PVDF membrane (BioRad). BDL-Lipid II was detected by blotting with streptavidin-HRP (1:10000 dilution, Pierce), and visualized using ECL Prime Western Blotting Detection Reagent (GE Ambersham) and Biomax Light Film (Kodak).

6.3 Chemistry experimental

6.3.1 General notes

NMR spectra were recorded using the following spectrometers: Varian INOVA 600, INOVA 500, INOVA 400, VNMR 400, Mercury 300, Bruker AVANCE III HD 600, Bruker NANO HD III 400, Bruker AVANCE 600 WB SSNMR and Bruker AVANCE III 300 WB SSNMR. Chemical shifts are reported in ppm relative to tetramethylsilane and with the indicated solvent as an internal reference. The following abbreviations are used to describe signal multiplicities: s (singlet), d (doublet), t (triplet), q (quartet), m (multiplet), br (broad), dd (doublet of doublets), dt (doublet of triplets), etc. Accurate mass spectra were recorded on a Thermo LTQ FTMS, infrared spectra were obtained using a Thermo Scientific Nicolet iS10 Smart Orbit FT-IR spectrophotometer and specific rotation measurements were collected using a 1 dm path length using a Perkin Elmer 341 Polarimeter. Non-aqueous reactions were performed under an atmosphere of argon, in flame-dried glassware, with HPLC-grade solvents dried by passage through activated alumina. Amine bases were freshly distilled from CaH_2 prior to use. Brine refers to a saturated aqueous solution of sodium chloride. Products purified via flash chromatography using Biotage Isolera Automated column. Reactions monitored via thin-layer chromatography (TLC) using EMD Millipore® TLC silica gel glass plates with $KMnO_4$ or vanillin stain. All products were observed as clear, colorless, or slightly tinted yellow oils.

6.3.2 Procedures and characterization

Representative Procedure A: Parikh-Doering Oxidation

A flame dried flask was charged with the monoprotected diol starting material and DCM. Dimethyl sulfoxide and then triethylamine were then added to the reaction mixture. The reaction was then cooled to 0 °C. SO_3•pyridine was added, and the reaction was allowed to warm to room temperature. After 1 hour of stirring at room temperature, the reaction mixture was diluted with DCM and then quenched with saturated aqueous solution of ammonium chloride. After

separation, the aqueous layer was extracted with ethyl acetate (x3). The combined organics were rinsed with brine (x2), dried over $MgSO_4$, filtered and concentrated.

Representative Procedure B: Roush Crotylation

A flask was charged with a stir bar and powdered 4Å mol sieves and was then flame dried. A solution of *E*-crotylboronate in toluene (prepared via literature procedure)[1] was added, followed by additional toluene. The solution was cooled to –78 °C. The aldehyde was added as a solution in toluene, slowly via syringe pump over ~20 minutes. The reaction was stirred for 3 hours at this temperature. NaOH was then added, and the reaction was transferred to a 0 °C cooling bath and stirred for 20 minutes. The reaction was filtered through a pad of celite. The organic layer was separated, and the aqueous layer was extracted with diethyl ether (x4). The combined organic layers were washed with H_2O and brine, dried over sodium sulfate, filtered, and concentrated. The product was obtained as a single diastereomer as determined by ^{1}HNMR.

Representative Procedure C: EDC Esterification

A flame dried flask was charged with argon, the carboxylic acid starting material and DCM. The reaction was subsequently cooled to 0°C, then DMAP and EDC were added consecutively. After 10 minutes, a solution of the alcohol in DCM was added via syringe pump. The reaction was stirred 24-30 hours depending on TLC analysis and then added to a separatory funnel containing equal volume of H_2O. The organic layer was separated, and the aqueous layer was extracted with DCM (3 x 15 mL). The combined organic layers were washed with brine, dried over $MgSO_4$, filtered and concentrated.

Representative Procedure D: Ring-Closing Metathesis

A flask was charged with the alkene starting material and DCM. Grubbs II generation catalyst was added, and the reaction was stirred at room temperature for 24 hours. The solvent was removed. NOTE: In our experience, adding a second equivalent of catalyst ~6 hours after start helps with starting material consumption.

Representative Procedure E: TBS removal

To a solution of protected macrocycle in THF, was added tetra-butylammonium fluoride (1M in THF). The reaction was stirred for 1 hour. The reaction was quenched with saturated aqueous ammonium chloride and diluted in diethyl ether. The organic layer was separated, and the aqueous layer was extracted with diethyl ether (x4). The combined organic layers were washed with water and brine, dried over sodium sulfate, filtered, and concentrated.

Representative Procedure F: Hydrogenation

A vial was charged with deprotected macrocycle, 1:1 EtOAc:EtOH and 10% Pd/C. Using a balloon, the vial was purged multiple times with H_2. Full hydrogenation was realized after 4 hours at which point the reaction mixture was poured over celite and condensed.

Representative Procedure G: TEMPO Oxidation

A vial was charged with deprotected macrocycle, acetonitrile, TEMPO, and sodium phosphate buffer (0.67 M, pH 6.7). The reaction was warmed to 35°C and stirred for 30 minutes. Then aqueous solutions of bleach and sodium chlorite were added to the reaction drop wise over 30 minutes. Reaction was stirred at 35°C for 24 hours at which time it was quenched with aqueous thiosulfate solution. The aqueous layer was extracted once with ethyl acetate (first ethyl acetate layer set aside). Then the aqueous layer was acidified to ~pH 4 and extracted with ethyl acetate (x3). The organics were washed with brine, dried over $MgSO_4$, filtered, and concentrated

Representative Procedure H: Acetonide Deprotection

To a solution of carboxylic acid macrocycle in THF was added HF pyridine and H_2O. The mixture was stirred for 4-6 hours and then quenched with 1 M NaOH. The aqueous layer was acidified to ~pH 4 and then the product was extracted with ethyl acetate (x3), washed with brine, dried over $MgSO_4$, filtered and concentrated.

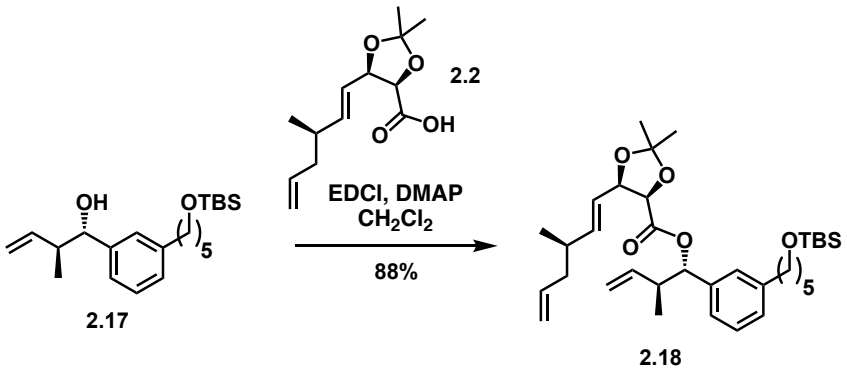

(4R,5R)-(1S,2S)-1-(3-(5-((tert-Butyldimethylsilyl)oxy)pentyl)phenyl)-2-methyl but-3-en-1-yl-2,2-dimethyl-5-((R,E)-3-methylhexa-1,5-dien-1-yl)-1,3-dioxolane-4-carboxylate (2.18)

Prepared according to Representative Procedure C: 2.17 (75.5 mg, 0.2081 mmol), in DCM (2.1 mL), DMAP (25.4 mg, 0.2081 mmol), EDCI (79.8 mg, 0.4161 mmol), and 2.2 (100 mg, 0.4161 mmol) in DCM (4.2 mL) yielded 119 mg (88%) of the ester. Purified by column chromatography (10 to 15% EtOAc in hexanes). ^{1}H NMR (400 MHz, $CDCl_3$) δ 7.22 (t, *J* = 7.4 Hz, 1H), 7.14 – 7.05 (m, 4H), 5.82 – 5.61 (m, 3H), 5.57 (d, *J* = 7.6 Hz, 1H), 5.14 – 5.06 (m, 2H), 5.03 (d, *J* = 2.7 Hz, 1H), 5.00 – 4.90 (m, 2H), 4.74 (t, *J* = 7.4 Hz,1H), 4.59 (dd, J = 7.0, 2.4 Hz, 1H), 3.60 (t, *J* = 6.6 Hz, 2H), 2.72 – 2.61 (m, 1H), 2.61 – 2.55 (m, 2H), 2.04 – 1.92 (m, 2H), 1.90 – 1.79 (m, 1H), 1.65 (s, 3H), 1.60 (m, 4H), 1.40 – 1.34 (m, 6H), 0.89 – 0.86 (m, 10H), 0.79 (d, *J* = 6.6 Hz, 3H), 0.04 (s, 6H). Spectrum matched literature.

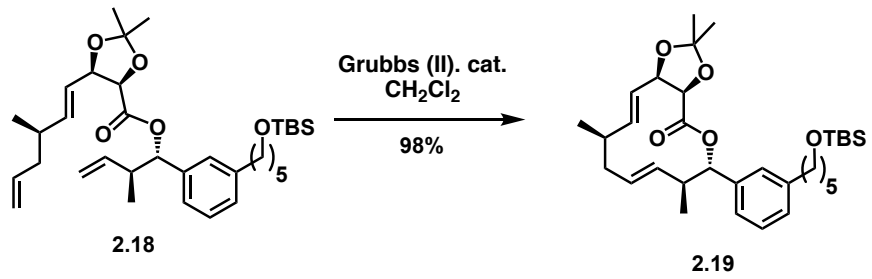

(3aR,6S,7S,8E,11R,12E,13aR)-6-(3-(5-((tert-Butyldimethylsilyl)oxy) pentyl)phenyl)-2,2,7,11-tetramethyl-6,7,10,11-tetrahydro-3aH-[1,3]dioxolo[4,5-c][1]oxacyclo dodecin-4(13aH)-one

(2.19) Prepared according to Representative Procedure D: 2.18 (104.5 mg, 0.1830 mmol), Grubbs 2nd Generation catalyst (8.8 mg, 0.0104 mmol, 5 mol%), and DCM (42 mL) yielded 0.0998 mg (98%) of the product as a clear oil. Purified by column chromatography (0 to 3% EtOAc in hexanes). ^{1}H NMR (400 MHz, $CDCl_3$) δ 7.24 – 7.19 (m, 1H), 7.14 – 7.08 (m, 3H), 5.85 – 5.78 (m, 1H), 5.57 (d, *J* = 10.8 Hz, 1H), 5.35 – 5.29 (m, 1H), 5.29 – 5.23 (m, 2H), 4.73 (m, 1H), 4.47 (d, *J* = 6.7 Hz, 1H), 3.60 (t, *J* = 6.6 Hz, 2H), 2.62 – 2.55 (m, 3H), 2.34 – 2.21 (m, 2H), 2.09 – 1.99 (m, 1H), 1.67 (s, 3H), 1.63 – 1.57 (m, 2H), 1.57 – 1.51 (m, 2H), 1.39 – 1.33 (m, 5H), 1.09 (d, *J* = 6.8 Hz, 3H), 0.89 (s, 9H), 0.75 (d, *J* = 6.8 Hz, 3H), 0.04 (s, 6H). Spectrum matched literature.

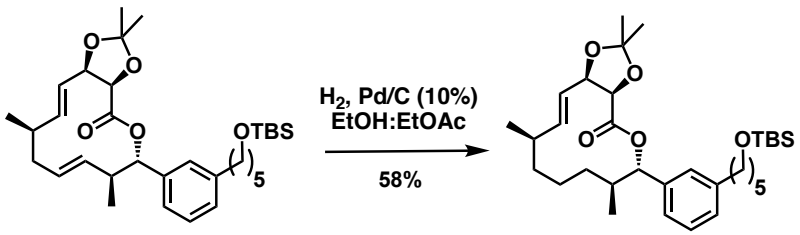

2.19 2.20

(3aR,6S,7S,11R,13aR,E)-6-(3-(5-((tert-Butyldimethylsilyl)oxy)pentyl)phenyl)-2,2,7,11-tetramethyl-6,7,8,9,10,11-hexahydro-3aH-[1,3]dioxolo[4,5-c][1]oxacyclododecin-4(13aH)-one (2.20) Prepared according to Representative Procedure F: (2.19) (55 mg, 0.0988 mmol), Pd/C (10% w/w, 8 mg), and EtOH (9.9 mL) yielded 32 mg (58%) of the product as a clear oil. Purified by preparative TLC (5% EtOAc in hexanes, eluted once). ^{1}H NMR (400 MHz, $CDCl_3$) δ 7.19 – 7.15 (m, 1H), 7.11 – 7.08 (m, 3H), 7.07 – 7.03 (m, 1H), 5.71– 5.60 (m, 2H), 5.49 (d, J = 11.5 Hz, 1H), 4.8 – 4.84 (m, 1H), 4.54 (d, *J* = 6.6 Hz, 1H), 3.59 (t, *J* = 6.6 Hz, 1H), 2.58 – 2.54 (m, 2H), 2.42 – 2.36 (m, 1H), 2.25 – 2.19 (m, 1H), 2.01 – 1.94 (m, 1H), 1.68 (s, 3H), 1.63 – 1.50 (m, 6H), 1.38 – 1.37 (m, 3H), 1.37 – 1.32 (m, 3H), 1.08 – 1.04 (m, 2H), 1.02 (d, J = 6.5 Hz, 3H), 0.89 (s, 9H), 0.68 (d, J = 7.0 Hz, 3H), 0.04 (s, 6H). Spectrum matched literature.

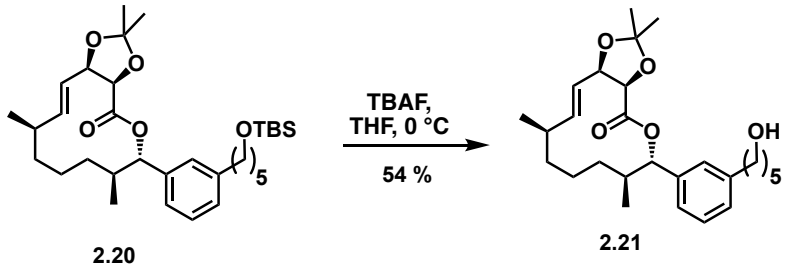

(3aR,6S,7S,11R,13aR,E)-6-(3-(5-Hydroxypentyl)phenyl)-2,2,7,11-tetramethyl-6,7,8,9,10,11-hexahydro-3aH-[1,3]dioxolo[4,5-c][1]oxacyclododecin-4(13aH)-one (2.21) Prepared according to representative Procedure E: 2.20 (66.2 mg, 0.1185 mmol), TBAF (1M in THF, 0.36 mL), and THF (1.2 mL) yielded 28.3 mg (54%) of the product as a clear oil. Purified by preparative TLC (30% EtOAc/hexanes). ^{1}H NMR (400 MHz, $CDCl_3$) δ 7.20 – 7.17 (m, 1H), 7.11 – 7.09 (m, 2H), 7.07 – 7.04 (m, 1H), 5.71 – 5.57 (m, 2H), 5.48 (d, *J* = 11.5 Hz, 1H), 4.85 (dd, *J* = 6.5, 3.2 Hz, 1H), 4.54 (d, *J* = 6.6 Hz, 1H), 3.62 (t, *J* = 6.6 Hz, 2H), 2.58 (t, J = 7.6 Hz, 2H), 2.43 – 2.35 (m, 1H), 2.28 – 2.18 (m, 1H), 2.04 –1.93 (m, 1H), 1.68 (s, 3H), 1.65 – 1.54 (m, 6H), 1.42 – 1.32 (m, 7H), 1.13 – 1.05 (m, 2H), 1.02 (d, *J* = 6.6 Hz, 3H), 0.68 (d, J = 7.0 Hz, 3H). Spectrum matched literature.

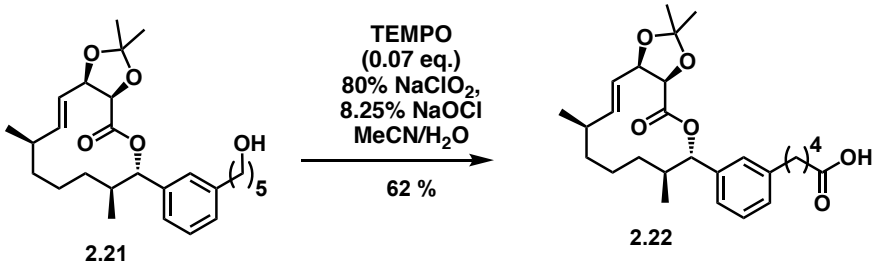

5-(3-((3aR,6S,7S,11R,13aR,E)-2,2,7,11-Tetramethyl-4-oxo-4,6,7,8,9,10,11,13a-octahydro-3aH-[1,3]dioxolo[4,5-c][1]oxacyclododecin-6-yl)phenyl)pentanoic acid (2.22) was synthesized according to Representative Procedure G: **2.21** (20 mg, 0.045 mmol), TEMPO (0.5 mg, 0.0032 mmol), sodium chlorite (10 mg, 0.1125 mmol) in 0.06 mL H_2O, bleach (8.25% sodium hypochlorite) (0.001 ml) in 0.17 ml H_2O, sodium phosphate buffer (0.67 M, pH 6.7, 0.17 ml) in CH_3CN (0.225 ml) yielded 12.8 mg of **(2.22)** (62% yield). Purified by column chromatography (0

to 50% EtOAc [with 0.01% acetic acid]:hexanes). **Rf** = 0.5 (50% EtOAc:Hexanes). ^{1}H NMR (500 MHz, $CDCl_3$) δ 7.18 (t, J = 7.5 Hz, 1H), 7.16 – 7.04 (m, 3H), 5.73 – 5.58 (m, 2H), 5.48 (d, *J* = 11.4 Hz, 1H), 4.85 (m, 1H),4.55 (d, *J* = 6.6 Hz, 1H), 2.59 (s, 2H), 2.41-2.20 (m, 5H), 2.0-1.94 (m, 1H), 1.68 (s, 3H), 1.63-1.59 (6 H), 1.37 (s, 3H), 1.06 (d, *J* = 8.8 Hz, 3H), 0.67 (d, *J* = 6.9 Hz, 3H). Spectrum matched literature.

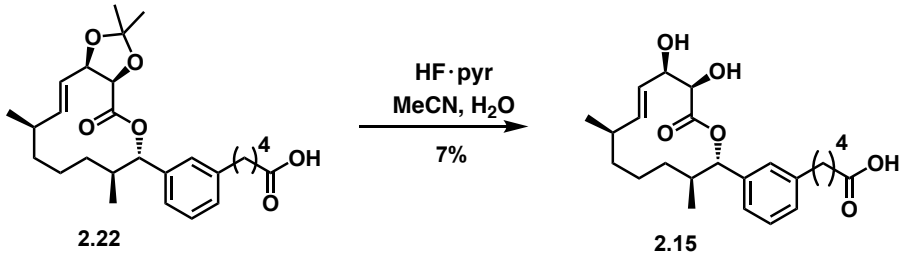

5-(3-((2S,3S,7R,10R,11R,E)-10,11-dihydroxy-3,7-dimethyl-12-oxooxacyclododec-8-en-2-yl)phenyl)penanoic acid (2.15) was synthesized according to Representative Procedure G: **(2.22)** (12.8 mg, 0.0279 mmol), HF·pyridine (0.3985 ml), H_2O (0.007 mL) in CH_3CN (5.6 mL) yielded 1.85 mg of **2.15** (7% yield). Purified by column chromatography (0 to 50% EtOAc [with 0.01% acetic acid]:hexanes). $\mathbf{R_f}$ = 0.38 (10% MeOH:DCM). ^{1}H NMR (400 MHz, $CDCl_3$) δ 7.22 (t, *J* = 7.5 Hz, 1H), 7.10 (dd, *J* = 12.4, 7.7 Hz, 3H), 5.57 – 5.38 (m, 2H), 5.19 (d, *J* = 11.4 Hz, 1H), 4.45 (dt, *J* = 4.1, 2.1 Hz, 1H), 4.17 (d, *J* = 3.6 Hz, 1H), 2.63 – 2.47 (m, 2H), 2.31 (ddd, *J* = 16.5, 11.6, 4.6 Hz, 1H), 2.24 (t, *J* = 7.0 Hz, 2H), 2.19 – 2.09 (m, 1H), 1.93 (td, *J* = 14.5, 9.4 Hz, 1H), 1.57 (ddd, J = 23.2, 15.5, 8.6 Hz, 4H), 1.40 – 1.14 (m, 7H), 1.02 (d, *J* = 9.0 Hz, 2H), 0.94 (d, *J* = 6.6 Hz, 3H), 0.61 (d, *J* = 7.0 Hz, 3H).

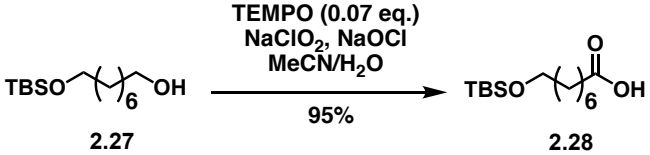

8-((*tert*-butyldimethylsilyl)oxy)octanoic acid (2.28) was synthesized according to Representative Procedure G: **2.27** (500 mg, 1.91 mmol), TEMPO (21 mg, 0.1344 mmol), sodium

chlorite (43.4 mg, 0.3.84 mmol) in 1.91 mL H_2O, bleach (8.25% sodium hypochlorite) (0.30 ml) in 0.59 ml H_2O, sodium phosphate buffer (0.67 M, pH 6.7, 7.109 ml) in CH_3CN (9.60 ml) yielded 501.6 mg of **(2.28)** (95% yield). Purified by column chromatography (0 to 50% EtOAc [with 0.01% acetic acid]:hexanes). $\mathbf{R_f}$ = 0.2 (30% EtOAc:Hexanes). ^{1}H NMR (400 MHz, $CDCl_3$) δ 3.59 (td, *J* = 6.6, 0.7 Hz, 2H), 2.39 – 2.31 (m, 2H), 1.63 (t, *J* = 7.3 Hz, 2H), 1.56 – 1.46 (m, 2H), 1.33 (d, *J* = 3.9 Hz, 6H), 0.89 (d, *J* = 0.8 Hz, 9H), 0.04 (d, *J* = 0.7 Hz, 6H). ^{13}C NMR (100 MHz, acetone) δ 63.22, 33.82, 32.76, 29.03, 25.97, 25.60, 24.62, 18.37, -5.27.

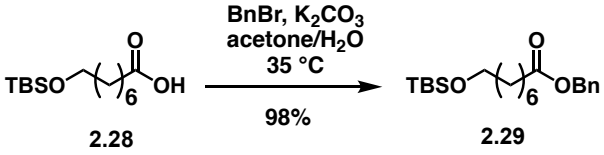

Benzyl 8-((tert-butyldimethylsilyl)oxy)octanoate (2.29) To a flask containing K_2CO_3 (598 mg, 4.32 mmol) and acetone (3.76 mL), **2.28** was added. Benzyl bromide (0.1337 mL, 1.12 mmol) was added dropwise. Following completion indicated by TLC, the reaction was placed in a separatory funnel and washed with brine (x2), concentrated, and purified by column chromatography (5% EtOAc/hexanes). $\mathbf{R_f}$ = 0.5 (10% EtOAc:Hexanes). **^{1}H NMR** (400 MHz, $CDCl_3$) δ 7.46 – 7.29 (m, 4H), 5.11 (s, 2H), 3.63 – 3.50 (m, 2H), 2.35 (t, *J* = 7.6 Hz, 2H), 1.63 (q, *J* = 7.3 Hz, 2H), 1.56 – 1.41 (m, 3H), 1.37 – 1.24 (m, 6H), 0.89 (d, *J* = 0.6 Hz, 9H). ^{13}C NMR (151 MHz, $CDCl_3$) δ 173.71, 136.17, 128.58, 128.21, 77.26, 77.05, 76.84, 66.10, 63.27, 34.35, 32.82, 29.15, 29.09, 26.02, 25.67, 24.95, 18.41, -5.22.

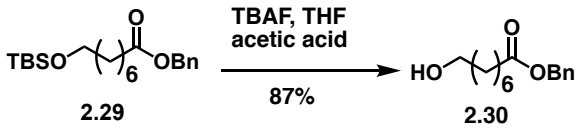

Benzyl 8-hydroxyoctanoate (2.30) was prepared using Representative procedure E. **2.29** (267 mg, 0.733 mmol), tetrabutylammonium fluoride solution (1 M, 2.20 ml, 2.198 mmol) in THF (7.33 ml) yielded 162 mg (87% yield). Purified by column chromatography (30% EtOAc:Hexanes). $\mathbf{R_f}$ = 0.4 (30% EtOAc:Hexanes). **^{1}H NMR** (400 MHz, Chloroform-*d*) δ ^{1}H NMR (400 MHz, $CDCl_3$) δ 7.40 – 7.29 (m, 4H), 5.11 (s, 2H), 3.63 (t, *J* = 6.6 Hz, 2H), 2.36 (t, *J* = 7.5 Hz, 2H), 1.69 – 1.60 (m, 2H), 1.54 (q, *J* = 6.8 Hz, 2H), 1.40 – 1.27 (m, 7H). ^{13}C NMR (101 MHz, $CDCl_3$) δ 173.64, 136.04, 128.52, 128.16, 77.32, 77.00, 76.68, 66.07, 62.94, 34.24, 32.63, 29.01, 28.97, 25.49, 24.81.

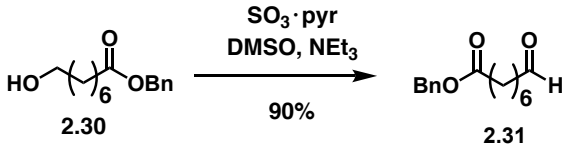

Benzyl 8-oxooctanoate (2.31) was synthesized according to Representative Procedure A: (563 mg, 2.258 mmol), dimethyl sulfoxide (3.219 mL, 45.16 mmol), sulfur trioxide pyridine complex (2.875 g, 18.064 mmol), triethylamine (3.15 mL, 22.58 mmol) in DCM (22.6 mL) yielded .5028 g of **6** (90% yield). Purified by column chromatography (0 to 10% EtOAc:Hexanes). **^{1}H NMR** 1 (400 MHz, $CDCl_3$-*d*) δ 9.75 (t, *J* = 1.8 Hz, 1H), 7.44 – 7.28 (m, 5H), 5.11 (s, 2H), 2.40 (td, *J* = 7.3, 1.8 Hz, 2H), 2.35 (t, *J* = 7.5 Hz, 2H), 1.64 (tt, *J* = 10.2, 6.7 Hz, 4H), 1.33 (p, *J* = 3.6 Hz, 4H). **^{13}C NMR** (100 MHz, $CDCl_3$*d*) δ 202.75, 173.58, 136.17, 128.66, 128.31, 66.27, 66.23, 66.19, 43.88, 34.28, 28.91, 28.86, 24.80, 21.94.

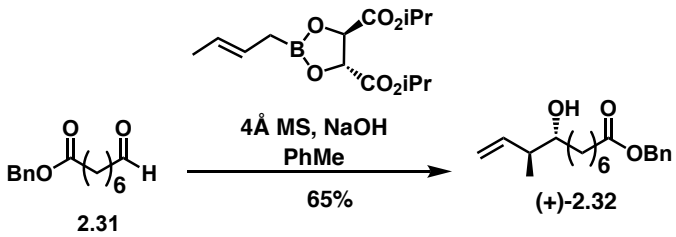

Benzyl (8*R*,9*S*)-8-hydroxy-9-methylundec-10-enoate (2.32) was synthesized according to Representative Procedure B: **2.31** (45 mg, 0.1812 mmol), *E*-crotylboronate (0.544 mL, 0.5436

mmol), toluene (1 mL), 4Å molecular sieves (12.14 mg), and 2 M NaOH (0.6795 mL) yielded 0.0254 g of **(+)-7** (46% yield). Purified by column chromatography (0 to 15% EtOAc:Hexanes). $\mathbf{R_f}$ = 0.5 (30% EtOAc:Hexanes). **^{1}H NMR** (400 MHz, Chloroform-*d*) δ 7.39-7.34 (m, 5H), 5.74 (ddd, *J* = 16.8, 10.7, 8.2 Hz, 1H), 5.14 – 5.05 (m, 4H), 3.42 – 3.31 (m, 1H), 2.35 (t, *J* = 7.5 Hz, 2H), 2.19 (h, *J* = 7.4 Hz, 2H), 1.64 (q, *J* = 7.2 Hz, 3H), 1.59 – 1.42 (m, 3H), 1.42 – 1.23 (m, 8H), 1.02 (d, *J* = 6.8 Hz, 3H).**^{13}C NMR** (100 MHz, Chloroform-*d*) δ 173.64, 140.47, 128.67, 128.30, 116.45, 77.48, 77.16, 76.84, 74.73, 66.21, 44.28, 34.42, 34.26, 29.44, 29.23, 25.67, 25.02, 16.44.

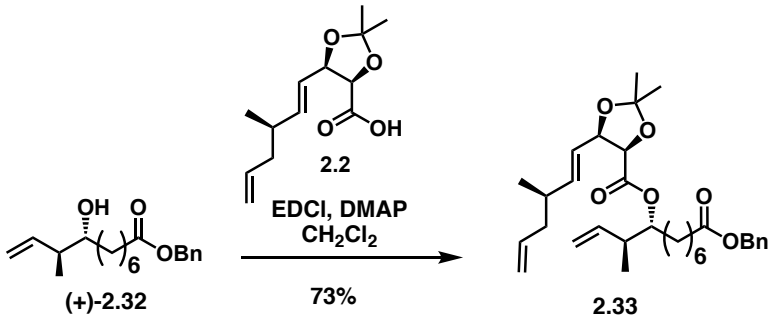

(3*S*,4*R*)-11-(benzyloxy)-3-methyl-11-oxoundec-1-en-4-yl (4*R*,5*R*)-2,2-dimethyl-5-((*R*,*E*)-3-methylhexa-1,5-dien-1-yl)-1,3-dioxolane-4-carboxylate (2.33) was synthesized according to Representative Procedure C: **(2.32)** (25 mg, 0.0834 mmol), acid precursor **2.2** (30 mg, 0.125 mmol), EDC (32 mg, 0.167 mmol), 4-(dimethylamino)pyridine (10 mg, 0.0083 mmol) in DCM (2.3mL) yielded 238 mg of **(2.33)** (73% yield). Purified by column chromatography (0 to 5% EtOAc:Hexanes). $\mathbf{R_f}$ = 0.50 (20% EtOAc:Hexanes). **^{1}H NMR** (400 MHz, Chloroform-*d*) δ 7.33 – 7.29 (m, 5H), 5.82 (dd, *J* = 15.4, 7.0 Hz, 1H), 5.73 (dddd, *J* = 12.3, 10.2, 6.6, 3.3 Hz, 1H), 5.37 (ddd, *J* = 15.4, 8.2, 1.3 Hz, 1H), 5.11 (s, 2H), 5.10 – 4.93 (m, 4H), 4.88 (dt, *J* = 8.4, 4.4 Hz, 1H), 4.75 (t, *J* = 7.6 Hz, 1H), 4.59 (d, *J* = 6.9 Hz, 1H), 2.47 – 2.39 (m, 1H), 2.33 (t, *J* = 7.5 Hz, 2H), 2.22 (p, *J* = 6.8 Hz, 1H), 2.13 (dt, *J* = 13.1, 6.5 Hz, 1H), 2.04 – 1.90 (m, 1H), 1.62 (s, 4H), 1.40 (s, 3H), 1.31 – 1.21 (m, 10H), 0.98 (dd, *J* = 9.3, 6.8 Hz, 7H). **^{13}C NMR** (100 MHz, Chloroform-*d*) δ

196.17, 173.64, 140.30, 136.06, 128.52, 128.15, 116.31, 93.23, 77.33, 77.01, 76.69, 74.57, 66.06, 44.13, 34.27, 34.09, 29.29, 29.06, 25.50, 24.85, 16.27.

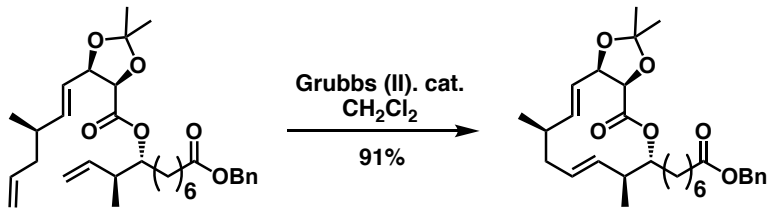

2.33 **2.34**

Benzyl-7-((3a*R*,6*R*,7*S*,8*E*,11*R*,12*E*,13a*R*)-2,2,7,11-tetramethyl-4-oxo-3a,6,7,10,11,13a-hexahydro- 4*H*-[1,3]dioxolo[4,5-*c*][1]oxacyclododecin-6-yl)heptanoate (2.34) was synthesized according to Representative Procedure D: **2.33** (24 mg, 0.0122 mmol), Grubbs II Generation Catalyst (0.5 mg, 0.0006 mmol) in DCM (2.4 mL) yielded 20.5 mg of **2.34** (91% yield). Purified by column chromatography (0 to 10% EtOAc:Hexanes). $\mathbf{R_f}$ = 0.50 (20% EtOAc:Hexanes). **^{1}H NMR** (400 MHz, Chloroform-*d*) δ 7.42 – 7.29 (m, 5H), 5.74 (dd, *J* = 15.7, 7.1 Hz, 1H), 5.25 (dd, *J* = 15.6, 7.0 Hz, 1H), 5.10 (d, *J* = 11.0 Hz, 4H), 4.83 – 4.69 (m, 3H), 4.52 (d, *J* = 6.7 Hz, 1H), 2.34 (t, *J* = 7.5 Hz, 2H), 2.26 – 2.13 (m, 3H), 1.61 (d, *J* = 7.7 Hz, 4H), 1.41 (s, 3H), 1.26 (d, *J* = 6.3 Hz, 4H), 1.05 (d, *J* = 6.7 Hz, 3H), 0.96 (d, *J* = 6.7 Hz, 3H). **^{13}C NMR** (100 MHz, Chloroform-*d*)) δ δ 173.58, 170.26, 138.61, 134.96, 129.85, 128.53, 128.16, 123.38, 110.94, 78.60, 78.31, 66.06, 42.23, 38.69, 35.93, 34.22, 32.28, 29.69, 29.21, 28.90, 26.78, 25.85, 24.84, 24.66, 21.13, 18.05.

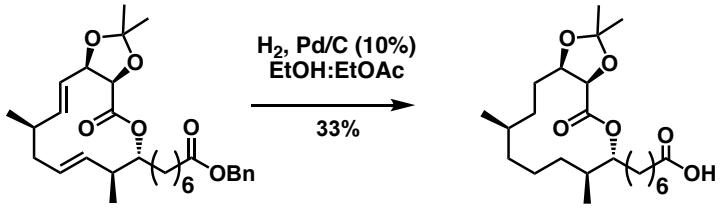

2.34 **2.37**

7-((3a*R*,6*R*,7*S*,11*R*,13a*R*)-2,2,7,11-tetramethyl-4-oxodecahydro-4*H*-[1,3]dioxolo[4,5-*c*][1]oxacyclododecin-6-yl)heptanoic acid (2.37) was synthesized according to Representative

Procedure F: **(2.34)** (37 mg, 0. 0740 mmol), Pd/C 10% (11 mg, 15 mol % catalyst load) in 1:1 EtOAc:EtOH (3.7 mL). The material was resubjected 4 times, yielding 9.9 mg of **2.37** (33% yield). Purified by column chromatography (15% EtOAc:hexanes + 0.01% AcOH). **R*f*** = 0.30 (30% EtOAc:Hexanes). **^{1}H NMR** (400 MHz, $CDCl_3$) 4.78 (ddd, *J* = 10.1, 6.3, 3.5 Hz, 1H), 4.57 (d, *J* = 6.1 Hz, 1H), 4.37 (ddd, *J* = 9.7, 6.1, 3.3 Hz, 1H), 2.34 (t, *J* = 7.5 Hz, 3H), 1.83 (ddt, *J* = 10.6, 7.1, 3.4 Hz, 1H), 1.75 – 1.66 (m, 3H), 1.66 – 1.60 (m, 6H), 1.52 – 1.42 (m, 4H), 1.38 (s, 3H), 1.28 (d, *J* = 14.1 Hz, 10H), 1.17 (d, *J* = 6.4 Hz, 3H), 0.89 (t, *J* = 6.5 Hz, 6H).

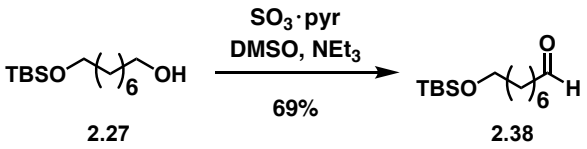

8-((*tert*-butyldimethylsilyl)oxy)octanal (2.38)) was synthesized according to Representative Procedure A: **2.27** (700 mg, 2.687 mmol), dimethyl sulfoxide (3.8 mL, 53.74 mmol), sulfur trioxide pyridine complex (3.421 g, 21.496 mmol), triethylamine (3.74 mL, 26.87 mmol) in DCM (27 mL) yielded 478 g of **11** (69% yield). Purified by column chromatography (0 to 10% EtOAc:Hexanes). **Rf** = 0.5 (25% EtOAc:Hexanes). ^{1}H NMR (399 MHz, Chloroform-*d*) δ 9.77 – 9.75 (m, 1H), 3.59 (t, *J* = 6.6 Hz, 1H), 2.42 (td, *J* = 7.4, 1.9 Hz, 1H), 1.63 (t, *J* = 7.2 Hz, 1H), 1.50 (t, *J* = 6.8 Hz, 1H), 1.32 (p, *J* = 3.1, 2.4 Hz, 4H), 0.89 (d, *J* = 0.5 Hz, 6H).

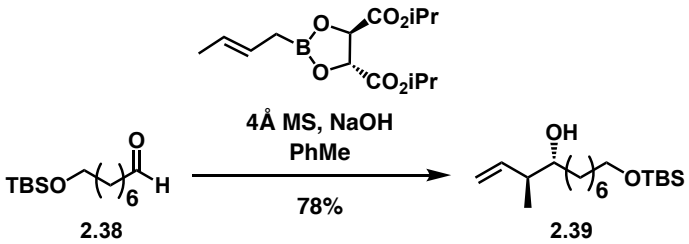

(3*S*,4*R*)-11-((*tert*-butyldimethylsilyl)oxy)-3-methylundec-1-en-4-ol (2.39) was synthesized according to Representative Procedure B: **2.38** (418 mg, 1.615 mmol), *E*-crotylboronate (9.5mL, 4.845 mmol), toluene (15 mL), 4Å molecular sieves (11 mg), and 2 M NaOH (6 mL) yielded 394

mg of **2.39)** (78% yield). Purified column chromatography (0 to 15% EtOAc:Hexanes). $\mathbf{R_f}$ = 0.3 (10% EtOAc:Hexanes). **^{1}H NMR** (400) MHz, Chloroform-*d*) δ 5.75 (ddd, *J* = 16.6, 10.8, 8.2 Hz, 1H), 5.16 – 5.05 (m, 2H), 3.59 (dd, *J* = 7.0, 6.2 Hz, 2H), 3.38 (s, 1H), 2.20 (h, *J* = 6.8 Hz, 1H), 1.56 – 1.45 (m, 4H), 1.41 – 1.31 (m, 1H), 1.31 (s, 8H), 1.03 (d, *J* = 6.9 Hz, 3H), 0.89 (d, *J* = 0.8 Hz, 9H), 0.04 (s, 3H). **^{13}C NMR** (100 MHz, Chloroform-*d*) δ 140.20, 116.11, 77.16, 76.84, 76.53, 74.51, 63.15, 43.96, 34.06, 32.70, 29.55, 29.26, 25.83, 25.61, 25.52, 16.16, -5.41. **$[\alpha]_{25}$D** +0.56 (*c* = 0.33 in $CHCl_3$).

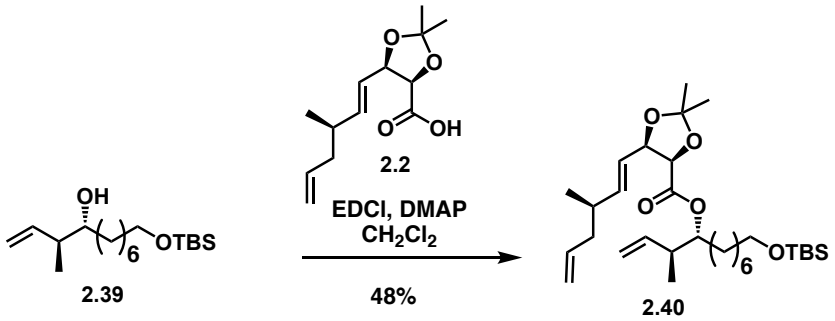

(3*S*,4*R*)-11-((*tert*-butyldimethylsilyl)oxy)-3-methylundec-1-en-4-yl (4*R*,5*R*)-2,2-dimethyl-5-((*R*,*E*)-3- methylhexa-1,5-dien-1-yl)-1,3-dioxolane-4-carboxylate (2.40) was synthesized according to Representative Procedure C: **2.39** (233 mg, 0.7094 mmol), acid precursor2 (256 mg, 1.0641 mmol), EDC (272 mg, 1.4188 mmol), 4-(dimethylamino)pyridine (8.7 mg, 0.0709 mmol) in DCM (17 mL) yielded 291 mg of **((–)-20)** (87% yield). Purified by column chromatography (0 to 5% EtOAc:Hexanes). $\mathbf{R_f}$ = 0.50 (10% EtOAc:Hexanes). **^{1}H NMR (**400 MHz, Chloroform-*d*) δ 5.82 (ddd, *J* = 15.3, 7.0, 0.8 Hz, 1H), 5.79 – 5.68 (m, 2H), 5.37 (ddd, *J* = 15.4, 8.2, 1.3 Hz, 1H), 5.07 (t, *J* = 1.2 Hz, 1H), 5.05 – 4.99 (m, 2H), 4.98 (t, *J* = 1.3 Hz, 1H), 4.89 (dt, *J* = 8.4, 4.4 Hz, 1H), 4.75 (ddd, *J* = 8.0, 6.9, 0.8 Hz, 1H), 4.60 (d, *J* = 6.9 Hz, 1H), 3.58 (t, *J* = 6.6 Hz, 2H), 2.44 (td, *J* = 7.5, 4.0 Hz, 1H), 2.22 (p, *J* = 6.7 Hz, 1H), 2.18 – 2.08 (m, 1H), 2.04 – 1.92 (m, 1H), 1.62 (s, 3H), 1.53 – 1.45 (m, 3H), 1.42 – 1.38 (m, 3H), 1.29 – 1.22 (m, 7H), 0.98 (dd, *J* = 9.3, 6.8 Hz, 6H), 0.89 (s, 9H), 0.04 (s, 6H).**^{13}C NMR** (126 MHz, Chloroform-) δ 142.63, 139.05, 136.49, 122.26, 116.20,

115.69, 110.69, 79.13, 78.25, 77.99, 77.25, 76.99, 76.74, 63.27, 40.77, 36.03, 32.82, 30.62, 29.49, 29.27, 27.03, 25.98, 25.75, 25.53, 19.09, 15.49, -5.27. **[α]$_{25}$D** -12.65 (*c* = 0.33 in $CHCl_3$).

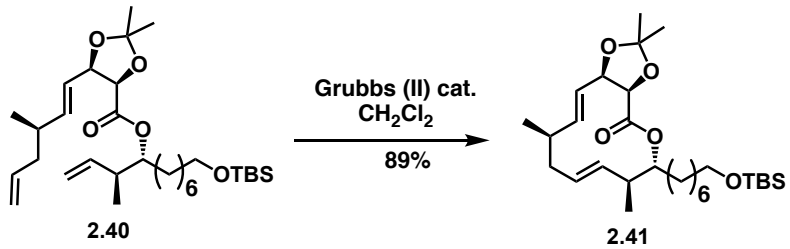

2.40 2.41

(3a*R*,6*R*,7*S*,8*E*,11*R*,12*E*,13a*R*)-6-(7-((*tert*-butyldimethylsilyl)oxy)heptyl)-2,2,7,11-tetramethyl- 3a,6,7,10,11,13a-hexahydro-4*H*-[1,3]dioxolo[4,5-*c*][1]oxacyclododecin-4-one (2.41) was synthesized according to Representative Procedure D: **(2.40))** (120 mg, 0.2169 mmol), Grubbs II Generation Catalyst (9.3 mg, 0.110 mmol) in DCM (43 mL) yielded 161 mg of **((–)-21)** (98% yield). Purified by column chromatography (0 to 10% EtOAc:Hexanes). **R_f** = 0.54 (10% EtOAc:Hexanes). **1H N**MR (400 MHz, Chloroform-*d*) δ 5.77 – 5.66 (m, 1H), 5.23 (ddd, *J* = 15.7, 6.9, 1.1 Hz, 1H), 5.11 – 5.01 (m, 2H), 4.82 – 4.68 (m, 2H), 4.50 (d, *J* = 6.7 Hz, 1H), 3.57 (t, *J* = 6.6 Hz, 2H), 2.23 – 2.12 (m, 2H), 1.99 – 1.86 (m, 1H), 1.68 (s, 3H), 1.51 – 1.36 (m, 7H), 1.24 (s, 11H), 1.03 (d, *J* = 6.7 Hz, 3H), 0.94 (d, *J* = 6.8 Hz, 3H), 0.87 (s, 9H), 0.87 (d, *J* = 5.8 Hz, 1H), 0.02 (s, 6H). **13C NMR** (100 MHz, Chloroform-*d*) δ 170.23, 138.55, 134.99, 129.78, 123.38, 110.90, 78.58, 78.41, 78.28, 77.30, 76.98, 76.66, 63.25, 42.26, 38.69, 35.93, 32.80, 32.36, 29.60, 29.20, 26.78, 25.97, 25.84, 25.72, 24.78, 21.12, 18.36, 18.05, -5.27.

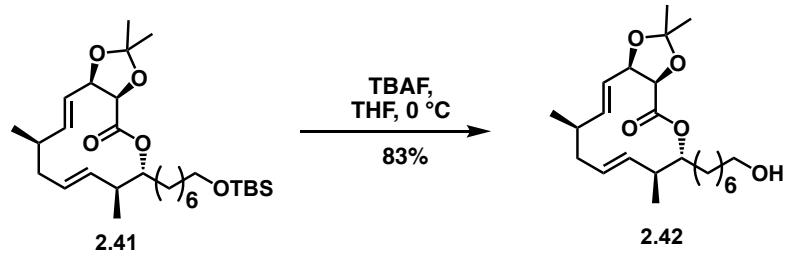

2.41 2.42

(3a*R*,6*R*,7*S*,8*E*,11*R*,12*E*,13a*R*)-6-(7-hydroxyheptyl)-2,2,7,11-tetramethyl-3a,6,7,10,11,13a-hexahydro-4*H*-[1,3]dioxolo[4,5-*c*][1]oxacyclododecin-4-one (2.42) was synthesized

according to Representative Procedure E: **(2.41)** (114 mg, 0.2131 mmol), tetrabutylammonium fluoride solution (1 M, 0.64 ml, 0.6392 mmol) in THF (1 ml) yielded 34.3 mg (83% yield). Purified by column chromatography (30% EtOAc:Hexanes). $\mathbf{R_f}$ = 0.39 (30% EtOAc:Hexanes). **^{1}H NMR** (400 MHz, Chloroform-*d*) δ 5.72 (ddd, *J* = 15.7, 7.5, 1.1 Hz, 1H), 5.30 – 5.16 (m, 1H), 5.12 – 4.98 (m, 2H), 4.82 – 4.68 (m, 2H), 4.51 (d, *J* = 6.7 Hz, 1H), 3.61 (t, *J* = 6z.6 Hz, 2H), 2.24 – 2.11 (m, 2H), 2.02 (s, 0H), 1.91 (dddd, *J* = 14.0, 9.9, 5.8, 2.6 Hz, 1H), 1.68 (s, 3H), 1.58 – 1.43 (m, 2H), 1.39 (s, 3H), 1.46 – 1.34 (m, 1H), 1.32 – 1.19 (m, 11H), 1.03 (d, *J* = 6.7 Hz, 3H), 0.94 (d, *J* = 6.8 Hz, 3H).

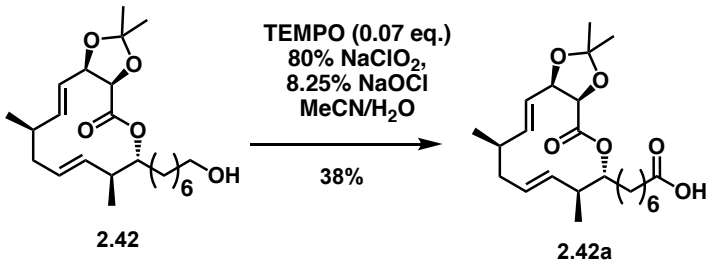

2.42 **2.42a**

7-((3a*R*,6*R*,7*S*,8*E*,11*R*,12*E*,13a*R*)-2,2,7,11-tetramethyl-4-oxo-3a,6,7,10,11,13a-hexahydro-4*H*- [1,3]dioxolo[4,5-*c*][1]oxacyclododecin-6-yl)heptanoic acid (2.42a) was synthesized according to Representative Procedure G: **(2.42)** (13 mg, 0.0335 mmol), TEMPO (4 mg, 0.0023 mmol), sodium chlorite (6.1 mg, 0.067 mmol) in 0.03 mL H_2O, bleach (8.25% sodium hypochlorite) (0.001 ml) in 0.01 ml H2O, sodium phosphate buffer (0.67 M, pH 6.7, 0.12 ml) in CH_3CN (0.17 ml) yielded **2.42a)** (38% yield). Purified by column chromatography (0 to 50% EtOAc [with 0.01% acetic acid]:hexanes). $\mathbf{R_f}$ = 0.2 (40% EtOAc:Hexanes). ^{1}H NMR (500 MHz, Chloroform-*d*) δ 5.74 (dd, *J* = 15.7, 7.1 Hz, 1H), 5.25 (ddd, *J* = 15.7, 6.9, 1.1 Hz, 1H), 5.15 – 5.00 (m, 2H), 4.85 – 4.69 (m, 2H), 4.53 (d, *J* = 6.7 Hz, 1H), 2.34 (t, *J* = 7.4 Hz, 2H), 2.18 (q, *J* = 6.7, 4.9 Hz, 3H), 1.70 (s, 3H), 1.45 – 1.37 (m, 3H).

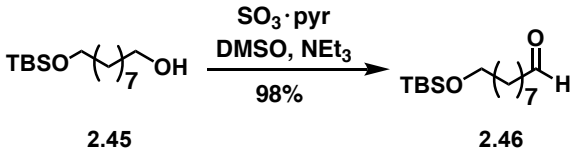

9-((*tert*-butyldimethylsilyl)oxy)nonanal (18) was synthesized according to Representative Procedure A: **17** (0.8338 g, 3.037 mmol), dimethyl sulfoxide (4.33 mL, 60.75 mmol), sulfur trioxide pyridine complex (3.867 g, 24.296 mmol), triethylamine (4.3 mL, 30.37 mmol) in DCM (30 mL) yielded 0.8148 g of **18** (98% yield). Purified by column chromatography (0 to 10% EtOAc:Hexanes). **Rf** = 0.79 (10% EtOAc:Hexanes). **1H NMR** (500 MHz, CDCl3) δ 9.76 (t, *J* = 1.8 Hz, 1H), 3.59 (t, *J* = 6.6 Hz, 2H), 2.42 (td, *J* = 7.4, 1.9 Hz, 2H), 1.62 (p, *J* = 7.4 Hz, 2H), 1.54 – 1.47 (m, 2H), 1.33 – 1.26 (m, 9H), 0.89 (s, 9H), 0.04 (s, 6H). **13C NMR** (126 MHz, CDCl3) δ 203.29, 63.66, 44.32, 33.23, 29.74, 29.62, 29.52, 26.39, 26.14, 22.48, 18.79, -4.85. **HRMS (ES+):** Found 273.22469 (0.94 ppm), C15H32O2Si (M+H+) requires 273.22443. **IR** 2929.02 (C-H), 1724.10 (CHO), 1463.11, 1264.73, 1093.86 cm-1.

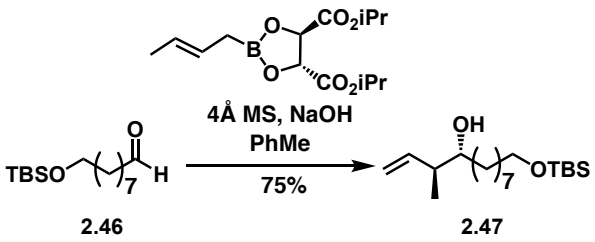

(3*S*,4*R*)-12-((*tert*-butyldimethylsilyl)oxy)-3-methyldodec-1-en-4-ol (2.47) was synthesized according to Representative Procedure B: **2.46** (750 mg, 2.7640 mmol), *E*-crotylboronate (4.341mL, 8.2920 mmol), toluene (26 mL), 4Å molecular sieves (19 mg), and 2 M NaOH (10 mL) yielded 674 mg of **2.47** (75% yield). Purified by column chromatography (0 to 15% EtOAc:Hexanes). **Rf** = 0.22 (30% EtOAc:Hexanes). **^{1}H NMR** (500 MHz, $CDCl_3$) δ 5.75 (ddd, *J* = 16.9, 10.7, 8.2 Hz, 1H), 5.13 (tt, *J* = 1.9, 1.1 Hz, 1H), 5.10 (ddd, *J* = 9.9, 1.9, 0.9 Hz, 1H), 3.59 (t, *J* = 6.6 Hz, 2H), 3.38 (ddd, *J* = 8.0, 5.9, 3.3 Hz, 1H), 2.24 – 2.16 (m, 1H), 1.53 – 1.48 (m, 4H),

1.41 – 1.33 (m, 2H), 1.29 (s, 10H), 1.03 (d, *J* = 6.9 Hz, 3H), 0.89 (s, 9H), 0.04 (s, 6H). **^{13}C NMR** (126 MHz, $CDCl_3$) δ 140.54, 116.40, 74.87, 63.49, 44.29, 34.43, 33.05, 29.84, 29.78, 29.57, 26.16, 25.96, 25.89, 18.55, 16.48, -5.08. **HRMS (ES+):** Found 329.28742, $C_{19}H_{41}O_2Si$ (M+H+) requires 329.28311. **IR** 3371.33 (OH), 2927.91, 2855.36 (C-H), 1638.69 (C=C), 1462.52, 1387.75, 1360.65, 1254.35, 1099.04 cm-1. **$[\alpha]_{25}$D** +0.28 (*c* = 1.0 in $CHCl_3$).

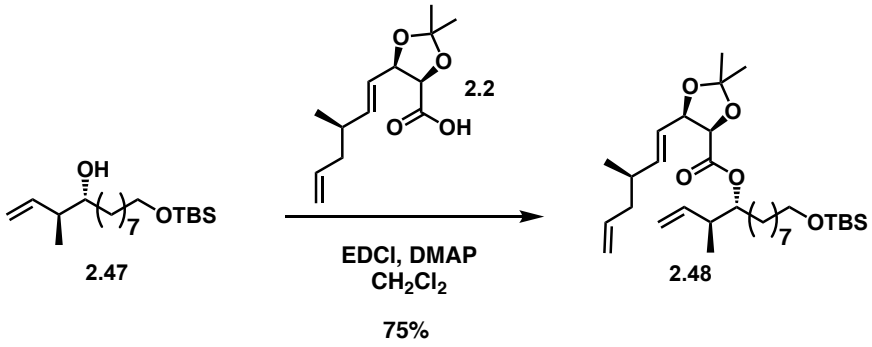

(3*S*,4*R*)-12-((*tert*-butyldimethylsilyl)oxy)-3-methyldodec-1-en-4-yl(4*R*,5*R*)-2,2-dimethyl-5-((*S*)-3- methylhex-5-en-1-yl)-1,3-dioxolane-4-carboxylate (2.48) was synthesized according to Representative Procedure C: **2.47** (233 mg, 0.7094 mmol), acid precursor 2.2 (256 mg, 1.0641 mmol), EDC (272 mg, 1.4188 mmol), 4-(dimethylamino)pyridine (8.7 mg, 0.0709 mmol) in DCM (17 mL) yielded 291 mg of **(2.48)** (75% yield). Purified by column chromatography (0 to 5% EtOAc:Hexanes). **R_f** = 0.50 (10% EtOAc:Hexanes). **^{1}H NMR** (500 MHz, CDCl3) δ 5.82 (dd, *J* = 15.4, 7.1 Hz, 1H), 5.79 – 5.68 (m, 2H), 5.37 (ddd, *J* = 15.4, 8.2, 1.2 Hz, 1H), 5.07 – 4.97 (m, 4H), 4.89 (dt, *J* = 8.5, 4.2 Hz, 1H), 4.77 – 4.72 (m, 1H), 4.59 (d, *J* = 6.9 Hz, 1H), 3.58 (t, *J* = 6.6 Hz, 2H), 2.43 (dq, *J* = 10.7, 6.8 Hz, 1H), 2.22 (p, *J* = 6.9, 6.4 Hz, 1H), 2.17 – 2.09 (m, 1H), 2.02 – 1.94 (m, 1H), 1.62 (s, 3H), 1.52 – 1.45 (m, 4H), 1.40 (s, 3H), 1.26 (s, 12H), 0.99 (d, *J* = 6.9 Hz, 3H), 0.97 (d, *J* = 6.7 Hz, 3H), 0.89 (s, 9H), 0.04 (s, 6H). **^{13}C NMR** (126 MHz, CDCl3) δ 169.67, 142.76, 139.23, 136.65, 122.44, 116.35, 115.83, 110.84, 79.29, 78.40, 78.17, 63.45, 40.94, 40.91, 36.19, 33.02, 30.79, 29.60, 29.53, 27.18, 26.13, 25.92, 25.89, 25.71, 19.25, 18.52, 15.65, -5.11. **HRMS (ES+):** Found 551.41263 (0.31 ppm), $C_{32}H_{58}O_5Si$ (M+H+) requires 551.41263. **IR** 2929.02,

2856.35 (C-H), 1754.22, 1736.84, 1729.15 (C=O), 1461.73, 1452.73, 1380.07, 1093.66 cm-1. **[α]^{25}D** -17.5 (c = 1.0 in $CHCl_3$).

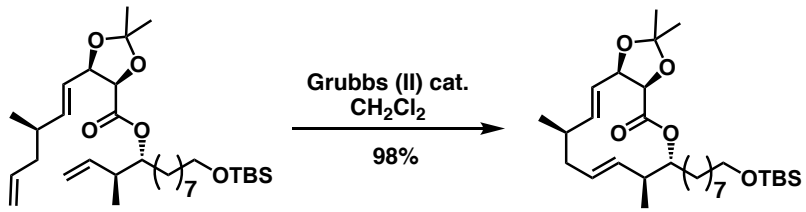

2.48 **2.49**

(3a*R*,6*R*,7*S*,8*E*,11*R*,12*E*,13a*R*)-6-(8-((*tert*-butyldimethylsilyl)oxy)octyl)-2,2,7,11-tetramethyl-3a,6,7,10,11,13a-hexahydro-4*H*-[1,3]dioxolo[4,5-*c*][1]oxacyclododecin-4-one (2.49) was synthesized according to Representative Procedure D: **(2.48)** (120 mg, 0.2169 mmol), Grubbs II Generation Catalyst (9.3 mg, 0.110 mmol) in DCM (43 mL) yielded 161 mg of **(2.49)** (98% yield). Purified by column chromatography (0 to 10% EtOAc:Hexanes). $\mathbf{R_f}$ = 0.54 (10% EtOAc:Hexanes). **^{1}H NMR** (400 MHz, CDCl3) δ 5.73 (ddd, *J* = 15.7, 7.4, 1.1 Hz, 1H), 5.25 (ddd, *J* = 15.7, 6.9, 1.1 Hz, 1H), 5.12 – 5.07 (m, 2H), 4.82 – 4.70 (m, 2H), 4.52 (d, *J* = 6.7 Hz, 1H), 3.58 (t, *J* = 6.6 Hz, 2H), 2.25 – 2.14 (m, 3H), 1.98 – 1.88 (m, 1H), 1.70 (s, 3H), 1.67 – 1.60 (m, 1H), 1.48 (q, *J* = 6.9 Hz, 3H), 1.41 (s, 3H), 1.25 (s, 12H), 1.05 (d, *J* = 6.7 Hz, 3H), 0.96 (d, *J* = 6.8 Hz, 3H), 0.89 (s, 9H), 0.04 (s, 6H). **^{13}C NMR** (100 MHz, CDCl3) δ 170.38, 138.68, 135.16, 129.93, 123.54, 111.05, 78.74, 78.57, 78.45, 63.43, 42.43, 38.85, 36.09, 32.98, 32.52, 29.70, 29.54, 29.50, 26.93, 26.12, 26.00, 25.88, 24.96, 21.28, 18.51, 18.21, -5.11. **HRMS (ES+):** Found 545.36404 (1.30 ppm), $C_{30}H_{54}O_5Si$ (M+Na+) requires 545.36327. **IR** 2928.56, 2856.00 (C-H), 1751.20 (C=O), 1461.80, 1379.01, 1253.12, 1223.29, 1186.18, 1088.12 cm-1. **$[\alpha]_{25}$D** -13.4 (*c* = 1.0 in $CHCl_3$).

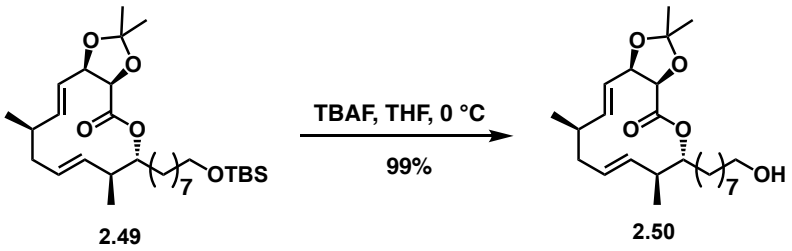

(3a*R*,6*R*,7*S*,8*E*,11*R*,12*E*,13a*R*)-6-(8-hydroxyoctyl)-2,2,7,11-tetramethyl-3a,6,7,10,11,13a-hexahydro- 4*H*-[1,3]dioxolo[4,5-*c*][1]oxacyclododecin-4-one (2.50) was synthesized according to Representative Procedure E: **(2.49)** (114 mg, 0.2131 mmol), tetrabutylammonium fluoride solution (1 M, 0.64 ml, 0.6392 mmol) in THF (1 ml) yielded 34.3 mg (99% yield). Purified by column chromatography (30% EtOAc:Hexanes). $\mathbf{R_f}$ = 0.39 (30% EtOAc:Hexanes). **^{1}H NMR** (400 MHz, $CDCl_3$) δ 5.74 (dd, *J* = 15.7, 7.1 Hz, 1H), 5.25 (dd, *J* = 15.8, 6.8 Hz, 1H), 5.09 (dd, *J* = 6.3, 3.0 Hz, 2H), 4.83 – 4.70 (m, 2H), 4.52 (d, *J* = 6.6 Hz, 1H), 3.63 (t, *J* = 6.6 Hz, 2H), 2.19 (ddd, *J* = 15.1, 9.5, 3.0 Hz, 3H), 1.94 (tdd, *J* = 13.9, 8.2, 4.1 Hz, 1H), 1.70 (s, 3H), 1.65 – 1.59 (m, 1H), 1.55 (p, *J* = 6.7 Hz, 3H), 1.41 (s, 3H), 1.32 – 1.22 (m, 12H), 1.05 (d, *J* = 6.7 Hz, 3H), 0.96 (d, *J* = 6.8 Hz, 3H). **^{13}C NMR** (100 MHz, $CDCl_3$) δ 170.37, 138.68, 135.11, 129.92, 123.48, 111.05, 78.71, 78.53, 78.40, 63.05, 42.43, 38.82, 36.05, 32.82, 32.48, 29.53, 29.40, 29.35, 26.89, 25.96, 25.73, 24.90, 21.24, 18.18. **HRMS (ES+):** Found 431.27696 (0.38 ppm), $C_{24}H_{40}O_5$ (M+Na+) requires 431.27680. **IR** 3430.00 (OH), 2928.10, 2855.58 (C-H)), 1753.69, 1745.55, 1726.59 (C=O), 1188.55, 1086.13 cm^{-1}. **$[\alpha]_{25}$D** -9.3 (*c* =1.0 in $CHCl_3$).

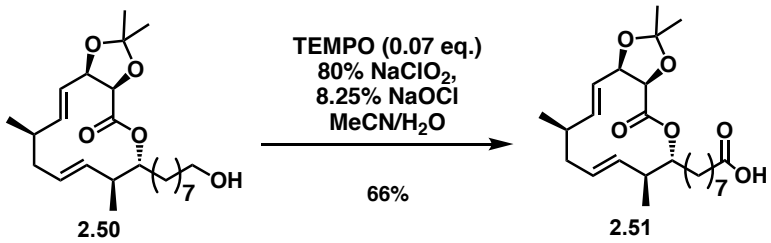

8-((3a*R*,6*R*,7*S*,8*E*,11*R*,12*E*,13a*R*)-2,2,7,11-tetramethyl-4-oxo-3a,6,7,10,11,13a-hexahydro-4*H*- [1,3]dioxolo[4,5-*c*][1]oxacyclododecin-6-yl)octanoic acid (2.51) was synthesized according to Representative Procedure F: **(2.50)** (34.5 mg, 0.0844 mmol), TEMPO (1.0 mg, 0.0059 mmol), sodium chlorite (19 mg, 0.1688 mmol) in 0.25 mL H_2O, bleach (8.25% sodium hypochlorite) (0.01 ml) in 0.25 ml H_2O, sodium phosphate buffer (0.67 M, pH 6.7, 0.31 ml) in CH3CN (0.4 ml) yielded 23.4 mg of **2.51** (66% yield). Purified by column chromatography (0 to 50% EtOAc [with 0.01% acetic acid]:hexanes). $\mathbf{R_f}$ = 0.12 (50% EtOAc:Hexanes). **^{1}H NMR** (500 MHz, $CDCl_3$) 5.73 (dd, *J* = 15.7, 7.2 Hz, 1H), 5.24 (dd, *J* = 15.6, 6.9 Hz, 1H), 5.11 – 5.07 (m, 2H), 4.80 – 4.72 (m, 2H), 4.53 (d, *J* = 6.7 Hz, 1H), 2.33 (t, *J* = 7.4 Hz, 2H), 2.22 – 2.15 (m, 3H), 1.96 – 1.89 (m, 1H), 1.69 (s, 3H), 1.61 (td, *J* = 13.3, 5.9 Hz, 4H), 1.41 (s, 3H), 1.29 – 1.24 (m, 8H), 1.05 (d, *J* = 6.7 Hz, 3H), 0.96 (d, *J* = 6.7 Hz, 3H). **^{13}C NMR** (126 MHz, $CDCl_3$) δ 179.37, 170.37, 138.75, 135.14, 129.97, 123.53, 111.14, 78.76, 78.56, 78.43, 42.43, 38.88, 36.11, 34.07, 32.48, 29.37, 29.03, 28.94, 26.93, 26.00, 24.84, 24.71, 21.27, 18.20. **HRMS (APCI-):** Found 421.26005 (0.49 ppm), C24H38O6 (M-H+) requires 421.25956. **IR** 2927.92, 2855.92 (C-H), 1747.04, 1708.65 (C=O), 1457.04, 1379.41, 1188.81, 1086.56 cm-1. **$[\alpha]_{25}$D** -10.2 (c = 1.0 in $CHCl_3$).

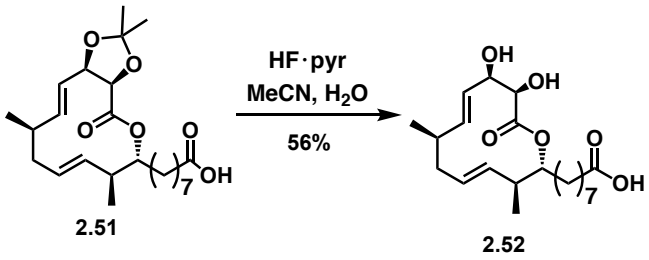

2.51 2.52

8-((2*R*,3*S*,4*E*,7*R*,8*E*,10*R*,11*R*)-10,11-dihydroxy-3,7-dimethyl-12-oxooxacyclododeca-4,8-dien-2- yl)octanoic acid 2.52 was synthesized according to Representative Procedure G: **(2.51)** (10 mg, 0.0237 mmol), HF·pyridine (0.34 ml), H_2O (0.01 mL) in CH3CN (5 mL) yielded 5 mg of **2.52** (56% yield). Purified by column chromatography (0 to 50% EtOAc [with 0.01% acetic acid]:hexanes). $\mathbf{R_f}$ = 0.38 (10% MeOH:DCM). **^{1}H NMR** (400 MHz, CDCl3) δ 5.35 – 5.24 (m, 2H),

5.14 (ddd, *J* = 14.8, 10.9, 3.8 Hz, 1H), 4.90 (dd, *J* = 15.0, 9.5 Hz, 1H), 4.73 (ddd, *J* = 10.7, 7.7, 2.9 Hz, 1H), 4.42 (s, 1H), 4.13 (d, *J* = 3.2 Hz, 1H), 2.34 (t, *J* = 7.3 Hz, 2H), 2.23 (td, *J* = 10.1, 6.8 Hz, 1H), 2.19 – 2.12 (m, 2H), 1.68 – 1.60 (m, 4H), 1.31 (s, 5H), 1.25 (s, 4H), 1.04 (d, *J* = 6.5 Hz, 3H), 0.95 (d, *J* = 6.8 Hz, 3H). **^{13}C NMR** (151 MHz, $CDCl_3$) δ 177.67, 172.80, 135.67, 134.74, 130.27, 126.41, 78.57, 73.55, 73.41, 41.99, 40.93, 38.10, 33.78, 31.83, 28.92, 28.67, 28.46, 24.59, 24.01, 21.29, 18.02. **HRMS (APCI-):** Found 381.22826 (0.33 ppm), $C_{21}H_{34}O_6$ (M-H+) requires 381.22826. **IR** 3422.41 (O-H), 2924.83, 2852.86 (C-H), 1717.21 (C=O), 1456.95, 1196.87, 1077.90 cm-1. **[α]$_{25}$D** +16.9 (*c* = 0.33 in $CHCl_3$).

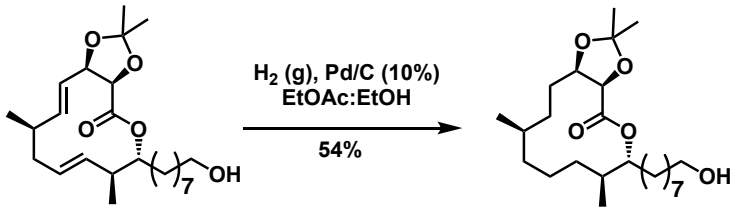

2.51 **2.53**

(3a*R*,6*R*,7*S*,11*R*,13a*R*)-6-(8-hydroxyoctyl)-2,2,7,11-tetramethyldecahydro-4*H*-[1,3]dioxolo[4,5-*c*][1]oxacyclododecin-4-one **2.53** was synthesized according to Representative Procedure H: **2.51** (32 mg, 0.0908 mmol), Pd/C 10% (14 mg, 15 mol % catalyst load) in 1:1 EtOAc:EtOH (4.5 mL) yielded 17.2 mg of **2.53** (54% yield). Purified by column chromatography (0 to 20% EtOAc:hexanes). **R_f** = 0.40 (20% EtOAc:Hexanes). **^{1}H NMR** (500 MHz, CDCl3) δ 4.78 (ddd, *J* = 10.0, 6.3, 3.4 Hz, 1H), 4.56 (d, *J* = 6.1 Hz, 1H), 4.36 (ddd, *J* = 9.7, 6.1, 3.2 Hz, 1H), 3.63 (t, *J* = 6.7 Hz, 2H), 1.83 (dp, *J* = 10.7, 3.7 Hz, 1H), 1.76 (ddd, *J* = 10.4, 5.1, 2.4 Hz, 1H), 1.70 (tt, *J* = 10.1, 4.3 Hz, 3H), 1.63 (s, 3H), 1.60 – 1.52 (m, 4H), 1.48 (ddt, *J* = 6.2, 3.7, 2.1 Hz, 3H), 1.38 (s, 3H), 1.31 – 1.25 (m, 11H), 1.19 – 1.14 (m, 2H), 1.03 (ddd, *J* = 11.0, 9.0, 4.8 Hz, 1H), 0.89 (dd, *J* = 8.6, 6.9 Hz, 6H). **^{13}C NMR** (151 MHz, CDCl3) δ 170.09, 110.01, 79.15, 78.18, 63.17, 36.06, 33.65, 32.89, 32.42, 31.70, 29.85, 29.72, 29.51, 29.41, 28.00, 27.36, 26.03, 25.78, 25.13, 25.11, 24.12, 21.96, 20.88, 16.96. **HRMS (ES+):** Found 413.32615 (0.68 ppm),

C24H44O5 (M-H+) requires 413.32615. **IR** 3369.45 (OH), 2928.27, 2856.35 (C-H), 1746.00 (C=O), 1379.54, 1184.56, 1077.92 cm-1. **[α]$_{25}$D** +38.9 (*c* = 1.0 in $CHCl_3$).

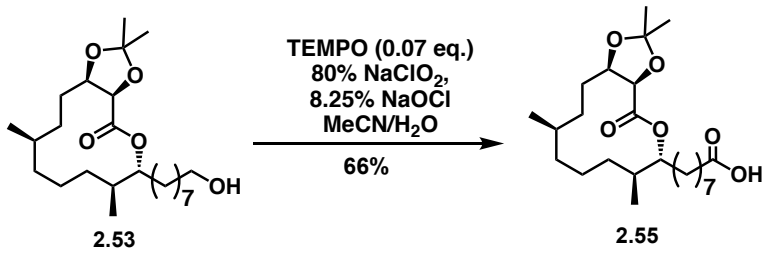

8-((3a*R*,6*R*,7*S*,11*R*,13a*R*)-2,2,7,11-tetramethyl-4-oxodecahydro-4*H*-[1,3]dioxolo[4,5-*c*][1]oxacyclododecin-6-yl)octanoic acid (2.55) was synthesized according to Representative Procedure G: **2.53** (15 mg, 0.0363 mmol), TEMPO (4.5 mg, 0.0029 mmol), sodium chlorite (8 mg, 0.0842 mmol) in 0.5 mL H_2O, bleach (8.25% sodium hypochlorite) (0.01 ml) in 0.5 ml H2O, sodium phosphate buffer (0.67 M, pH 6.7, 0.2 ml) in CH_3CN (0.2 ml) yielded 10.6 mg of **(2.55)** (66% yield). Purified by column chromatography (0 to 50% EtOAc [with 0.01% acetic acid]:hexanes). **R$_f$** = 0.67 (50% EtOAc:Hexanes with acetic acid). **^{1}H NMR** (600 MHz, $CDCl_3$) δ 4.78 (ddd, *J* = 10.1, 6.3, 3.4 Hz, 1H), 4.58 (d, *J* = 6.1 Hz, 1H), 4.37 (ddd, *J* = 9.7, 6.1, 3.2 Hz, 1H), 2.34 (t, *J* = 7.4 Hz, 2H), 1.84 (dddd, *J* = 14.0, 10.5, 6.9, 3.3 Hz, 1H), 1.75 (dd, *J* = 9.6, 5.2 Hz, 1H), 1.69 (ddd, *J* = 14.4, 9.3, 3.9 Hz, 3H), 1.64 (s, 3H), 1.47 (ddt, *J* = 16.2, 12.8, 4.3 Hz, 3H), 1.32 – 1.27 (m, 8H), 1.25 (s, 4H), 1.17 (dp, *J* = 11.4, 4.4 Hz, 3H), 1.04 (ddd, *J* = 13.9, 9.1, 4.7 Hz, 1H), 0.89 (dd, *J* = 9.7, 6.8 Hz, 6H). **^{13}C NMR** (151 MHz, $CDCl_3$) δ 178.29, 171.70, 109.96, 79.05, 78.10, 33.78, 33.50, 32.24, 31.44, 29.72, 29.26, 28.68, 27.83, 27.20, 27.13, 25.89, 24.93, 24.57, 23.80, 20.73, 20.00, 19.19, 19.12, 16.83. **HRMS (ES+):** Found 449.28747 (0.24 ppm), $C_{24}H_{42}O_6$ (M+Na+) requires 449.28736. **IR** 2929.50, 2857.77 (C-H), 1746.37, 1709.13 (C=O), 1461.66, 1379.86, 1245.98, 1184.66, 1079.39 cm-1. **[α]$_{25}$D** +24.16 ($_c$ = 1.0 in $CHCl_3$).

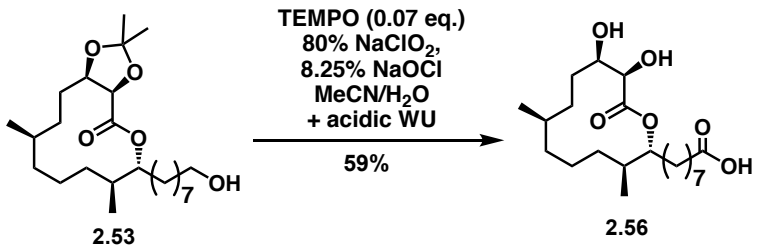

2.53 2.56

8-((2*R*,3*S*,7*R*,10*R*,11*R*)-10,11-dihydroxy-3,7-dimethyl-12-oxooxacyclododecan-2-yl)octanoic acid (2.56) was synthesized according to Representative Procedure G: **2.53** (15 mg, 0.0363 mmol), TEMPO (4.5 mg, 0.0029 mmol), sodium chlorite (8 mg, 0.0842 mmol) in 0.5 mL H_2O, bleach (8.25% sodium hypochlorite) (0.01 ml) in 0.5 ml H_2O, sodium phosphate buffer (0.67 M, pH 6.7, 0.2 ml) in CH_3CN (0.2 ml) yielded 10.6 mg of **2.56** (59% yield). During the workup, the solution was allowed to stir in an acidic solution to facilitate acetonide removal. Purified by column chromatography (0 to 50% EtOAc [with 0.01% acetic acid]:hexanes). $\mathbf{R_f}$ = 0.67 (50% EtOAc:Hexanes with acetic acid). **^{1}H NMR** (600 MHz, $CDCl_3$) δ 4.82 (ddd, *J* = 10.9, 6.4, 3.2 Hz, 1H), 4.44 (d, *J* = 2.3 Hz, 1H), 4.07 (ddd, *J* = 7.6, 5.8, 2.4 Hz, 1H), 2.34 (t, *J* = 7.3 Hz, 2H), 1.95 (ddt, *J* = 10.9, 7.5, 3.9 Hz, 1H), 1.79 (dtd, *J* = 14.9, 7.5, 3.9 Hz, 1H), 1.71 (ddt, *J* = 17.3, 13.8, 3.7 Hz, 2H), 1.61 (dd, *J* = 10.3, 4.3 Hz, 3H), 1.54 – 1.46 (m, 2H), 1.35 – 1.26 (m, 11H), 1.19 – 1.09 (m, 4H), 1.04 (ddt, *J* = 16.7, 8.2, 3.8 Hz, 1H), 0.90 (dd, *J* = 15.6, 6.8 Hz, 7H). **^{13}C NMR** (151 MHz, $CDCl_3$) δ 216.82, 171.96, 71.03, 36.00, 34.60, 33.74, 32.44, 29.82, 29.70, 28.52, 28.00, 37.73, 29.12, 28.73, 28.00, 27.03, 24.52, 23.73, 22.68, 16.23. **HRMS (APCI^{-}):** Found 385.25979 (0.59 ppm), $C_{21}H_{38}O_6$ (M-H+) requires 385.259.

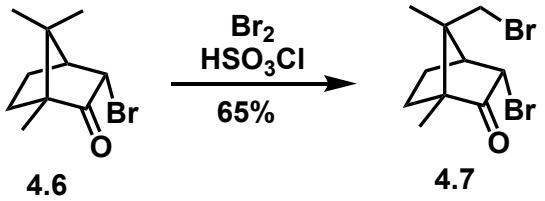

4.6 4.7

(1*S*,3*S*,4*S*,7*S*)-3-bromo-7-(bromomethyl)-1,7-dimethylbicyclo[2.2.1]heptan-2-one (4.7)

To a 3-necked flask with a condenser, stirrer, and thermometer that has been cooled to 10 ºC was added chlorosulfonic acid (8 mL, M = 5.4), bromine (2.26 mL, 44 mmol), and 3-bromocamphor (**4.6**) (10 g, 43.3 mmol). The reaction temperature was maintained at 25 ºC. Reaction progress was monitored by TLC. The reaction mixture was quenched by slowly pouring it over ice. The product was stirred until it became granular. Excess bromine was decomposed with solid sodium bisulfite and the product precipitated out. The precipitate was washed with H_2O, 5% Sodium hydroxide, followed by H_2O. The crude product was pressed dry. Subsequently, hot methanol with a few drops of sodium methoxide was added. The product required further purification via column chromatography (5% EtOAc/hexanes), yielding a white crystalline solid (8.66 g, 65%). $\mathbf{R_f}$ = 0.2 (8% EtOAc:Hexanes) ^{1}H NMR (400 MHz, $CDCl_3$) δ 4.57 (ddd, *J* = 4.8, 2.0, 1.0 Hz, 1H), 3.65 (dd, *J* = 10.4, 1.2 Hz, 1H), 3.36 – 3.21 (m, 1H), 2.69 (t, *J* = 4.5 Hz, 1H), 2.18 (ddd, *J* = 13.2, 9.5, 3.5 Hz, 1H), 1.94 – 1.83 (m, 1H), 1.78 – 1.68 (m, 1H), 1.51 (td, *J* = 9.4, 4.7 Hz, 1H), 1.10 (d, *J* = 1.1 Hz, 3H), 1.02 (s, 3H). Spectrum matched literature.

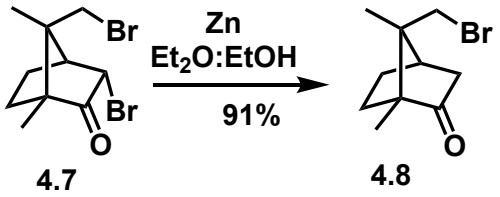

4.7 4.8

(1*S*,4*R*,7*S*)-7-(bromomethyl)-1,7-dimethylbicyclo[2.2.1]heptan-2-one (4.8)

Dibromocamphor (**4.7**) (3.861 g, 12.45 mmol) was dissolved in Et_2O: EtOH (1:1) (0.6M). The reaction mixture was cooled to 0 ºC. Zinc (2.05 g, 31.12 mmol) was added over 1 h. The reaction temperature was maintained below 20 ºC. The reaction was stirred for 4 h until completion was indicated by TLC. Celite was added to the mixture and the solution was filtered, then washed with 50% brine, H_2O (x2), $NaHCO_3$ (x6, or until solution is basic), brine, and dried over $MgSO_4$. The crude product was recrystallized with MeOH, yielding **4.8** (2.36 g, 91%). $\mathbf{R_f}$ = 0.3 (8% EtOAc:Hexanes) ^{1}H NMR (400 MHz, cdcl$_3$) δ 3.63 – 3.56 (m, 1H), 3.23 (dt, *J* = 10.3, 0.6 Hz, 1H), 2.49 (t, *J* = 4.5 Hz, 1H), 2.35 (dt, *J* = 18.5, 4.0 Hz, 1H), 1.99 – 1.89 (m, 2H), 1.77 – 1.64 (m, 1H), 1.55 – 1.39 (m, 2H), 1.02 – 0.94 (m, 6H). Spectrum matched literature.

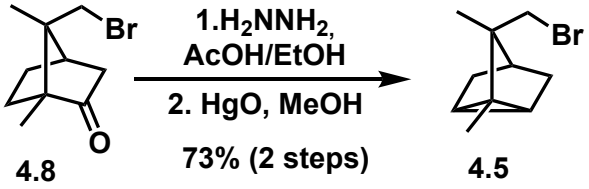

4.8 4.5

7-(bromomethyl)-1,7-dimethyltricyclo[2.2.1.0^{2,6}]heptane (4.5) 9-bromocamphor (**4.8**) (5.19 g, 22.45 mmol) was dissolved in EtOH (16 mL, 3x wt), Hydrazine (31 mL, 987.5 mmol) was added very slowly. Then acetic acid was added until the solution was acidic (approx. 14 mL, 246.95 mmol). The reaction was stirred for 4 h then concentrated. The concentrated crude product was dissolved in Et_2O and the hydrazine layer was removed. The organic layer was washed with 10% NaOH saturated with NaCl, brine (x3), and concentrated. The hydrazone was used crude in the next reaction. The hydrazone was dissolved in MeOH (9.76 mL). Yellow mercuric oxide (7.78 g, 35.92 mmol) was added. The reaction was heated to 40 ºC and stirred overnight. The reaction

mixture was filtered over celite and rinsed with pentane (excess). The mixture was added to a separatory funnel and saturated with NaCl. The layers were separated, and the aqueous layer was extracted with pentane. The combined organic layers were washed with brine and dried with $MgSO_4$. The product was purified by column chromatography (100% hexanes). ^1H NMR (400 MHz, $CDCl_3$) δ 3.63 – 3.56 (m, 1H), 3.23 (dt, *J* = 10.3, 0.6 Hz, 1H), 2.49 (t, *J* = 4.5 Hz, 1H), 2.35 (dt, *J* = 18.5, 4.0 Hz, 1H), 1.99 – 1.89 (m, 2H), 1.77 – 1.64 (m, 1H), 1.55 – 1.39 (m, 2H), 1.02 – 0.94 (m, 6H). $\mathbf{R_f}$ = 0.7 (5% EtOAc:Hexanes). Spectrum matched literature.

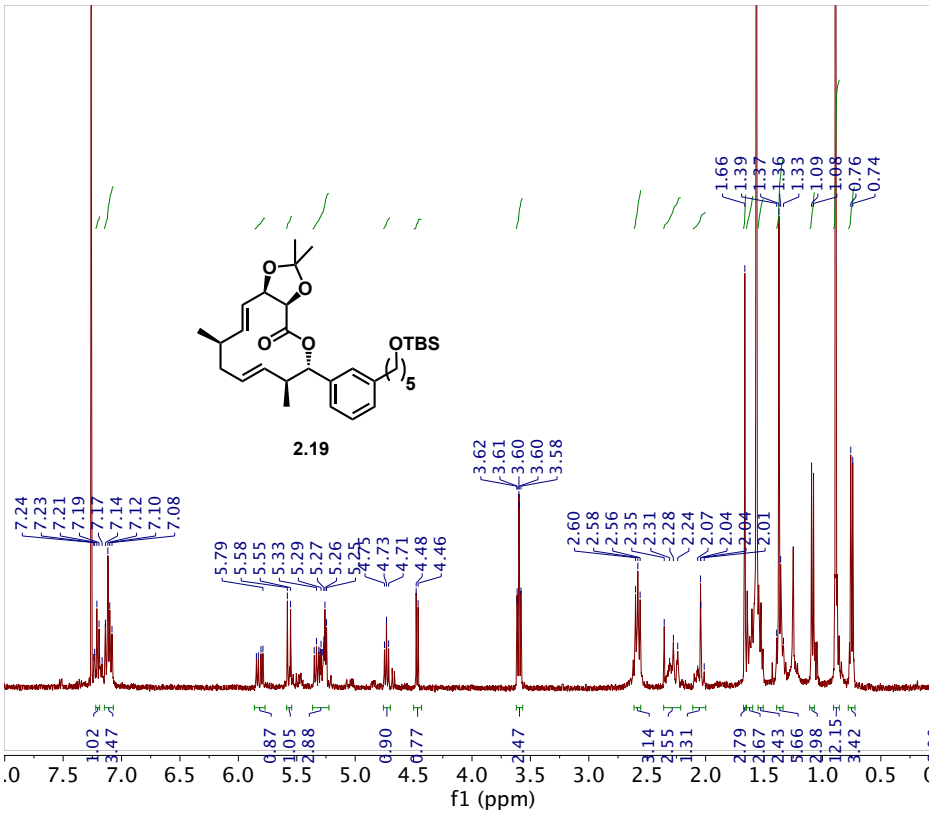
OTBS
5
2.19
f1 (ppm)

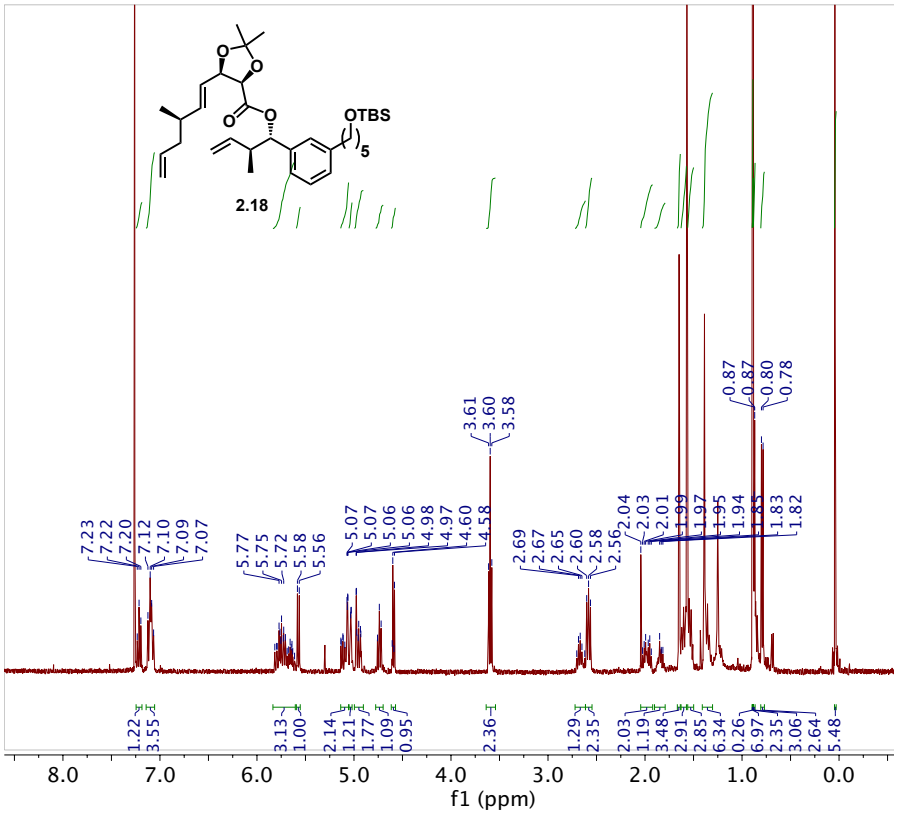
OTBS
5
2.18
f1 (ppm)

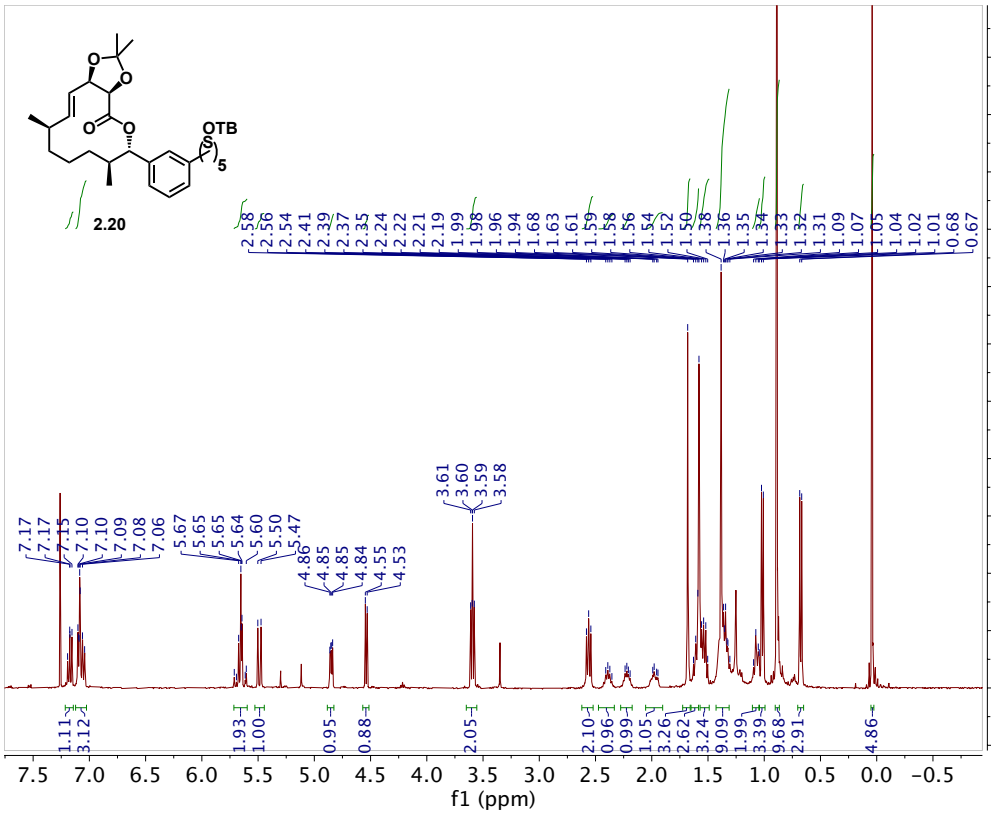
OTB
5
2.20
f1 (ppm)

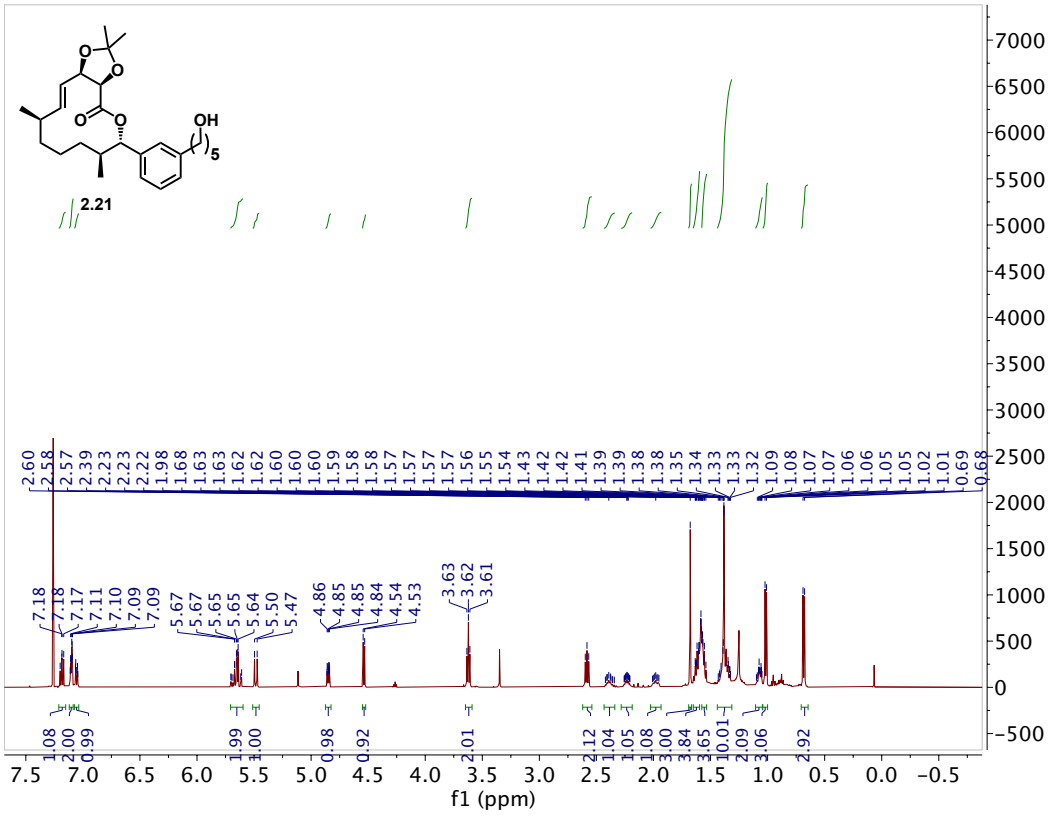
OH
5
2.21
f1 (ppm)

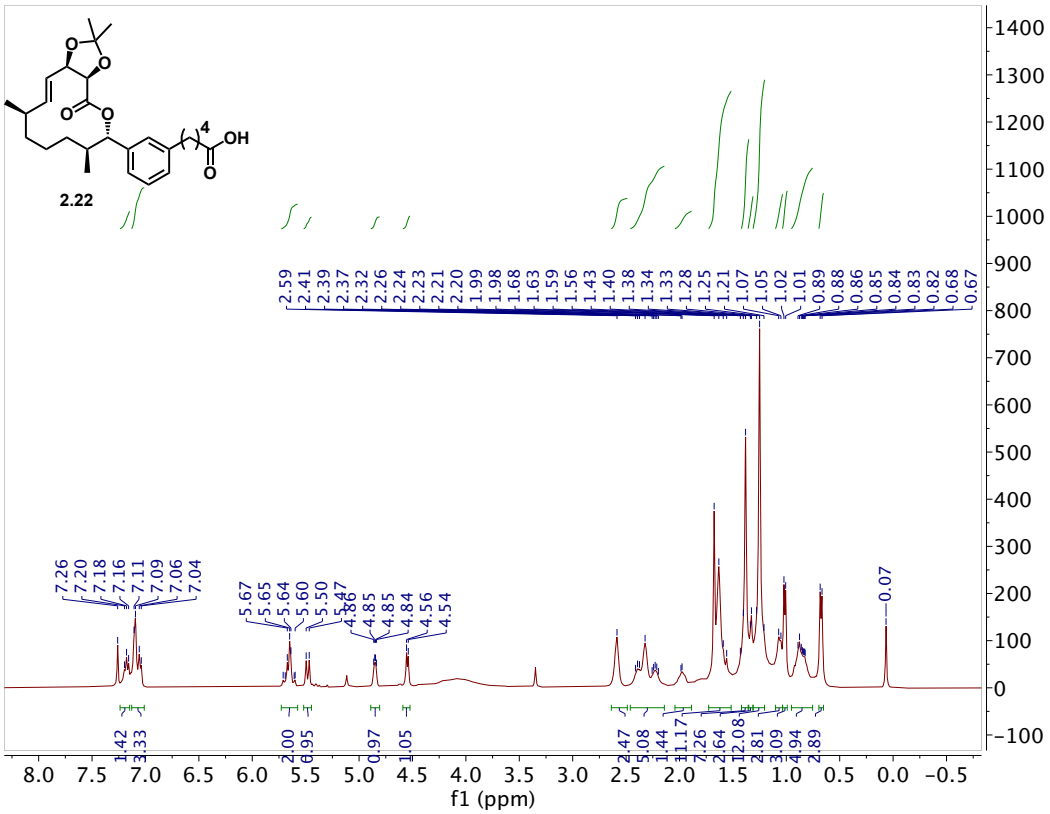
2.22
f1 (ppm)

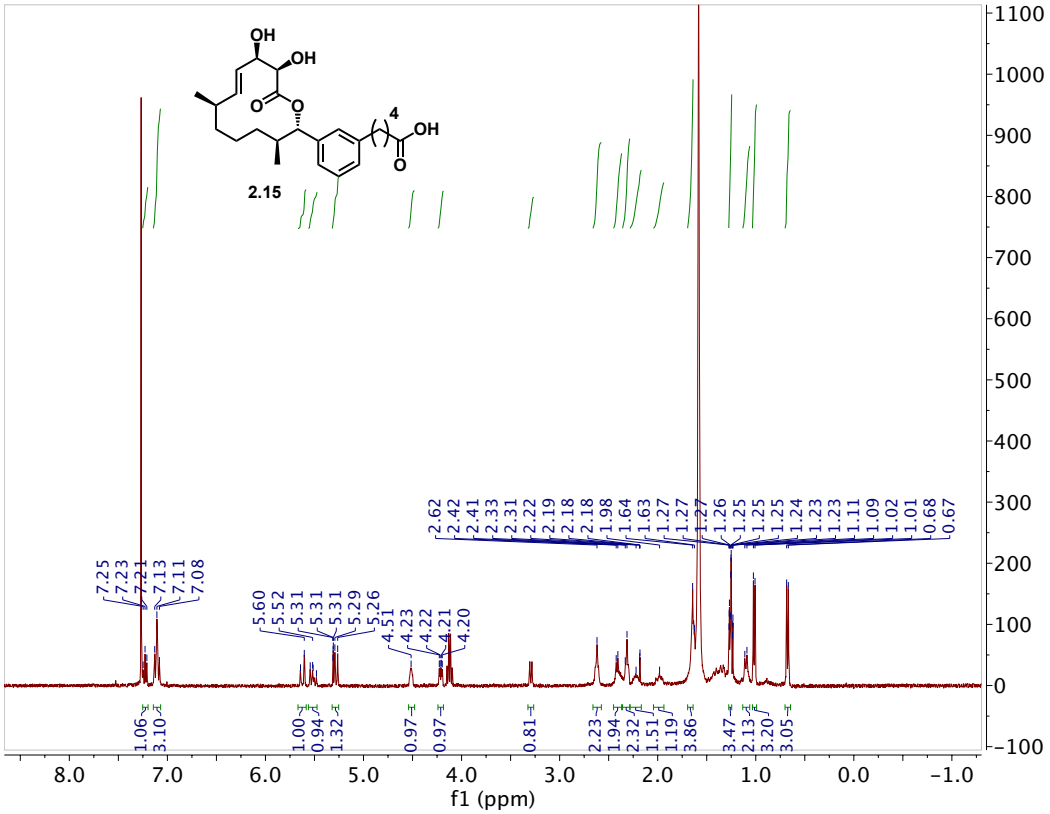
2.15
f1 (ppm)

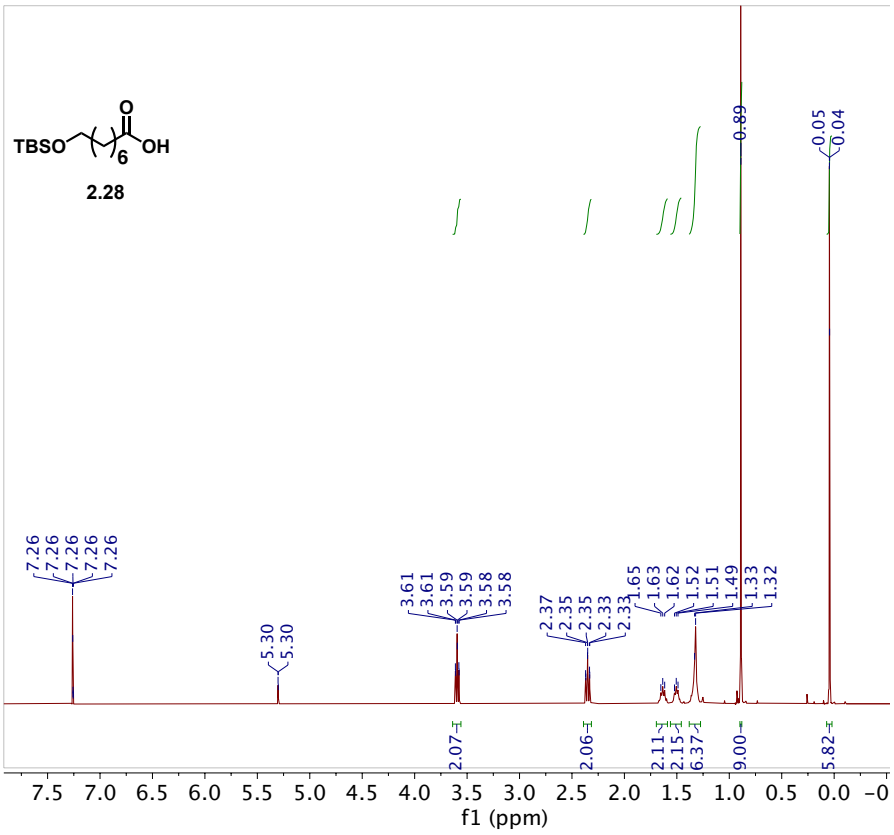
TBSO
6
OH
2.28
7.26
5.30
3.61
3.59
3.58
2.37
2.35
2.33
1.65
1.63
1.62
1.52
1.51
1.49
1.33
1.32
0.89
0.05
0.04
2.07
2.06
2.11
2.15
6.37
9.00
5.82
f1 (ppm)

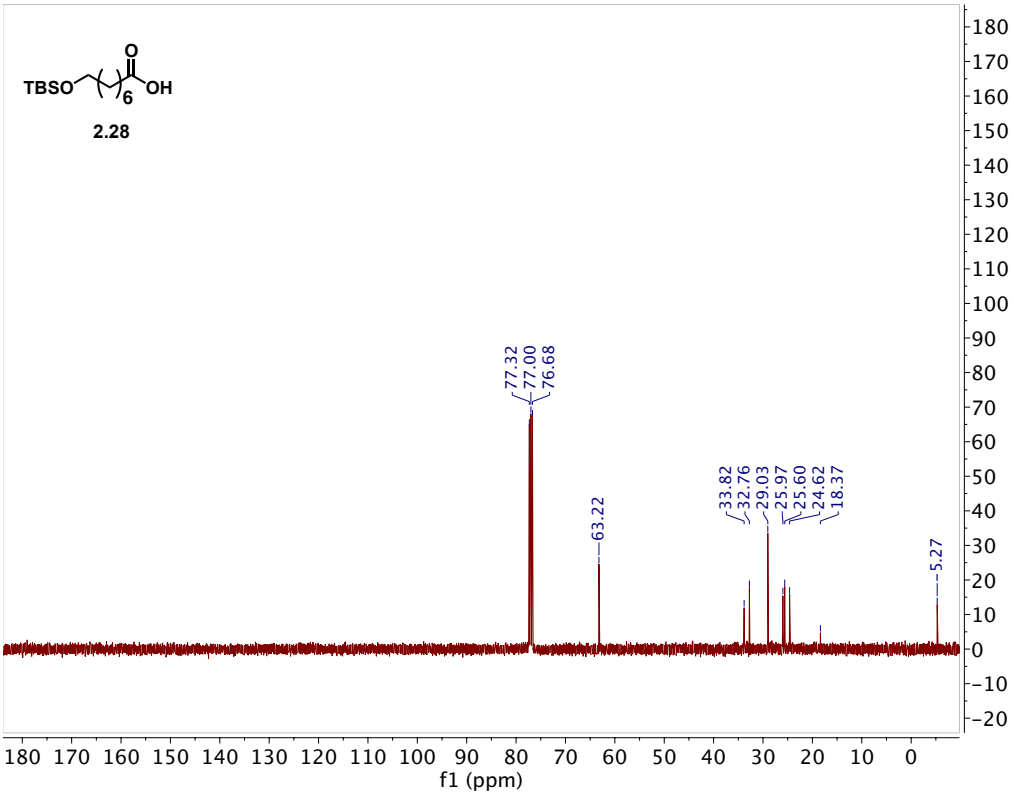
TBSO
6
OH
2.28
77.32
77.00
76.68
63.22
33.82
32.76
29.03
25.97
25.60
24.62
18.37
5.27
f1 (ppm)

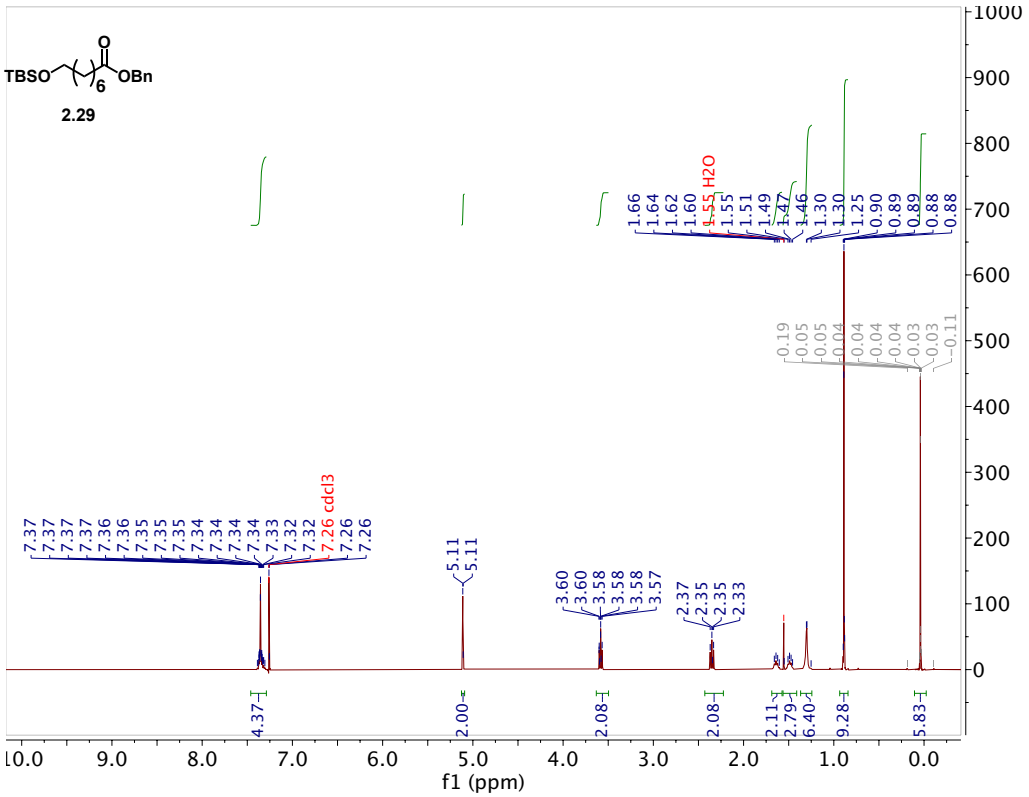
TBSO
OBn
6
2.29
f1 (ppm)

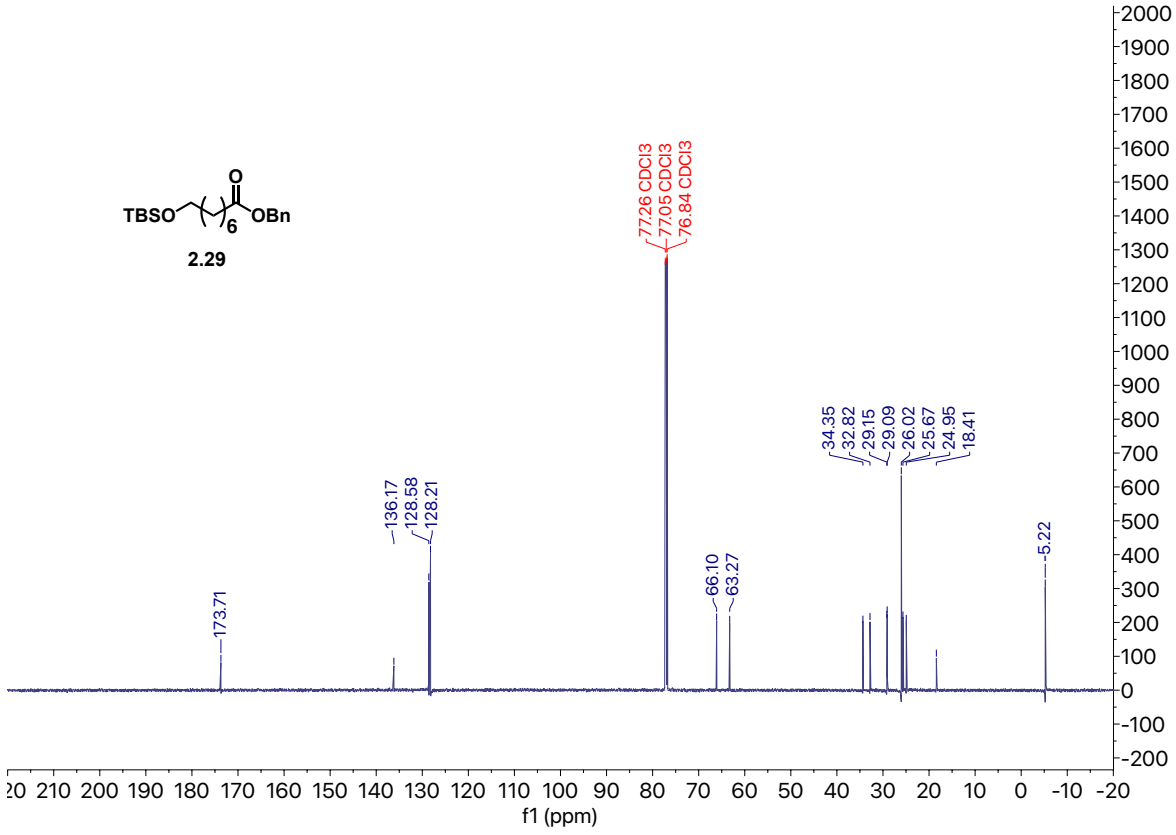
TBSO
OBn
6
2.29
f1 (ppm)

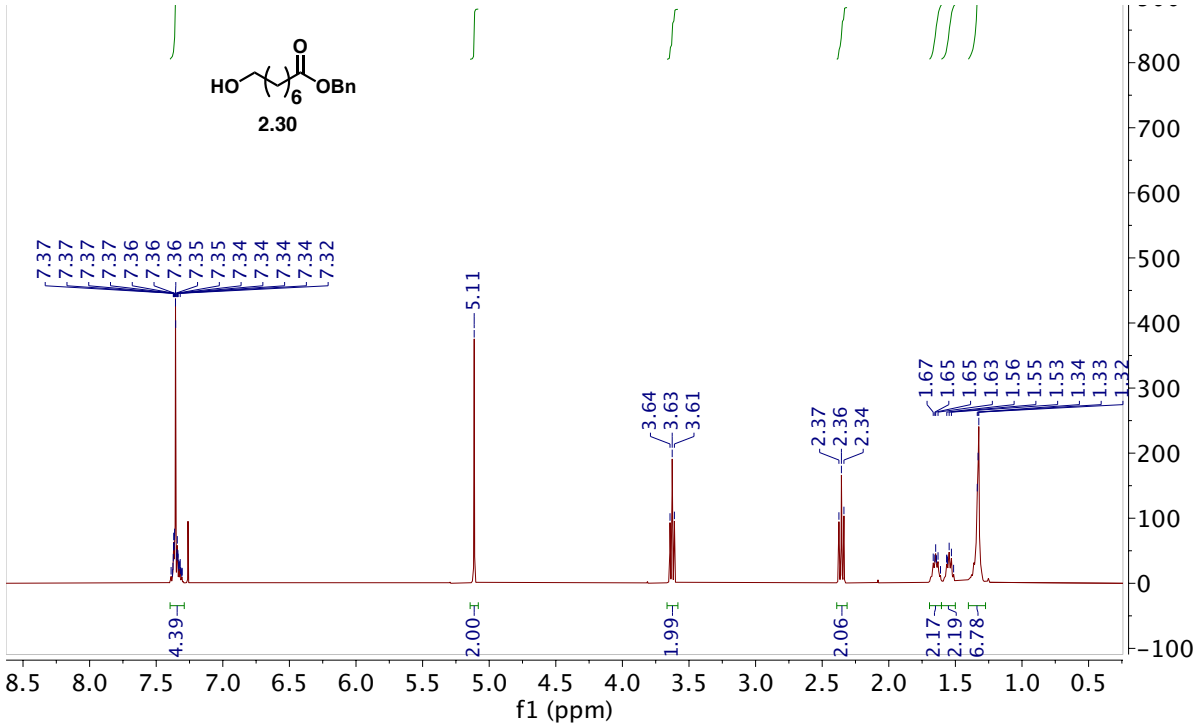
HO
6
OBn
2.30
7.37
7.37
7.37
7.37
7.36
7.36
7.35
7.35
7.34
7.34
7.34
7.34
7.32
5.11
3.64
3.63
3.61
2.37
2.36
2.34
1.67
1.65
1.65
1.63
1.56
1.55
1.53
1.34
1.33
1.32
4.39
2.00
1.99
2.06
2.17
2.19
6.78
f1 (ppm)

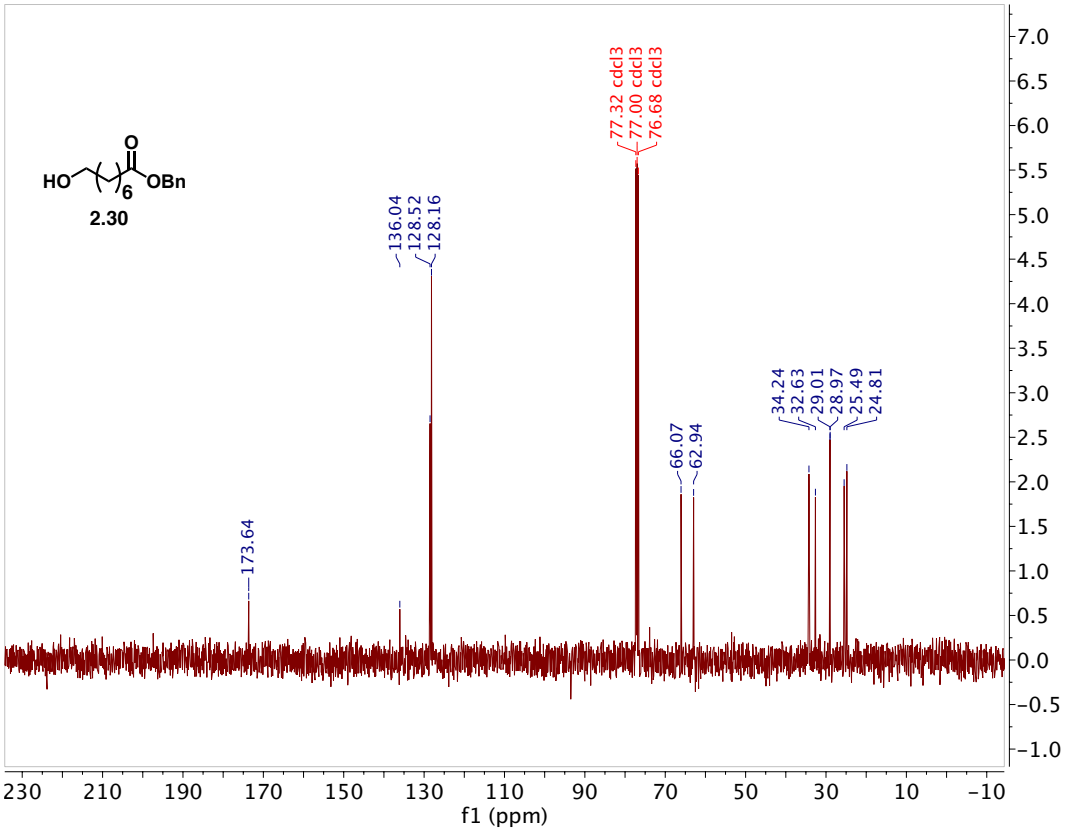
HO
6
OBn
2.30
77.32 cdcl3
77.00 cdcl3
76.68 cdcl3
136.04
128.52
128.16
66.07
62.94
34.24
32.63
29.01
28.97
25.49
24.81
173.64
f1 (ppm)

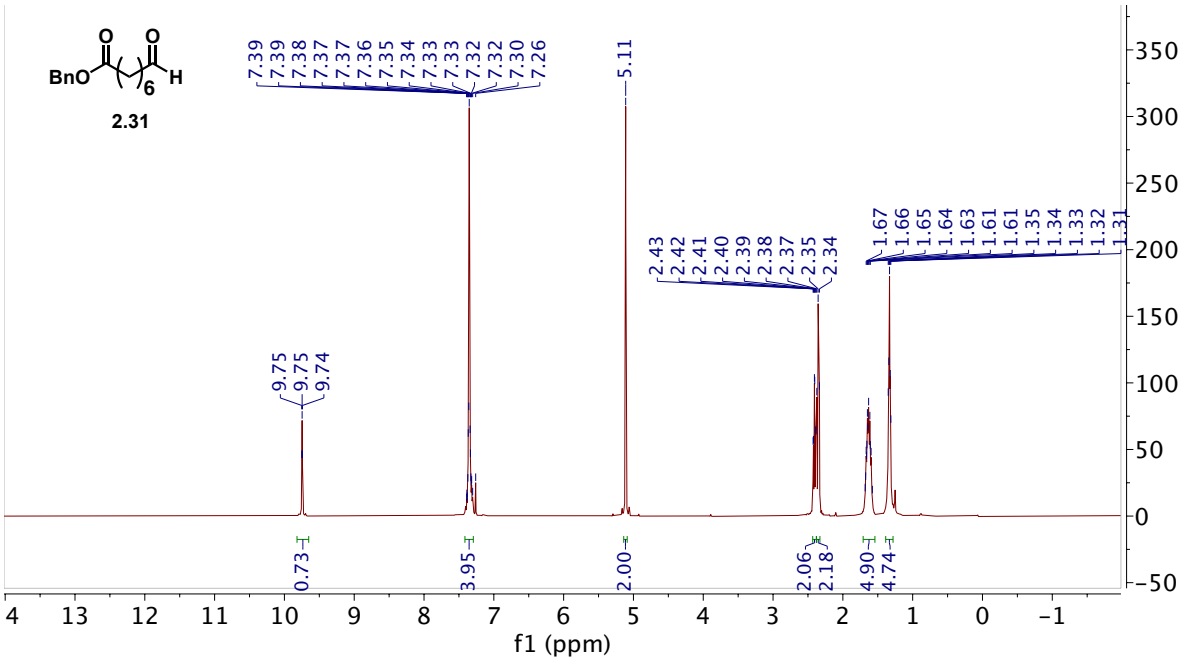
BnO
O
O
H
6
2.31
7.39
7.39
7.38
7.37
7.37
7.36
7.35
7.34
7.33
7.33
7.32
7.32
7.30
7.26
5.11
2.43
2.42
2.41
2.40
2.39
2.38
2.37
2.35
2.34
1.67
1.66
1.65
1.64
1.63
1.61
1.61
1.35
1.34
1.33
1.32
1.31
9.75
9.75
9.74
0.73
3.95
2.00
2.06
2.18
4.90
4.74
f1 (ppm)

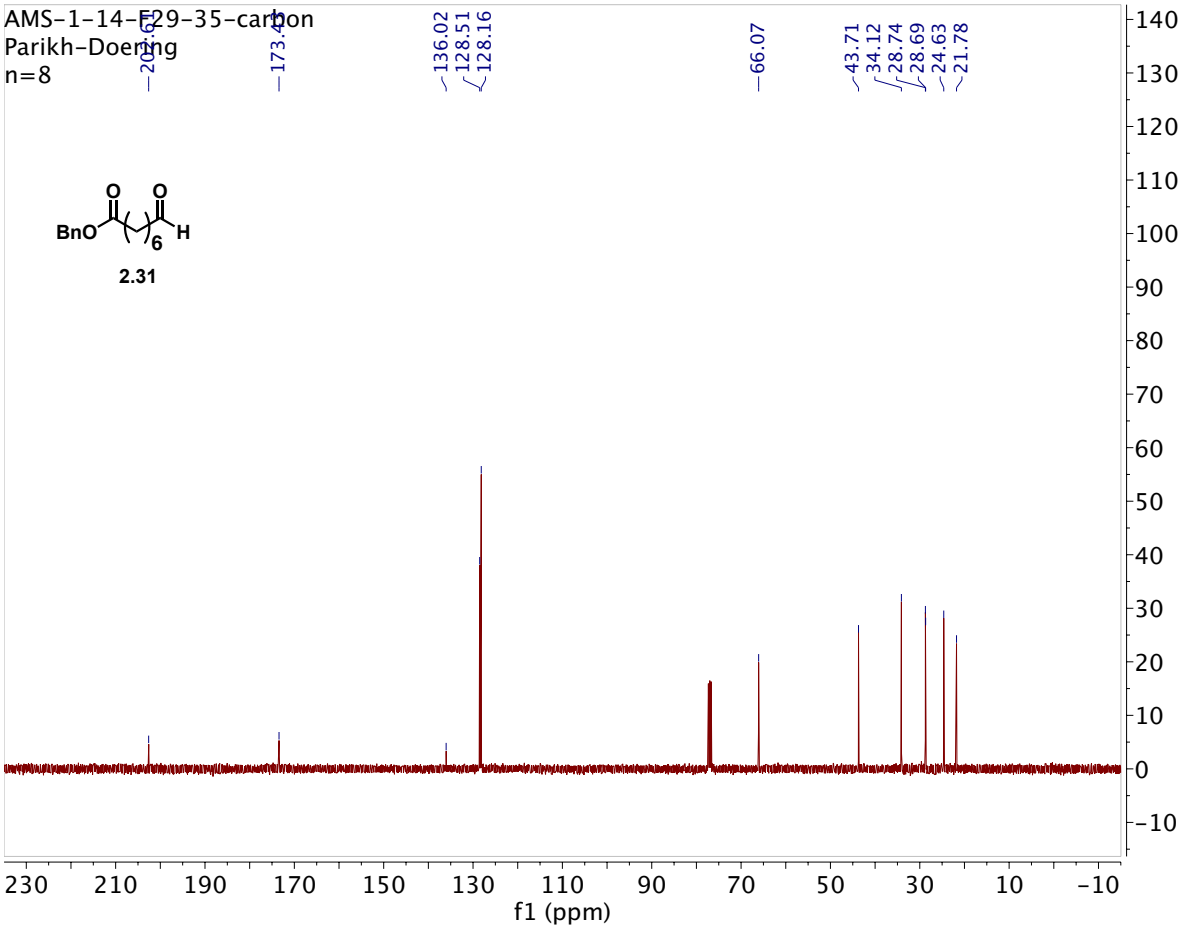
AMS-1-14-F29-35-carbon
Parikh-Doering
n=8
BnO
O
O
H
6
2.31
136.02
128.51
128.16
66.07
43.71
34.12
28.74
28.69
24.63
21.78
f1 (ppm)

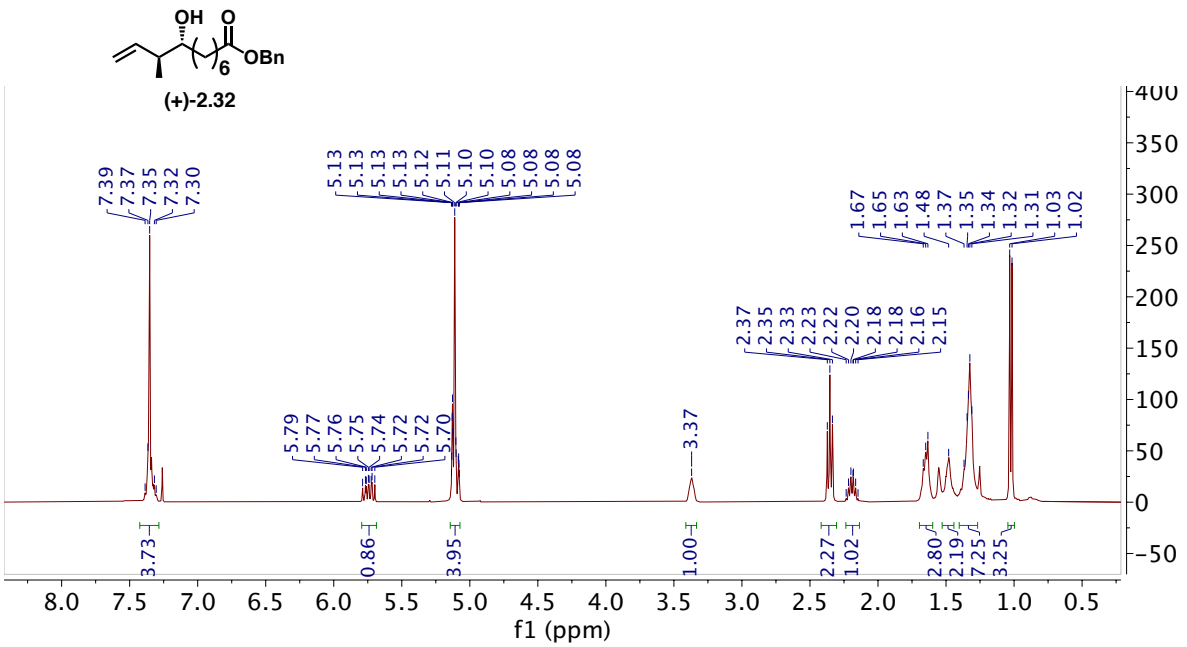
OH
O
OBn
6
(+)-2.32
7.39
7.37
7.35
7.32
7.30
5.13
5.13
5.13
5.13
5.12
5.11
5.10
5.10
5.08
5.08
5.08
5.08
1.67
1.65
1.63
1.48
1.37
1.35
1.34
1.32
1.31
1.03
1.02
2.37
2.35
2.33
2.23
2.22
2.20
2.18
2.18
2.16
2.15
5.79
5.77
5.76
5.75
5.74
5.72
5.72
5.70
3.37
3.73
0.86
3.95
1.00
2.27
1.02
2.80
2.19
7.25
3.25
f1 (ppm)

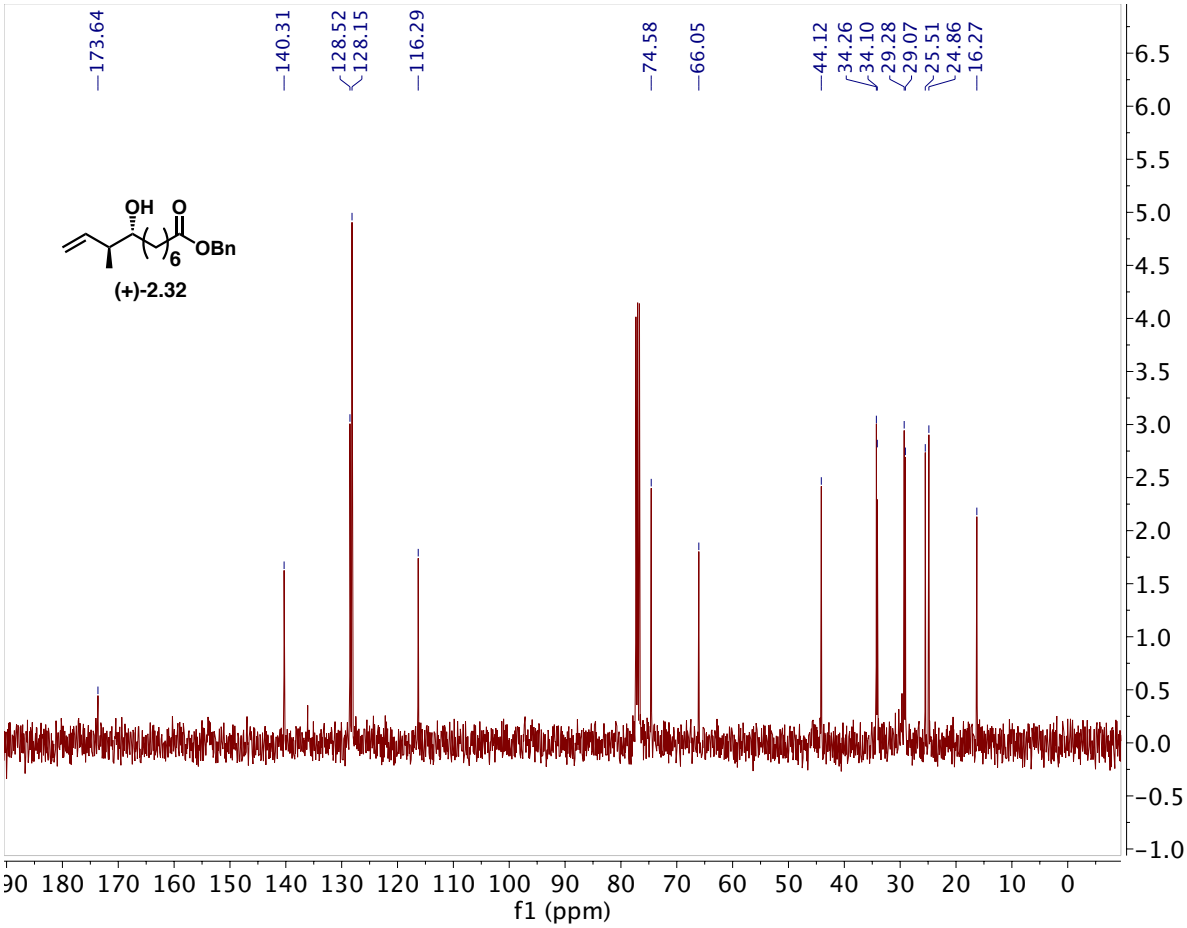
173.64
140.31
128.52
128.15
116.29
74.58
66.05
44.12
34.26
34.10
29.28
29.07
25.51
24.86
16.27
OH
O
OBn
6
(+)-2.32
f1 (ppm)

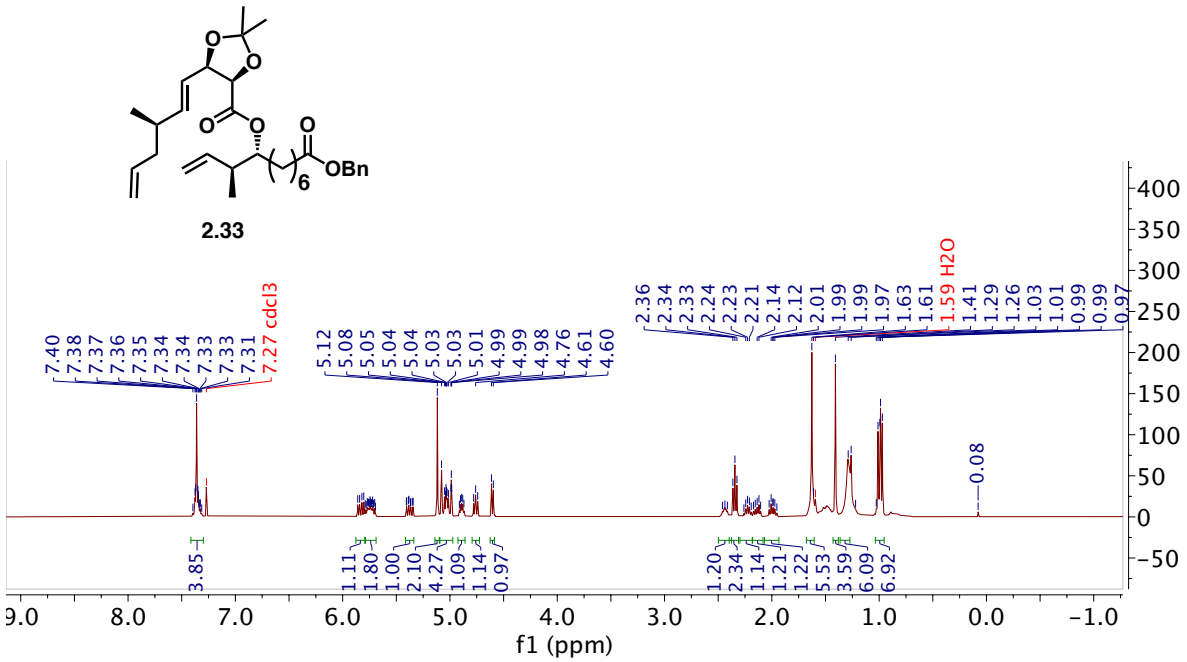
2.33
7.40
7.38
7.37
7.36
7.35
7.34
7.34
7.33
7.33
7.31
7.27 cdcl3
5.12
5.08
5.05
5.04
5.04
5.03
5.03
5.01
4.99
4.99
4.98
4.76
4.61
4.60
2.36
2.34
2.33
2.24
2.23
2.21
2.14
2.12
2.01
1.99
1.99
1.97
1.63
1.61
1.59 H2O
1.41
1.29
1.26
1.03
1.01
0.99
0.99
0.97
0.08
3.85
1.11
1.80
1.00
2.10
4.27
1.09
1.14
0.97
1.20
2.34
1.14
1.21
1.22
5.53
3.59
6.09
6.92
f1 (ppm)

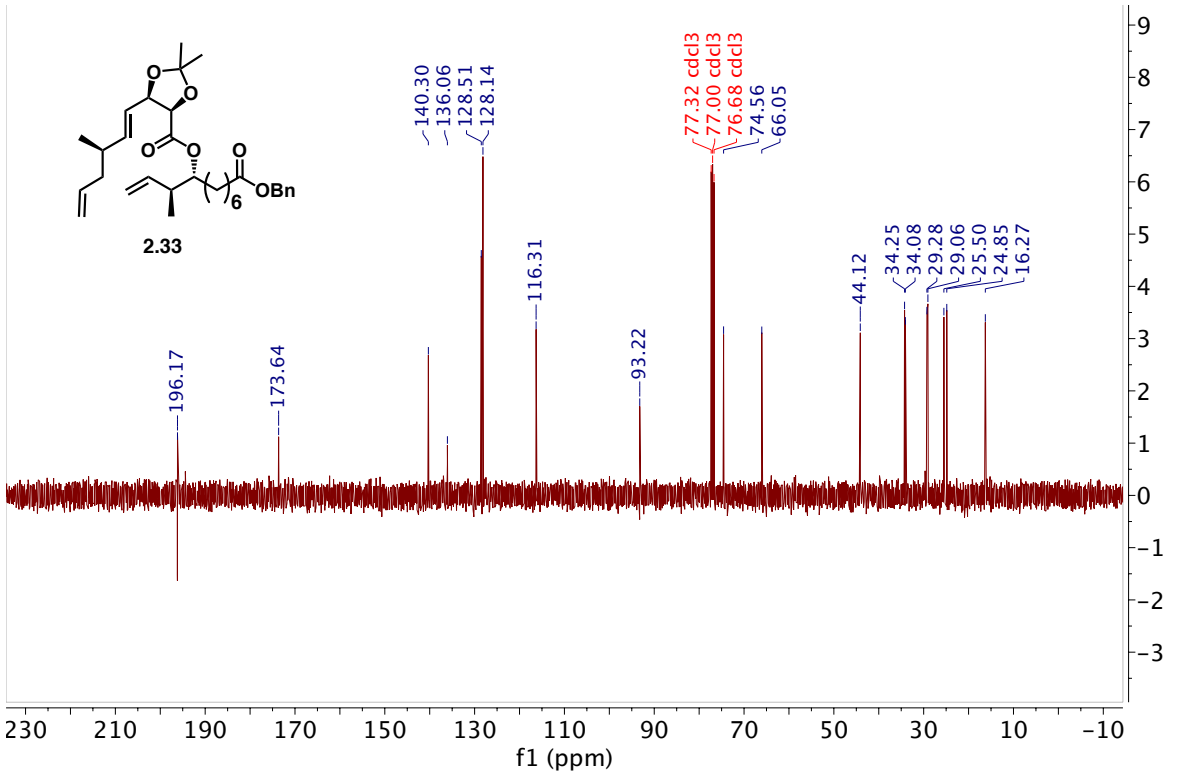
2.33
140.30
136.06
128.51
128.14
77.32 cdcl3
77.00 cdcl3
76.68 cdcl3
74.56
66.05
116.31
93.22
44.12
34.25
34.08
29.28
29.06
25.50
24.85
16.27
196.17
173.64
f1 (ppm)

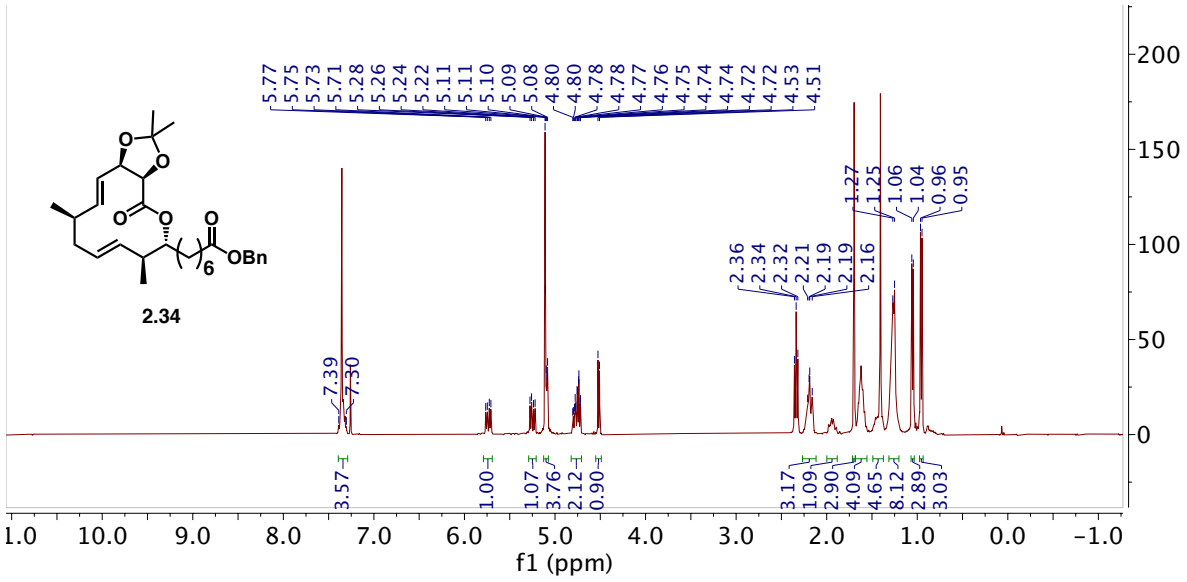
2.34
f1 (ppm)

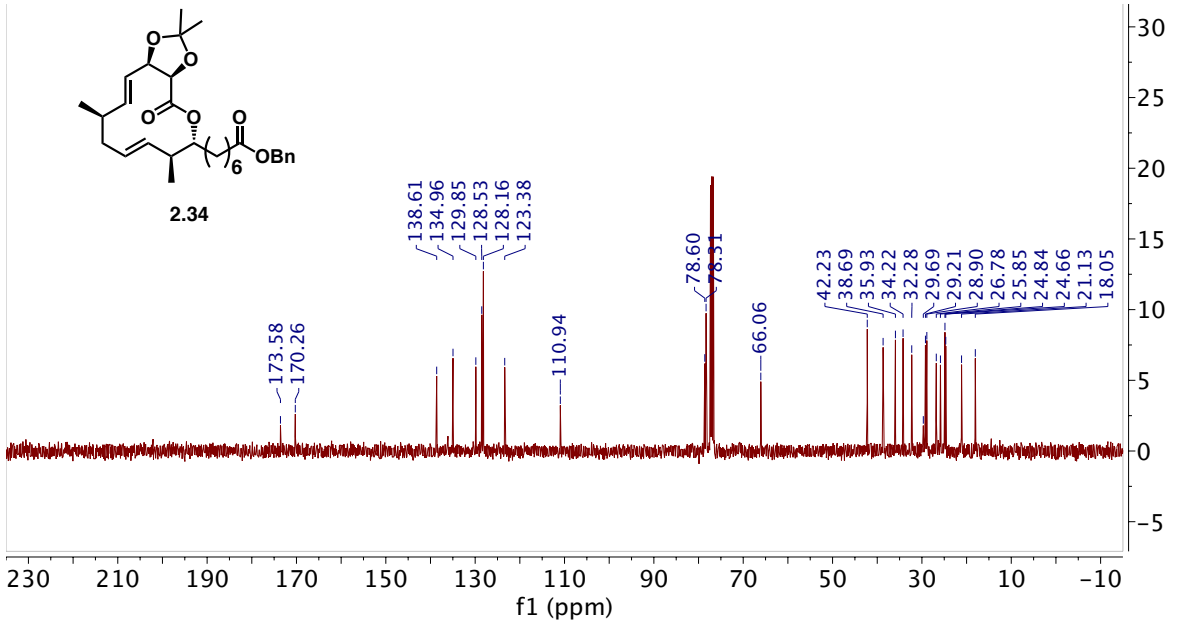
2.34
f1 (ppm)

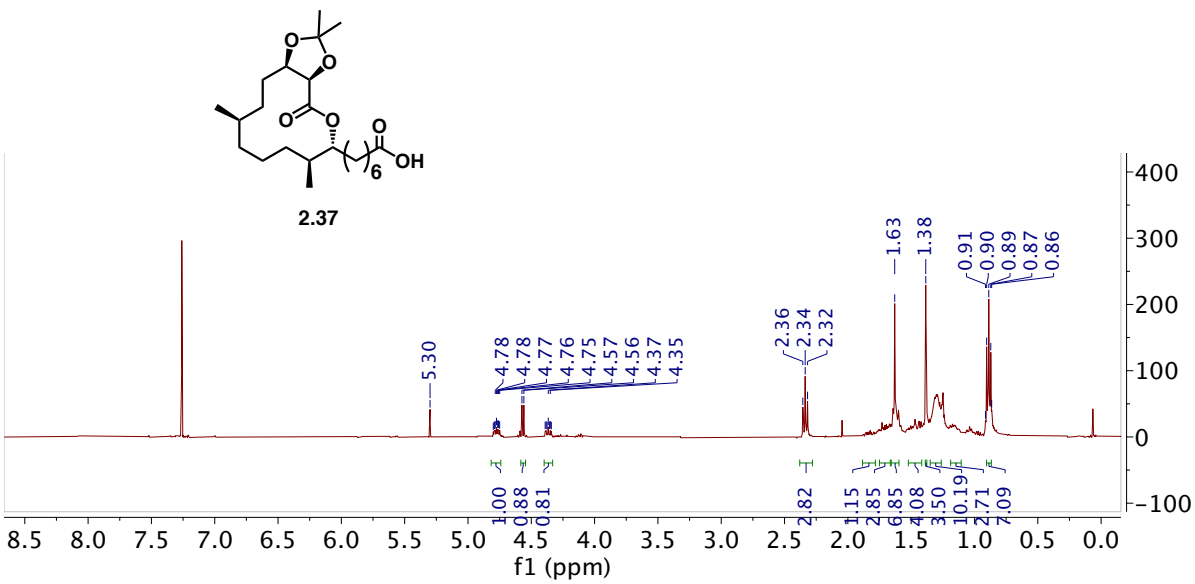
2.37
5.30
4.78
4.78
4.77
4.76
4.75
4.57
4.56
4.37
4.35
2.36
2.34
2.32
1.63
1.38
0.91
0.90
0.89
0.87
0.86
1.00
0.88
0.81
2.82
1.15
2.85
6.85
4.08
3.50
10.19
2.71
7.09
f1 (ppm)

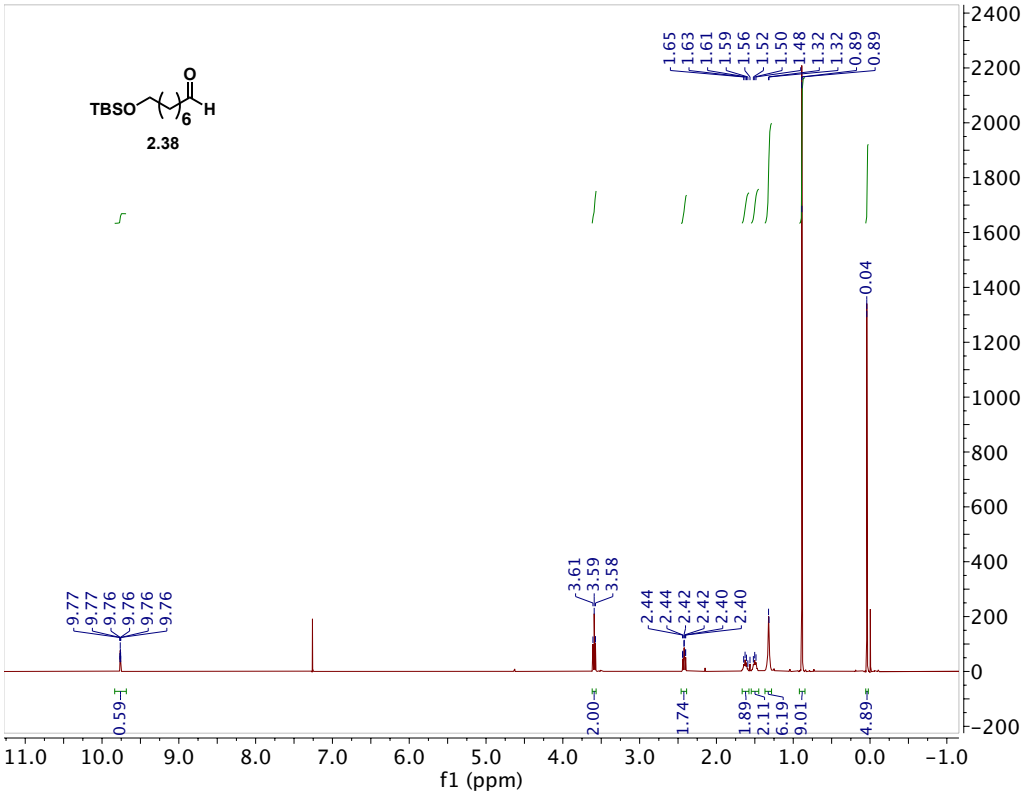
TBSO
6
O
H
2.38
9.77
9.77
9.76
9.76
9.76
9.76
3.61
3.59
3.58
2.44
2.44
2.42
2.42
2.40
2.40
1.65
1.63
1.61
1.59
1.56
1.52
1.50
1.48
1.32
1.32
0.89
0.89
0.04
0.59
2.00
1.74
1.89
2.11
6.19
9.01
4.89
f1 (ppm)

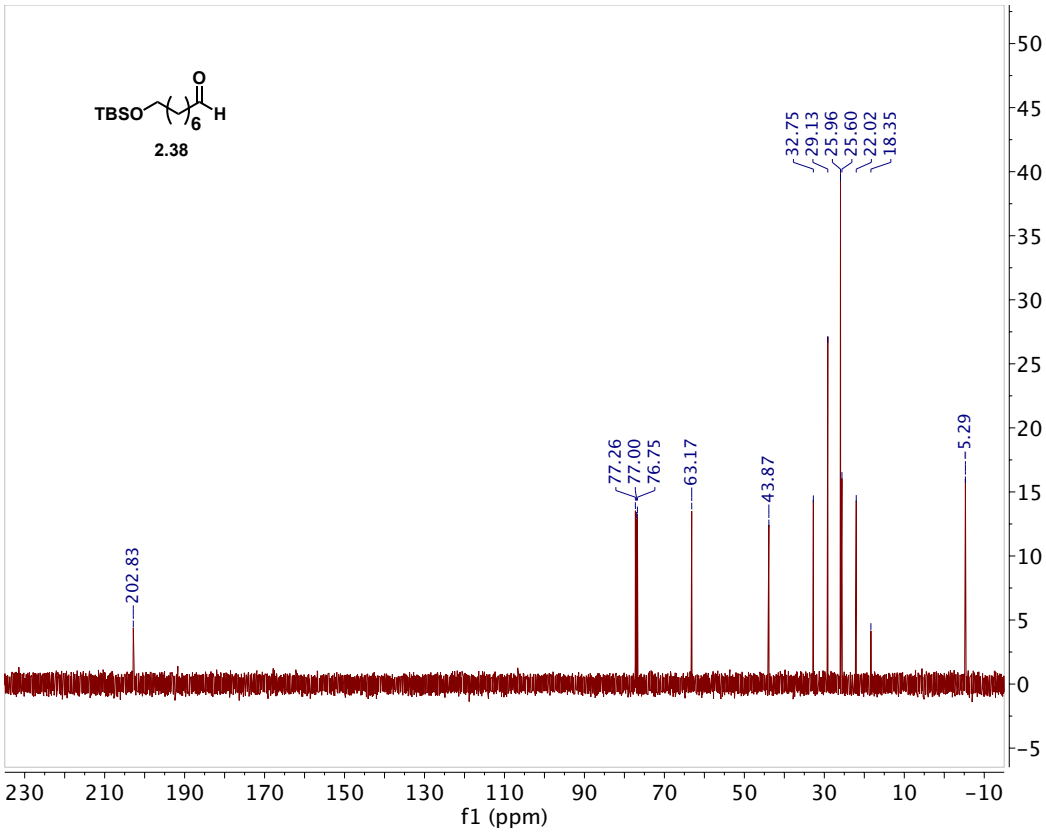
TBSO
6
O
H
2.38
202.83
77.26
77.00
76.75
63.17
43.87
32.75
29.13
25.96
25.60
22.02
18.35
5.29
f1 (ppm)

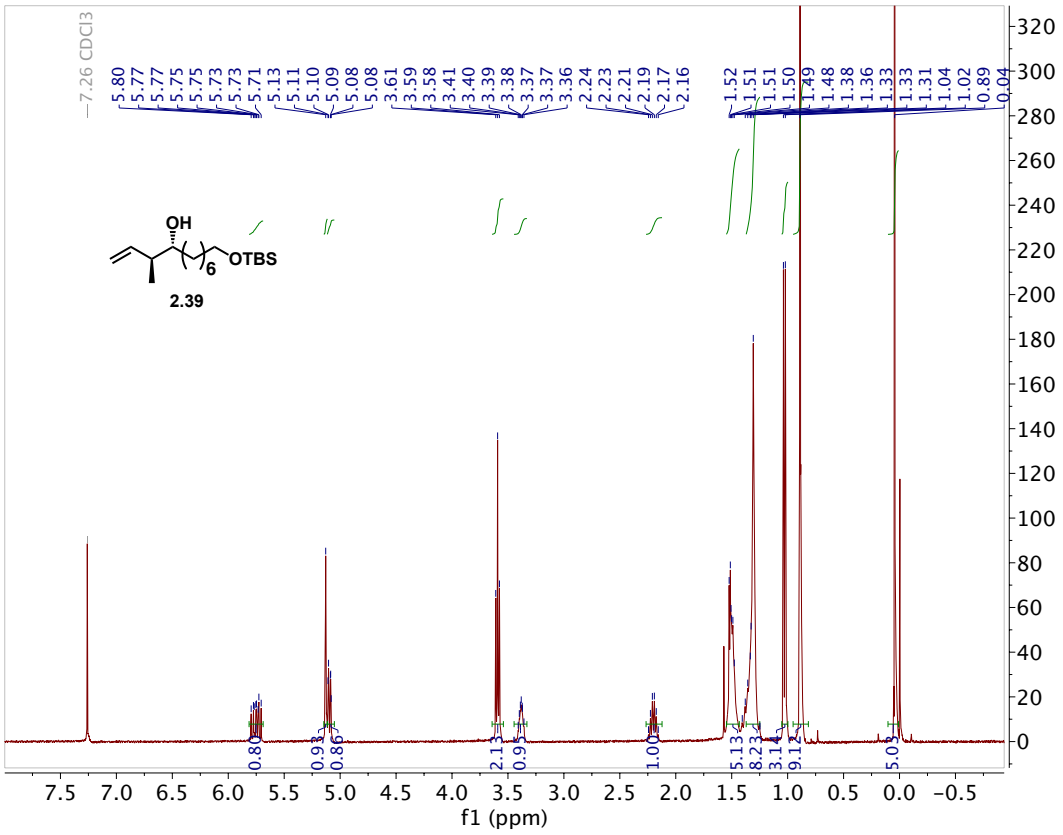
OH
OTBS
6
2.39
f1 (ppm)

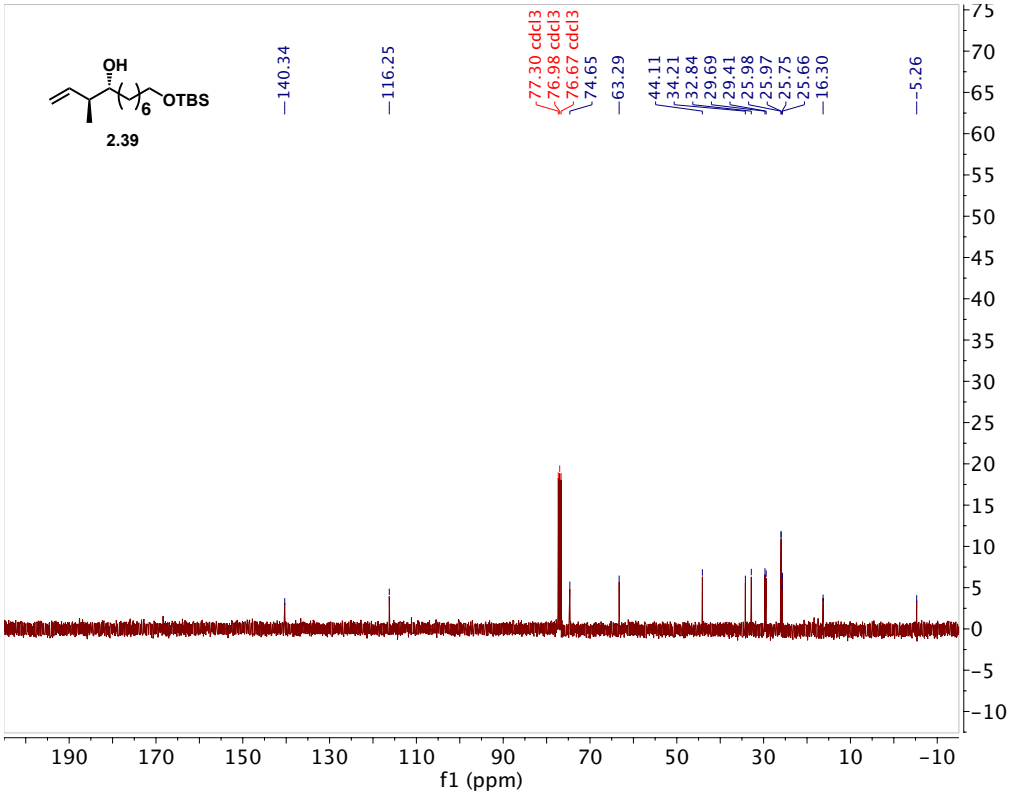
OH
OTBS
6
2.39
f1 (ppm)

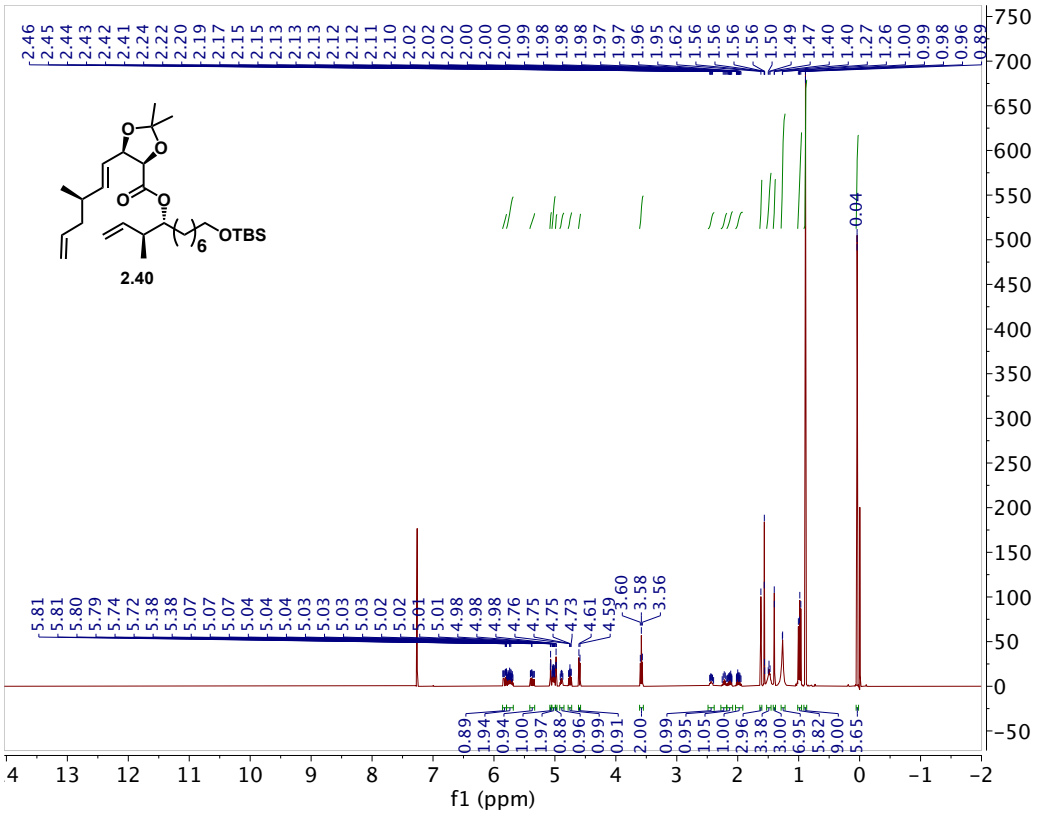
OTBS
6
2.40
f1 (ppm)

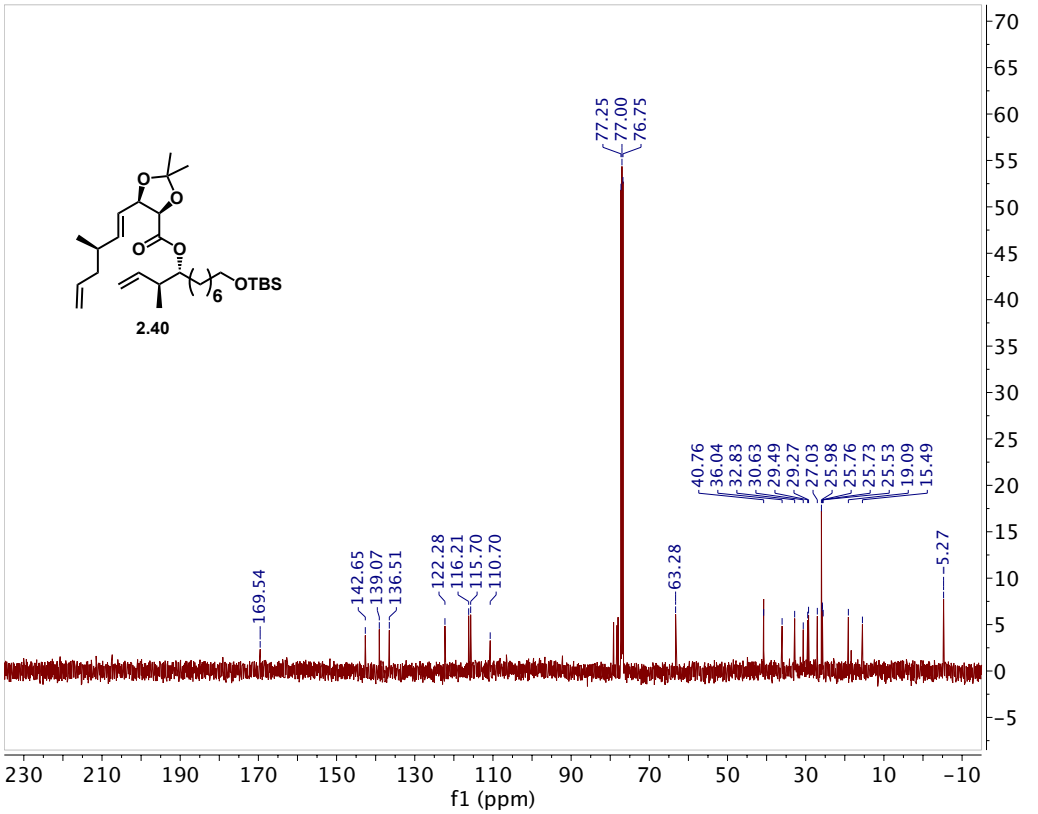
OTBS
6
2.40
f1 (ppm)

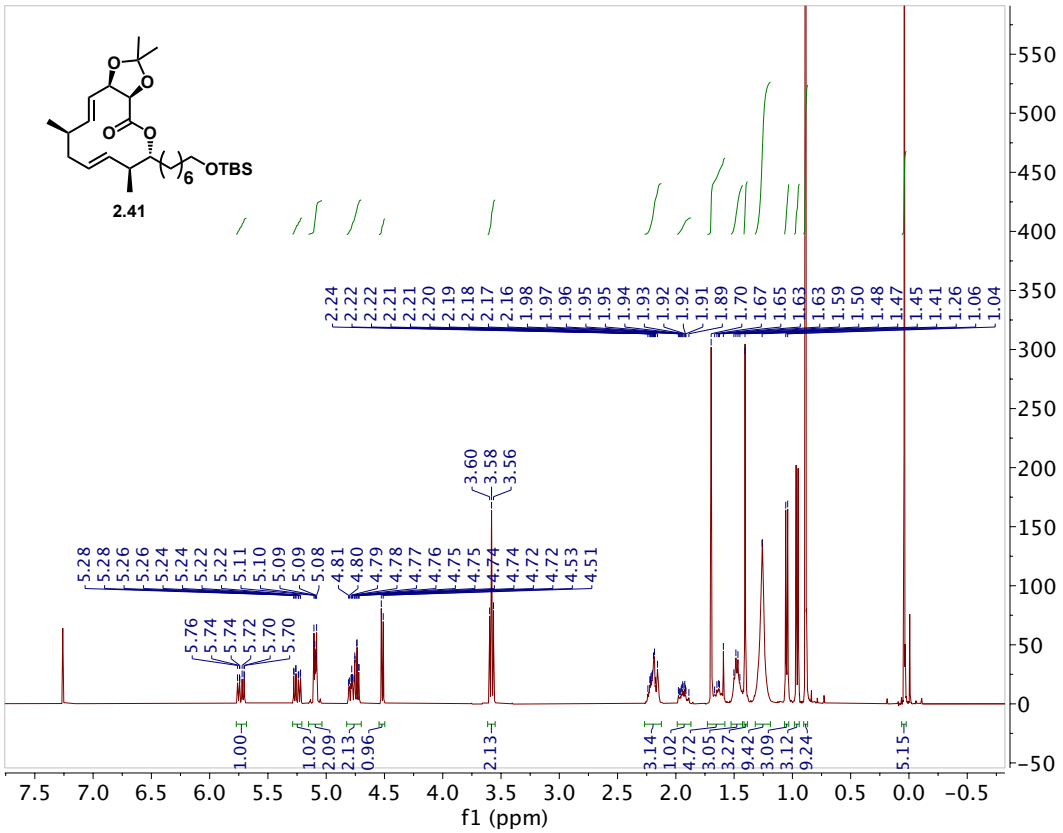
OTBS
2.41
f1 (ppm)

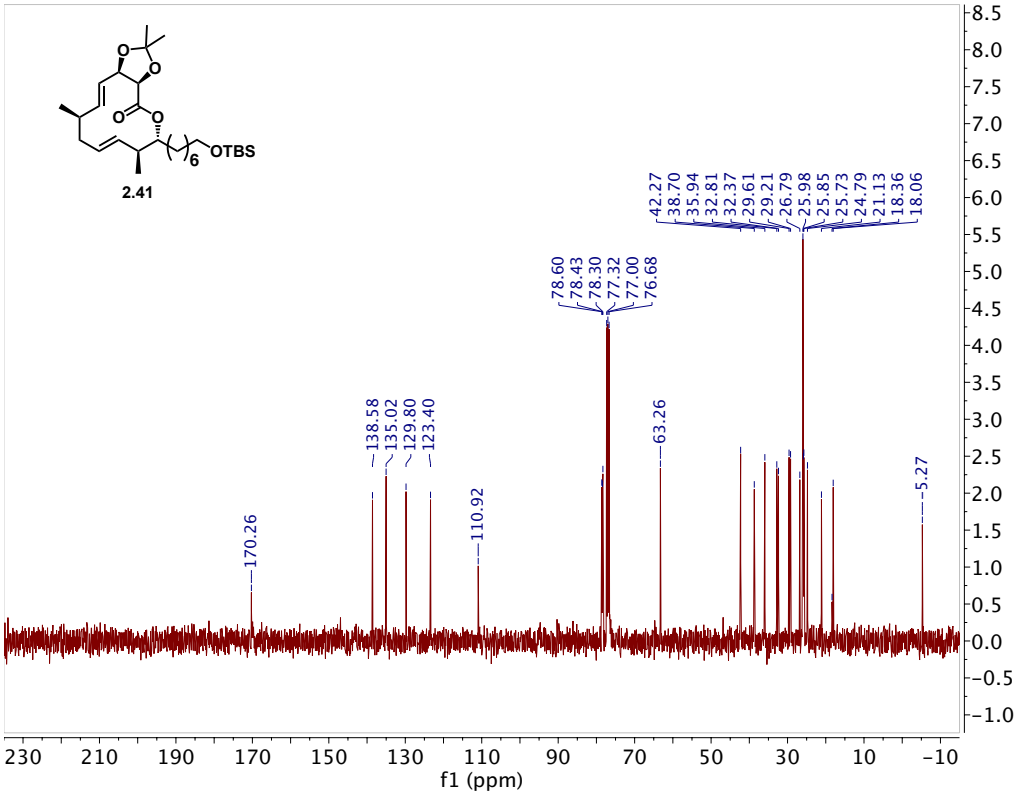
OTBS
2.41
f1 (ppm)

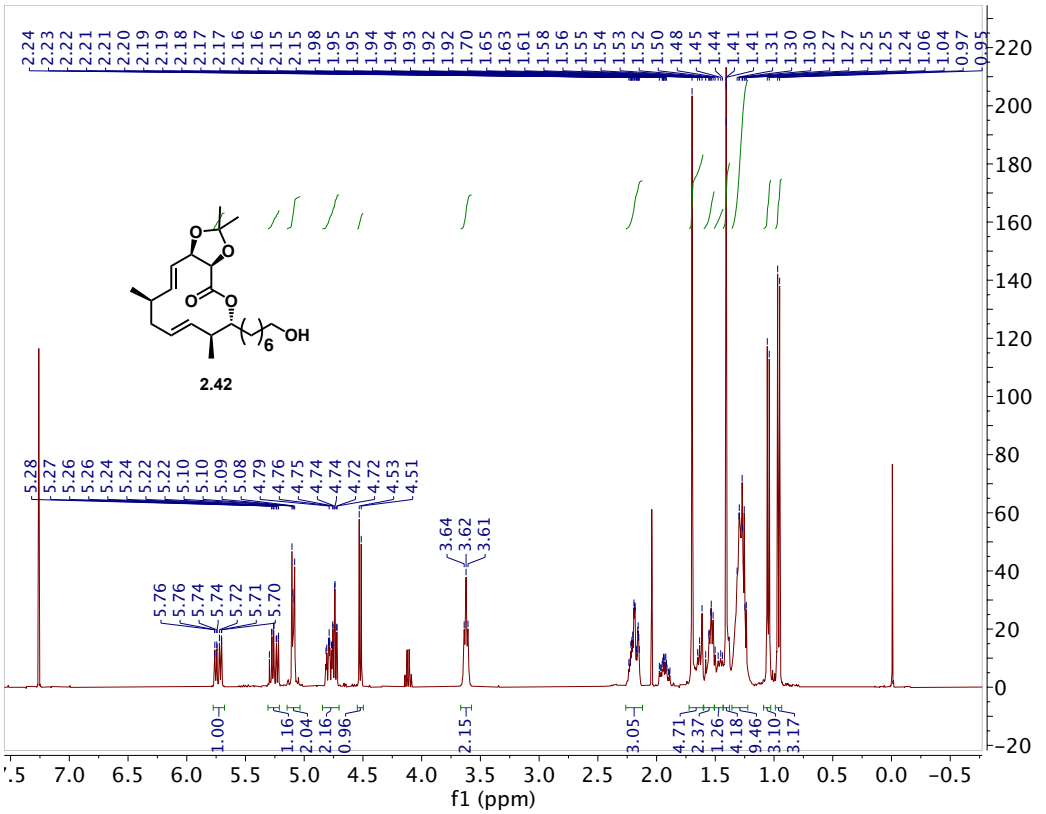
2.42
f1 (ppm)

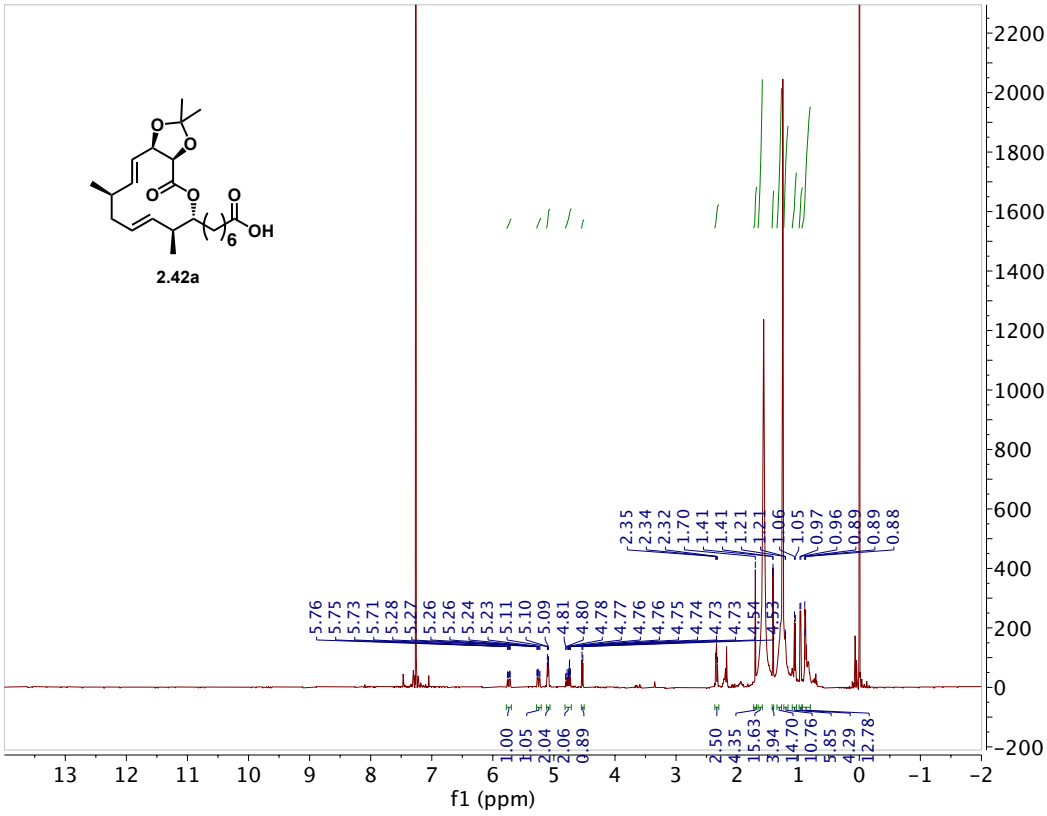
2.42a
f1 (ppm)

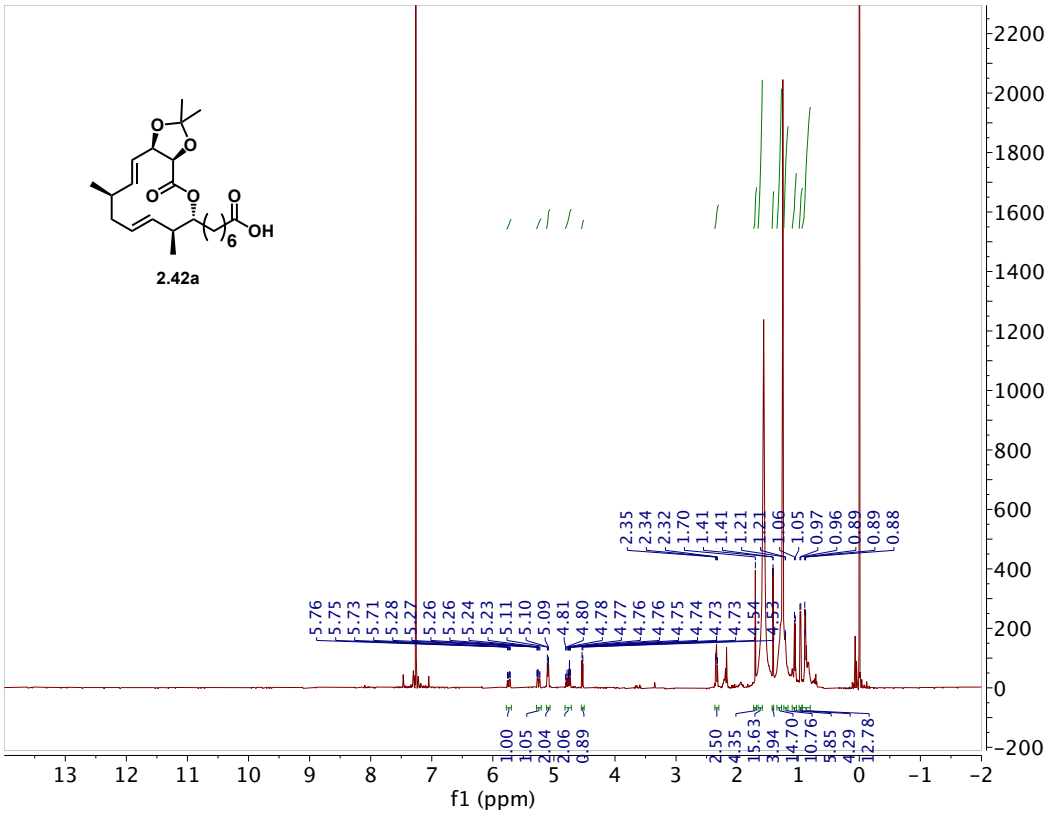
2.42a
f1 (ppm)

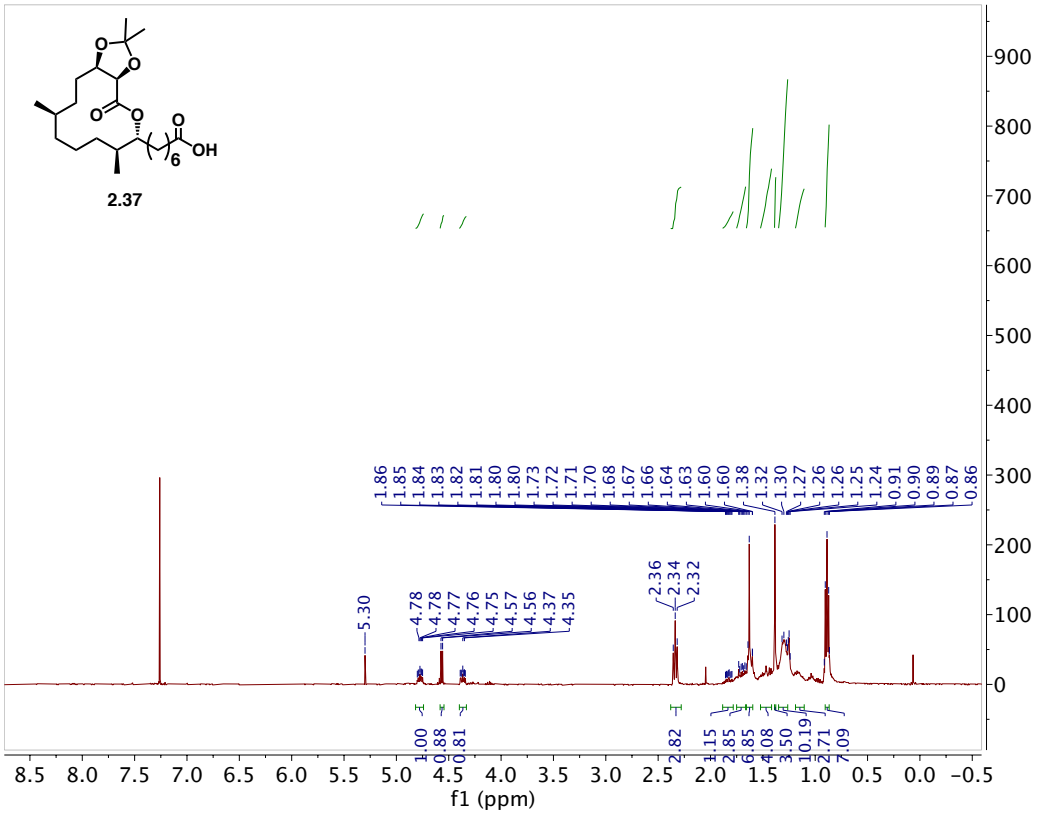
2.37
f1 (ppm)

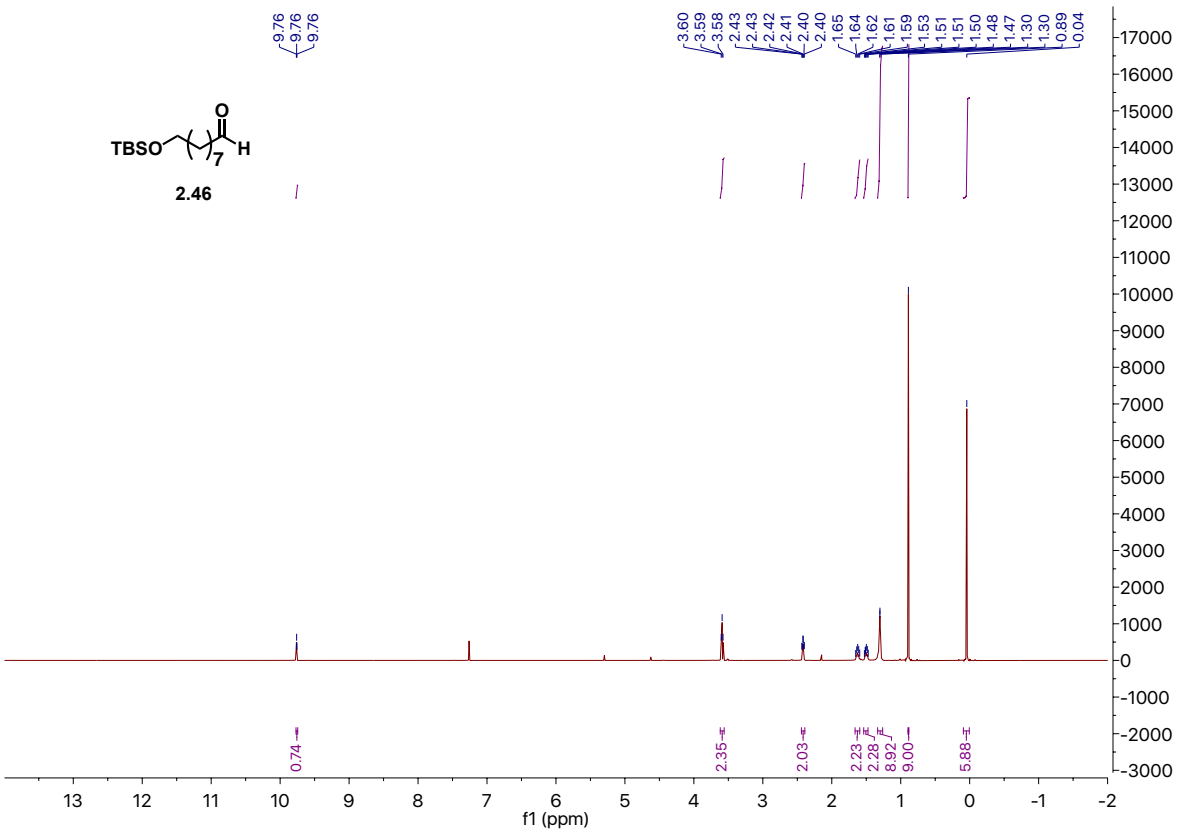
TBSO
O
H
7
2.46
9.76
9.76
9.76
3.60
3.59
3.58
2.43
2.43
2.42
2.41
2.40
2.40
1.65
1.64
1.62
1.61
1.59
1.53
1.51
1.51
1.50
1.48
1.47
1.30
1.30
0.89
0.04
0.74
2.35
2.03
2.23
2.28
8.92
9.00
5.88
f1 (ppm)

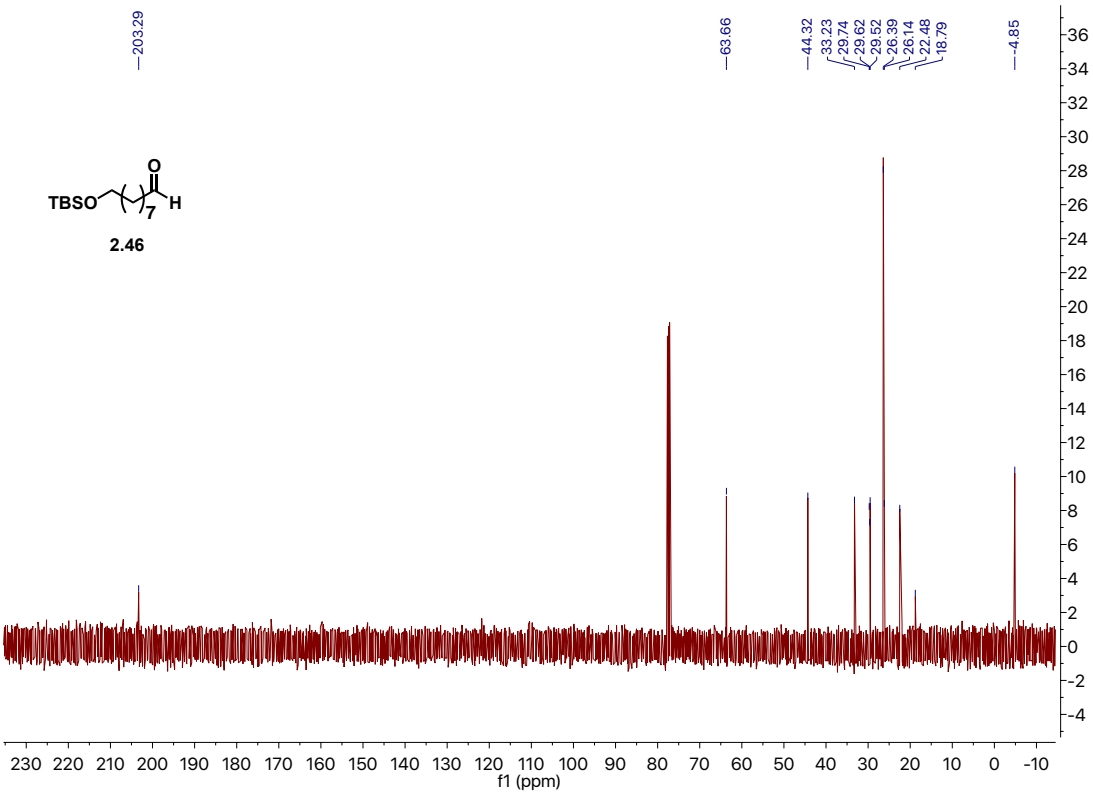
TBSO
O
H
7
2.46
203.29
63.66
44.32
33.23
29.74
29.62
29.52
26.39
26.14
22.48
18.79
4.85
f1 (ppm)

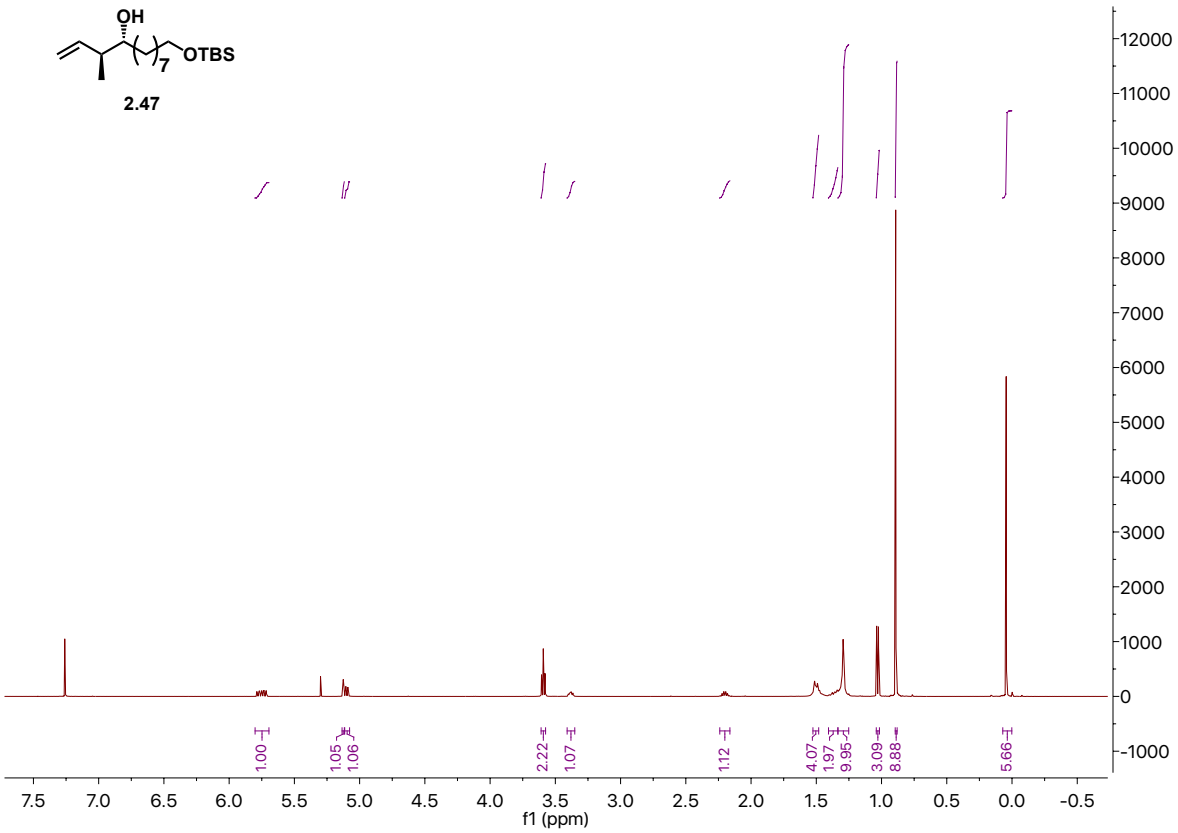
OH
OTBS
7
2.47
1.00
1.05
1.06
2.22
1.07
1.12
4.07
1.97
9.95
3.09
8.88
5.66
f1 (ppm)

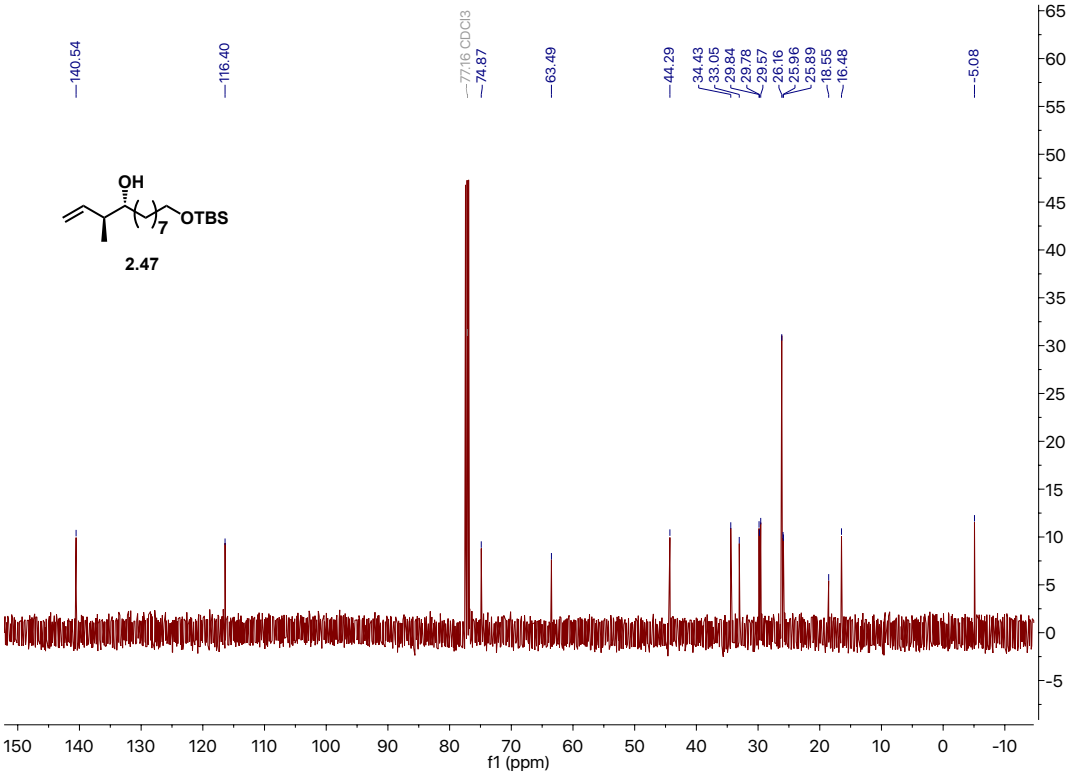
140.54
116.40
77.16 CDCl3
74.87
63.49
44.29
34.43
33.05
29.84
29.78
29.57
26.16
25.96
25.89
18.55
16.48
-5.08
OH
OTBS
7
2.47
f1 (ppm)

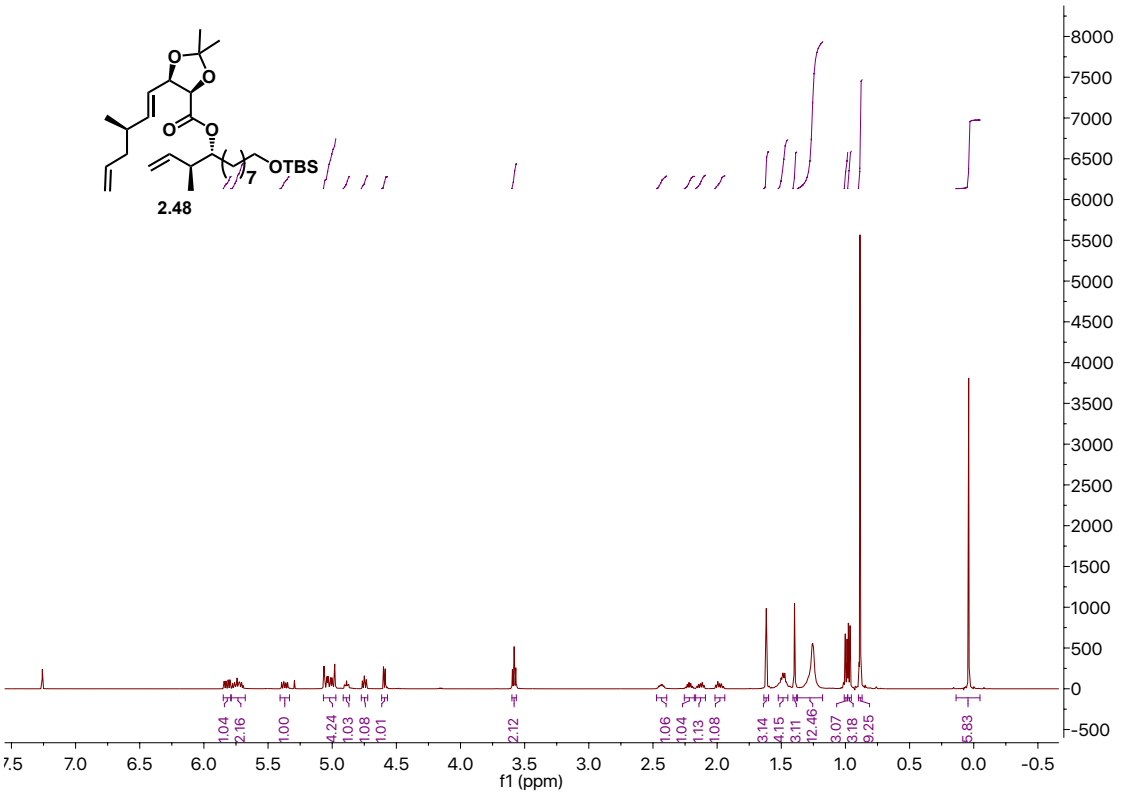
OTBS
7
2.48
1.04
2.16
1.00
4.24
1.03
1.08
1.01
2.12
1.06
1.04
1.13
1.08
3.14
4.15
3.11
12.46
3.07
3.18
9.25
5.83
f1 (ppm)

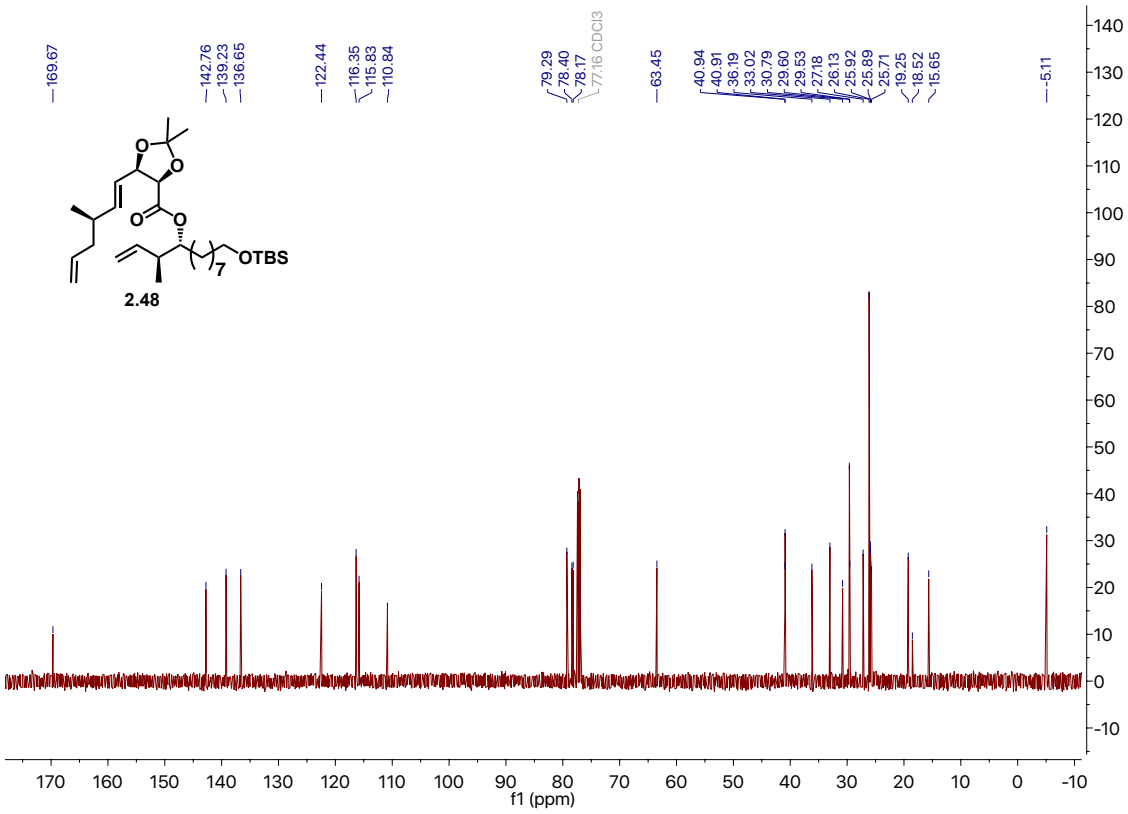
169.67
142.76
139.23
136.65
122.44
116.35
115.83
110.84
79.29
78.40
78.17
77.16 CDCl3
63.45
40.94
40.91
36.19
33.02
30.79
29.60
29.53
27.18
26.13
25.92
25.89
25.71
19.25
18.52
15.65
-5.11
OTBS
7
2.48
f1 (ppm)

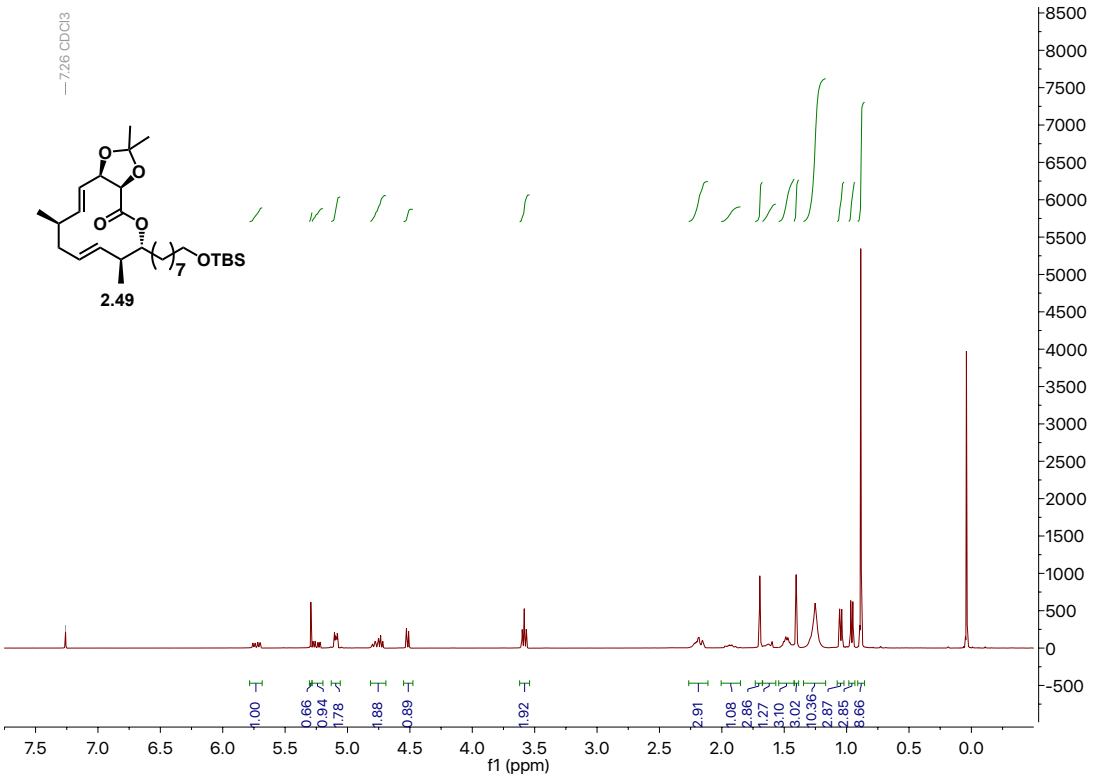
7.26 CDCl3
OTBS
2.49
1.00
0.66
0.94
1.78
1.88
0.89
1.92
2.91
1.08
2.86
1.27
3.10
3.02
10.36
2.87
2.85
8.66
f1 (ppm)

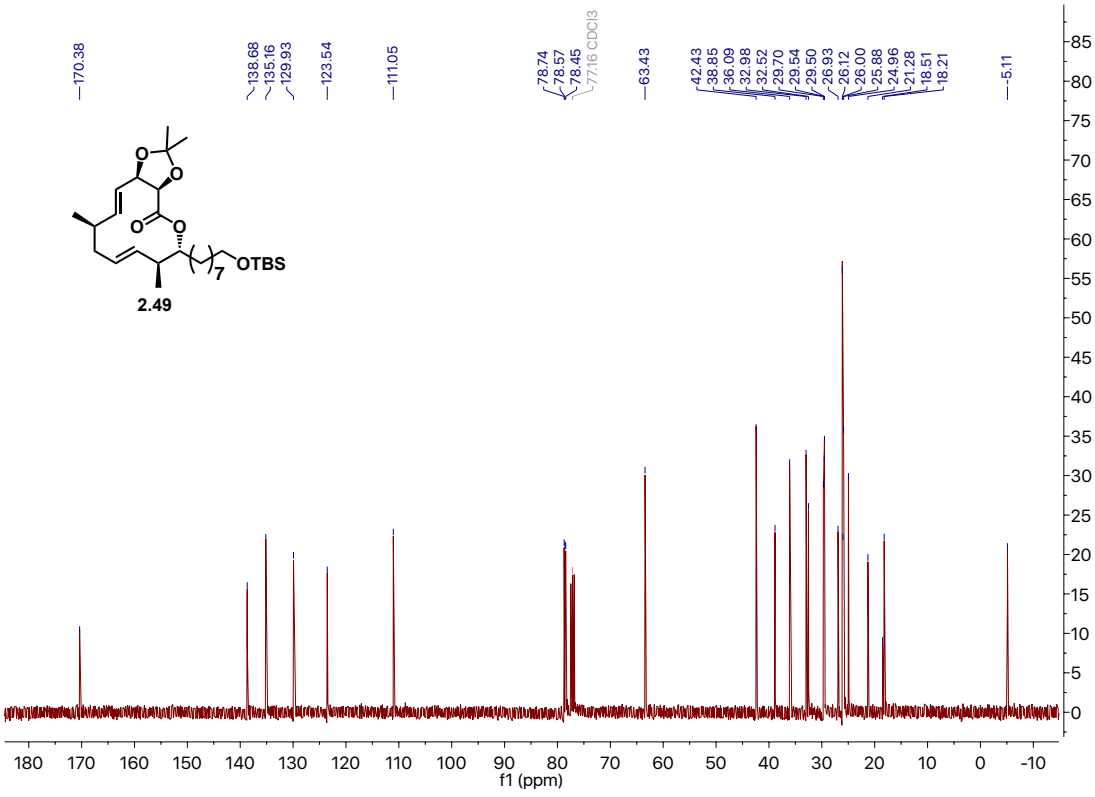
170.38
138.68
135.16
129.93
123.54
111.05
78.74
78.57
78.45
77.16 CDCl3
63.43
42.43
38.85
36.09
32.98
32.52
29.70
29.54
29.50
26.93
26.12
26.00
25.88
24.96
21.28
18.51
18.21
5.11
OTBS
2.49
f1 (ppm)

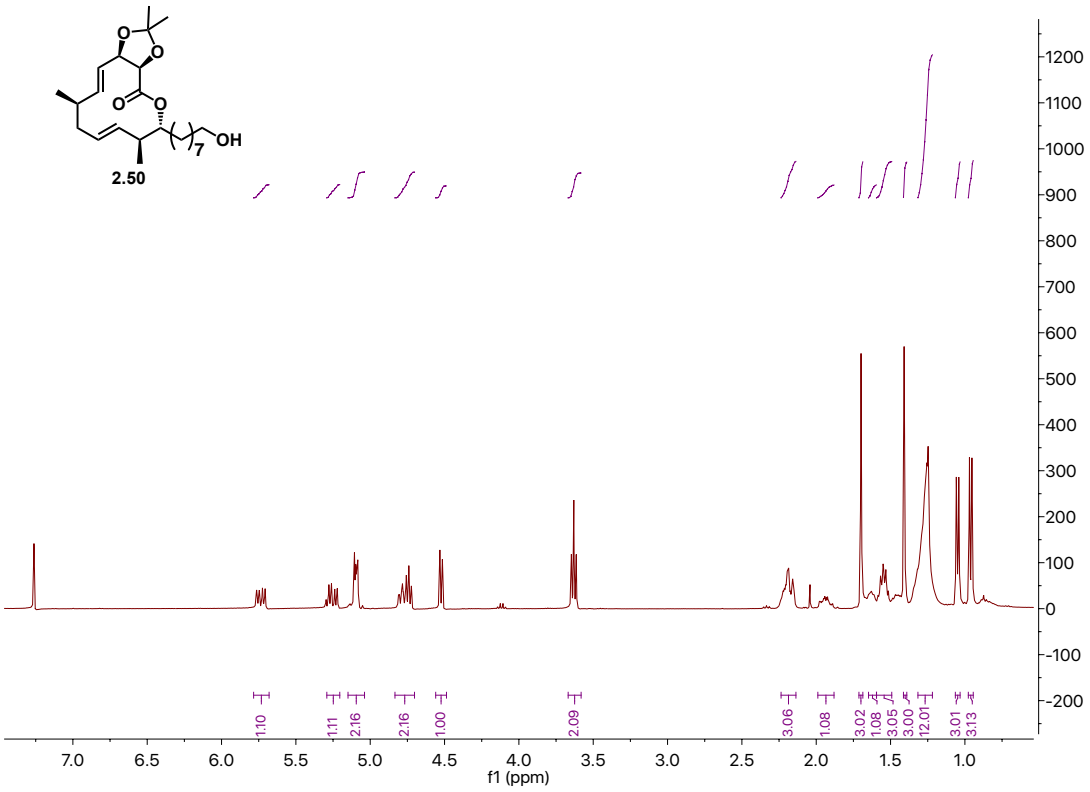
2.50
1.10
1.11
2.16
2.16
1.00
2.09
3.06
1.08
3.02
1.08
3.05
3.00
12.01
3.01
3.13
f1 (ppm)

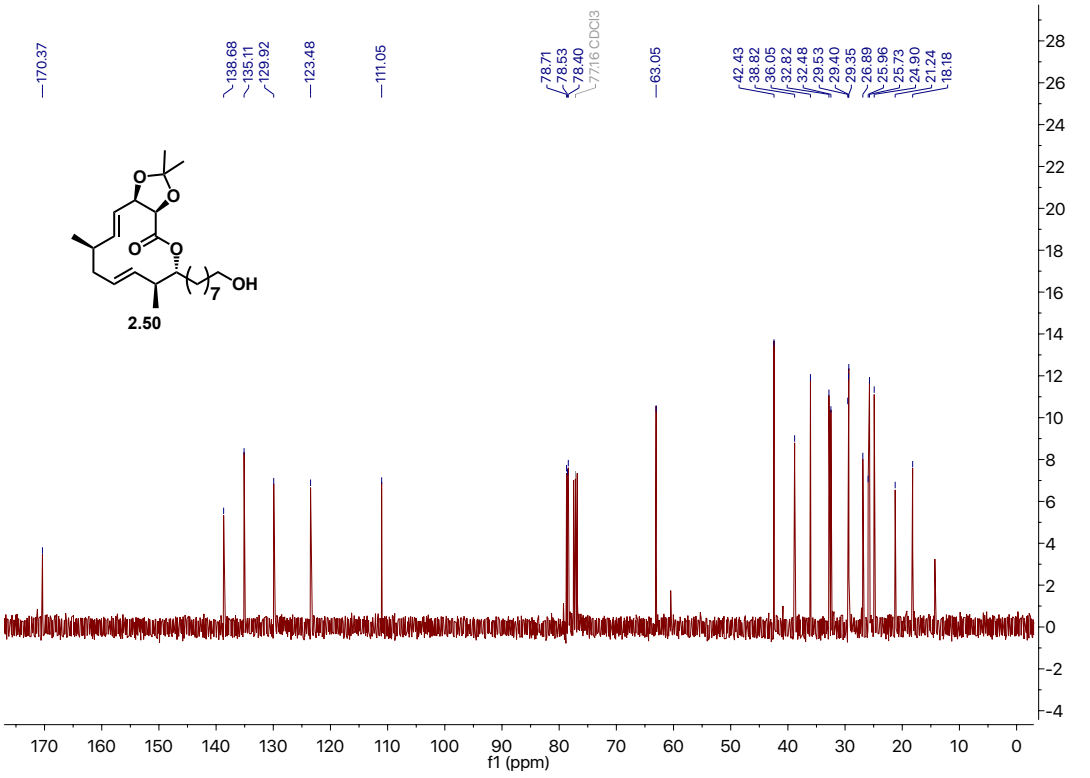
170.37
138.68
135.11
129.92
123.48
111.05
78.71
78.53
78.40
77.16 CDCl3
63.05
42.43
38.82
36.05
32.82
32.48
29.53
29.40
29.35
26.89
25.96
25.73
24.90
21.24
18.18
2.50
f1 (ppm)

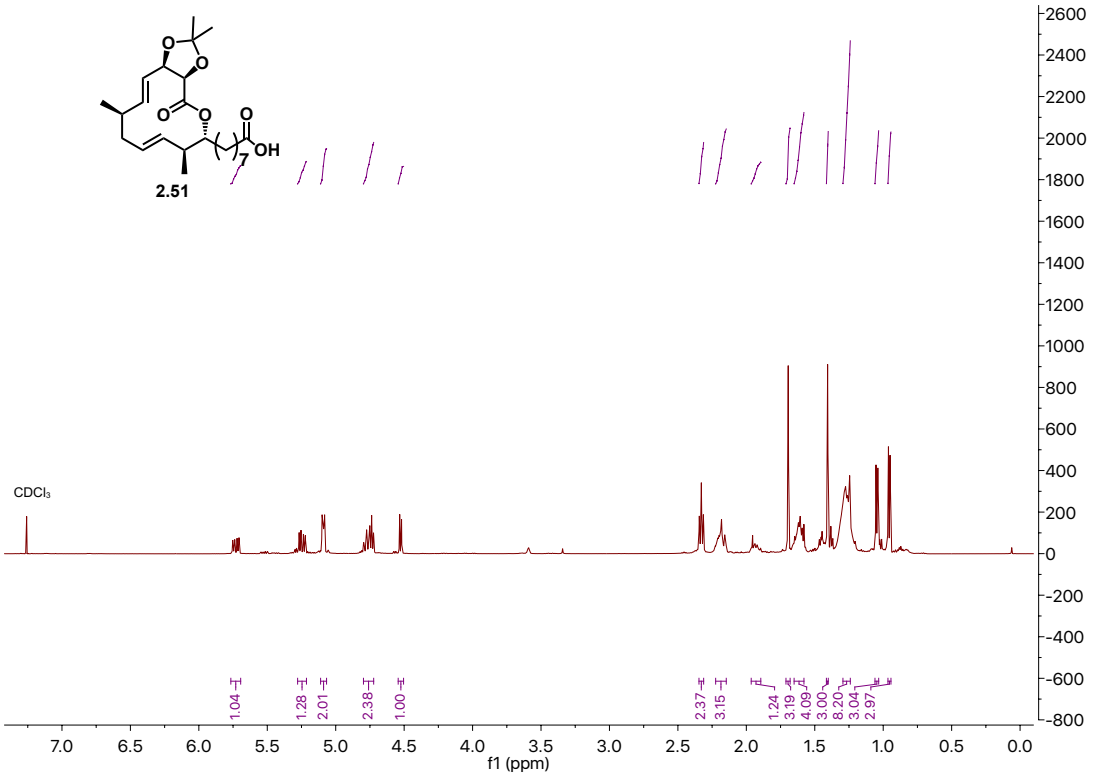
2.51
CDCl3
1.04
1.28
2.01
2.38
1.00
2.37
3.15
1.24
3.19
4.09
3.00
8.20
3.04
2.97
f1 (ppm)

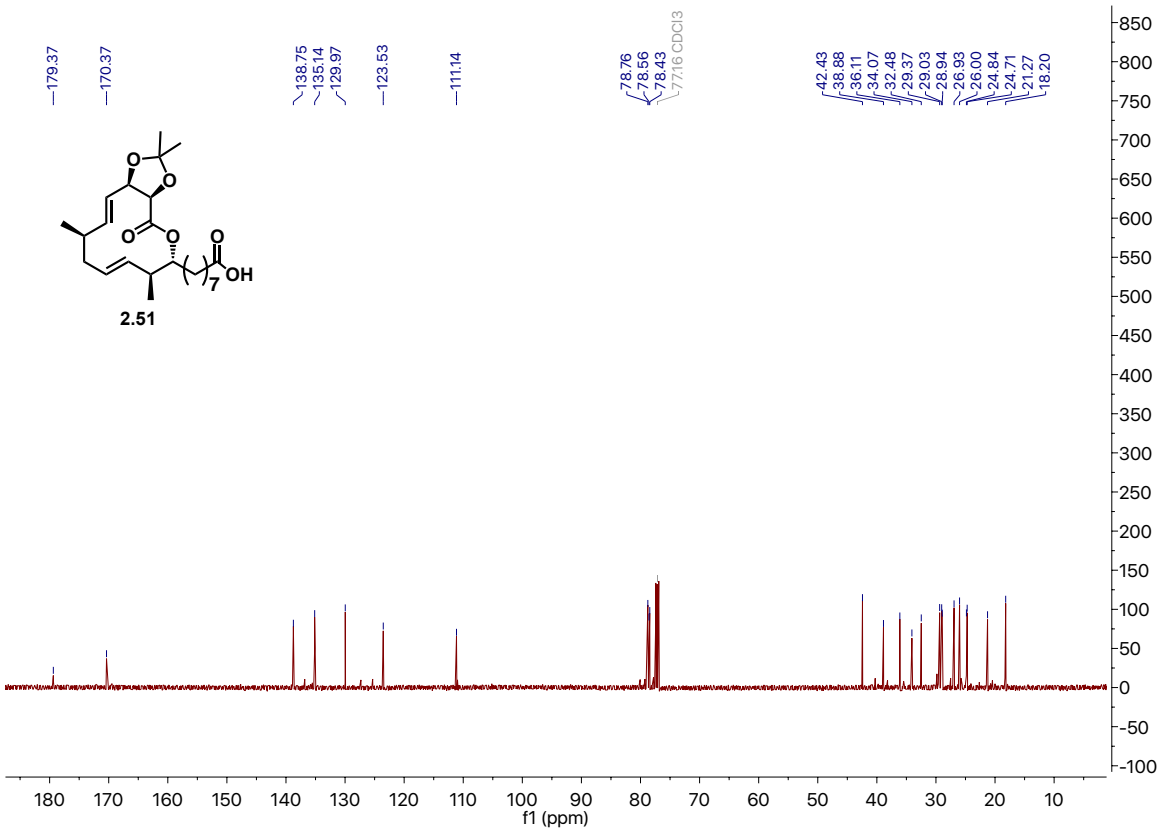
179.37
170.37
138.75
135.14
129.97
123.53
111.14
78.76
78.56
78.43
77.16 CDCl3
42.43
38.88
36.11
34.07
32.48
29.37
29.03
28.94
26.93
26.00
24.84
24.71
21.27
18.20
2.51
f1 (ppm)

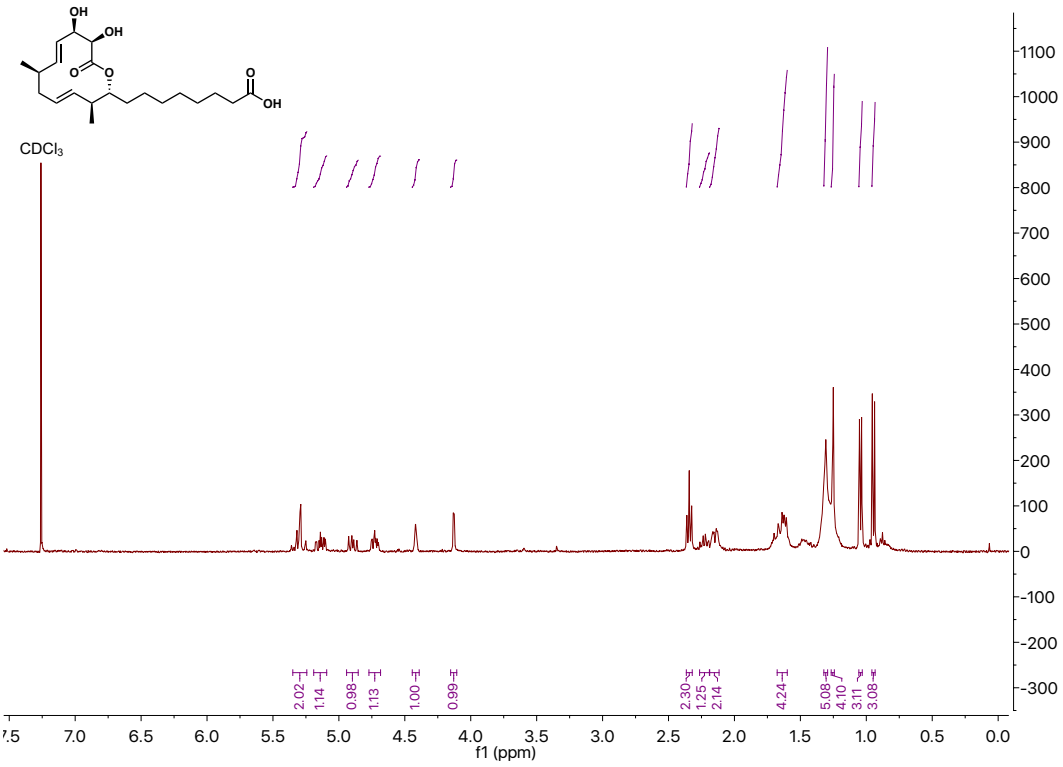
OH
OH
O
O
O
OH
CDCl3
2.02
1.14
0.98
1.13
1.00
0.99
2.30
1.25
2.14
4.24
5.08
4.10
3.11
3.08
f1 (ppm)

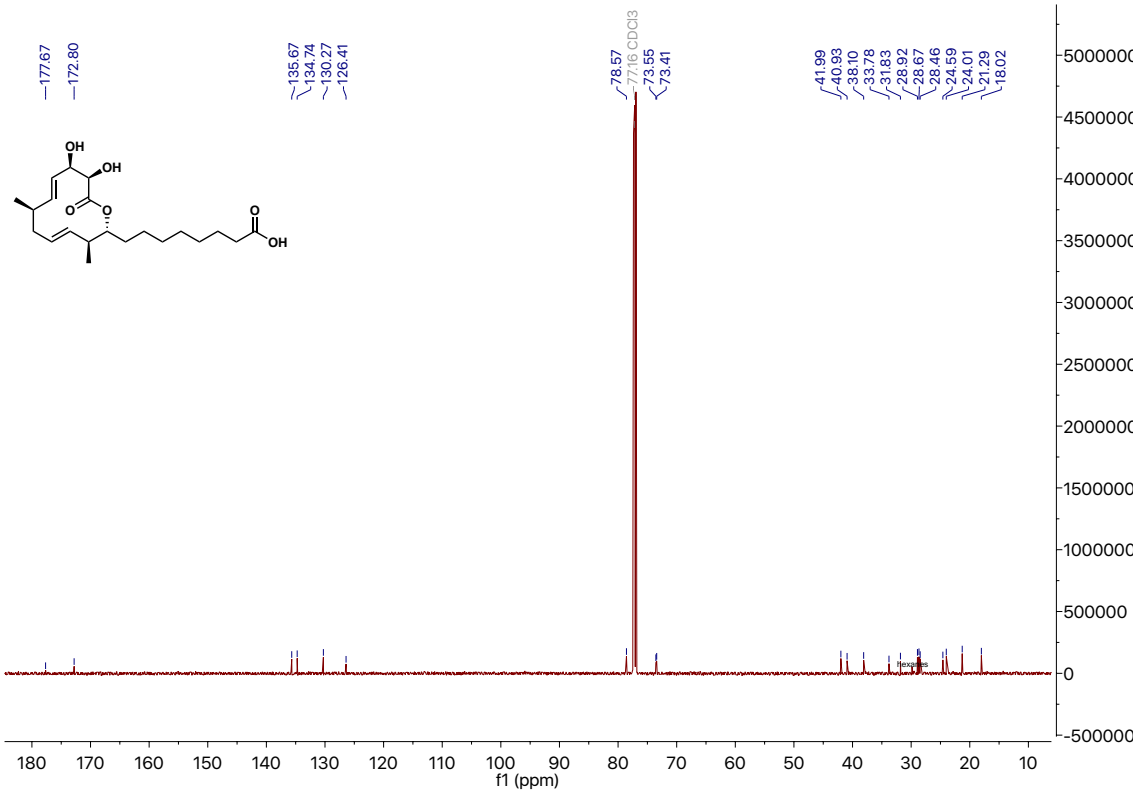
177.67
172.80
135.67
134.74
130.27
126.41
78.57
77.16 CDCl3
73.55
73.41
41.99
40.93
38.10
33.78
31.83
28.92
28.67
28.46
24.59
24.01
21.29
18.02
OH
OH
O
O
O
OH
f1 (ppm)

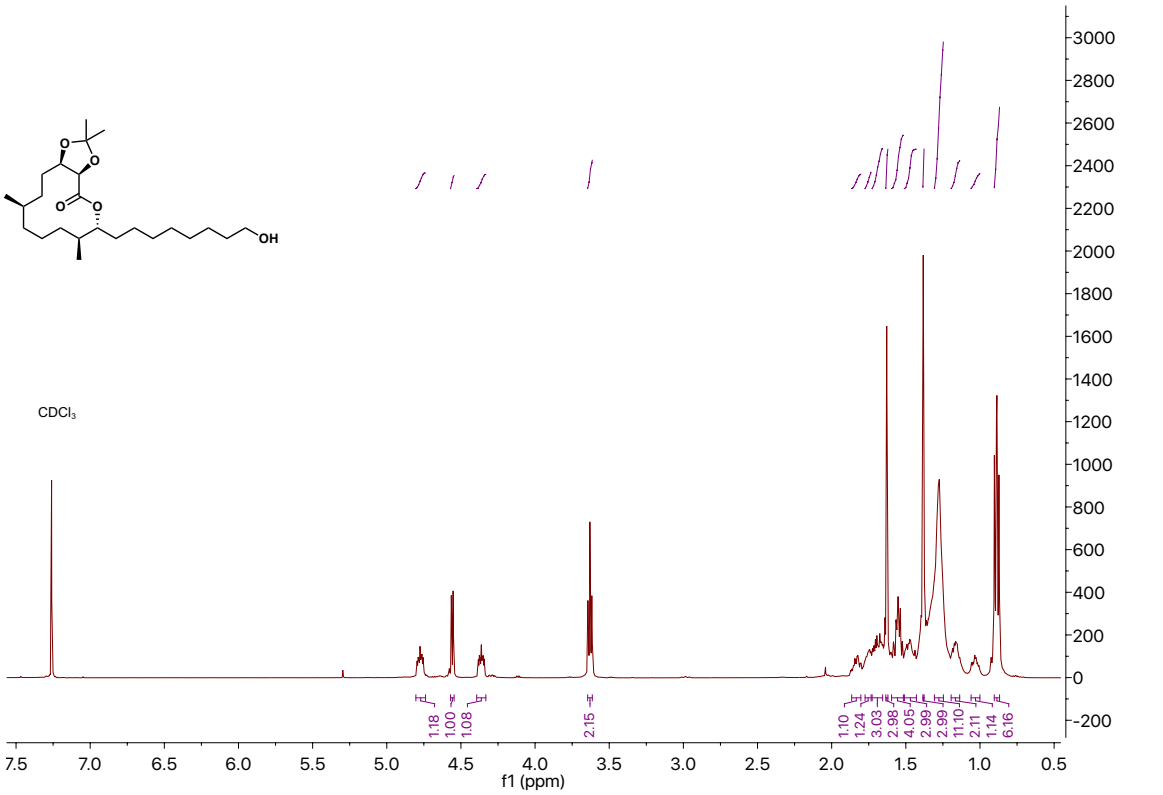
OH
CDCl3
1.18
1.00
1.08
2.15
1.10
1.24
3.03
2.98
4.05
2.99
2.99
11.10
2.11
1.14
6.16
f1 (ppm)

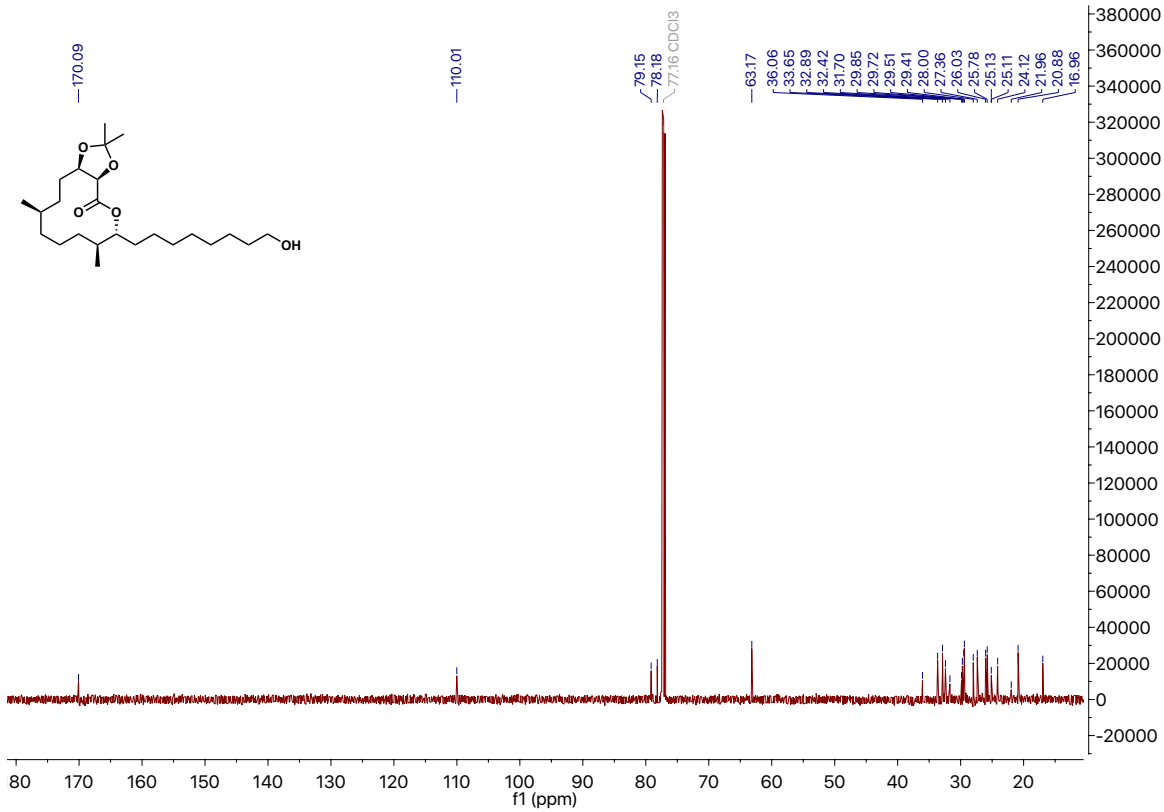
OH
170.09
110.01
79.15
78.18
77.16 CDCl3
63.17
36.06
33.65
32.89
32.42
31.70
29.85
29.72
29.51
29.41
28.00
27.36
26.03
25.78
25.13
25.11
24.12
21.96
20.88
16.96
f1 (ppm)

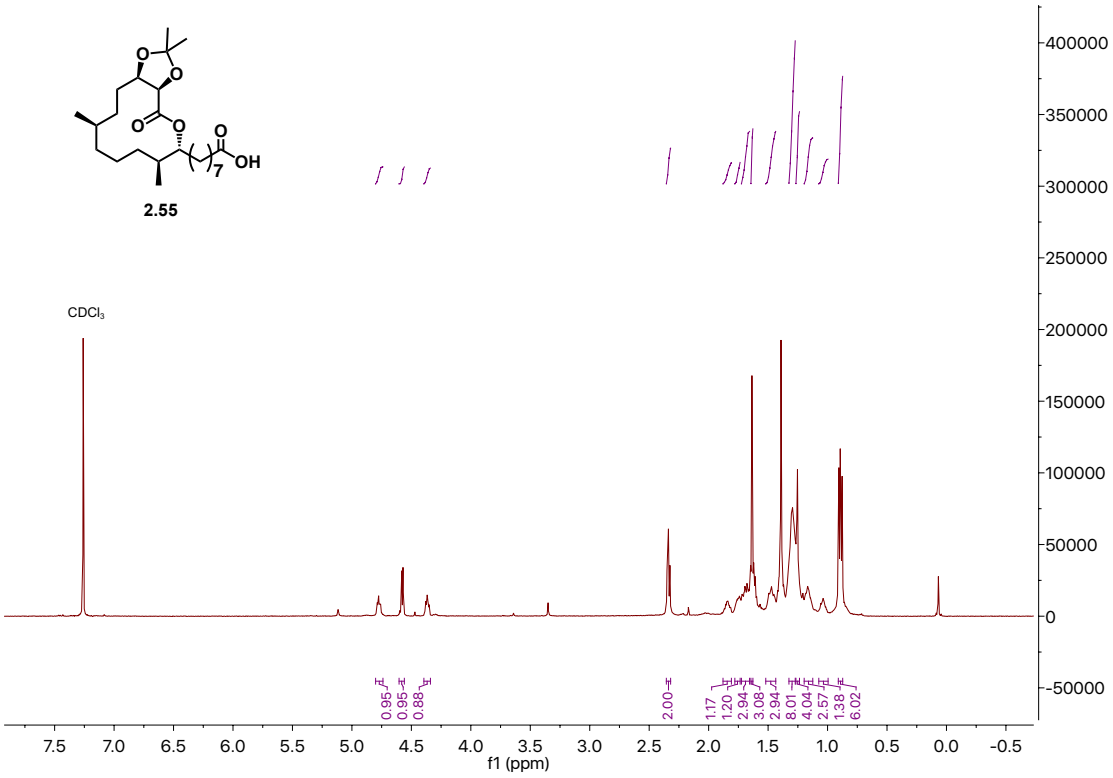
2.55
CDCl3
0.95
0.95
0.88
2.00
1.17
1.20
2.94
3.08
2.94
8.01
4.04
2.57
1.38
6.02
f1 (ppm)

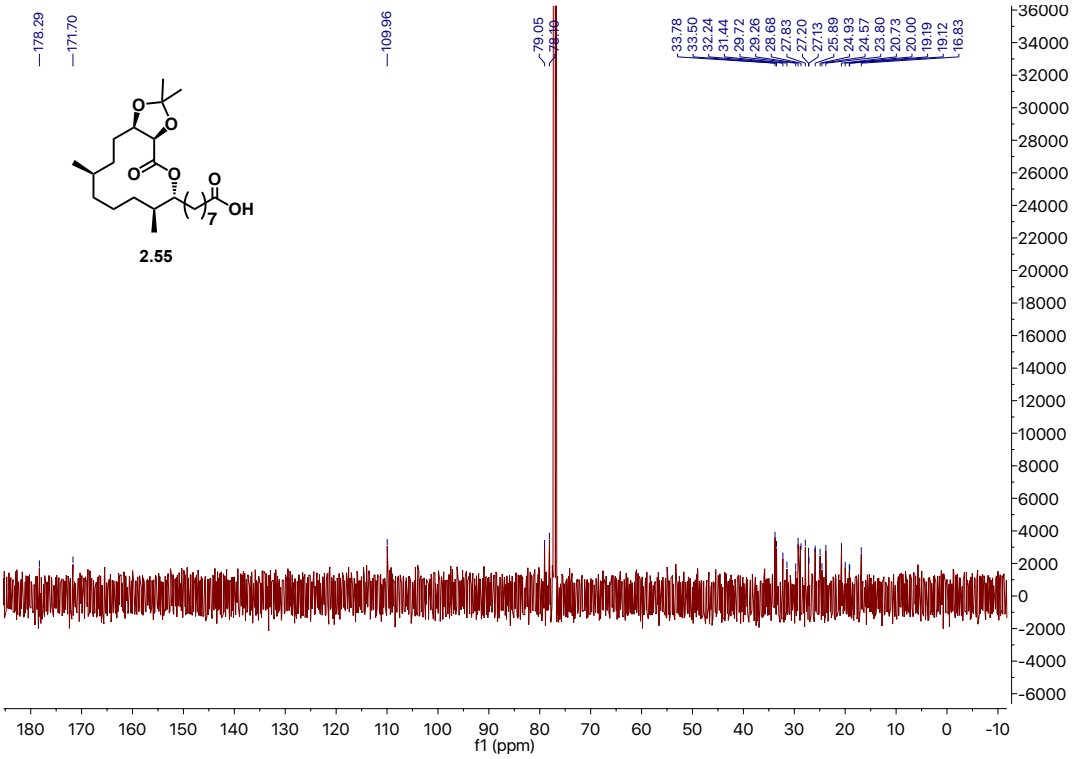
178.29
171.70
109.96
79.05
78.40
33.78
33.50
32.24
31.44
29.72
29.26
28.68
27.83
27.20
27.13
25.89
24.93
24.57
23.80
20.73
20.00
19.19
19.12
16.83
2.55
f1 (ppm)

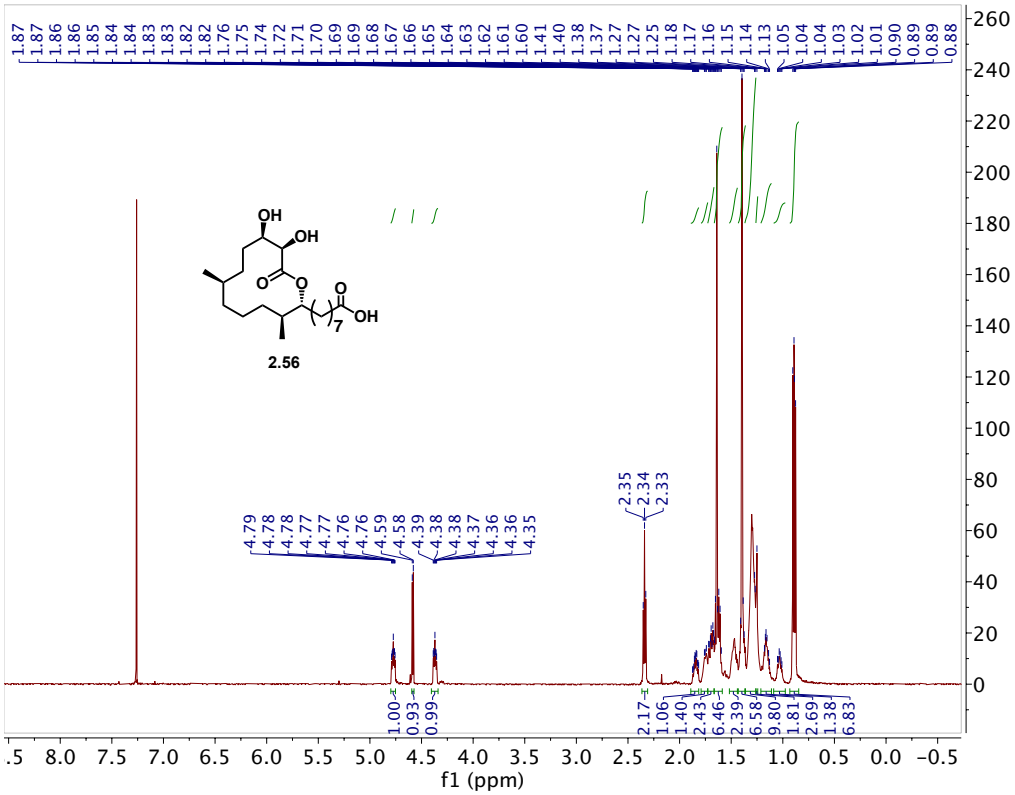
OH
OH
O
O
O
OH
7
2.56
f1 (ppm)

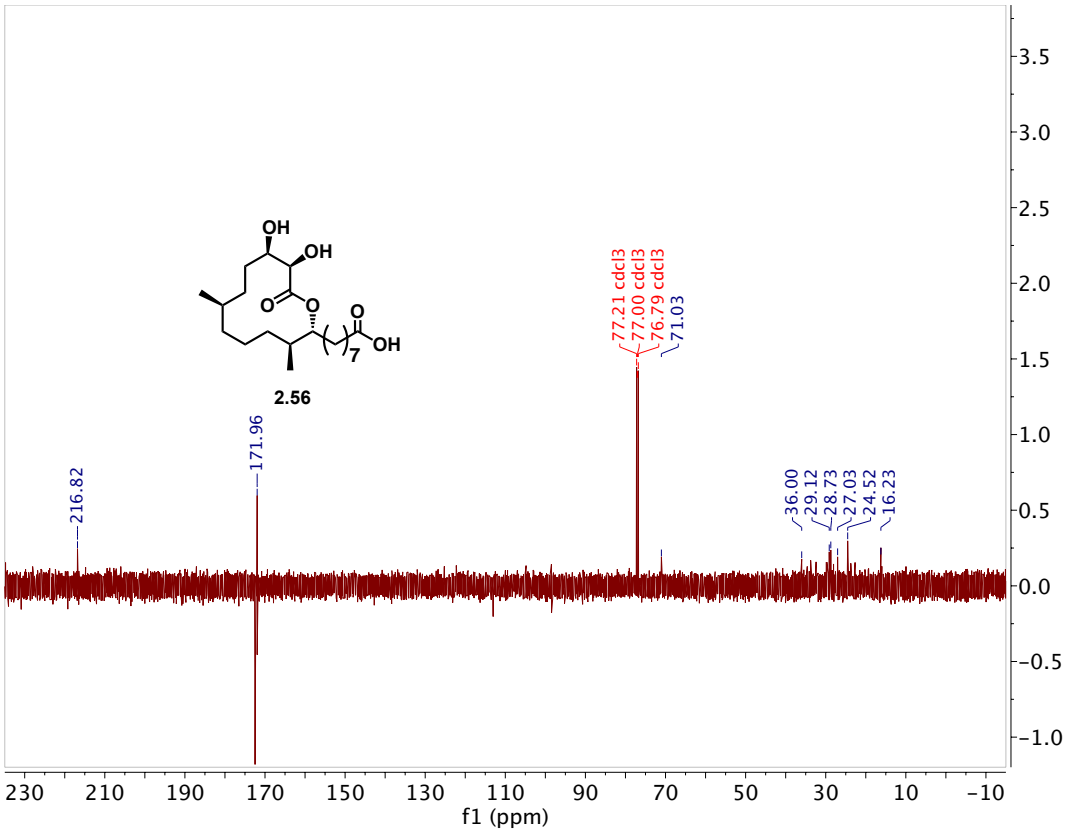
OH
OH
O
O
O
OH
7
2.56
77.21 cdcl3
77.00 cdcl3
76.79 cdcl3
71.03
216.82
171.96
36.00
29.12
28.73
27.03
24.52
16.23
f1 (ppm)

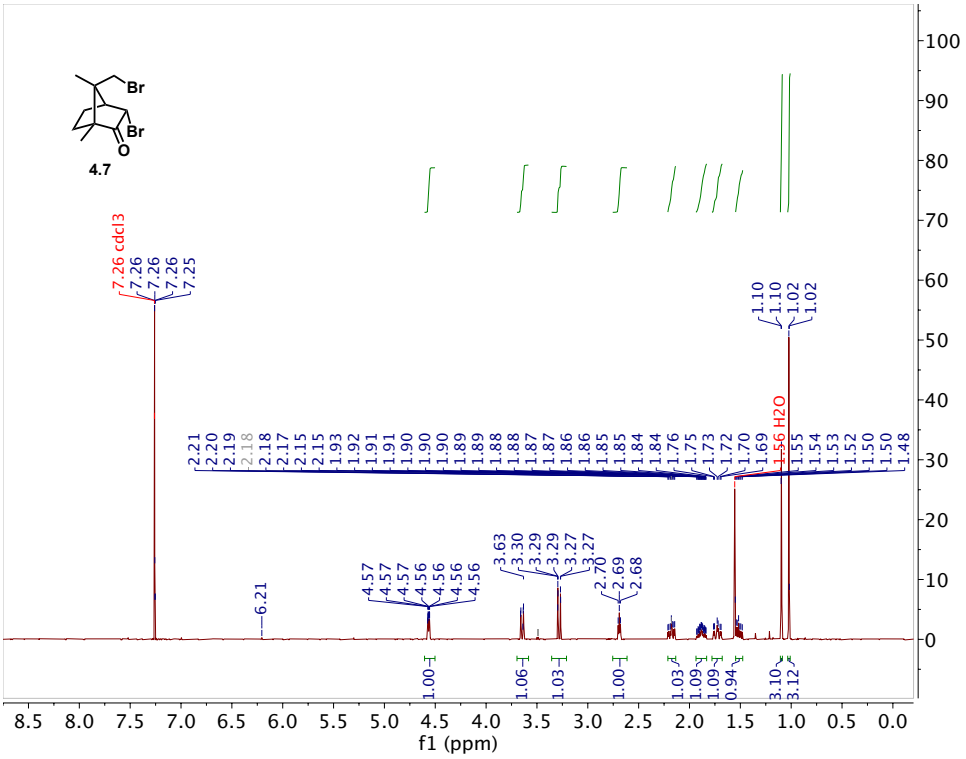
Br
Br
O
4.7
7.26 cdcl3
1.56 H2O
6.21
f1 (ppm)

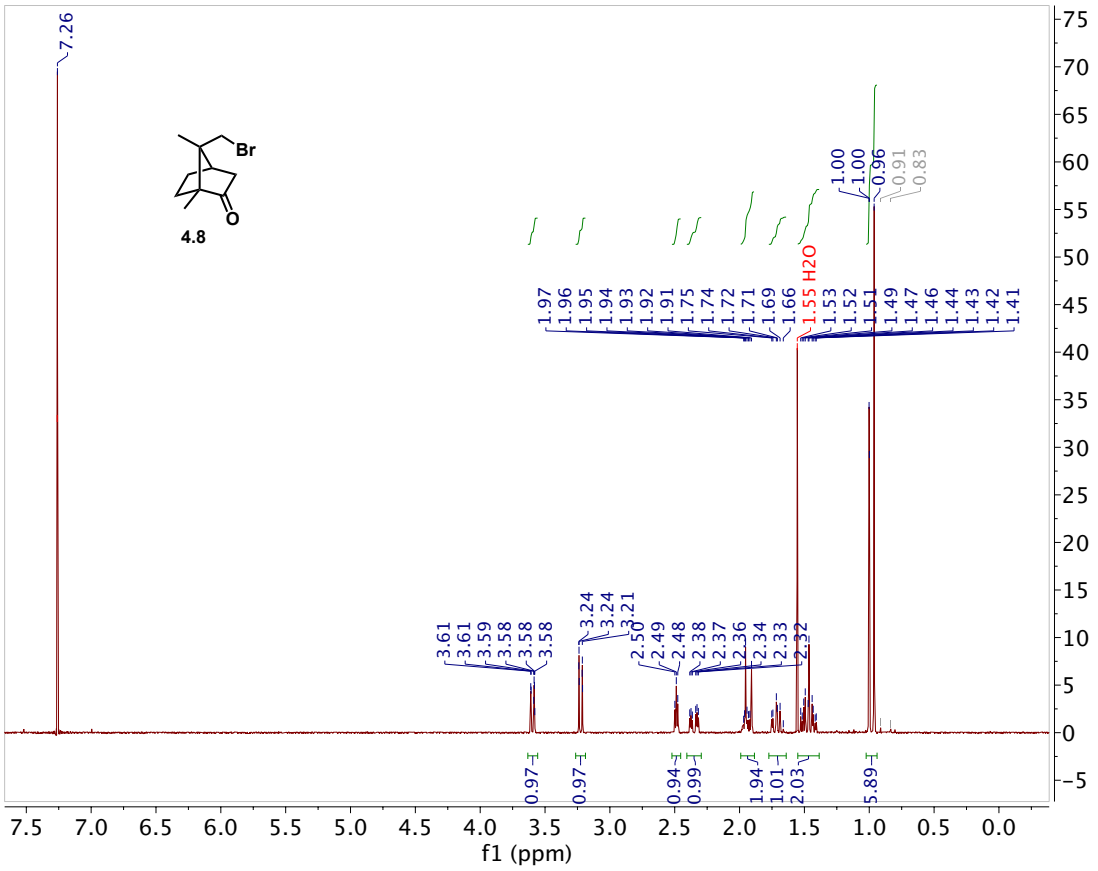
Br
O
4.8
7.26
1.55 H2O
f1 (ppm)

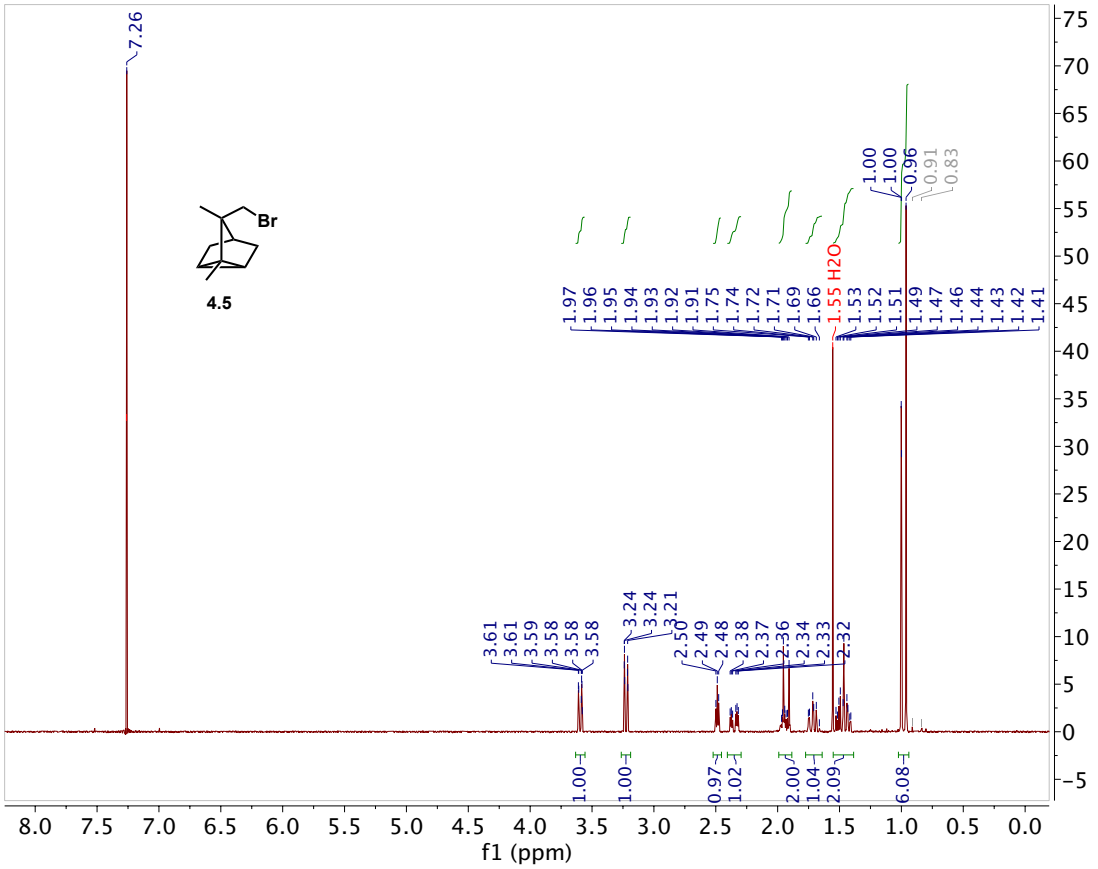
7.26
Br
4.5
H2O
f1 (ppm)